EUSKAL HERRIKO UNIBERTSITATE EHU/UPV

Ullmann coupling reaction in unconventional surfaces

Author:
Mikel ABADIA GUTIERREZ

Supervisor:
Dr. Celia ROGERO, Dr. Jens BREDE

A thesis submitted in fulfillment of the requirements for the degree of Doctor of Philosophy in Material Physics

Departamento de Física de Materiales

May 24, 2017

"To family and friends "

Mikel Abadia

Abstract

Ullmann coupling reaction in unconventional surfaces

by Mikel ABADIA GUTIERREZ

Extremely high electron mobility as well as its low dimensionality makes the graphene a good candidate to be incorporated in future organic-devices such as field effect transistors (FET). However, prior to its implementation a band gap must be introduced in the graphene. Towards this end, one of the most promising strategies is quantum confinement, i.e. shrinking the size of the graphene into smaller structures such as graphene-nanoribons (GNR), where the band gap is controlled by the lateral confinement of the final structure.

The surface assisted Ullmann coupling allows the synthesis of said GNRs. However, reasonable reaction yields and sufficiently extended GNRs can so far only be realized on coinage metals where the GNRs properties are inherently coupled to the surface and therefore inaccessible for device applications such as the FET. Consequently, the next step forward in the field either requires the larger scale synthesis of GNRs for *ex situ* transfer protocols onto more suitable substrates or the *in situ* synthesis of GNRs directly on technologically relevant surfaces.

Here, we synthesize poly-p-phenylene (PPP) wires, the smallest possible GNR, *via* the Ullmann coupling reaction on three unconventional surfaces. We achieve the first PPP synthesis on a magnetic template, where it is demonstrate that the intermixing of elements in the bimetallic $GdAu_2$ surface alloy is a viable strategy to improve the reaction conditions by synergistic effects while maintaining the extraordinary alignment and extensions of individual PPP generally only achievable on Au (111) surfaces. Another strategy to optimize the reaction conditions and alignment of GNRs is the use of surface steps. We employ a curved Au (111) crystal, where the surface step density is continuously varied across the same sample, to synthesize PPPs. The comparison of the reaction on different parts of the crystal performed under identical conditions, such as reaction temperature and molecule coverage, allows us to unambiguously isolate the influence of the steps. The central finding is a lowering of the reaction temperature by 25 K when using the right kind of surface step orientation and density. In the last chapter, we demonstrate the formation of PPP wires on the dielectric TiO_2 (110) surface, a model surface for the realization of a FET. Optimized reaction temperatures and yields are achieved when an external catalyst is employed while simultaneously suppressing unwanted side reactions.

The on-surface synthesized PPPs offer the possibility of characterization by well-established surface science techniques. Specifically, we employ scanning tunneling microscopy (STM) and low energy electron diffraction (LEED) to elucidate geometric structures of the PPPs, angle resolved photoemission spectroscopy (ARPES) to probe the valence band of the PPPs and x-ray photoelectron spectroscopy (XPS), the core technique of this work, to study reaction yields and mechanisms. The combination of our design strategies and the experimental multi-technique approach has established novel substrates for the realization of next generation GNR-based devices such as the FET.

Laburpena

Ullmann coupling reaction in unconventional surfaces

by Mikel ABADIA GUTIERREZ

Elektroien mugikortasun paregabea eta dimentsio baxuak medio, grafenoa etorkizuneko material bezala ezagutzen da gaur egun. Hala ere, grafenoan oinarrituriko gailu mekaniko, elektriko naiz optoelektrikoak sortu ahal izateko, "gap" bat ireki behar da grafenoaren propietate elektronikoetan, eta hauxe da bada, zientziak gaur egun duen erronkarik haundienetariko bat.

Gap hau irekitzeko modu ugari aurkeztu diren arren, agian erakargarriena grafenoaren konfinamentu kuantikoan datza, hau da, grafenoaren tamaina ikaragarri murriztean (bi dimentsiotik dimentsio batera) alegia. Ondorioz, grafenoa, grafeno hari bihurtzen da, eta hari hauei *graphene nanorribon* (GNR) deritzaie. GNR hauek, grafenoaren propietate elektriko antzekoak izateaz gain, gap intrintseko bat dute. Beraz, etorkizuneko gailuetan erabiltzeko grafenoa baino aproposagoak dira.

Gainazal batek bideraturiko Ullmann erreakzioaren bitartez, GNRak modu oso kontrolatuan sortu daitezke gaur egun, euren egitura atomikoaren gain kontrola mantenduaz. Oinarria, aurrez diseinaturiko molekula organiko batzuk gainazal baten gaitasun katalitikoaz baliatuz erreakzionaraztea da. Azken hamarkadan, lan ugari egin da Ullmann erreakzioaren inguruan, eta esan daiteke, gainazal metalikoetan behintzat, GNRaren sintesia guztiz barneratua dagoela. Baina gailu elektronikoetan erabili ahal izateko, GNR hauek ezin dira gainazal metalikoekin kontaktuan egon, beraien propietateak metalarenarekin elkarbanatzen baitira. Ondorioz, hurrengo erronka, eta hemen aurkezten ari garen lanaren helburua, GNRak zuzenean teknologikoki erakargarriagoak diren gainazaletan sortzea da.

Lan honetan, Ullmann erreakzioaz baliatuz, poly-p-phenylene (PPP) izeneko polimeroaren sintesia, teknologikoki esanguratsuak diren hiru gainazal ezberdinetan frogatuko da. PPPa, tamainaz lortu daitekeen GNRrik txikiena da eta ondorioz interesgarria bai transistore zein aplikazio optoelektrikoetarako. Bestalde, erreakzioa bultzatzeko erabiliko diren hiru gainazalak ondorengoak dira:

1. $GdAu_2$ aleazio bimetaliko ferromagnetikoa.
2. Urre kurbatua c-Au (111).
3. Oinarrizko erdi-eroale moduan, titanio dioxidoa TiO_2 (110).

Lehen atalean, PPPak gainazal magnetiko baten gainean nola hazten diren azaltzen da. Konkretuki $GdAu_2$ izeneko aleazio bimetaliko ferromagnetikoaren gainean. Material magnetikoen erreaktibitate handia dela eta, normalean molekulekin kontaktuan jartzean, azken hauen disoziazio edo suntsipena eragiten dute. Arrazoi hau eta beste hainbat medio, orain arte ez da lanik izan Ullmann erreakzioa gainazal magnetiko baten gainean erabili daitekela frogatu duenik. Arlo honetan beraz, gure lanak ate berriak ireki ditzakela uste dugu.

Bestalde, gainazaletako eskaloi edo koxkek, Ullmann erreakzioaren etekinean duten eragina aztertu da. Jakina da gainazal koxkak katalizatzaile eraginkorrak direla. Koxkak osatzen dituzten atomoek, gainazal bat osatzen dituezten atomo guztietatik koordinazio baxuena dute eta honek, erreakzio kimikoetan, elektroi zein karga desberdinak partekatzeko ahalmena ematen die. Ondorioz, gure interesa, Ullmann erreakzioa gauzatzeko beharrezkoa den energia, koxkek murriztu dezaketen jakitea da. Horretarako urre kurbatu bat, c-Au (111) erabili dugu, batik bat bi arrazoirengatik. Alde batetik, Ullmann erreakzioa oso ezaguna da urrezko gainazaletan eta beraz erreferentzitzat erabil daiteke. Bestetik, urre kurbatuaren gainazalak koxka dentsitate aldakorra du, kurbaduraren izkinetan dentsitatea haundia izanik eta erdi aldean aldiz baxua. Ezaugarri hauek medio, Ullmann erreakzioa gainazal osoan zehar gauzatu ostean, 25 K erreakzio temperature diferentzia dagoela frogatu da koxka eta gainazal lauaren artean. Ondorioz, goraipatua geratu da gainazal koxken gaitasun katalitikoa. Etorkizun batean, GNRaren erabilera industri mailara iritxi ezkero, gainazal koxkadunak energia kontsumoa murrizteko estrategi bezala erabili ahal izango dira.

Azkenik, Ullmann erreakzioaren bitartez PPPak TiO_2 (110) gainazal erdi-eroalean sintetizatu dira. Material erdi-eroaleak, gaur egungo transistore industriaren oinarriak dira eta ondorioz, hauen gainean GNRak sortzeak interes handia sorrarazten du. Badira iada lanak, Ullmann erreakzioaren gaitasuna beste gainazal erdi-eroaletan aztertu dituztenak. Hala ere, eta emaitza esanguratsuak aurkeztu izan arren, lorturiko GNRen kalitatea ez da guztiz ona izan eta gainaera, gainazalaren paper katalitikoa ez da garbi deskribatu. Guk TiO_2-aren gainean kalitate altuko GNRak sortu daitezkela frogatu dugu. Gainera, erreakzioan zehar gainazalaren eragina sakonki aztertu ostean, erreakzioa beste gainazal esanguratsu batzuetara mugitzeko "errezeta" baliagarri bat proposatu dugu. $GdAu_2$-rekin bezala, gure aurkikuntzak ate berriak ireki ditzakela espero dugu.

Orain arte deskribaturiko aurkikuntza guztiak, gainazal zientzian ezagunak diren ikerkuntza teknika jakin batzuen bidez lortu dira. Alde batetik, gainazal desberdinetan zehar GNRek duten geometria eta estruktura tunel efektuko mikroskopio (STM) eta energia baxuko elektroien difrakzio (LEED) bidez ikertu da. Bestetik, GNRren propietate elektrikoak, grafenoaren pareko egiten dutenak, angulu erresoluzio dun fotoemisio espektroskopia (ARPES) bidez aztertu dira. Azkenik, erreakzioaren oinarri kimikoak, X izpiko fotoemisio espektroskopia bidez argitu dira.

Acknowledgements

To everyone I had the privilege to meet during this amazing journey
and specially to
Celia for always trusting on me, and to
Jens for showing me how science should be and is not.

...

Contents

List of Figures

Dedicated to curiosity

Chapter 1

Introduction

The most prominent features of graphene are its high charge-carrier mobility and ultimate thinness of just one atomic layer. These two properties alone, lead researchers to envision new electronic and optoelectronic applications of the material [1, 2]. The key obstacle toward graphene based devices is, however, the intrinsic lack of a band gap, which makes it challenging to switch the device between "on" and "off" state. Therefore, the next step forward in device implementation was to open an electronic gap while preserving the other extraordinary properties of graphene.

Graphene nanoribbons (GNRs), blend many of the exotic electronic properties observed in graphene sheets with a structurally tuneable band gap. Quantum effects imposed by parameters such as width, length, edge symmetry, and doping pattern allow the GNR band structure to be rationally designed [3–8]. As a consequence, GNRs have emerged as promising candidates for replacing graphene in high performance, nanoelectronic, spintronic, and optoelectronic devices due to their unique and relatively easily tunable physical properties.

While a variety of top-down approaches have pioneered the synthesis of GNRs the harsh reaction conditions and the limited structural control of lithography-based manufacturing techniques have thus far prevented access to nano-scale and atomically precise GNRs with sizeable bandgaps required for many electronics applications [9–12]. An alternative strategy towards GNR production is the bottom-up synthesis. Surface-assisted chemical reactions of specifically designed organic precursors provides an alluring alternative toward atomically precise GNR production. Besides, the symbiosis of GNR synthesis and surface science has opened the unique opportunity to directly study, using advanced characterization techniques previously unavailable, the exotic properties of GNRs. Spin polarized edge states, size dependant band gaps, effective mass determinations, n and p type doping and chemical functionalization , are some of the GNRs properties that have been addressed experimentally by scanning tunneling microscopy (STM) and angle-resolved photoemission spectroscopy (ARPES) techniques [4, 7, 13–15].

The most widely used recipe for precise surface assisted GNR synthesis consist on two chemical processes, known as the Ullmann coupling and cyclodehydrogenation reactions. While the former is the responsible of binding the precursor molecules through dehalogenation and homo coupling processes, the latter is responsible of either expanding or fusing the previously synthesize polymer constituents by cyclodehydrogenation [6]. However, it is well established that the Ullmann coupling, the first step of the reaction, is often limiting the successful GNR formation.

In the early 1900's Fritz Ulllmann first reported that heating of o-Bromnitrobenzol in fine copper powder resulted in the dinitrobiphenyl [16] and a little later that o-chlorobenzoic acid, aniline and copper led to the formation of N-Phenylanthranilic acid with "impressive" yields [17, 18]. The pioneering work demonstrated aromatic

nucleophilic substitution mediated by copper which is now known as the "Ullmann condensation reaction" with the copper mediated synthesis of biaryls from aryl halides commonly known as the "Ullmann reaction". More than a hundred years after the discovery by Ullmann, the reactions is used in numerous industrial applications, e.g. as intermediates in pharmaceutical and polymer chemistry, and reaction pathways were continuously optimized and modified [19, 20]. The advent of one of these modified Ullmann reactions was in the early 1990s in the field of surface science: Zou and co-workers [21] as well as Xi and Bent [22, 23] used a variety of surface science techniques to study the homocoupling of aryl halides on noble metal surfaces under UHV conditions.

In particular the influence of different metal surfaces, such as Ag(111) and Cu(111), on the activation temperatures of the reaction were elucidated and the detection of phenyl radicals as intermediates in the reaction was achieved. In 2000 Hla *et al.* used STM to induce the homo-coupling of iodobenzene on a Cu(111) surface at low temperatures [24]. While McCarty and Weiss demonstrated the viability of the surface confined Ullmann reaction for the synthesis of extended oligomers in 2004 [25] it was perhaps not until the work by Grill *et al.* in 2007 [26] that the reaction became widely studied topic in particular with STM under ultra-high vacuum (UHV) conditions. Much of the interest was fostered as, in the wake of graphene, atomically precise graphene nanoribbons were synthesized using, in the first step, the Ullmann coupling on an Au(111) surface, [27, 28] as introduced above .

On the one hand, the understanding of the Ullmann coupling reactions of various molecules on the three coinage metals, Cu, Ag, and Au under UHV conditions explored by many groups is beginning to reach a comprehensive pictures concerning reaction yields, polymer length, network quality, activation temperatures and organometallic as well as radical intermediate states [29–31], on the other hand, the maturity, in particular in the field of graphene nanoribbon synthesis, poses new challenges. Specifically, the next step in the field toward device applications requires the transfer of the UHV synthesized GNRs from the Au(111) surface onto suitable, e.g. semiconducting or magnetic substrates for the realization of *e.g.* FET and spin-FET transistors. Transfer-protocols are already well established for large scale chemical vapour deposition (CVD) grown graphene and first experimental results [32, 33] of device fabrication based on Au(111) grown GNRs transferred onto SiO_2 are encouraging. Consequently, new methods for larger scale GNR fabrication optimizing yield and energy consumption while preserving the properties and extension of GNRs, so-far only achievable on Au(111), are desired.

In the present work, Ullmann based bottom-up synthesis of the smallest possible GNR, i.e. poly-p-paraphenylene (PPPs), is accomplished on the bimetallic (and ferromagnetic) $GdAu_2$, curved Au (111) and semiconductor TiO_2 (110) surfaces.

In chapter 4 the synthesis of PPP is achieved on a magnetic substrate. The ferromagnetic $GdAu_2$ surface alloy, on the one hand presents a viable route toward studying emergent intrinsic magnetic properties in these novel molecular structures [34], a promising route for supplementing rational design strategies for single molecular magnets [35]. On the other hand, surface alloying is a way to extend and tune the range of physical and chemical properties of a metallic system. Therefore its implementation in the reaction is presented as a strategy to tune the surface catalytic properties and optimizing reaction conditions while preserving mesoscale extension and alignment of the individual GNRs.

In chaper 5 another route toward the optimization of the on-surface Ullmann reaction toward GNR fabrication follows the field of heterogeneous catalysis, where

steps are known to be some of the most efficient sites for triggering catalytic processes. An instructive example is the oxidation of CO by gold nanoparticles. Despite the inert character of Au [36], Janssens *et al.* [37] demonstrated increased catalytic activity of Au nanoparticles with decreasing particle size, i.e. by increasing the step atoms per surface area. Therefore, enhancing the density of steps is envisioned as a promising strategy to also improve the catalytic properties of a given surface for GNR synthesis. Toward this end, a curved crystal is a perfect template to systematically study the influence of the step density, which is tuned continuously across the crystals curvature, while keeping all other reaction parameters identical across the entire surface.

Another and perhaps technologically more relevant strategy for an all in-situ synthesis of a GNR based FET is explored in chapter 6. Here, the growth of PPP on the semiconductor rutile TiO_2 (110) surfaces is demonstrated.

The first step towards the demonstration of GNR formation on a semiconducting surface was given in 2011 by *Kittelmann et al* [38]. They showed the covalent linking of halide-substituted benzoic acid molecules by thermal activation (contrary to the surface catalyzed reaction on coinage metals) on insulating calcite (104) surface. Later, the works performed by Olszowski *et al*. [39] and Kolmer *et al*. [40] probed the coupling of halogenated precursors on hydrogenated Ge(001) and rutile TiO_2 (011) semiconductor surfaces, respectively. However, in these works, the coupling products observed were rather short and very few compared to the results achieved on metal surfaces. Besides, the reaction paths where not fully elucidated. Here we achieve substantially improved polymerization yields compared to the previously reported ones. Based on novel insights into the reaction mechanisms the optimized reaction conditions are achieved when an external catalyst is employed while simultaneously suppressing unwanted side reactions.

Ultimately, it can be envisioned that the realization of GNR on the model semiconductor TiO_2 (110) paves a new path towards the integration of these structures into multifunctional electronics devices.

Chapter 2

Experimental part

Throughout this work, we use a multitechnique approach to address the characteristic features of the surface catalyzed Ullmann coupling reaction.

With scanning tunneling microscope (STM), we obtain a sub molecular resolution of the adsorbate molecules and their local arrangements, as well as the local structure of the surface. Complementary diffraction technique, particularly low energy electron diffraction (LEED), is used to obtain information of the surface average structure. With X-ray and UV light photoemission spectroscopy (XPS and UPS) we attain chemical specificity and follow the reactions *in situ*. Finally, by angle resolved photoemission spectroscopy (ARPES) measurements, we map the dispersive and non-dispersive character of the molecular bands.

In this chapter, the basic principles of the aforementioned techniques are summarized, focusing mainly on those aspects relevant for this work.

2.1 Scanning tunneling microscopy

Scanning tunneling microscopy (STM) is a microscope able to attain at the atomic level, a direct real space determination of the surface structure in three dimensions, including non-periodic structures. Its development in 1981 earned its inventors, Gerd Binnig and Heinrich Rohrer, the Nobel price in physics in 1986 [41].

In STM, a metallic tip (usually made of W, PtIr or Au) is brought into such a close proximity ($\approx$ -3-5 Å) to an electrically conducting sample surface, that an overlap occurs between the tip and the sample wave functions (which decays exponentially into the junction gap, see figure 2.1 (a)). If a small bias voltage is applied between the tip and the sample, the overlap of the electron wave functions permits quantum mechanical tunneling and establishes a small tunnel current within the nano-ampere range. Depending on the polarization of the applied bias, current can flow from the tip to the sample and vice versa, probing the occupied and unoccupied states of both systems.

A design of the STM is sketched in figure 2.1 (b). The simplest set-up, consist on a conducting tip, controlled normally by piezoelectric transducers, that is used to scan a sample surface. Taking into account that the tunneling current depends exponentially on the distance between the tip and the surface, small variations of the local surface structure entails variations on the tip sample distance and therefore, changes on the tunneling current. The most used STM operational mode, and the one employed throughout this work, is the "constant current mode". The tunneling current is compared with a pre-set constant current value and the difference between the measured and preset values derives in a feedback signal. This signal provides a correction voltage to the z piezo transducer that causes the change in the tip-sample z

distance. Consequently, by recording the variation the feedback signal as a function of the lateral (*x*,*y*) tip position, a map of the surface topography is yielded.

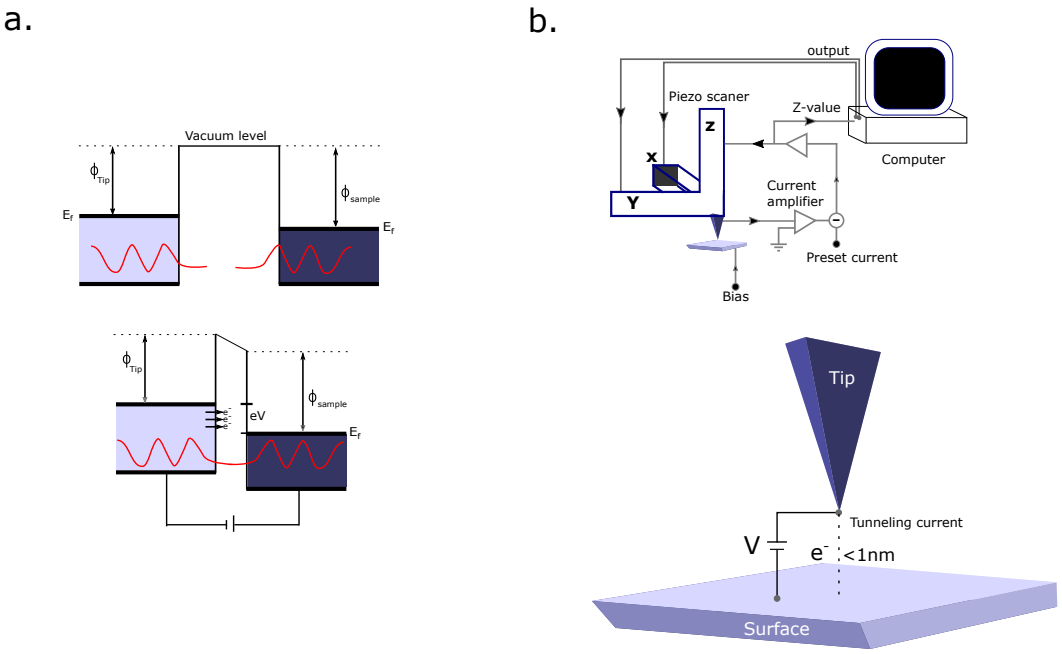

FIGURE 2.1: Scanning tunneling microscopy. The basis of the tunneling process between two electrodes is sketched in (a). At sufficient small distances and under an applied bias, the electron wave function of both electrodes can overlap and therefore current can flow. A regular STM set-up is shown in (b)

2.1.1 Tunneling theory

The most accepted theories for electron tunneling in an STM are based on the "perturbative-transfer Hamiltonian" formalism introduced by Bardeen for tunneling between two parallel electrodes separated by and insulator [42]. In this formalism, the tunneling current is evaluated from the overlap in the gap region of the wave function of the sample and the tip, ψ_s and ψ_t, considered as separate systems [43]:

$$I(V) = \frac{4\Pi e}{\hbar} \sum_{s,t} |T_{s,t}|^2 \, \delta(E_s - eV - E_t) \times (f(E_s - eV, T)[1 - f(E_t, T)] \\ - f(E_t, T)[1 - f(E_s - eV, T)] \tag{2.1}$$

where

$$T_{s,t} = -\frac{\hbar^2}{2m_e} \int_{S_0} dS(\psi)_t^* \bigtriangledown \psi_s - \psi_t \bigtriangledown \psi_t^* \tag{2.2}$$

In Eq. 1.1 the summation goes over all quantum states *s* and *t* of the unperturbed sample and tip; the eigenvalues E_s and E_t are given respect to the common Fermi level, f is the Fermi-Dirac distribution function, and T is the temperature. Dirac function takes into account that tunneling occurs from filled to unfilled states. The

integral 1.2 gives the tunnel matrix element $T_{s,t}$ and must be evaluated over any surface S_0 that lies within the gap region. Indeed, the main difficulty in this approach consists in evaluating $T_{s,t}$. An smart simplification of the problem was introduced by Tersoff and Hamann using as tip functions the solutions of the Schrödinger equation for a spherical potential wall (s-wave approximation) [44]. Assuming a low temperature where the Fermi distribution can be replaced by an step function, and a low bias situation (states close to Fermi energy) the current given by this approximation is,

$$I(V,x,y,z) \propto e^{-2z}\sqrt{\frac{2m_e\overline{\Phi}}{\hbar^2}}\int_0^{eV} dE\rho_s(E,x,y,z)\rho_p(E-eV). \tag{2.3}$$

where

$$\overline{\Phi} = (\Phi_s + \Phi_t)/2 \tag{2.4}$$

is the average value of the tunneling barrier with respect to E_f and

$$\rho_s(E,x,y,z) = \sum_t |\psi_t(x,y,z)|^2\,\delta(E-E_t) \tag{2.5}$$

is the LDOS of the sample surface at the position (*x,y,z*) of the center of the tip.

Two main conclusions can be extracted from this approximation [45]: the first is that the tunneling current decays exponentially with increasing distance z in between the tip and the sample. The second is that constant-current STM topographs are simply interpreted as contours of constant $\rho_s(E_f)$ of the surface. This is because the largest contribution to the integral in Eq 1.3 comes from the highest-lying energy states of the sample, while the tip electronic structure can be considered flat, i.e ρ_t is taken to be constant.

2.2 Photoemission spectroscopy

Electron spectroscopy based techniques are extraordinary tools in surface science. The working principle behind is to probe and extract electrons from matter using photons or electrons as an external stimulus. The analysis of these ejected electrons offers a way to experimentally probe the properties of matter. Besides, working with electrons entails some experimental advantages [46, 47]:

1. electrostatic fields provide an easy way to focus electrons and analyse their energy and momentum.
2. contrary to ions or atoms often employed as probes in surface science techniques, electrons are easy to count and vanish after being detected.
3. due to the escape depth of electrons (few Å) surface sensitivity is attain. See figure 2.2 for more details.

In the present research work we use electron spectroscopy to gather insight on the chemical and electronical properties of individual molecules, polymers and the surfaces employed during the Ullmann coupling reaction.

We made a distinction of two different photoelectron spectroscopy processes according to the type of information that is accessed : a) X-ray and Ultra violet photoemission spectroscopy to probed filled electronic states and b) X-ray adsorption to probe the empty states.

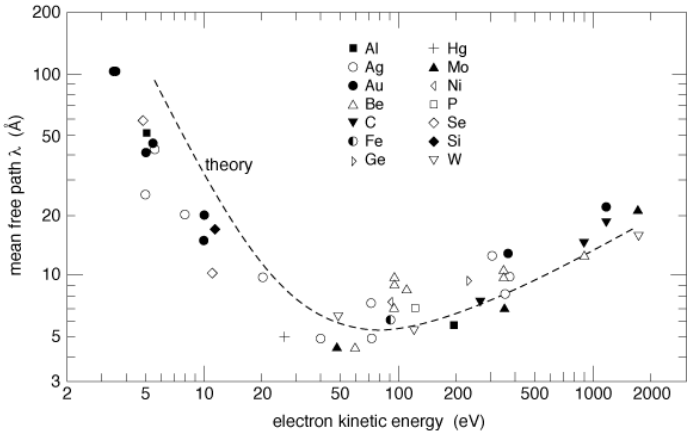

FIGURE 2.2: The mean free path of electrons in solid as function of their kinetic energy. The dots are experimental measurements while the dashed curve is a theoretical calculation. The table is taken from [48].

2.2.1 Electronic structure of matter

In an oversimplified picture, the binding energy of electrons in an atom is related to the grade of confinement within the Columbic potential well of the nucleus. The binding energy of such electrons, which are located in atomic orbitals (AO), decreases when moving away from the nucleus (see figure 2.3 (a)).

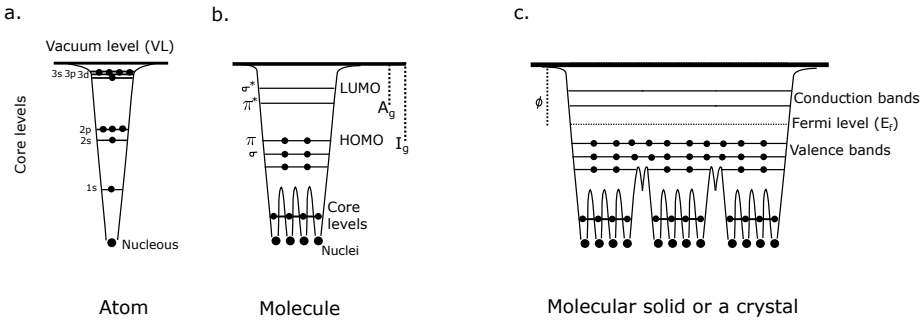

FIGURE 2.3: Electronic structure represented with potential wells. (a) single atom (b) polyatomic molecule and (c) organic solid or a crystal. Images based on [49].

When atoms bound to form molecules, the total effective potential that an electron feels is created from all the atomic nuclei and electrons comprising the molecule (figure 2.3 (b)). As a consequence, the electrons in the AOs close to the nucleolus, still are localized in the individual atomic potential wells (core levels), whereas the upper AOs mix to form molecular orbitals (MO), where the electrons can be delocalized. The energy separations from the highest occupied MO (HOMO) or lowest unoccupied MO (LUMO) to the vacuum level (VL) limits the gas phase ionization energy (I_g) or the electron affinity (A_g) of the molecule, respectively. The character of the formed bond governs the grade of electron delocalization, with electrons in the sigma bond (σ) being highly localized and the electrons in a pi (π) bond less localized. The extreme case of electron de-localization is achieved when a huge amount of atoms are collectively bounded, for example, in a crystal (see figure 2.3 (c)). In

those cases, the electrons form bands by filling the energy levels following the Fermi statistics. The bands close to the Fermi level (E_f) are called valence bands and the energy difference to the VL is called the work function ϕ [49].

Photoemission spectroscopy provides access to both core and valence electrons.

2.2.2 Photoelectric effect and the three step model

A simplified scheme of the photoemission process is shown in the figure 2.4 (a). In its basis, an incident electromagnetic beam of energy $h\nu$, impinges a surface and an electron is ejected.

The process can be described by using the three step model shown in figure 2.4 (b): First an electron is optically excited (1), and then it travels to the crystal surface (2). Along this path, the electrons may suffer scattering events with other electrons, phonons, or plasmons and lose the initial energy and momentum information. The distance travelled by an electron before being scattered is called the mean free path, and depends on the initial energy of the electrons. The core electrons (valence electrons) for example, have typical kinetic energy values of 100-500 eV (0-50 eV) and a mean free path of around 0-10 Å, as reported in the figure 2.2. This, indeed, is why PES is a surface sensitive technique, as the electrons originated from the very first layers are the ones with less probability to be scattered and able to reach the surface. Finally in the last step, the electron overcomes the surface work function (ϕ) and is ejected to the vacuum with a certain kinetic energy (E_k). With an electron energy analyzer, the kinetic energy of the outgoing electrons can be measured, as well as their dependence with the emission angle.

A theoretical description of the photoemission process was given by Einstein in 1905 with the following formula [50]:

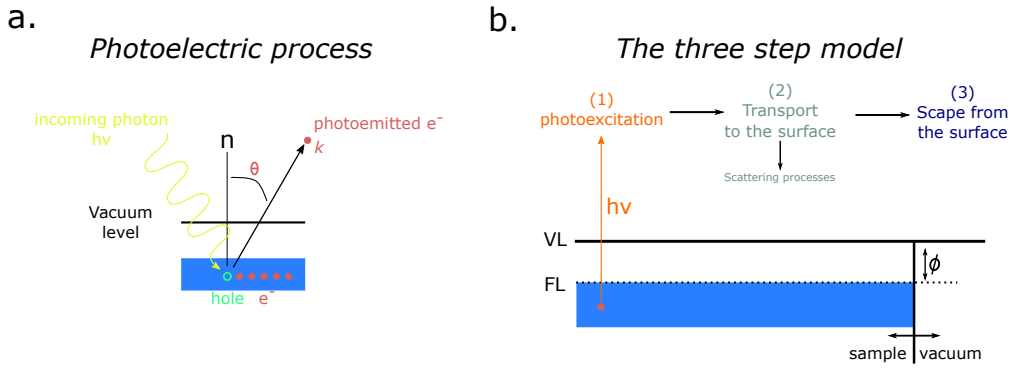

FIGURE 2.4: A model of the photoelectric effect is shown in (a). The three step model shown in (b), describes the path followed by the photo ejected electron until it scapes from the surface.

$$E_k = E_b - h\nu - \phi \tag{2.6}$$

As a consecuence, once the kinetic energy(E_k) of the ejected electron and the surface work function(ϕ) are known, the electron binding energy E_b can be obtained. On the other hand, the momentum of the electrons inside the solid can be determined through the energy of the outcoming electrons and the angle formed between the detector and surface normal θ [51].

2.2.3 X-ray photoemission spectroscopy

The photoemission of CL electrons is achieved with soft X-rays sources with typical energies ranging between 100-1500 eV. The binding energy of CLs constitute chemical fingerprints of elements and the access of these quantities is what defines the well-known elemental sensitivity of X-ray photoemission spectroscopy (XPS).

Throughout this work we use XPS mainly for studying the chemical structure of molecules and in-situ follow chemical reactions.

Chemical specificity

XPS is sensitive to the different elements comprising a molecule or a surface. As we explained before, since the BE of and electron depends on the nucleus potential well, in an XPS spectra, the different lines corresponds to electrons of different atomic elements or shells. As an example, an XPS spectrum measured after phthalocyanine molecules were deposited onto a copper surface is shown figure 2.5 (a) (see ref [52] for further information). The spectrum covers a BE range of 500 eV and the carbon and nitrogen elements, constituents of the molecule, and copper atoms, part of the surface, are clearly resolved evidencing the chemical sensitivity of XPS. From the integrated intensity of the peaks, the ratio between the elements comprising the molecule and the surface coverage can be obtained [53–55].

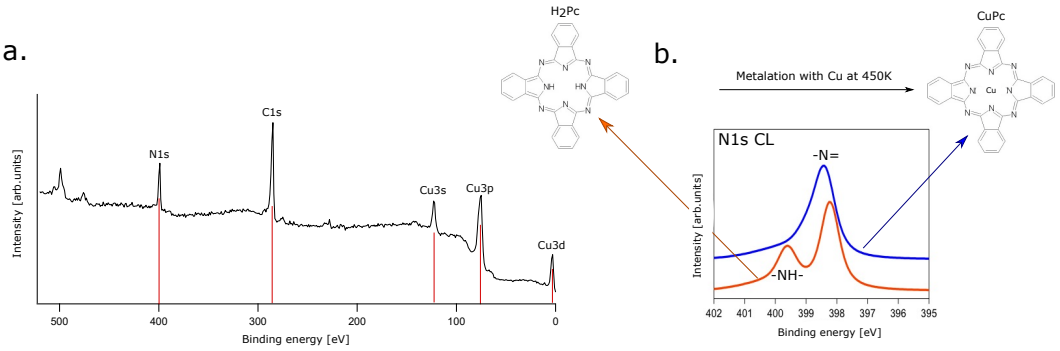

FIGURE 2.5: Chemical specificity of XPS. An overview XPS spectra measured after the adsorption of a monolayer of H_2-phthalocyanine molecules on Cu(110) is shown in (a). The different elements present in the surface are highlighted with red lines. The N1s CL of free and copper based phthalocyanine molecules are gathered in figure (b).

More importantly, XPS is also sensitive to the electronic environment surrounding an atom. In the figure 2.5 (b) the N 1s CL spectra of non-metalated and copper metalated phthalocyanine molecules are shown. Details of the experiments can be found on [52]. In the spectra, the binding energy goes from 402 to 395 eV, the range in which the N 1s CL appears in figure 2.5 (a). For the non-metalated metal phthalocyanine (orange spectrum), two peaks are distinguished. The reason behind is that there are two type of nitrogen atoms in the molecule, i.e. the pyrrolic nitrogen (-NH-) and the iminic nitrogen (-N=). Although subtle, the changes in the nitrogen bonding are clearly distinguished in the spectrum. For copper phthalocyanine (blue spectrum), since all nitrogens are iminic, the spetrum resembles a single peak. Thus, besides being element specific, XPS also provides information about the bonding nature of elements.

Temperature dependant XPS

Temperature dependant XPS (TD-XPS) is a powerful technique to study *in-situ* chemical reactions on surfaces. Therefore, in this research work, it has been extensively used for studying the Ullmann coupling reaction. The experiment consist on tracing *in-situ* the temperature evolution of a certain CL, normally the element involved in the reaction. Taking into account that XPS can address the bonding nature of elements and considering that on a chemical reaction bonds are either formed or destroyed, the CL temperature evolution of certain elements are the fingerprints of chemical reactions.

An example of a TD-XPS measurement is shown in figure 2.6. Normally, the x axis comprises the binding energy, the y axis the temperature and with the color scale the CL intensity is represented. In this particular case, the Br 3d CL of 4,4"-Dibromo-p-therphenyl (DBTP) molecule is monitored while annealing. Details can be found on [56] and in the chapter 6. The measurement permits to distinguish a sudden Br 3d CL intensity drop and energy shift at around 430 K which is the fingerprint of the Ullmann reaction. Thus, by TD-XPS, the activation temperatures and intensity profiles throughout the reaction are obtained.

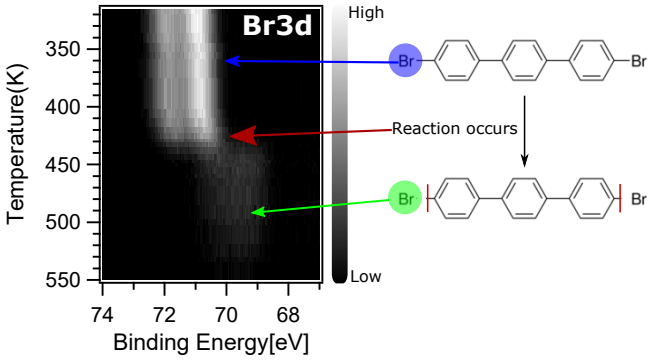

FIGURE 2.6: Temperature dependant XPS measurement. The graph shows the changes produce in the Br 3d CL of DBTP molecule within polymerization. A reaction transition temperature is evidenced by the clear Br 3d CL shift, pointed out with the red arrow. The chemical structure of the initial reactant and the final product are included in the right side of the figure.

2.2.4 Angle-resolved ultra violet photoemission spectroscopy

Angle-resolved ultra violet photoemission spectroscopy (ARPES) measures the momentum and energy of the electrons comprising the valence band regions a of a crystal, emitted during the photoelectric process. This is possible due to the energy and momentum conservation laws [57–59]. A geometry of the ARPES experiment is shown in figure 2.7. By collecting the photoelectrons with an electron energy analyzer characterized by a finite acceptance angle, one measures the electron kinetic energy E_k for a given emission direction. This way, the wave vector momentum $k = p/\hbar$ of the photoelectrons in vacuum is also completely determined: its modulus is given by $k = \sqrt{2mE_K}/\hbar$ and its components parallel ($k_{||} = k_x + k_y$) and perpendicular ($k_\perp = k_{||}$) to the sample surface are obtained in terms of the polar ϑ and azimuthal φ emission angles defined by the experiment.

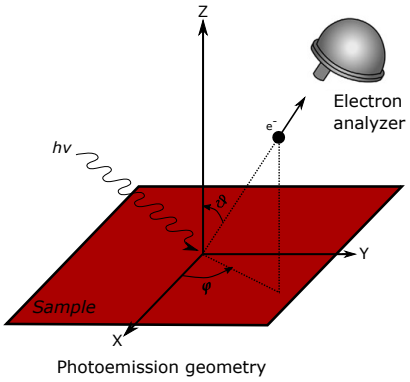

FIGURE 2.7: Basic ARPES measurement set-up. Rotation of the sample in the azimuthal and polar angles, enables the electron analyzer to obtain the angular distribution and the kinetic energy of the ejected photoelectrons.

$$k_x = \frac{1}{\hbar}\sqrt{2mE_k}sin\vartheta cos\varphi, \tag{2.7}$$

$$k_y = \frac{1}{\hbar}\sqrt{2mE_k}sin\vartheta sin\varphi, \tag{2.8}$$

$$k_z = \frac{1}{\hbar}\sqrt{2mE_k}cos\vartheta. \tag{2.9}$$

The final goal of the measurement is to deduce the electronic dispersion relation E(**K**) i.e the relation between binding energy and momentum k of electrons in the valence band.

Throughout this work, we are particularly interested in characterizing the band character (dispersive or non-dispersive), of discrete molecules and extended polymers.

Orbitals and bands in molecules

In order to understand the nature of the molecular bands, here we extend the explanations introduced in section 2.3 about molecular orbitals [60].

Lets imagine the set of aromatic hydrocarbons depicted in figure 2.8 . In a ethylene molecule, (first column) composed by two carbon atoms, there is a bonding σ (π) molecular orbital (MO) bellow an anti-bonding σ^* (π^*) MO. For cyclopropenyl, there is one orbital bellow two degenerate ones. For cyclobutadiene, (second column) there are two degenerate orbitals in between another two, and so on. Except for the lowest (and occasionally the highest) level, due to symmetry constrains the orbitals come in degenerate pairs. The energy distribution of these MO depends on the amount of nodes (lower probability to find an electron in the region). Thus, the number of nodes, increases as the energy is rise up. Same happens on an infinite polymer i.e the lowest level is nodeless, the highest has the maximum number of nodes, and in between levels come in pairs with a growing number of nodes forming a continuum in energy. All the level comprises what we call a molecular band.

These orbital representation can be written by making use of the translational symmetry. Consider a lattice with $n = 0, 1, 2, 3, 4, etc.$, points as shown in equation 2.9. If each lattice points represents a basis function (a C 1s atomic orbital), $x_0, x_1, x_2, x_3, x_4, etc.$, then the symmetry-adapted linear combinations are given by

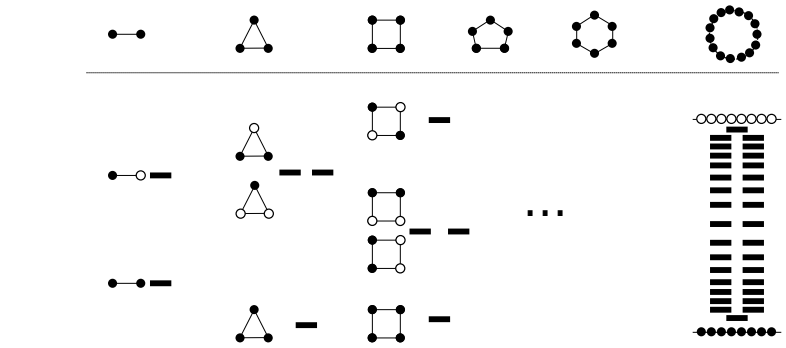

FIGURE 2.8: Simple representations of the constructions of molecular orbitals for molecules with increasingly amount of C atoms. Based on the ref [60].

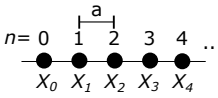

$$\Psi_k = \sum_n e^{ikna} X_n$$

FIGURE 2.9:
Symmetry-adapted (the block functions) linear combinations of AOs.

ψ_k as shown in equation 2.9. Here, a is the lattice spacing of the unit cell in one dimension and k is the momentum, which for now is an index that labels which irreducible representation of the translation group ψ transforms as. The process of symmetry adaptation in solid state physics is known as the formation of Bloch functions. Now we use two different k values in equation 2.10:

Referring back to figure 2.8, we see that the wave function corresponding to k=0 is the most bonding one and the one for k=$\frac{\pi}{a}$ the top of the band. With other values of K we get a net description of the other levels in the band. Therefore, k counts nodes as well. Nevertheless, there is a range of k and if one goes outside of it, one does not get a new wave function but rather repeats an old one. The unique values of k are the interval $\frac{-\pi}{a} \leq |k|$ or $|k| \leq \frac{\pi}{a}$. This is called the first Brillouin zone (BZ), the range of unique k that comprises the so called reciprocal of momentum space. The

$$k = 0$$

$$\Psi_0 = \sum_n e^0 X_n = \sum_n X_n$$

$$= X_0 + X_1 + X_2 + X_3 + X_4$$

$$k = \frac{\pi}{a}$$

$$\Psi_{\frac{\pi}{a}} = \sum_n e^{\pi i n} X_n = \sum_n (-1)^n X_n$$

$$= X_0 - X_1 + X_2 - X_3 + X_4 \cdots$$

FIGURE 2.10:
Symmetry-adapted linear combinations of AOs for two different wavevectors.

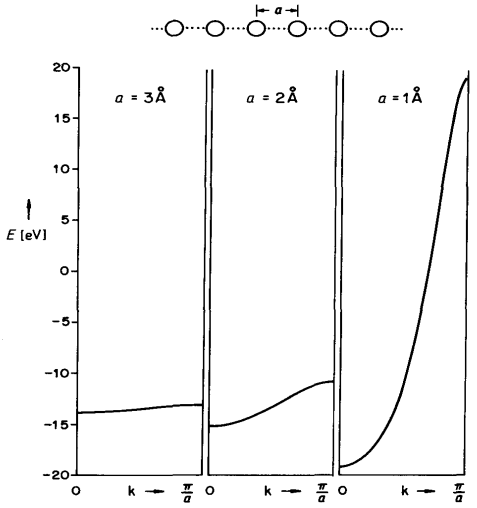

FIGURE 2.11: Relation between the bandwidth (dispersive character of a band) and the inter atomic distances. The bands for hydrogen atoms separated by 3 Å, 2 Å and 1 Åare shown in the figure. The energy for an isolated hydrogen atoms is -13.6 eV. Figure taken from [60].

number of k is subject to the number of translations available inside the Brillouin zone, and there is a unique energy level E(k) for each k. This is what is measure by ARPES i.e the E(k) distribution of electrons, and thus graphs of E(k) vs k are called band structures.

In this work, we are interested in the energy momentum dispersion relation i.e the energy variation of an electron in a band throughout the BZ. This somehow reflect the grade in which electrons are localized in a band. Higher the dispersion, higher the electron de-localization. Indeed, the dispersion of a band is a direct consequence of the overlap between the interacting orbitals. This is illustrated in the figure 2.11, where the molecular bands formed after the combination of s function AOs of a linearly bound hydrogen atoms with different inter atomic distances are compared. With a 3 Å inter-atomic spacing, the energy of electrons is almost constant across the BZ. On contrary, when the atoms are brought closer (2 Å and 3 Å) the slope of the band becomes evidently higher and the energy of electrons changes abruptly slightly moving in k. Thus at 3 Å the band is considered as non dispersive whereas at a distance of 1 Å is highly dispersive.

With these concepts in mind, here we introduce the band structure of the DBTP molecule, and explain why is ARPES so usefull to trace the Ullmann polymerization reaction for this particular molecule.

The energy vs momentum (E vs K) ARPES maps calculated for finite PPP oligomers with 2 (left), 6 (center) and 20 (right) phenyl rings is shown in figure 2.12 (b). On the calculations, only the pz orbital is considered, illustrated in figure 2.12 (a). The reason behind is that the overlap is maximum between pz AOs, leading to a hybridization and formation of a π system in where electrons are de-localized throughout the phenyl ring. Details about the calculations can be found in [13]. The π MO of a molecule with two phenyl rings, left graph in figure 2.12 (b) presents a discontinuous band with discrete non dispersive intensity profiles distributed in the momentum space. On contrary, when a larger amount of pz AO are involved in the π system, the band character is transformed. For the extreme case of 20 phenyl rings, the π

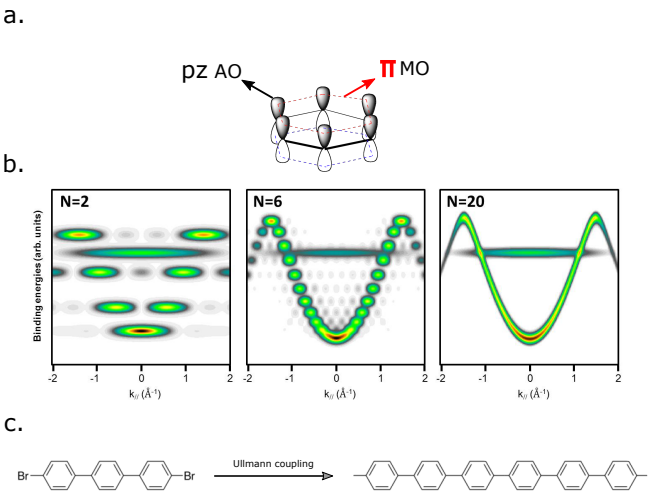

FIGURE 2.12: π band dispersion as function of phenyl rings. b) The π (shown in (a)) band dispersion of molecules constituted with 2,6 and 20 phenyl rings. The figure is extracted from [13] c) Polymerization of the DBTP molecule (three phenyl rings) onto PPP (with infinity amount of phenyl rings.)

band shows a strong dispersive behaviour and it can be traced from the lowest to the highest energy with a continuous line. The evolution from discrete (two phenyl rings) to dispersive band (20 phenyl rings) brings back the picture shown in figure 2.8.

Now let's consider the reaction shown in figure 2.12 (c). The DBTP molecule is composed by three phenyl rings (with two bromine atoms saturating the edges), whereas after the reaction, it is transformed to an infinite (in the ideal case) chain of phenyl rings. By using ARPES measurements and considering the picture proposed in figure 2.12 (b), one can probed whether the reaction has worked or not, by tracing the band character of the reaction products.

2.3 Near-edge X-ray adsorption spectroscopy

Due to the relatively lower (compared to the above presented techniques) importance of the Near-edge X-ray adsorption spectroscopy (NEXAFS) measurements throughout this work, here we only introduce the practical aspects concerning the technique. A more detailed description can be found in [61–63].

Contrary to XPS and UPS, NEXAFS is used to probed **unoccupied** molecular levels. If the energy of the incoming photon matches the energy difference between a core level and an empty orbital, there is a finite probability that a resonant excitation of the core electron into the empty orbital to occur. This process is represented in figure 2.13(a). Then, the excited system decays via either the emission of a photon of lower energy, a process called fluorescence, figure **??**(b), or the emission of an Auger electron, figure 2.13(c). Both decays can be exploited for recording NEXAFS, however, the strong predominance of Auger emission over fluorescence for the lighter elements ($Z < 35$) [64], makes Auger electrons a convenient tool to explore the electronic and structural properties of organic compounds and therefore the measurement mode used during this work.

During the measurement, the sample is irradiated with monochromatic x-rays, the energy of which is varied around the interval where the energy difference of the

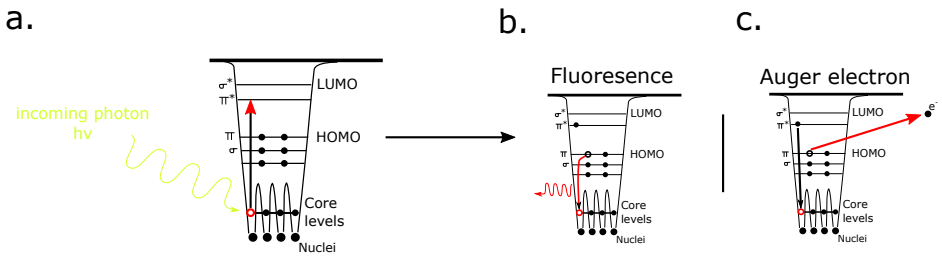

FIGURE 2.13: The adsorption process on a NEXAFS experiment. (a) Photo-excitation of an electron from an atomic core level to an unoccupied level and the subsequent de-excitation paths, where the excited atom decays to its ground state either by (b) emission of a photon (fluorescence) or (c) emission of an Auger electron are shown in the figure.

core and the empty state is located. Therefore, synchrotron based radiation, where a broad interval of electromagnetic radiation is produced, is required for the experiment.

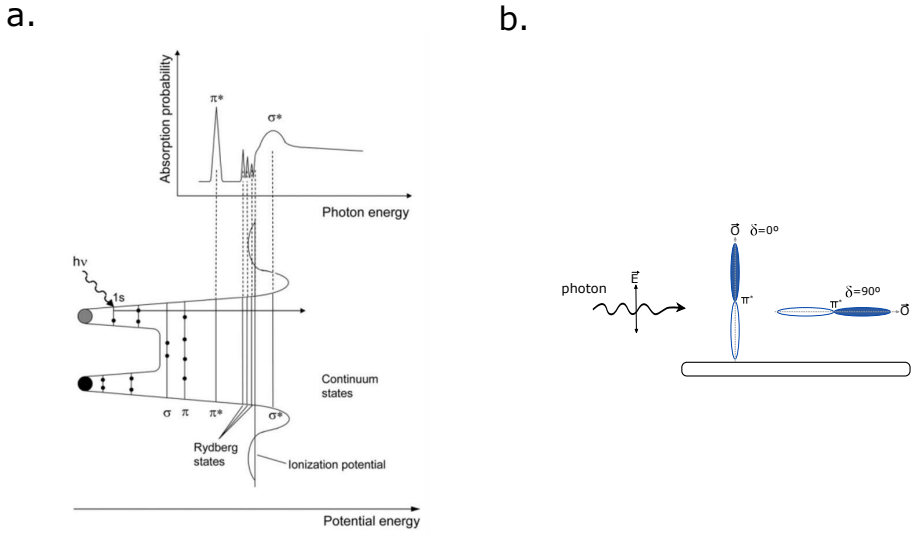

FIGURE 2.14: (a) NEXAFS spectra of a diatomic molecule with the different resonant processes highlighted. (b) Angular dependence of NEXAFS resonances for a π molecular orbital. The resonance is maximized when the electric field vector $\vec{E}$ is parallel to the direction of the molecular orbital $\vec{O}$(left) and minimum the other way around (right). Figure adapted from ref[64].

The adsorption spectra of a diatomic molecule is shown in figure 2.14 (a). It is constituted by three type of resonance processes that can be distinguished considering their shape and photon energy difference when compared to the ionization energy of the molecule. The first resonance, is a narrow feature that corresponds to the excitation of a core electron into a π^* orbital. Higher in energy, sharp but less intense peaks are associated with Rydberg orbitals. These resonances are normally quenched in organic molecules due to the large spatial extent of the MO which favours a fast delocalization of the excited electron into the empty states of the substrate. Excitation into a σ^* orbitals comes after since the energy gap to the CL electron (compared to π^*) is higher. For neutral molecules, these orbitals are often found

above the vacuum level and therefore the lifetime of the excited state is reduced and the resonance peak appears broader.

Interestingly, NEXAFS can also be used to investigate the orientation of molecules on a surface, as shown in figure 2.14(b). The spatial orientation of an orbital can be obtained by taking NEXAFS measurements at more than one angle of incidence. For linearly polarized light (such as that produced in a synchrotron), it follows the Fermi's Golden Rule that states that the transition probability from a 1s initial state to a directional final state is proportional to $\cos^2 \delta$, where δ is the angle between the electric field vector **E** and the direction of the final state orbital **O**. As a consequence, the intensity of a resonance is largest when the electric field vector **E** lies along the direction of the orbital and vanishes when it is perpendicular to it.

2.4 Low energy electron diffraction

Low energy electron diffraction (LEED) is a technique used for determining the surface structure of single-crystalline materials [65]. It consist on bombarding a surface with a collimated beam of low energy electrons (20–200 eV) and only measuring the back-scattered electrons as spots on a fluorescent screen as shown in figure 2.15 (a). The origin of the diffraction pattern observed on LEED is related to the similar Broglie wavelength of the low energy electrons $(\lambda) = \frac{h}{p}$ and the inter-atomic distances in crystals (Å). Due to the low energy of the electrons that are use, the penetration thought the surface is very small, making the LEED a surface sensitive technique. The size of the beam is around 1 mm^2. In this work, we use LEED measurement to complement STM data as an surface averaging technique to unravel the adsorption geometry of the surface molecular overlayer.

The analysis of the diffraction pattern is performed in the reciprocal space ($\overrightarrow{g_i}$) instead of the real space ($\overrightarrow{g_a}$). The reciprocal lattice of a surface is defined as follows,

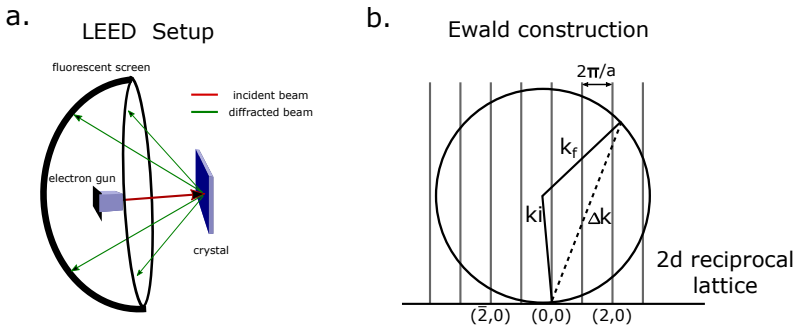

FIGURE 2.15: a) Experimental representation of a LEED set-up. b) The Edwall sphere showing the Laue condition for the existence of a diffracted beam.

$$\overrightarrow{g_i} = \frac{2\Pi(\overrightarrow{a_j} \times \overrightarrow{n})}{|\overrightarrow{a_i} \times \overrightarrow{a_j}|} i, j = 1, 2 \tag{2.10}$$

Considering the Laue conditions in a two dimensional system (the conditions required for diffraction to occur) given by,

$$\left(\overrightarrow{k_i} \times \overrightarrow{k_f}\right) \overrightarrow{a_i} = 2\pi k, i = 1, 2 \tag{2.11}$$

and that energy conservation requires that

$$\left|\overrightarrow{k_f}\right| = \left|\overrightarrow{k_i}\right| \tag{2.12}$$

Both conditions can be represented in the Edwald contruction shown in figure 2.15 (b). Rods, in grey, represent the reciprocal lattice of the surface(2D). The initial momentum vector ($\overrightarrow{k_i}$) is drawn ending at the origin of the reciprocal lattice, thus, a circle of radius $\left|\overrightarrow{k_i}\right|$ contains all the possible ($\overrightarrow{k_f}$), according to the energy conservation law. The intersection between the circle and the rods gives the ($\overrightarrow{k_f}$) vectors fulfilling the Laue conditions and showing the diffraction maxima.

2.5 Ultra high vacuum and the experimental set-up

The keystone of most surface science experiments is to work under the Ultra High Vacuum (UHV) regime (pressures bellow 1.0^{-9} mbar) since it permits to prepare samples free of defects and most importantly, preserved them relatively clean for the duration of the experiment. Besides, electron based techniques, can only be used in UHV environments as the mean free path of electrons is directly related and limited to the pressure of the chamber (see section 2.2 for more details). Therefore, all the measurements presented here are performed in pressures bellow 1.0^{-9} mbar.

During the thesis work, most of the experiments were accomplished in two independent UHV systems, depicted in figure 2.16, at the Donostia/San Sebastian Nanophisics lab.

In both chambers, samples are introduce from a fast entry lock, and afterwards, prepared in a very similar way by ion bombardment and annealing cycles. The systems are equipped with sputter guns and various annealing stages, where either direct current or electron bombardment can be applied. For the molecular deposition, we use an exchangeable evaporator that can be mounted in both chambers, while keeping a similar distance to the sample. This ensures reproducibility throughout the molecular deposition processes independently of the employed system. Besides, the evaporation rates are always monitored with a quartz micro balance.

Regarding the analysis techniques, we carried out the XPS experiments in the chamber (a) shown in figure 2.16. The chamber is equipped with a non monochromatic X-ray generator source, with Al kα and Mgα x-ray lines. The electron analyzer is an SPECS Phoibos 100 with a channeltron detector. ARPES measurement on contrary are accomplished in chamber (b). The chamber is equipped with a UV light source and a monochromatizer. The manipulator enables to rotate the sample in the azimuthal and polar angles and the angular distribution and kinetic energy of the photoejected electrons is measured with a SPECS Phoibos 150 anaylzer equipped with a channelplate. LEED measurements are also accomplished in this chamber. Finally, both systems have variable temperature STM's (SPECS in (a) and OMICRON in (b)) operated with the same Nanonis electronics, therefore, we performed similar STM measurements in both chambers.

2.5.1 Synchrotron measurements

We carry out further photoemission measurements at synchrotron radiation facilities. In particular, the data shown in this work were obtained at the Aloisa beam-line of the Elettra synchrotron, Trieste.

SR combines extremely high intensity, high collimation, tunability, and provides a continuous energy spectrum, features that are unreachable on a laboratory set up.

a.

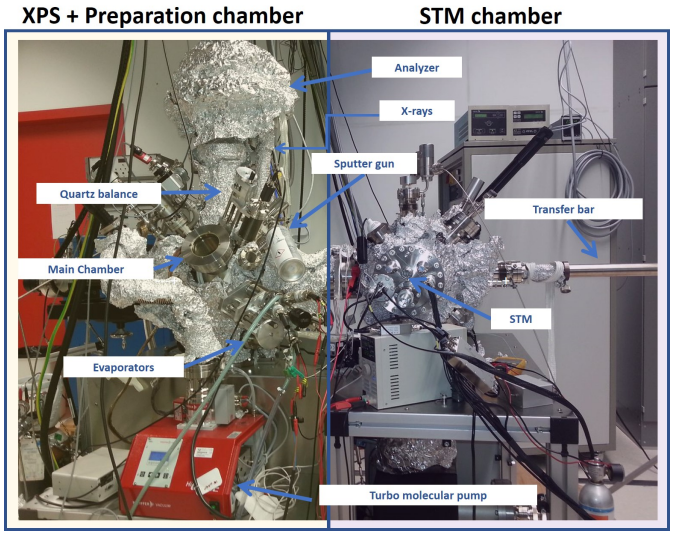

b.

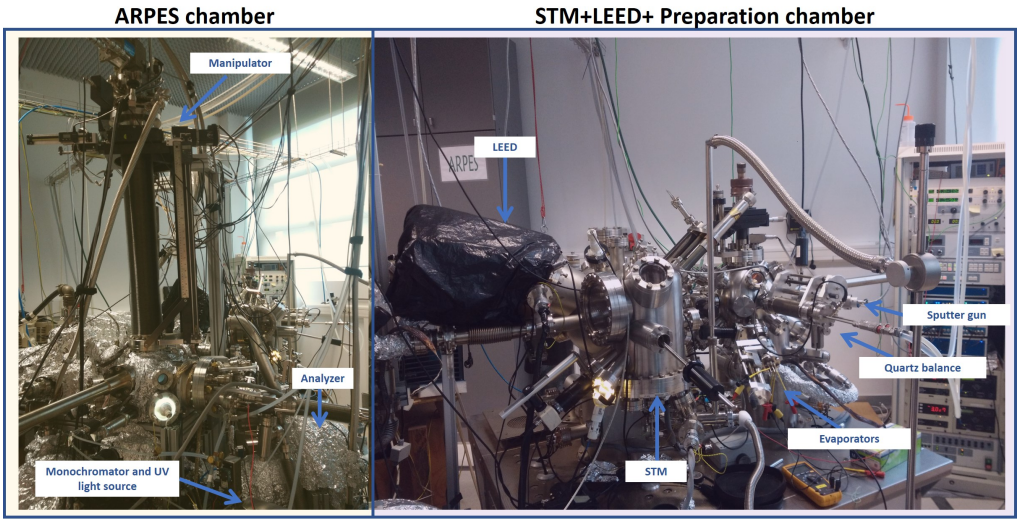

FIGURE 2.16: The two UHV systems, with their respective equipment labelled in the figure, that hosted most of the experiments performed during this work. The labs are located in the Material Physics Center (CFM) in Donostia/San Sebastian and are used by the people of the Nanophysics group lead by Profesor Enrique Ortega.

TABLE 2.1: Lab light vs Synchrotron light

	Lab source	Synchrotron source
Energy resolution (meV)	1000	50
Beam size (mm)	<0.150	>1
Beam energy	Fixed	Tunnable
Photon flux (ph/s)	order of magnitudes lower	$5x10^{10}$ - $2x10^{11}$

To properly visualize the differences in the XPS measurements when using lab photon source or SR, in the table 2.1, we collect the specification of both systems.

Higher chemical sensitivity can be obtained in a SR facility due to the higher energy resolution and photon flux. This is illustrated, in figure 2.17, by comparing the C 1s CL spectrum of the DBTP molecule measured at the same conditions, but in different set-ups i.e lab vs synchrotron. It is rather obvious that the peak asymmetry observe in the lab spectrum (marked in the figure with an arrow), is due to the convolution with a second peak which is clearly resolved with the SR.

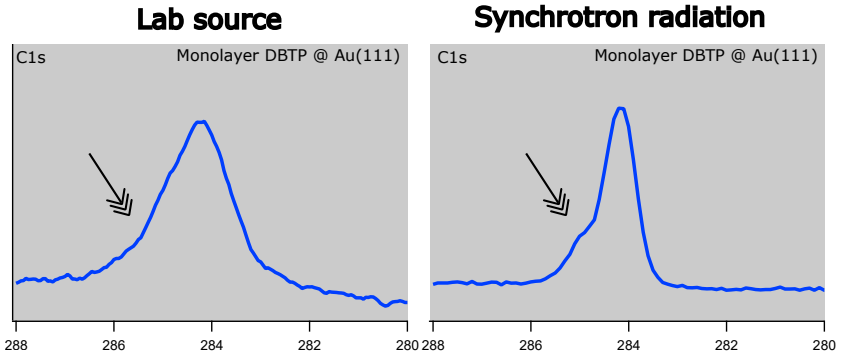

FIGURE 2.17: Comparison between lab source and synchrotron radiation based XPS measurements. From left to right, the C 1s spectra acquired for a monolayer DBTP adsorbed on Au(111) and measured in the lab and in the synchrotron facilities.

Another advantage on a synchrotron facility is the capability of changing the energy of the beam in a wide spectrum range which allows to do techniques such as NEXAFS, that are otherwise impossible in a lab source due to the fix photon energy.

Finally, and interesting for us, is the fact that due to the small synchrotron beam size (μm) and the high photon flux, different parts of a sample can be measured independently. In a laboratory XPS, this can also be realized with the use of mirrors and slits in the analyzer, however, the remaining signal intensity is normally under the resolution limit. We use this great advantage of the SR to measure the curved c-Au(111) crystal in the chapter 4.

Next, we explain the measurement conditions at the Aloisa beam-line. This is important to particularly understand the data presented in chapter 5, and related with the curved Au (111) crystal (c-Au (111)).

Sketched in the figure 2.18, is the measurement configuration of the Aloisa chamber for the c-Au (111) crystal. A six-degree of freedom manipulator (X,Y,Z & R1, R2, R3), coaxial to the photon beam, host the sample. The photon beam enters to the chamber through a port view and impinges the sample at a grazing incidence. To

properly align the sample with respect to the beam, first, the sample is translated in the X, Y and Z coordinates. Then, considering that the sample holder features three angular degrees of freedom (R1,R2,R3), the measurement parameters are set:

1. With R1 we select the desired surface orientation with respect the photon polarization. In the case of the c-Au (111) for example, the photon beam impignes parallel to the step direction.

2. With R2 we select the azimuthal orientation of the surface relative to the scattering plane.

3. With R3 we set the grazing incidence angle.

Therefore, a complete arbitrary configuration between the beam, the sample and the detectors is achieved and makes possible to measure different parts of the crystals within the beam size limitation.

Nonetheless, in the particular case of a curved crystal, there is a minor drawback. To characterize the crystal along its curvature (i.e by translating in Z) and always keep the same photon incidence angle, a correction needs to be added in Y. If this is not properly done, it can lead into alterations on the signal intensity when comparing different parts of the crystal. For NEXAFS measurements and dichorism analysis for example, this can be a mayor issue.

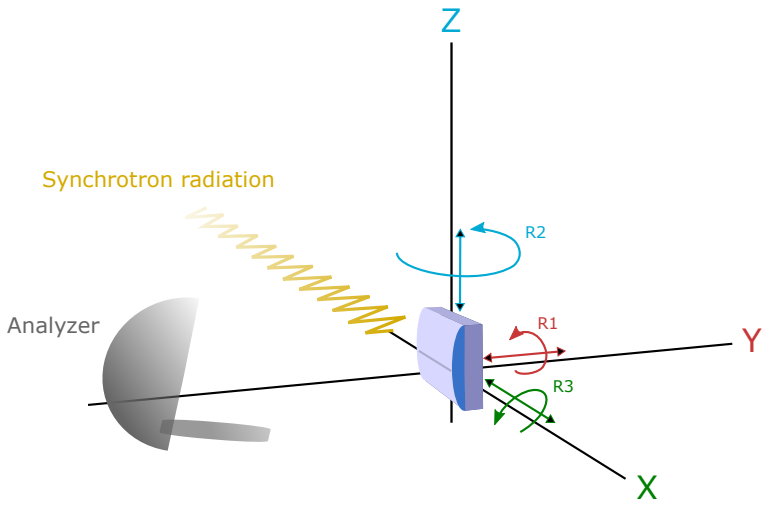

FIGURE 2.18: Measurement set up on the Aloisa beam line. All the rotational degrees of the sample respect to the photon beam and the analyzer are sketched.

Chapter 3

The on-surface Ullmann coupling reaction: Some general aspects

In this chapter, we introduce some basic concepts that will help to understand and interpret the experimental data. First, we give a short general introduction of a chemical reaction and catalyst. Then, we outline the different Ullmann coupling reaction mechanisms that have been proposed since its discovery in 1901. Finally, we give a brief overview of surface catalyzed Ullmann reactions, discovered in the early 90s, and review different proposed mechanisms.

3.1 What is a chemical reaction?

A chemical reaction is a process in which atoms and molecules rearrange themselves in such a way that results in the maximum possible dispersion of thermal energy. The quantity that measures the spreading and sharing of this energy is the free energy of the system and as a chemical reaction takes place, the system minimizes its free energy. When the minimum value is reached, the system is said to be in equilibrium. Thus, thermodynamics enables to predict the energetics and the net direction of a reaction.

However, although a chemical reaction is guided and driven by energetics, the actual route it takes and the speed at which it occurs is the subject of dynamics. Dynamics themselves can be divided into two general areas: kinetics, which deals with the rate at which reactants are changed and mechanistic, which relates the "road map" that links the reactants to the products. As a consequence, the "time-frame" at which reaction proceeds plays no role whatsoever in the systems thermodynamics but in its dynamics.

3.1.1 Reaction rate

The reaction rate defines the speed of a chemical reaction and is defined as the change in concentration over the time:

$$rate = \frac{\Delta(concentration)}{\Delta(time)} \tag{3.1}$$

For a reaction of the form A -> B, the rate is expressed in terms of the change in concentration of any of its components:

$$rate = -\frac{\Delta[A]}{\Delta(time)} = \frac{\Delta[B]}{\Delta(time)} \tag{3.2}$$

where $\Delta[A]$ is the change in the A concentration per time interval $\Delta t = t_2 - t_1$:

$$\Delta[A] = [A]_2 - [A]_1 \tag{3.3}$$

By definition (equation 3.2), the rate of a reaction is always positive and the negative sign indicates that the concentrations always decreases with time.

In chapter 5 we deduce reaction rates from temperature dependent XPS measurements.

3.1.2 Reaction yield

From the conservation of mass follows that the reaction yield may directly be inferred from the stoichiometry of the reactants. However, this assumes that only one reaction occurs and that the limiting reactant reacts completely. This is almost never the case and the actual yield consequently is bellow this theoretical limit. Some factors limiting the reaction yield are listed below:

1. If a reaction is not unidirectional and can be reversed, the final state contains both reactants and products in a state of chemical equilibrium.
2. Two or more reactions may occur simultaneously, leading to undesired side products.
3. Impurities on the molecular source which do not react, are initially account as a reactant.

Here, we deal with an on-surface Ullmann homo coupling reaction (discussed in detail afterwards) and the reaction yield is simply evaluated from XPS data relating the amount of dehalogenated molecules to the initial amount of unreacted molecules.

3.1.3 Reaction mechanisms

The time frame in which the reaction occurs also depends on the reaction mechanism, which is the description of molecular-level events whose sequence leads from reactants to products. Normally, the events are either described by particle "*collisions*" into more complex units, or by molecule "*dissociations*" into a simpler units. Here we focus on the former.

Collision theory

Within collision theory a homocoupling reaction (A -> B) will proceed when two reactants A approach each other enough to disrupt their existing bonds and subsequently permits the creation of new ones establishing the final product. Therefore, for the reaction to proceed, the collision must have enough kinetic energy to disrupt these initial bonds and the frequency of collisions will depend on the density of the reactant. Interestingly, the succeed of a collision is, for some particular reactions, subject to the direction in which the reactants approach. For the Ullmann homo coupling reaction studied here, the halide functional groups of two molecules must encounter or collide in order to drive the reaction, therefore a configuration that favours the collision of two halide groups, will favour the reaction. This will be discussed later on in the chapter.

In order to disrupt a chemical bond, its energy needs to be overcome. A simple description of a chemical bond relates the bond length, i.e. the distance between

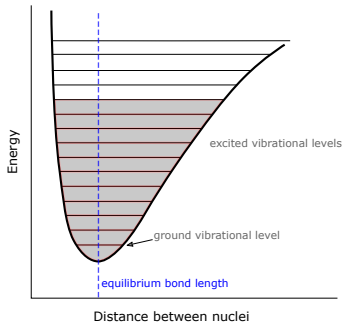

FIGURE 3.1: Diagram illustrating the potential energy of a bonding electron as a function of internuclear distance. As the electron is excited into higher vibrational levels, away from its ground state, the distance between nuclei, widens and the electron becomes less bound until the bond is eventually broken.

two nuclei, with the bonding electrons potential energy as sketched in figure 3.1. Consequently, when the bonding electron adsorbs energy (either from heating or due to a collision) it will be excited to a higher level and weaken the bond strength, as shown in the curve. Therefore, a bond affected by a collision, is more susceptible to cleavage.

Within this simplistic picture we can already see that thermal energy supplied to a reaction, e.g. by heating, has a two-fold effect: a) it will excite the bonds (and thereby weakening them) of a reactant and b) increase the reactants overall kinetic energy which enhances the probability of collisions and the amount of kinetic energy transferred per collison.

Activation energy

The minimum energy required for a reaction to proceed (either by stretching, bending or distorting one or more bonds) is known as the activation energy. A conceptual way to understand a chemical reaction and its activation energy is normally done using activation energy diagrams, as shown in figure 3.2.

In a very simplistic way, the reaction coordinate plotted along the abscissa, represents the changes in atomic coordinates when passing from reactant to product. Transition states refer to the states of a reaction which are situated at the peak of the respective activation energy curves (Ea1 and Ea2, respectively) . These transition states only exist during e.g. collision of reactants (which typically last about 0.1 picoseconds) and are too short lived to be observed experimentally. However, in certain cases, the reactants form a stable intermediate which may be observable, before the reaction proceeds via another transition state to the final reaction product. Noteworthy is the distinction of "exothermic", i.e. a decrease of free energy (H) and "endothermic", i.e. an increase of free energy of the system which is entirely determined by the reactions thermodynamics. Interestingly, an exothermic reaction my proceed via the endothermic formation of reaction intermediates as depicted in figure 3.2.

The activation energy is often supplied as thermal energy and when products are formed the energy dissipates via inter- and intramolecular vibrations. However, if we consider that a reaction solely depends on thermal activation, the reaction is limited to the molecules that possess enough kinetic energy to react at a given temperature. The number of molecules possessing Ea is given by the Maxwell-Boltzmann

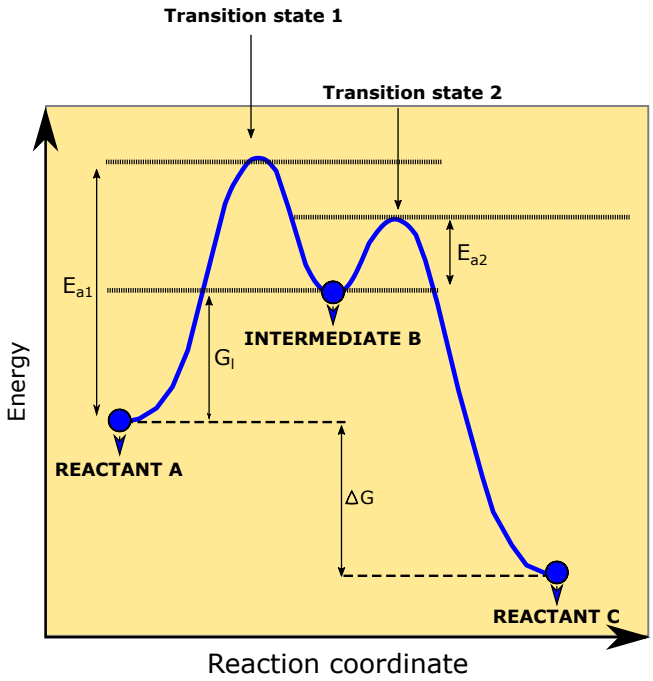

FIGURE 3.2: Shematics of a simple reaction that proceeds via an intermediate. First the reactant (A) need to overcome the activation barrier Ea1 and proceeds via the transition state 1 to a reaction intermediate (B). In a second step, another activation barrier (Ea2) needs to be overcome before the final product (C) and the completion of the reaction. Note that while the total reaction is exothermic (ΔG is negative), the creation of the intermediate B is endothermic.

distribution. In figure 3.3 the number of molecules possessing the necessary activation energy Ea for a reaction to proceed are shown for two temperatures, T_1 and T_2, where $T_1 < T_2$. It is immediately clear that higher temperature results in more molecules with sufficient energy to overcome the reaction barrier. This will be an important concept in order to understand the subtle differences in the reaction mechanism and activation temperatures observed during the Ullmann reaction for different surfaces presented along this work.

The Arrhenius law

The concept of activation energy and Maxwell-Boltzmann distribution leads to one of the most important relationships in physical chemistry , the Arrhenius law:

$$k = Ae^{-\frac{E_a}{RT}} \tag{3.4}$$

Here k is rate constant, E_a is the activation energy, R the universal gas constant, and T the absolute temperature of the system. The pre-exponential factor "A" is for now a simple constant . The Equation 3.4 relates the magnitude of the rate to the ratio of the activation energy to the average kinetic energy, i.e. larger the ratio $\frac{E_a}{RT}$ the smaller the rate (hence the negative sign). In short, the Arrhenius law tells us both higher temperatures and lower activation energies favour larger rate constants and thus speeds up a reaction. Moreover, due to the exponential dependence, the effects on the rate are rather substantial.

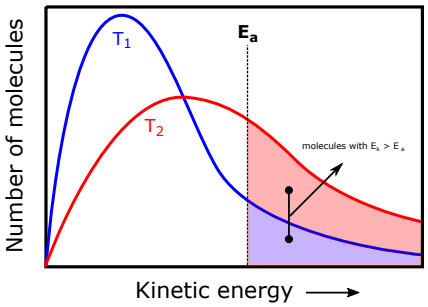

FIGURE 3.3: Maxwell-Boltzmann distribution of molecule's kinetic energy for two different temperatures. The dashed line, E_a, is the minimum particle energy required for a given reaction to proceed.

The aforementioned pre-exponential factor A is related to the amount of molecules that would react if either the activation energy were zero (exothermic reaction), or if the kinetic energy of all the molecules exceeded E_a. In such cases, $k = A$, and the rate would be limited by the probability at which reactant molecules come into contact. A is defined as:

$$A = Zx\rho \tag{3.5}$$

Z is known as *frequency* or *collision factor* which is calculated from the kinetic molecular theory. Interestingly the term ρ is known as the *steric factor* and comprises the geometrical factors affecting a reaction rate such as the constrains to overlap the electrons clouds needed for the reaction to proceeds. Since we perform the reaction on a surface, were the adsorption energy of the molecules constrains their adsorption geometry, the way in which molecules self assemble will affect the steric factors required for the reaction to proceed and consequently the rate.

3.2 Catalysts

Before we start explaining how the Ullmann reaction works, it is important to explain the role played by catalysts in a chemical reaction. As depicted in figure 3.4, a *catalyst* is a substance that speeds up (changes the rate) a reaction by lowering the activation energy without being consumed. Basically, it promotes a alternative reaction mechanism that requires an smaller activation energy. Obviously, a specific affinity between the catalyst and the reactant is required and thus, selecting the proper catalyst for a given reaction is not an easy task. We should also bare in mind that a catalyst affects only the kinetics of a reaction and does not alter the thermodynamics, i.e the value of ΔH remains unchanged.

Catalyst are conventionally divided in two categories: *homogeneous*, in which the catalyst is present in the same phase as the reactant, and the *heterogeneous*, in which the catalyst is in a separate phase. Surface catalyze reactions are considered heterogeneous processes.

The first prerequisite for a surface catalyze chemical process, is the adsorption of molecules, which depending on the extent at which they interact with a surface, leads to two different absorption behaviours. When the adsorption happens via weak van der Walls interactions, ΔE_{abs} tends to be small and the process is described as *physisorption*. On the contrary, when an adsorbate is bound to the surface via a

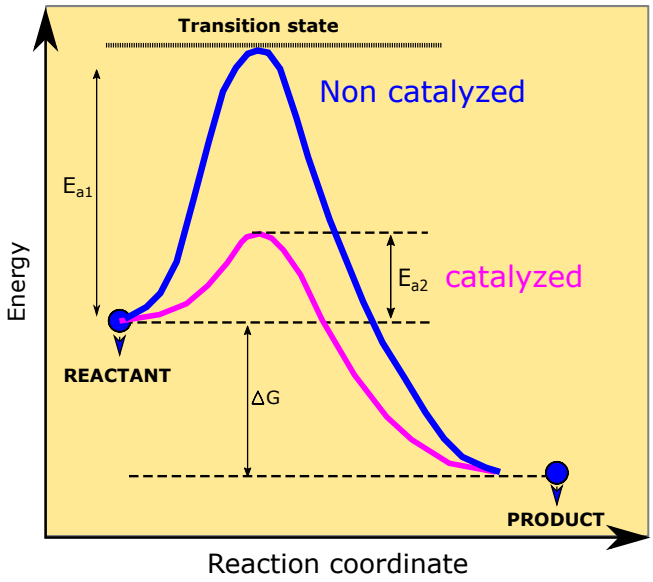

FIGURE 3.4: The effect of a catalyst on a chemical reaction represented in the activation energy diagram. With a catalyst, the reaction follows the pink path, which has a considerable lower E_a.

chemical bond, the process is known as *chemisorption*. Normally the latter is driving catalytic phenomena.

The actual mechanisms by which adsorption of a molecule onto a catalytic surface facilitates the cleavage of a bond varies greatly from case to case. Here, we define the surface properties on which the heterogeneous catalysts mostly depends. In the figure 3.5, a combination of five different catalyst surfaces, whose properties are similar to the ones employed in this works are shown. On metals, the free electron gas present at the surface can perturb the bonding in the adsorbate, or stabilize reactive intermediates such as radicals. In a similar way, semiconductors (including many oxides) can supply electrons, thermally excited through reasonably small band gaps. Of note is that doping or defect related in-gap states in semiconductor may substantially enhance the reactivity of such catalyst by reducing the excitation gap. Transition metal surfaces have d and f vacant orbitals that provide a variety of coordination sites to interact with the adsorbates orbitals. Oxides and ionic solids act differently. Oxides on the one hand, often have H^+ and/or OH^- groups present on the surface able to act as acid or base catalyst. Technically, these groups defy the stric definition of a catalyst as the finite number of H/OH available on the surface are potentially consumed throughout the reaction. On ionic solids , surfaces and edges are sites of intense electric fields able to interact with ions and polar molecules and promote new reaction paths.

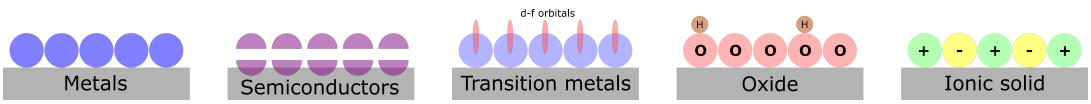

FIGURE 3.5: Representation of some catalyst surfaces. From left to right: Metals, semiconductors, transition metals, oxides and ionic solids.

Together with the properties of the most common surface catalyst, we highlight

the two most common molecule surface interactions that are the responsible for the majority of chemical reactions on surfaces:

1. Oxidation-reduction catalysis: Redox processes participate in the reaction, in which electrons are transferred between the catalyst and adsorbate. It requires on the one hand ions capable of existing in two oxidation states, often metal or transition metals, on the other hand, the adsorbate molecule must have vacant orbitals to accept the electrons to destabilize the chemical bonding.

2. Acid-base catalysis: Many reactions are catalyzed by the presence of an acid or a base. The mechanism involves the addition or removal of a proton, changing the reactant into a more kinetically labile form. Is likely to happen in reactions between molecules adsorb in oxide surfaces.

Finally, we should bare in mind that heterogeneous catalysis requires direct contact between the reactant and the catalytic surface, and often, there are two more crucial aspects affecting the catalyst efficiently:

1. Surface topography: A real surface will always possess a variety of defects such as surface cluster, vacancies, steps, kink edges and corners, which often are more active than the surface itself.

2. Steric factors: When chemisorption occurs at two or more locations on the reactant, efficient catalysis requires that the spacing of the active centers on the catalytic surface to be such that surface bonds can be formed without significant angular distortion. This is one of the reason why many metallic catalysts exhibit different catalytic activity on different crystal faces.

After explaining the basis concepts behind a chemical reaction and the role played by a catalyst in it, now we introduced a detailed description of the Ullmann coupling reaction, which is the reaction employed all along the present work.

3.3 The Ullmann coupling reaction

The Ullmann coupling reaction is the name given to the process in which two aromatic halide molecules are coupled. During the reaction, the carbon-halogen bonds are broken in favour of a carbon-carbon bond. It was first proposed in the early 1900s by Fritz Ullmann, after adding copper powder at elevated temperature into different aryl halide based solutions [**Ullmann1901**, **Ullmann1903**, **Ullmann1904**]. An sketch of the reaction is shown in figure 3.6. Although the coupling conditions that were first reported are still widely used, a host of modifications have been made to the reaction, some of then including the use of activated and alternative metals, often resulting in much lower coupling temperatures.

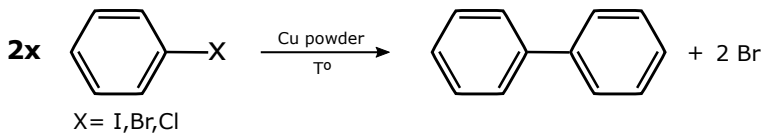

FIGURE 3.6: Reactants, catalyst and products of the Ullmann coupling reaction.

It was not until the early 1990s, that the reaction became of interest in surface science. At that time, Zou and co-workers[**Zhou1990**] as well as Xi and Bent [**Xi1992**, **Xi1993**] used a variety of surface science techniques to study the coupling of aryl halides on noble metal surfaces under UHV conditions for the first time. Ever since, a lot of work have demonstrated the viability of the surface confined Ullmann reaction. However, it was not, until, in the wake of graphene, research interest has intensified as atomically precise graphene nanoribbons are synthesized using, in the first step, the Ullmann coupling reaction.

In the present work we deal with surfaces which so far have not been employed to catalyze the Ullmann reaction. Therefore, we might encounter unexplored reaction paths and mechanism. In order to interpret our data, here, we recall the different Ullmann coupling mechanisms that have already been reported in both solution chemistry and surface science.

3.4 The Ullmann reaction mechanism

First, we recall the bonding nature and reactivity of aryl halide molecules. In general, aryl halides are rather stable compounds and quite unreactive when compare to their homologous alkyl halide compounds, in where the halogen atom can be easily removed or replaced by a nucleophile. In order to understand their improved stability, one has to consider the bonding configuration of the molecule, which is represented in figure 3.7.

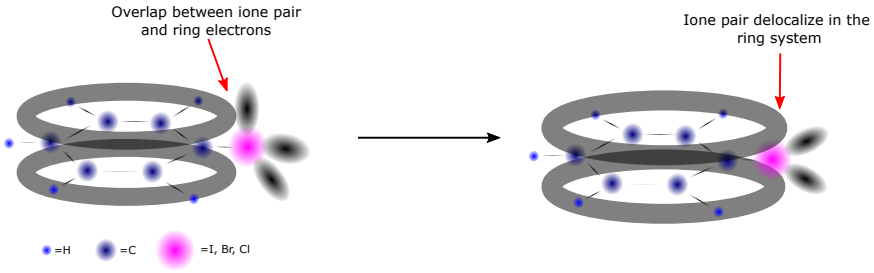

FIGURE 3.7: Simplified chemical structure of an aryl halide. The black circles represent the de-localized π^* system. Due to the overlap between the π^* system and the ione pair of the halogens (left figure), the halogene electrons end up participating in the π^* system extending it over the entire molecule (right figure).

Like in a benzene molecule, the carbon atoms that constitute the phenyl ring of aryl halides create an aromatic system, where electrons are de-localized in the π system formed by the combination of six *pz* atomic orbitals. Neglecting the strongest bonding in the molecule, i.e. the σ bonding of the sp^2 hybrids, it is interesting that, as pointed out in the figure, the unpaired electrons of the halogen atoms overlap with the electron cloud of the phenyl ring, and participate in the delocalization of the π system, which strengthens the carbon-halogen bonding. As a side effect, there is some backdonation of charge away from the halogen and towards the ring. As consequence the molecule is less polar than what one would otherwise have expected and thus more stable.

If we now think in terms of molecule reactivity, the carbon atom attached to the halogen is slightly more positive than the rest and therefore the most reactive. Normally this carbon atom could be easily attacked by a nucleophile. However, due to

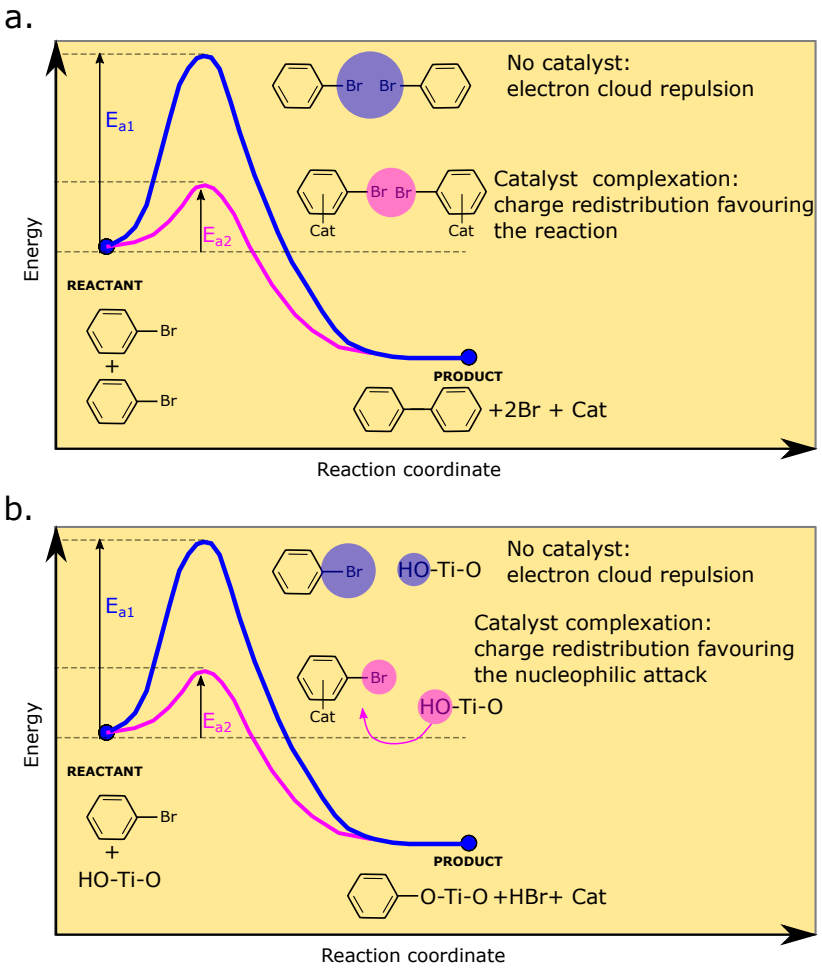

FIGURE 3.8: Energy diagrams for two hypothetical catalyst induced aryl halide C-Br bond activation. The metal complexation to a phenyl ring redistributes the charge around the molecular π^* system in such a way that allows the homo coupling of two aryl halide molecules (a) or the nucleophilic attack to the halogen bonded carbon atom of the hydroxylated TiO_2 nanoparticle.

the extension of the π system onto the halogen atoms in aryl halides, the nucleophile has to overcome the electron cloud surrounding the bond. Therefore, a catalyst driving the Ullmann coupling reaction may "only" weaken the carbon-halogen bond by disrupting the extension of the π system onto the halogen atom. Two hypothetical reaction pathways are depicted in figure 3.8. The catalyst complexation, e.g. a non covalent interaction (electrostatic) of a metal atom with the aryl halide phenyl ring, activates the carbon halogen bond allowing a homo coupling reaction to proceed via collision at substantially lower temperature (figure 3.8 (a)). In another hypothetical scenario (see figure 3.8 (b)), a hydroxylate TiO_2 nanoparticle may bind to an aryl halide through a nucleophilic attack to the halogen bonded carbon atom, when the latter has been activated by a catalyst. In the above examples the catalyst does not have to facilitate the comple C-X scission. However, as we will see below, depending on the properties of the catalyst, it is commonly assumed and understood, that also the σ bonds between halogen and carbon atoms are broken by the catalyst.

3.4.1 The original Ullmann coupling mechanism: solution chemistry

The mechanism of the copper-mediated homocoupling of aryl halides is still under debated. However, the most accepted interpretations of the coupling either involve the formation or the coupling via discrete copper aryl species [19, 20, 66].

Despite ongoing debate about the actual mechanism there is consensus in the identification of a catalyst that promotes the cleavage of the halide. The coupling reaction follows the order I>Br>Cl, which is the opposite of that commonly expected for aromatic nucleophilic substitution, but follows the overall carbon halide bonding strength [67]. Therefore, it is sufficient to simply determine which C-halogen bond cleaves at a lower temperature to exclude aromatic nucleophilic substitution.

Coupling via aryl radicals

The first proposed reaction mechanism involves an electron transfer from the copper atom to the aryl halide, which produces an aryl radical. Subsequently, a direct aryl radical dimerization results in the termination of the sequence. The reaction equation and path are sketched bellow.

$$\mathrm{ArX} + \mathrm{Cu}_{(0)}\mathrm{ArX}^{\bullet -} + \mathrm{Cu(I)}^{+}$$
$$\mathrm{ArX}^{\bullet -} + \mathrm{Cu(I)}^{+}\mathrm{Ar}^{\bullet} + \mathrm{Cu(I)X}$$
$$\mathrm{Ar}^{\bullet} + \mathrm{Ar}^{\bullet}\mathrm{Ar{-}Ar}$$

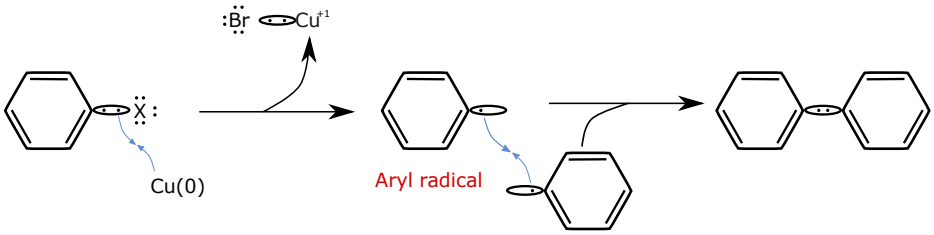

FIGURE 3.9: Scheme of the reaction path of the radical Ullmann coupling mechanism. The different oxidation states of the metal atom are also indicated.

There is some controversy on how the electron transfer takes place, i.e. whether an electron is directly transfer to the molecule via the interaction of the copper atom with the aromatic system of the molecule, which is called the "single electron transfer mechanism (SET)" [68], or if the interaction is directly driven by the halogen atom, known as the "halogen atom transfer (HAT)" mechanism [69]. In either cases, the interaction implies the single electron oxidation of the copper atom and formation of the aryl radical.

Coupling via aryl copper intermediate

The most widely accepted Ullmann reaction mechanism involves the formation of an aryl copper intermediate. Once these radical intermediates are formed, instead of their direct coupling, there is a net oxidative addition of copper atoms that promotes the formation of ArCu(II)X species, which afterwards lead to the biaryl compounds by another oxidative addition/reductive elimination mechanism. Again for clarification, the reaction equation and paths are shown below.

$$\mathrm{ArX + Cu_{(0)} ArX^{\bullet -} + Cu(I)^{+}}$$
$$\mathrm{ArX^{\bullet -} + Cu(I)^{+} ArCu(II)X}$$
$$\mathrm{ArCu(II)X + Cu_{(0)} ArCu(I) + Cu(I)X}$$
$$\mathrm{ArCu(I) + ArX ArCu(III)XAr}$$
$$\mathrm{ArCu(III)XArAr{-}Ar + Cu(I)X}$$

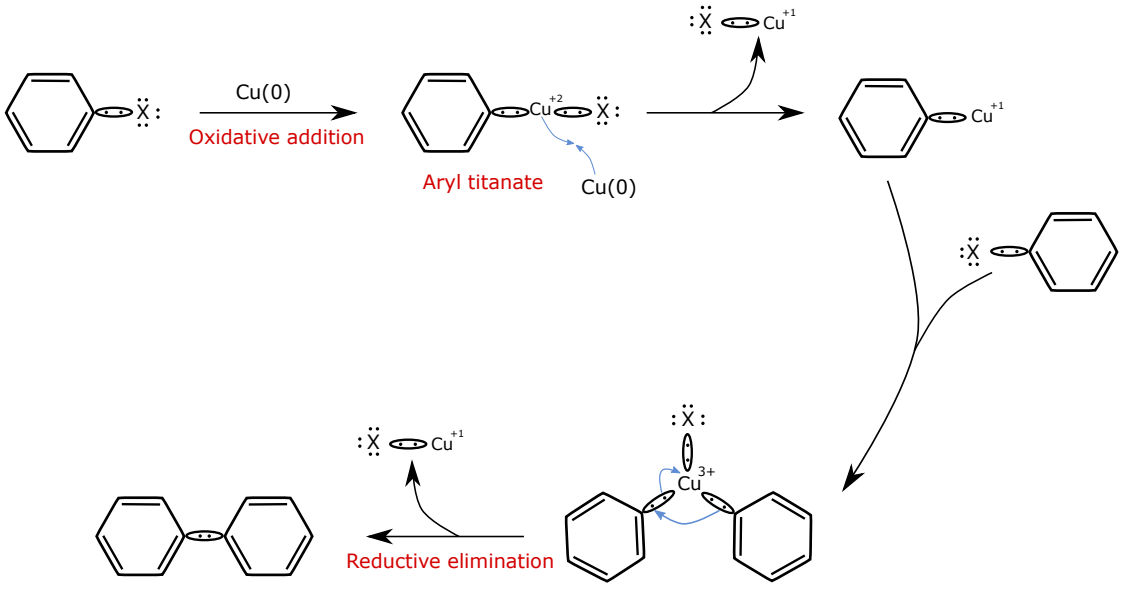

FIGURE 3.10: Scheme of the reaction path of the Ullmann coupling mechanism via aryl copper intermediate. The carbon-halogen and the subsequent structure bonds are represented with a Lewis structure form i.e each electron is drawn as a dot. The different oxidation states of the metal atom are also indicated.

Overall this reaction mechanism differs from the previous one in two aspects. First, during the reaction different ArCu(x) intermediate species are created, with the copper been in various oxidization states. The reaction path is an extension of

the first proposed mechanism, however, since the intermediate organocopper complexes have been isolated [70, 71] makes this mechanism the most plausible one. There is also some consensus that ArCu(I) is the true catalyst, since it is capable of reversibly disproportionating into Cu(II) and Cu(0). The second difference is that the reaction requires the metal atoms to have higher (up to +3 at least) oxidization states. For copper, the ionization potential of higher oxidization states is energetically accessible and therefore the reaction is likely to happen. However, it is clear that catalyst with relatively high oxidization potentials (specially for second and third oxidization states) will drastically increase the reaction barrier.

Nickel and palladium, frequently used Ullmann reaction catalyst in solution, also promote the reaction via an intermediate complex formation. Interestingly, both elements, which normally are found at (+1) state, have to be reduced to (0) in order to be able to catalyze the reaction [72, 73]. This again demonstrates that the catalyst has to at least donate two electrons to participate in the reaction (if the reaction proceeds via the organometallic intermediate).

3.4.2 Surface catalyzed Ullmann coupling reaction mechanism

The surface confined Ullmann coupling reaction resembles many of the aspects we have discussed in solution. Similarly, it is accepted that the reaction is composed of two steps, which are the homolytical scission of the -C-X- (X=I,Br,Cl) bond and the subsequent coupling of the radical entities.

In terms of molecule reactivity, again, the halogen cleaved follows the trend of I>Br>Cl. At room temperature for example, the C-I bonds are spontaneously cleaved on Cu, Ag and Au surfaces [74–76] whereas bromine, instead, is fully split off on copper [13, 77–79], but only partially on silver [76, 80] and not at all on gold, where additional thermal activation becomes necessary [76, 81]. From these results we can readily exclude a reaction via nucleophilic substitution path and that the surface must act as a catalyst.

Importantly, on copper and silver surfaces, the scission of the carbon-halogen bond is followed by an organometallic intermediate phase which precedes the final homo coupling step [13, 67, 77–79, 82]. On gold surfaces, no organometallic intermediates are observed and the coupling reaction completes directly upon dehalogenation. However, there are some isolated reports [83, 84] of organogold compounds in very specific oligomeres but further experiments are required to understand and establish their nature. A sketch summerizing both processes is shown in figure 3.11. This indicates that even for noble metal surfaces, the molecular de-halogenation paths can be different. On gold, the reaction somehow illustrates the radical mechanism shown in figure 3.9 whereas on copper and silver surfaces the reaction path is similar to the intermediate mechanism shown in figure 3.10. Note, however, that an experimental distinction between a direct radical mechanism and an organometallic intermediate with a very low reaction barrier toward the final product requires an extremely high time resolution, generally not present in the employed technique.

In the organometallic phase found on silver and copper, the two organic moieties are connected via the metal catalyst as shown in the figure 3.11 (a). Even though nowadays the net description of the organometallic phase is well-accepted, previously its has been subject to different interpretations. The early 2000s works done by McCarty and Weiss [85, 86] proposed that the radicals in the intermediate phase were connected by molecule-molecule and surface mediated interactions and this scenario was afterwards reproduced by Nguyen et al [87] using ab initio calculations. However, later on, Lewis and co-workers [82] as well as the group of Wang

et al [88], by using low temperature STM measurements and DFT calculations, gave unambiguous evidence at the single-molecule level, for an organometallic intermediate phase consisting of C-Cu-C bridging species. Nowadays this is the most accepted organometallic intermediate configuration and we point out that the metal atom is not just raised-up from the surface but extracted from it. Knowing whether the reaction is activated exclusively by the chemical properties of individual metal atoms or if on the contrary the surface properties (such as the states close to Fermi level) are responsibles for activation can completely change the interpretation of the reaction mechanism.

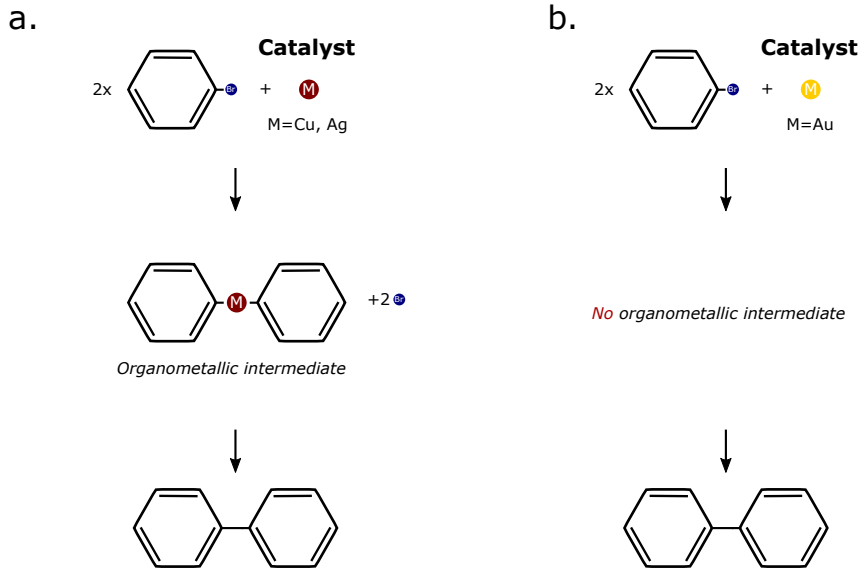

FIGURE 3.11: The different phases isolated experimentally when the Ullmann reaction has been performed in the copper, silver and gold surfaces. For the first two, figure (a), an organometallic intermediate phase has been revealed whereas on gold, figure (b) this phase has not been observed.

Concerning the origin of the linking metal atom, Lewis et al postulate [82] that the metal atom was extracted from the steps. They derived this conclusion taking into account that at the temperature at which the intermediate phase was encounter, there was not an appreciable 2D gas of Cu adatoms and besides they did not observed any increase in Cu surface defects compared to the clean surface. Moreover, the fact that the energy barrier was 50 % greater to remove a Cu atom from the terrace compared to steps further support their interpretation. Thus, the surface mobility and adatom diffusion energies can also influence the reaction path and yield.

With all these aspects in mind, we conjecture why the organometallic phase is found on copper and silver and not on gold.

First of all we consider the case where the -C-X- bond cleavage is drive by the chemical properties of the single atom (and not surface) present on the organometallic phase. This simplifies the problem to the interpretation valid in solution, where the capability of the catalyst to donate electrons (to oxidize) limits the intermediate mechanism figure 3.4.1. A comparison of the ionization energies of Cu, Ag and Au [89, 90] reveals that the barrier of electron removal is twise as high for Au compared to Cu and Ag. Hence, the fact that the organometallic phase is not found on gold reflects the Au atoms limited ability to donate electrons and oxidize.

Another aspect is in general the reactivity of a metal surface. A first glimps at this extremely complex topic can be discussed based on the work called *why gold is the noblest of all metals* performed by Hammer and Norskov [36] where the adsorption and dissociation behaviour of H_2 on metal and transition metal surfaces is studied by DFT calculations.

The main conclusion of the work is that the degree of filling of the antibonding molecule/substrate hybridize states and the degree of overlaping of the adsorbate and surface orbitals dictates the reactivity of the surface. Lets explore the meaning of these two concepts. In a very simple system, when the electronic states of two atoms overlap, quantum mechanics dictates that they have to be orthogonal to each other. This requires energy due to the so-called Pauli repulsion and in the work this energy is defined as $V_s{}^{sd}$, which is the coupling matrix element. However, due to the overlap of the adsorbate and surface states, hybridization occurs and creates new bonding and antibonding states. When only the bonding state becomes occupied, the hybridization effect counteract the orthogonalization energy cost. On contrary, if both states become occupied, no hybridization energy is gained and the orthogonalization energy cost prevails. This simple two-level problem can be transfered to the case of chemisorbed molecules on metal and transition metal surfaces. The degree of interaction will dictated the filling of the antibonding state and the amount of orbital overlap.

The table bellow relates these two effects with the different metals and transition metals.

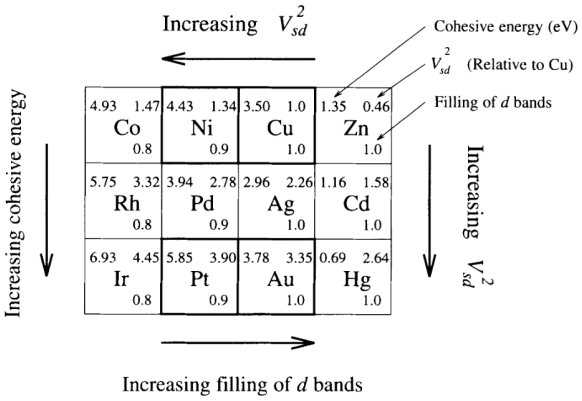

FIGURE 3.12: The orbital coupling matrix element $V_s{}^{sd}$ (where the higher value means lower overlap), the filling of metal d bands and the cohesive energy for metals in the vicinity of gold in the periodic table. Taken from ref. [36].

On the one hand, the orthogonalization energy cost, $V_s{}^{sd}$, increases down through the periodic table and thus for the three noble metals renders the highest value (lowest reactivity) for gold and lowest (highest reactivity) for copper. The reason behind is the highest extension of the 5d states of gold respect to the 3d states of copper.

On the other hand, the filling of the d-bands dictates the degree of filling of the bonding and antibonding states. Its value increases towards the right side thought the periodic table with no noticeable differences for the noble metals. As a consequence of the filling, in noble metals the antibonding states are often located close to or bellow the Fermi level, which gives rise to repulsive interactions. On the contrary, on transition metals the antibonding levels are located above Fermi, which produces

an extra attractive interaction. This is the reason behind the higher catalytic activity of transition metals. Concerning the gold surface, the net result is that Au has both a filled antibonding adsorbate-metal d-state and the largest energy required for the orbital overlap which makes it the noblest of the metals. The lower the surface reactivity of gold when compared to copper and silver noble metals can induce differences in the adsorbtion, diffusion, and stabilization of the adsorbate molecules. These factors will also decidedly dictate the Ullmann coupling mechanism.

Interestingly in the picture developed above, the nobleness of gold is related to the size of the overlap between the interacting atoms or molecule and the gold d states. Clearly, the longer the bond, the smaller the overlap and its energy cost. This explains why gold is one of the best elements to form metallic alloys, since in there bonds are very long. The clearest example is the $GdAu_2$ surface alloy that we employed in the next chapter.

3.5 Conclusion

As a conclusion we remark that a chemical reaction is part of a complex process with many factors (such as temperature, catalyst, molecule-molecule interactions, molecule-catalyst interaction) dictating its performance and reaction mechanism.

In the particular case of the Ullmann reaction, we isolated some particularly relevant reaction parameters:

1. The redox properties of the system: the amount of electrons that the catalyst can donate will constrain the reaction mechanism to a radical or intermediate mechanism.

2. Molecule substrate interactions: The overlap and filling of the molecule-substrate hybrid states will dictated the adsorption and surface diffusion energies of the molecule. As deduced from collision theory, molecular mobility will affect both activation energies as well as reaction probabilities and hence will influence reaction rates.

3. Diffusion of surface adatoms: The energy cost for extracting a catalyst atom from the terrace or steps side plus its diffusion energy, is crucial in the formation of an organometallic intermediate state in surface Ullmann reactions.

4. On oxide surfaces, where the presence of H^+ and OH^- is common, the acid-base catalysis must be taken into account as an alternative reaction path.

Chapter 4

Ullmann coupling reaction of DBTP on $GdAu_2$

4.1 Introduction

The reactivity of the surface catalyzed Ullmann reaction greatly depends on the template that is employed. On Cu [91] and Ag [92] surfaces the reaction occurs already at (or bellow) room temperature (RT) and proceeds via an organometallic intermediate state while higher activation temperatures and no intermediate state are observed on Au [67, 81]. These are but two examples how the properties of the surface decisively influence the reaction properties (see chapter 3 for more details).

In this chapter, we explore how to extend and tune the range of physical and chemical properties of a given metal surface by admixing additional elements to generate inter-metallic compounds or alloys [93, 94]. By synergistic effect i.e, by increasing each other's effectiveness, individual atoms can lead to catalytic properties that are enhanced compared to the pure metal [95]. An instructive example is the activation of a carbon-chlorine bond at RT by bimetallic gold-palladium nanoparticles [96]. The admixture of Pd atoms, with a large number of d-states near the Fermi-level, to the inert Au atoms, allows for efficient charge transfer from the catalyst to the C-Cl bond, thereby activating it for the reaction (see chapter 3.3). Therefore, the high reactivity of such a bimetallic alloys makes them great candidates for the heterogeneous catalysis of the Ullmann reaction.

In general, surface alloys are ideal candidates for studying several aspects concerning the chemistry of the Ullmann reaction mechanism. On the on hand, the surface selectivity towards the alloyed elements provides valuable information about the affinity of the reaction towards a certain catalyst. On the other hand, synergistic effects can be used to improved the reaction conditions.

Here, we study the effect of the admixture of Gd atoms to the Au(111) surface - forming a $GdAu_2$ surface alloy [97]: since Gd is an electropositive atom when compared to Au, a charge redistribution towards the Au atom is expected to improve the red-ox properties of the later, which is a key ingredient for the Ullmann reaction, as we have already discussed in the chapter 3.

Experimentally, the use of $GdAu_2$ entails some advantages. The alloy presents a mesoscopic ordering and a single dominant phase [97] (see section 4.2). This homogeneity allows to use surface averaging techniques. Moreover, Gd and Au atoms are regularly arranged at the surface which creates the ideal situation for studying the surface selectivity during the de-halogenation process.

The mayor drawback of using $GdAu_2$ as a template is its presumable high reactivity. Normally, magnetic surfaces are very reactive and rather difficult to preserve clean [98]. Contrary to the Au(111), cobalt, iron and nickel based surfaces (the three prototypical ferromagnets) all have partially filled d-shells with very high density of

states near Fermi and hence are very reactive. As consequence, often molecules bind so strongly to the magnetic film that they break before diffusing across the surface [99].

We discuss and infer in these points all along the chapter.

4.2 The $GdAu_2$ surface alloy

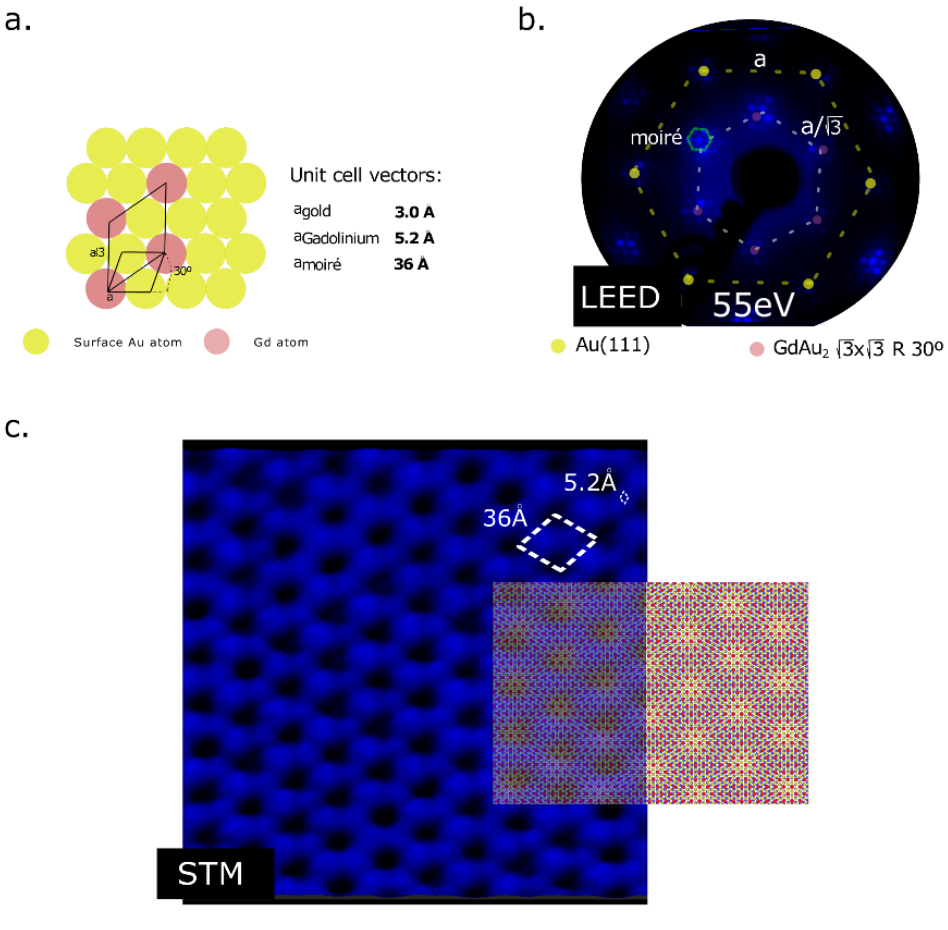

FIGURE 4.1: Characterization of the clean $GdAu_2$ surface. The atomic arrangement of the surface alloy is presented in (a). The LEED image shown in (b) is measured with an electron energy of 55 eV, and the diffraction spots of both Au(111) and $GdAu_2$ lattices are resolved and marked with yellow and pink hexagons respectively. Additional spots due the formation of a moiré pattern are indicated by a green hexagon. The STM image of the clean surface, measured at U_{bias} = 2.5.5 V I_{set}, = 50 pA is included in (c). In the image, individual gadolinium atoms can be resolved and the unit cell of the alloy and the moiré are marked with the white rhombuses. A model of the surface is partially superimposed onto the image.

The unit cell of the $GdAu_2$ surface is depicted in the figure 4.1 (a). The alloy presents $\sqrt{3}$ x $\sqrt{3}$ R30° structure where Gd atoms are exclusively surrounded by Au atoms, giving a total of 1Gd/2Au concentration. The inter atomic distance of two neighbouring Gd atoms is of 5.2 Å while the distance between the nearest Gd and Au atoms is of 3.0 Å.

Due to the differences in lattice constants (3.0 Å $GdAu_2$ and 2.88 Å Au(111)) and a rotation close to 30° of the $GdAu_2$ layer with respect to the underlying Au(111) plane, the $GdAu_2$ surface alloy presents a characteristic moiré pattern that can be nicely visualize both by LEED in figure 4.1(b) and STM in figure 4.1 (c).

The superstructure due to the moiré pattern has a periodicity of 36 Å (marked with a white dashed rhombus in the figure 4.1 (c)) and a corrugation close to 0.6 Å, which give rise to a porous structure that extends all over the surface. In the STM image, and due to the particular measurement conditions, only gadolinium atoms are resolved (red atoms in the scheme of the figure 4.1 (a)). The LEED pattern consist of the 1x1 of Au(111)(red) and the $\sqrt{3}$ x $\sqrt{3}$ R30° of the $GdAu_2$ (yellow). The moiré pattern is highlighted in green. It is important to notice that the moiré overstructure follows the Au(111) lattice orientation and is about 30° rotated with respect to the $GdAu_2$ lattice.

A more detailed characterization of the surface can be found in [97].

4.3 Reaction fingerprints

In this section, using a multi-technique approach, we described the Ullmann coupling reaction of 4'4-dibromo-p-therpenyl (DBTP) molecules on the $GdAu_2$ surface and compare the results with the ones obtained in the bare Au(111) surface. First, by high resolution XPS, we compare the CL energy of DBTP molecules. Then, using *in-situ* TD-XPS, we determine the onset of dehalogenation of DBTP precursors and the temperature at which Br-atoms desorb from the surface. The different thus determined phases are subsequently studied locally by STM and well-ordered molecule and polymer lattices are resolved. Indeed, LEED analysis demonstrates that the local order extends to mesoscale dimension suitable for ARPES characterization. Next, we discuss the ARPES data and show a clear transition from a localized highest occupied molecular orbital in case of DBTP to a fully developed and strongly dispersing band after polymerization into PPP arrays. Finally, we probed the robustness of the $GdAu_2$ surface by polymerizing on top different precursor molecules.

4.3.1 C 1s and Br 3p CLs of DBTP and PPP on $GdAu_2$

The RT phase

In order to see whether DBTP molecules adsorb intact on top of the $GdAu_2$ surface, we compare the CLs of a multilayer DBTP, with the monolayer DBTP adsorbed on the clean Au(111) surface and on the $GdAu_2$ alloy. The results are depicted in figure 4.2.

The DBTP molecule (top part of the figure) consist of three phenyl rings interconnected at the para position and terminated by Br atoms respectively. Due to the chemical composition of the molecule, three types of carbon atoms are found in the molecule and labelled as 1, 2 and 3 in the figure. They all have a common sp^2 hybridization but the electronic environment surrounding the atoms is different. C_1 is bonded to two carbons and one hydrogen atom. C_2 is bound to three carbons and finally C_3 is attached to two carbons and one bromine atom. Whereas the C 1s CL energy position of C_1 and C_2 is almost identical and therefore indistinguishable in XPS [56, 79, 81, 91], the CL position of the C3 is considerably different. Due to the high electronegative character of the Br atom, the electronic charge surrounding the C_3-Br bond is effectively polarized towards the Br atom. This lowers the screening and consequently the kinetic energy of the ejected C_3 photo-electron, which produces

a CL shift of about 1 eV to higher B.E (slightly varies depending on the employed surface) on C_3 with respect to C_1 and C_2 [56, 79, 91, 100].

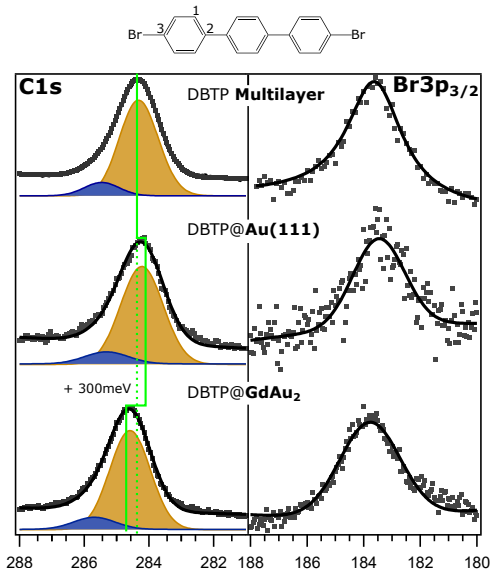

FIGURE 4.2: Comparison of C 1s and Br $3p_{3/2}$ CLs of DBTP molecule (chemical structure drawn on top) for a reference multilayer deposition on Au(111) and a monolayer adsorption on both Au(111) and $GdAu_2$ surfaces.

The C 1s and Br $3p_{3/2}$ CL spectra measured for the DBTP in the three mentioned scenarios, i.e. multilayer and monolayer on Au(111) and monolayer on $GdAu_2$ respectively are shown in the figure 4.2. Compared to the C 1s CL, the resolution of the Br 3p CL is rather poor due to a low absorption cross section (for the current experimental conditions) and a relative scarcity within the molecule (1 Br every 9 C atoms). Thus we use the C 1s CL as reference for comparing the three different scenarios.

In all cases, the C 1s peak is deconvoluted using two peaks which are separated by less than 1 eV, in agreement to the cases found in the literature for halogenated poly-aromatic molecules [56, 79, 81]. The orange peak is attributed to $C_{1,2}$ of DBTP while the blue peak originates from C_3. Considering the adsorption cross section reference values for C 1s and Br 3p [101], the integrated intensity ratio of the peaks is 1:8, the expected C_3 to $C_{1,2}$ ratio of the intact molecule. Moreover, the total CL integrated intensity between Br 3p and C 1s (not shown) agrees with the ratio of the intact molecule.

As indicated by the green lines, the energy position of the C 1s and Br 3p peaks are different. On the one hand, for both multilayer and Au(111) cases, the CL energy position of C 1s (284.25 eV) and Br 3p (183.6 eV) is, within the experimental resolution, the same. Considering the multilayer scenario as the energy reference for the isolated non interacting DBTP molecule, it suggest a rather low molecule substrate interaction on Au(111) compared to the $GdAu_2$ case, which is reasonable considering the low reactivity of gold surfaces [36] (3.12). On the other hand, compared to the adsorption on the Au(111) surface, the CL BEs of DBTP appear 0.3 eV shifted towards higher energy on $GdAu_2$. Assuming vacuum level alignment of DBTP within both surfaces and the same Au $4f_{7/2}$ CL energy reference, the observed BE difference

suggest a lowering of the work function of the $GdAu_2$ surface compared to the clean Au(111) surface.

In conclusion, we find similar results for DBTP on $GdAu_2$ and the well studied multilayer [102] and monolayer DBTP on Au(111) [81] phases, indicating that the molecules are not dissociated upon adsorption on the $GdAu_2$ surface. Importantly, this implies that neither dehalogenation nor organometallic intermediates are formed on the $GdAu_2$, at least at RT.

Temperature dependant XPS

In previous XPS experiments a 2 eV bromine CL shift towards lower BE has been isolated as the signature of the scission of the C_3-Br bond [5, 67, 79, 103]. Therefore we follow the evolution of XP spectra of a ML of DBTP on $GdAu_2$ and on Au(111) as function of temperature to identify the transition temperature.

On the Au(111) surface, the transition is known to happen at around 360-390 K [81], and if we look in the figure 4.3 (a), the Br CL energy shift happens close to the reported temperature. The onset of C_3-Br bond scission is accompanied with a drop in the integrated Br 3p intensity (see the red traces in the intensity profile shown in figure 4.3 (c)). Concurrently, Br-Au species are formed leading to a shift by almost 2 eV toward lower BE of the Br 3p doublet. Close to 450 K all C_3-Br bonds are cleaved and Br atoms are either desorbed or are found as Br-Au species. Finally, at 560 K Br-Au bonds break and Br desorbs, as is evidenced by the complete loss of integrated Br 3p intensity (red line 4.3 (c)).

The same temperature ramp is performed on $GdAu_2$ and the results are presented in the figure 4.3 (b). The evolution of the Gd $3d_{5/2}$ CL , located at 1187.3 eV, is also included. Like on Au (111), a clear shift of the Br 3p CL (to 182.9 eV) signifies the C-Br bond cleavage, which again is accompanied by a drop in the integrated Br 3p CL intensity (black line in figure 4.3 (c)). Nevertheless, the temperature at which the C_3-Br scission occur presents some differences. Contrary to Au(111), where the Br $3p_{3/2}$ CL energy shifting is not completed until a temperature of around 450 K, on the $GdAu_2$, the dehalogenation starts earlier and is completed at lower temperature (380 K). Moreover, the desorption of the chemisorbed Br atom occurs close to 700 K, a considerably higher temperature than on the Au (111) surface. Interestingly, during the time interval where the Br atoms remain chemisorbed on the $GdAu_2$ surface, the Gd $3d_{5/2}$ CL shifts 500 meV toward higher BE, as indicated by the blue trace in the high resolution spectra shown the right panel, and the integrated Gd $3d_{5/2}$ CL intensity increases by about 30% , figure4.3 (c).

On the one hand, changes in the C_3-Br scission temperature indicates a lowering of the reaction activation energy on $GdAu_2$. Concomitantly, the reaction is completed faster on $GdAu_2$ as no more C_3-Br species are found at temperatures above 400K, while on Au(111), temperatures of more than 450K are needed. On the other hand, the correlation of the Gd $3d_{5/2}$ CL shift with the chemisorbed Br atoms, as well as the considerably higher desorption temperature compared to the Au (111) surface, suggest the formation of stable Br-GdAu structures. During this period, the Gd $3d_{5/2}$ intensity increase by about 1/3 before decreasing simultaneously with the Br 3p intensity close to 700 K. While the complex line shape of the Gd CL makes a quantification of the Gd to Br ratio challenging, we can perform an estimate based on geometrical considerations. Assuming a full ML coverage of DBTP on perfect $GdAu_2$, we can deduce from our adsorption model (shown in figure 4.5 (a)) that we have 2 Br atoms per 4 surface Gd atoms at RT. This leads to 4/3 Br atoms after

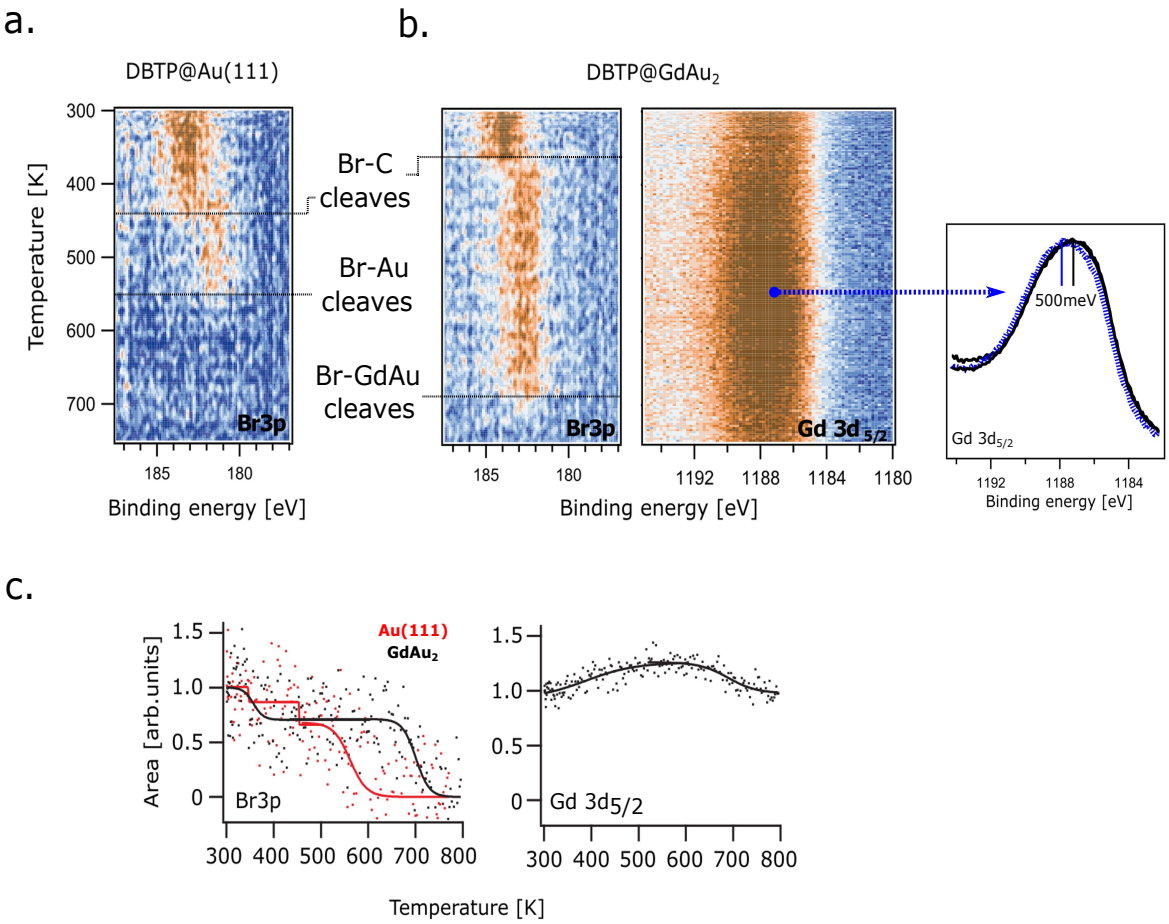

FIGURE 4.3: TD-XPS measurements done for DBTP on Au(111) and $GdAu_2$. For the Au(111) surface, figure (a), only the Br 3p CL temperature evolution is shown whereas for $GdAu_2$, figure (b), the temperature evolution of both Gd $3d_{5/7}$ Br 3p CLs is shown. Single Gd $3d_{5/7}$ CL spectra extracted at RT (black), 500 K(blue dashed), and 700 K(black) are added in the right graph. The temperature evolution of the core level areas are gather and compared in the figure (c).

dehalogenation due to a 1/3 desorption (as is evident from the drop in Br 3p intensity to about 2/3). Thus, the increase of 1/3 in the Gd intensity matches precisely the remaining Br atoms, i.e. 4/3 Gd atoms per 4/3 Br atoms. This correlation suggest a direct interaction between Br and Gd atoms, however further experiments are required to unambitious establish a causation.

In conclusion, the TD-XPS measurements do not elucidate whether the C_3-Br bond cleavage is promoted by Au or Gd atoms even though a high affinity between bromine and surface gadolinium atoms is deduced from the simultaneous shit in Br and Gd CLs.

4.3.2 Polymerization fingerprint by high resolution XPS

The polymerization fingerprint is obtained by analyzing the evolution of the high resolution XP spectra measured in the three transition phases identified in the temperature ramps: (i) At RT, where the molecules are still intact (ii) at 500 K, after the C_3-Br bond cleavage but with chemisorbed Br atoms present in the surface and (iii)

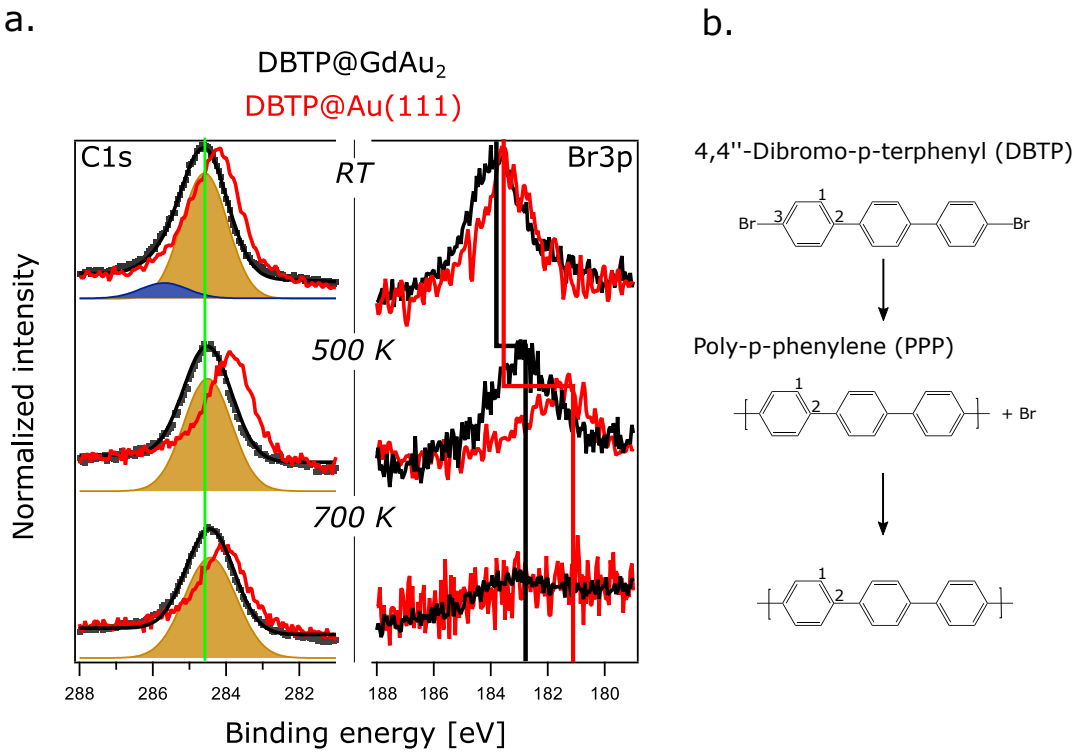

FIGURE 4.4: High resolution XPS spectra measured for the DBTP adsorbed on $GdAu_2$ (black) and Au(111) red at RT, 500 K and 700 K. The corresponding C 1s and Br 3p CLs are shown in (a). The chemical structure of DBTP and poly-p-phenylene (PPP) is shown in (b).

after the Br desorption, at 700 K. Again, the C 1s and Br 3p CLs measured in both $GdAu_2$ (black) and Au(111) (red) are gathered in the figure 4.4 (a) for comparison purposes. The C 1s peak deconvolution is only performed in the $GdAu_2$ case, since on Au(111), the polymerization path by XPS is already well established [81].

Upon annealing, the higher binding energy peak component of the C 1s CL spectra (the blue peak at RT) dissapears. Since the feature is related to the C_3 atom of DBTP (see figure 4.4 (b)), its disappearance indicates the breaking of the C_3-Br bond. Interestingly, the bond cleavage is not preceded by and organometallic phase, since this would induce the appearance of a new peak in the low binding energy side of the spectrum [79]. On the contrary, the peaks at 500 K and 700 K are rather symmetric and in the deconvolution, only the $C_{1,2}$ peak is present, as expected for the poly-p-phenyline (PPP) structure shown at the bottom of the figure 4.4 (b). The high temperature C 1s peak deconvolution on Au (111), although not included, behaves equivalently [81].

Again the lower BE position persisting upon annealing for both C 1s and Br 3p core levels (delimited by the green line in the figure) is likely a consequence of the surface work function differences.

Finally it is striking that the Br 3p CL energy difference between C_3-Br and the chemisorbed Br atoms is slightly lower on $GdAu_2$ (1.3 eV) than on Au (111) (2 eV) (follow the red and black lines). Additional experimental and theoretical studies are required to explain the lowering of the core hole screening of the chemisorbed bromine atoms on the $GdAu_2$. However, differences in the adsorption position, adsorption heights and atomic coordination of the bromines, are some intuitive factors

that could explain the observed effect.

4.3.3 STM and LEED characterization

Herein we use STM and LEED to characterize the formation of PPP on $GdAu_2$ from the precursor DBTP molecule. First we study the molecular phase at RT and afterwards we anneal the sample to 500 K, since we know from the previous XPS measurement (figure 4.3) that at this temperature the molecules are already dehalogenated. Results are summarized in figure 4.5.

After the deposition at RT of DBTP molecules on the $GdAu_2$ surface, new diffraction spots, marked with the white hexagon, appear in the LEED image (figure 4.5 (a)). The new spots have the same $GdAu_2$ lattice orientation (pink hexagon) and form a $2\sqrt{3}$ x $2\sqrt{3}$(R30°) pattern. The diffraction spots due to the moiré lattice appear very faint. Since the image is taken at a beam energy of 25 eV, the (1,1) spots of the Au(111) surface are no longer on the LEED screen.

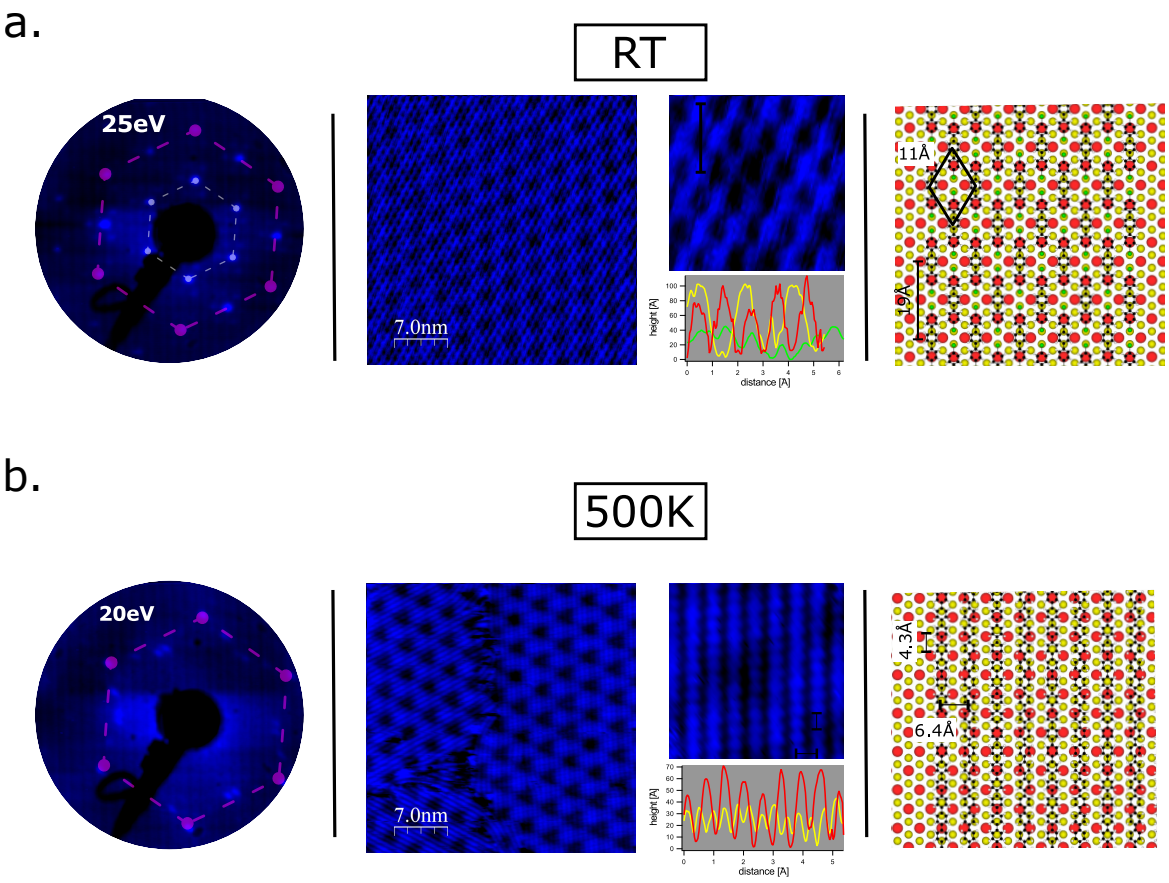

FIGURE 4.5: Adsorption geometry of DBTP and PPP on $GdAu_2$. In (a), from left to right, LEED, STM and a schematic model for the DBTP monolayer adsorbed on $GdAu_2$ at RT. In (b) the same measurements performed after the sample was annealed to 500K. STM image acquisition parameters U_{bias} = 1.0 V I_{set}, = 100 pA.

The STM images measured after the adsorption of DBTP shows a new ordered structure on top of the moiré superstructure, which is still faintly visible underneath. Thus, in a first approximation, the stoichiometry and structure/order of the $GdAu_2$ alloy is preserved underneath the DBTP molecular overlayer. The molecules create

a new super periodicity which is enhanced and clearly visible in the 5.5nm x 5.5nm zoom-in image after removing the moire pattern via a low pass filter.

A periodicity close to 19 Å (yellow trace) in the symmetry related [1-21] and [-1-12] directions, respectively is resolved. In the symmetry related [-101], [01-1], and [1-10] directions a periodicity of about 11 Å (green line) is resolved. Note, that a periodicity of 11 Å in the direction of the close packed rows of the $GdAu_2$ alloy is equivalent to a $2\sqrt{3}$ x $2\sqrt{3}$ (R30°) super structure with respect to the buried Au(111) interface. Thus, the STM data is in complete agreement with the LEED image. Finally, the periodicity of 19 Å matches closely the periodicity of DBTP molecules arranged in one dimensional chains [56]. A model summarizing the supra molecular phase is included in the right part.

Upon heating the sample to 500 K, the LEED image evolves to a rather complex superposition of diffraction spots with an overall star-like shape. The $GdAu_2$ lattice (pink hexagon) is still clearly visible and the moiré pattern can barely be identified. The arrangement of the resulting organic overlayer can easily be interpreted from the STM images. As for the case of the supra molecular phase measured at RT, the moiré superstructure is clearly visible and therefore preserved after the annealing. On top of it, a new stripe pattern appears, roughly oriented along the three high symmetry direction of the moiré lattice underneath. The profiles extracted from the image amplification give an inter chain spacing of 6.4 Å (red trace) and a 4.3 Å intra change spacing (yellow trace). Interestingly, the latter matches the expected 4.2 Å phenyl-phenyl distance for the PPP polymer [13, 56].

In conclusion, by STM and LEED we unravel the formation of long range order stripes at 500 K where the intra chain periodicity resembles the periodicity expected for the PPP polymer. Besides, the visualization of the surface moire pattern upon the molecular adsorption and polymerization, indicates that the alloy underneath is preserved.

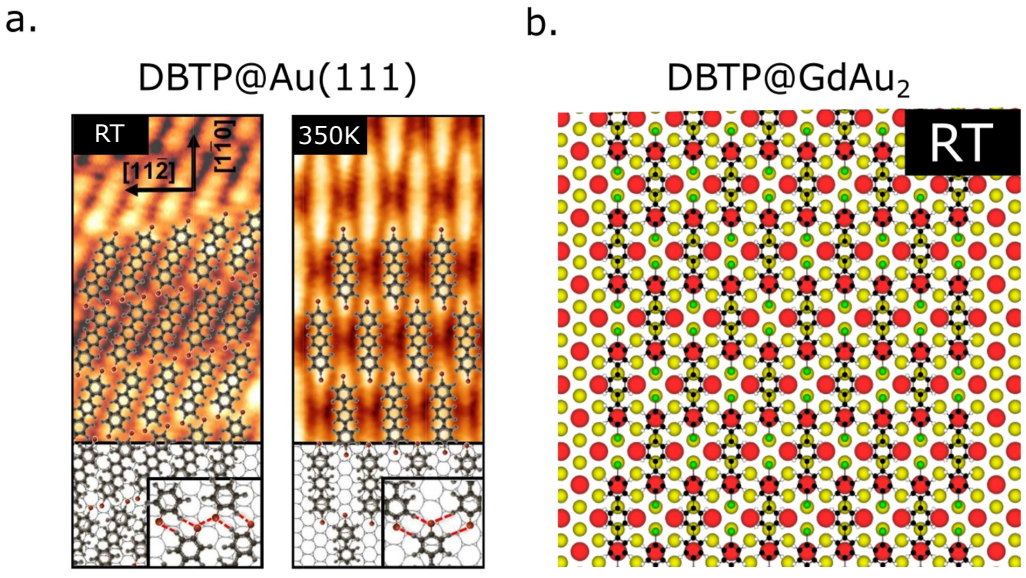

FIGURE 4.6: Comparison of the adsorption geometry of DBTP on Au(111) and $GdAu_2$. The STM and sketch models shown in (a) are taken from [81] whereas in (b) our proposed model for the adsorption of DBTP on $GdAu_2$ is shown.

In terms of reaction mechanism, the molecular arrangement of DBTP on Au(111)

is decisively different compared to $GdAu_2$. In the figure 4.6, we compare the model of the DBTP phase we found on $GdAu_2$, with the models and experimental STM images of DBTP adsorbed on the regular Au(111) taken from [81]. Interestingly Basagni *et al*, reported a supra molecular phase transition from RT to 350 K prior polymerization, that resembles the one we get in the $GdAu_2$. Thus, only at temperatures higher than 350 K, molecules are linearly arrange with the bromine atoms phasing each other. Within *collison* theory (see chapter 3) this alignment of DBTP molecules is ideal to facilitate the Ullmann coupling reaction at very high yield. If we assume that the geometrical transition from the RT phase (figure 4.6 (a) left) to the one observed at 350 K by Basagni *et al* proceeds slower than the time frame covered in our temperature dependant XPS data, i.e. the rearrangement into the "350 K" phase is not completed until much higher temperatures in our ramp, we have isolated a factor that explains the higher reaction rate on $GdAu_2$ where molecules are already properly aligned at RT. Note that in agreement with our interpretaion, during the experiment of Basagni *et al*, the sample was annealed to the given temperature for several hours prior to characterization by STM, while it took roughly 1 hr to increase the temperature from 340 K to 400 K in our measurements.

4.3.4 Electronic properties determined by ARPES

Next we investigate the electronic properties of both supra molecular and polymeric phase as well as of the clean surface.

The measurements are performed along the $\overline{\Gamma M}$ direction of the $GdAu_2$ first Brillouin zone shown in figure 4.7 (a). We opted to scan in this area because it is the direction that follows the growth of the PPP polymer. This is better understood by comparing the Brillouin zones of both GdAu2 and the moiré that are shown in figure 4.7 (b).

We stated before that the polymer growth is preferentially oriented along the high symmetry directions of the moiré lattice (see the white lines in figure 4.7 (c)). The lattice and equivalently, the brillioum zone of the moiré (orange hexagon) is 30° rotated with respect the $GdAu_2$ (blue hexagon). Therefore, the polymer follows the $\overline{\Gamma K}$ direction of the moiré BZ and equivalently the $\overline{\Gamma M}$ direction of the $GdAu_2$ BZ. The surface parallel and perpendicular wave vector values of both brillioum zones are included in the figure.

The band structure of the clean $GdAu_2$ was characterized previously [104, 105] and is shown in figure 4.7 (d) . Particularly, along the $\overline{\Gamma M}$ direction it presents a pronounce dispersive band with the top of the band near the Fermi energy (E_F) at k= 1.34 $Å^{-1}$. The top of the band is highlighted with the yellow line.

After the adsorption of DBTP (figure 4.7 (e)), the $GdAu_2$ bands are strongly attenuated and barely visible. Interestingly, a new band emerges at -2.3 eV, with its energy value constant along the $\overline{\Gamma M}$ direction and centred around k=1.43 $Å^{-1}$ (and highlighted with the arrow). The non-dispersive character of the band is attributed to the localized highest molecular orbitals of DBTP [13, 15, 56].

When the sample is heated to 500 K, the discrete and flat molecular band evolves into a highly dispersive band (indicated by the arrow in figure 4.7 (f)). The band maximum is at -1.85 eV and a wave vector of 1.43 $Å^{-1}$. This band was previously assigned to the PPP polymer on Au [15], Cu [13] and TiO_2(110) [56]. Thus, the ARPES results, in agreement with XPS, STM and LEED data, proves the successful polymerization of DBTP precursors into PPP on the $GdAu_2$ surface.

Nonetheless, we notice that the polymeric band shares similarities both in E and k with one of the bands present in the clean $GdAu_2$ (marked with the arrow). To

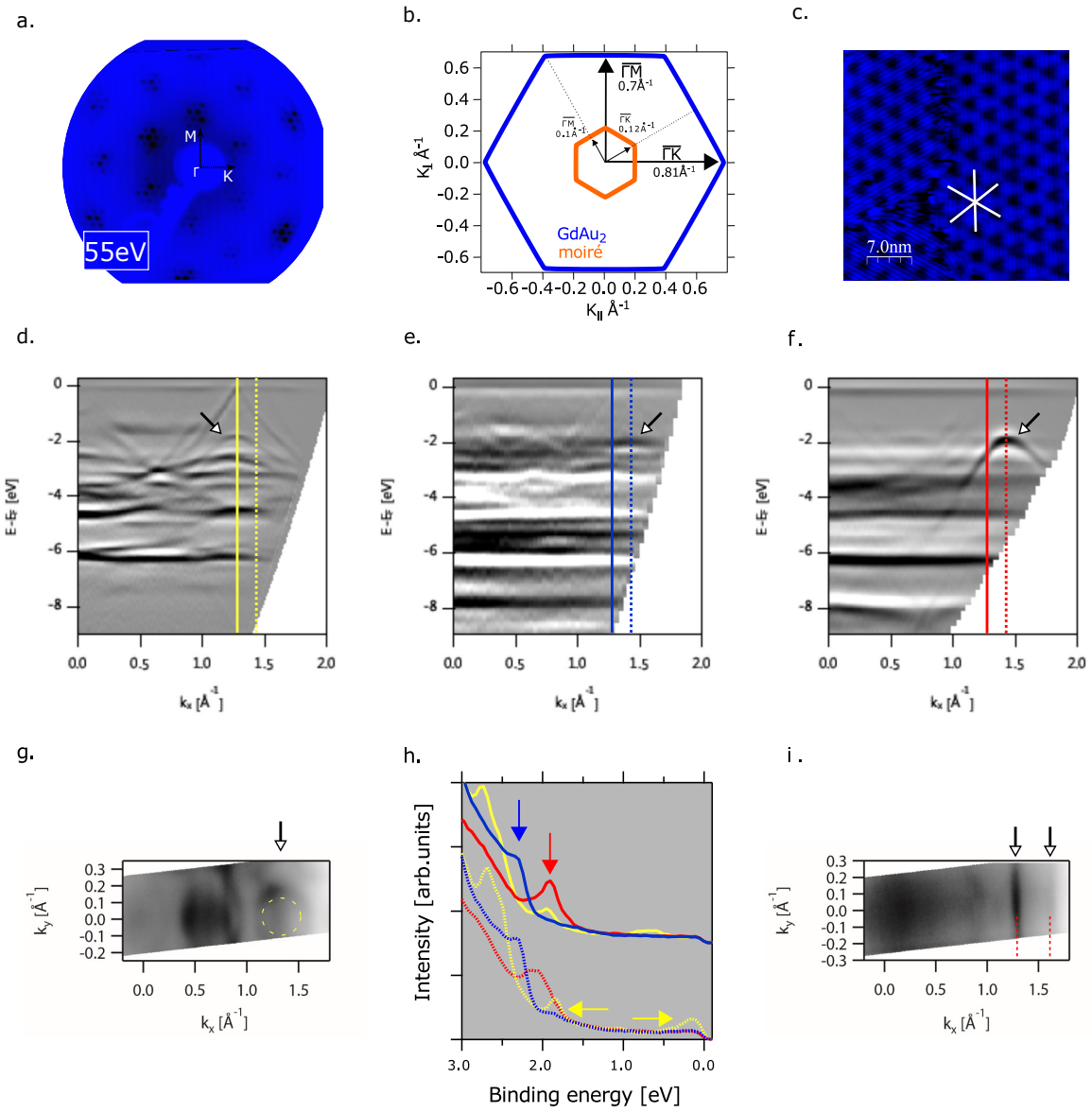

FIGURE 4.7: ARPES valenc band (VB) measurements of DBTP and PPP on $GdAu_2$. An sketch of the $GdAu_2$ and the moiré BZs is shown in (b). In (a) and (c), the corresponding clean $GdAu_2$ surface LEED and STM measurements are included where the high symmetry directions are marked. From (d-f), the 2nd derivative of the VB measurements acquired on the clean $GdAu_2$ and DBTP and PPP covered surface along the $\overline{\Gamma M}$ direction are plotted, respectively. Iso-energy surfaces (cuts at BE of -2.2 eV) of (e) and (f) are plotted on (g) and (i). Last, in (h), energy distribution cuts (EDC) taken along the solid and dashed lines of (d-f) are plotted.

discern between them, in figure 4.7 (g) and (i) and, we present iso-energy maps taken at -2 eV for the clean and PPP covered surfaces respectively. Whereas on PPP the band presents a 1D character (red arrows), in the clean surface the band disperses in 2D (dashed circular lines). Thereby, the PPP band can be unambiguously identify.

Finally, we include in the figure 4.7 (h), energy distribution cuts (EDC) taken at k= 1.34 $Å^{-1}$ and k=1.43 $Å^{-1}$ (dashed and solid lines in 4.7 (d),(e),(f)) to clearly distinguish the energy position of the different bands described above.

4.3.5 The reaction selectivity

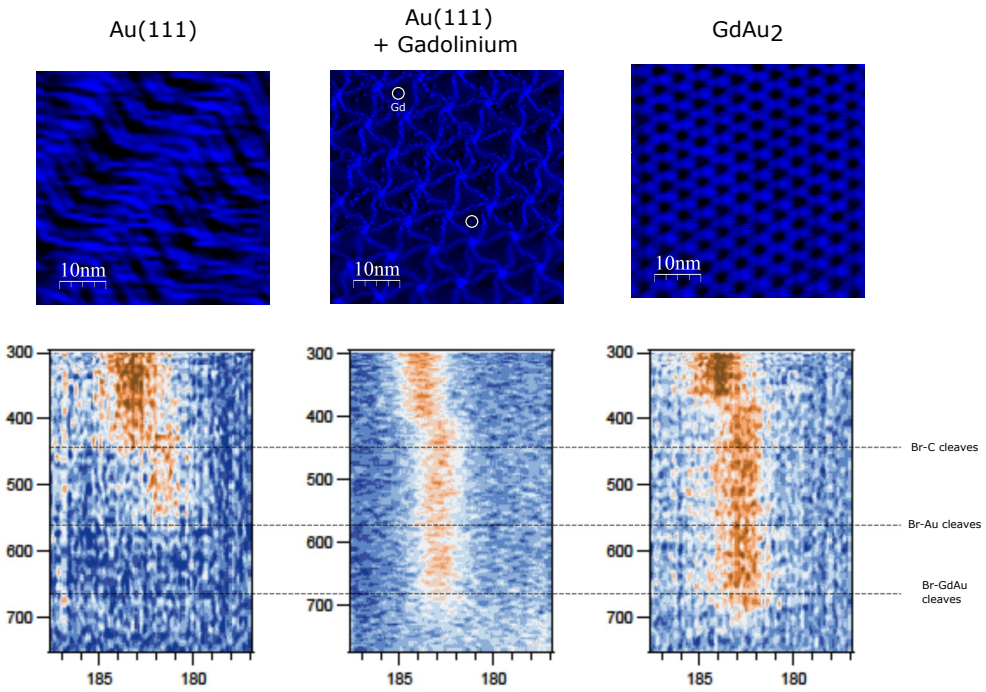

FIGURE 4.8: Ullmann reaction as function of the Gd coverage. From left to right, STM and temperature dependant XPS measurements of DBTP covered Au(111) surface, sub monolayer Gd covered Au(111) surface and on the $GdAu_2$. STM image acquisition parameters U_{bias} = 2.5 V I_{set}, = 50 pA.

With the successful polymerization of DBTP on $GdAu_2$ established, we now address the selectivity of the reaction toward the two different elements present in the alloy, i.e Gd and Au. For doing this, as shown in figure 4.8, we compare by XPS the de-halogenation process of DBTP on three surfaces containing different amounts of Gd.

The Br 3p CL waterfall plots shown in first and last columns are measured after the adsorption of a monolayer DBTP on Au(111) and $GdAu_2$ respectively, and their evolution was already discussed within figure 4.3. In the middle column , the Au (111) surface is covered with a small amount of Gd atoms. It is impossible to quantify with our lab source XPS the relative amount of gadolinium compared to the full $GdAu_2$ surface but we estimate it to be lower than 5 % of a ML. However, at this Gd coverage, a new trigon like phase is created, as illustrated in the middle STM image. Curiously, at the given tunneling conditions, single Gd atoms can be distinguished in the figure. A detailed description of this phase can be found in

[97]. The temperature dependant XPS ramp presents an intermediate scenario when compared to the $GdAu_2$ and Au (111) cases. Within our resolution, the onset of C_3-Br bond scission starts at 410 K, earlier than on Au(111) which occurs at 450 K, and later than on $GdAu_2$ (360 K). Overall, this indicates the addition of Gd atoms to the Au(111) surface, directly or indirectly, decreases the activation barrier of dehalogenation process. Directly refers to the case where gadolinium atoms are the surface catalytically active sites. Indirectly on contrary refers to the enhancement of the DBTP self assembled structure upon addition of gadolinium that favours the reaction, as we discussed above. Unfortunately , the XPS signal originated from the Gd atoms is under our resolution limit and thus, we can not quantify the ratio between Gd and DBTP molecules. After scission, the chemisorbed Br atoms remain on the surface up to almost 700 K as for the case of $GdAu_2$ ascribed to the strong Br-GdAu bond interaction. Interestingly, the drop of the integrated Br 3p intensity is close to the 33 % for both Gd containing surfaces. Thus, already for the submonolayer case, there is enough Gd to bound with the chemisorbed bromine atoms.

4.3.6 DITP and 2N-DBTP on $GdAu_2$

Another aspect that we study is whether the $GdAu_2$ template is suitable for polymerizing different precursor molecules via the Ullmann reaction. In particular, we use two reactant molecules, named 4,4"-Diiodo-p-therphenyl (DITP) and nitrogen doped DBTP (2N-DBTP). Their chemical structure, together with the DBTP, is shown in the top part of the figure 4.9.

On the one hand, the use of DITP, figure 4.9 (b), is motivated by the lower activation barrier for the C_3-I bond compared to the C_3-Br bond [67, 106] (see also chapter 3). Consequently, at least in the noble metal surfaces, the activation energy of the Ullmann coupling reaction is lower when iodine groups are employed. The temperature dependent XPS measurement shows the characteristic shift of the I $3d_{5/2}$ toward lower BE already close to 350 K. Thus the activation temperature is considerably lower than the 380 K determined for DBTP on $GdAu_2$ (see section 4.3.1). Thereafter, the chemisorbed I atoms desorb close to 580 K, a considerably lower temperature than for Br atoms which, as discussed above, stay on the surface up to around 700 K. This is in reasonable agreement with the adsorption energies found for halide ions in noble metal surfaces [107]. Moreover, the higher iodine desorption temperature on $GdAu_2$ compared to Br on Au(111) further reinforces our interpretation of the formation of X-GdAu x=Br,I species. After annealing the sample to 700 K, PPP chains are formed as is evidenced in the STM image. Since the final product, PPP, is the same for both DBTP and DITP, the periodicity and the direction of growth of the polymer are the same in both cases. Overall the results demonstrate that the polymerization of DITP is also catalytically activated by the template underneath. Indeed, due to the lower C_3-I bond energy with respect to C_3-Br, the reaction proceeds earlier in agreement with similar studies on other surfaces [76]. Finally, we attribute the lower (higher) iodine (bromine) desorption temperature to the lower(higher) electronegative character of the atom and thus weaker (stronger) interaction with the Gd atoms underneath.

On the other hand, we choose the 2N-DBTP, figure 4.9 (c), due to the stronger surface affinity of nitrogen groups containing organic molecules [108, 109]. The temperature dependant XPS measurement taken after 2N-DBTP adsorption is shown in the bottom right part of the figure. Overall the temperature evolution of the Br $3p_{3/2}$ CL is similar to the one measured for the DBTP (and shown in the left bottom part). The temperature onset for C_3-Br cleavage is at 360 K and the chemisorbed Br species

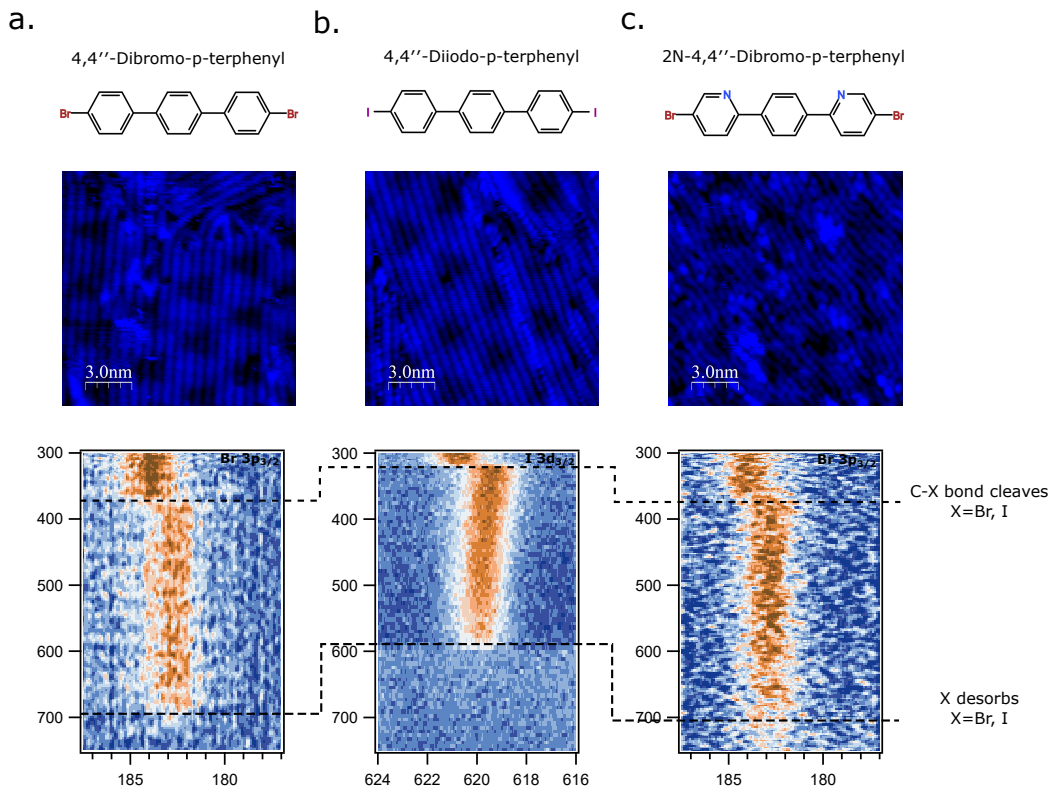

FIGURE 4.9: $GdAu_2$ assisted Ullmann coupling reaction of DBTP (a), DITP(b) and 2N-DBTP (c). For each molecule, STM images taken after the polymerization are shown on top and underneath, the corresponding temperature dependant XPS measurements. STM image acquisition parameters U_{bias} = 1.5 V I_{set}, = 100 pA.

desorbs at temperatures above 700 K. Nevertheless, the differences produced by the N doping of the DBTP molecule are clearly visible in the STM image. The characteristic moiré pattern of $GdAu_2$ is again preserved, but the polymer chains are twisted and not as well aligned compared as the straight lines observed for DBTP. This is a direct consequence of the stronger nitrogen-Gd interaction, that tends to destabilize the structure of the final polymer. An interesting question is the band structure of the 2N-PPP chains. On Au(788), it was demonstrated that the top of the VB of 2N-PPP chains is 340 meV lower than that of PPP chains [15]. Given the high BE of the top of the VB of PPP chains ($\approx$ 1.9 eV) on $GdAu_2$, it may be possible to shift the bottom of the CB below EF for 2N-PPP chains on $GdAu_2$. Indeed, recently it was demonstrated that the PPP chains may be metalized on Cu(110) [13]. Therefore, further VB measurements are on the line to unravel the electronic properties of such a polymeric bands.

4.4 Conclusions

In the present chapter, the successful polymerization of DBTP on $GdAu_2$ has been established. By STM we have identified long range ordered PPP chains and their electronic properties have been established by ARPES measurements. During the different reaction steps that we have been able to identify by STM and LEED, the preservation of the characteristic moiré pattern of the surface indicates the suitability of the $GdAu_2$ surface for said reaction.

Interestingly, by temperature dependant XPS measurements we have established a lower reaction activation temperature on the $GdAu_2$ surface compared to the bare Au (111). We were able to identify two factors underlying the improved reaction conditions: firstly, on the $GdAu_2$ alloy, the DBTP precursors are already favourably aligned at RT, while on Au(111) additional kinetic energy is needed and the rearrangement into the most favourable reaction geometry only takes place upon heating to about 350 K [81]. Within collision theory (see chapter 3) this additional barrier can account for measured difference in activation temperature. Secondly, we observed an increase in Gd intensity as well as a CL shift toward higher BE at temperatures above the C-Br bond scission of DBTP covered surfaces. The increase in Gd signal correlates perfectly with the amount of chemisorbed Br atoms that remained on the surface, i.e. one additional Gd atom for every Br atom. Moreover, the antagonistic shift in Br and Gd CL suggest a direct bond of Br to Gd. Strikingly the Gd signal decreases again concurrently with the Br one at temperatures close to 700 K (presumably Br-Gd is either desorbed or adsorbed). While these correlations decisively favour a scenario with direct Gd-Br bonding, no signatures of an organometallic phase involving in particular Gd atoms could be observed. Whether this is due to an intrinsic effect, such as an inestabilty of the organometallic intermediate, as is the case on the bare Au(111) surface, or if the experimental signatures of said organometallic phase are beyond our experimental resolution must be explored in further experimental and theoretical work.

The suitability of the $GdAu_2$ for using it as a template with more reactive molecules is also demonstrated by the successful polymerization of DITP and 2N-DBTP molecules.

Finally, we point out that it has not escaped our notice, that there is considerable fundamental and technological interest in the use of ferromagnetic surfaces for Ullmann coupling reactions [104] . The possibility of growing *in-situ* conjugated organic nano wires on top makes the $GdAu_2$ an extremely appealing template. However, this work aims to comprehend the chemistry of the Ullmann reaction and therefore we have not addressed the magnetism of the system at this point.

Chapter 5

Ullmann coupling reaction of DBTP on c-Au(111)

5.1 Introduction

In the present chapter we investigate *the role played by steps* during the surface assisted Ullmann coupling reaction.

In the field of heterogeneous catalysis, steps are known to be active sites capable of triggering catalytic processes. The oxidation of carbon monoxide (CO) or the dissociation of nitric oxide (NO) are some of the many examples [110–113]. Normally, the higher reactivity of steps is attributed to their lower atomic coordination. Consequently, step atoms have metal d-states closer to the Fermi energy than the higher coordinated surface atoms. These higher lying d-states, in-turn, may readily interact with adsorbate valence states [37].

An interesting approach to exploit the use of steps in heterogeneous catalysis is the use of metallic nanoparticles [114, 115]. An instructive example is the oxidation of CO by gold nanoparticles. Despite the generally accepted inert character of Au [36], Janssens *et al.* [37] found increased catalytic activity of Au nanoparticles with decreasing particle size. Decreasing the particle size is equivalent with increasing the number of lower coordinated atoms present at steps per surface area.

In surface science, most studies of the influence of steps catalytic reactions/activity are limited to diatomic molecules such as H_2O, NO,CO,N_2. [111–113, 116]. Only recently, few works deal with stepped surfaces to trigger reactions with larger organic molecules. Zhang *et al*, report a linear alkane coupling at the step edges of Cu surfaces by the C-H bond activation of terminal methyl groups [117]. In the field of Ullmann coupling , Saywell *et al*, identify the kink sites of the Au (10,7,7) surface as catalytic sites for Br atom removal from dibromoterfluorene (DBTF) molecules prior to polymerization. While their STM study directly revealed the preferential activation by low coordinated kink atoms [118], they neither quantify the lowering of the reaction barrier compared to a flat, higher coordinated, Au (111) terrace, nor do they elucidate if multiple reaction pathways are present simultaneous.

During our investigation of the polymerization of DBTP on Au (111) introduced in the chapter 3, we noticed that STM images of sub ML DBTP deposited on a slightly warm Au (111) surface (T = 300 $\pm$ 30 K) figure 5.1, shows PPP chains covering the step edges (red squares) while on the terrace sites (blue squares) the supra molecular assembly of DBTP molecules prevails. Motivated by these findings, in the present chapter we systematically investigate the interaction of DBTP molecules with a variety of surface steps. We specifically use a curved Au (111) crystal (c-Au (111)) that provides a variety of step (S) to terrace (T) atom ratios (S:T) on the same crystal. The steps can be further classified as (111)- or (100)-like (see also figure 5.2). Moreover, the c-Au(111) was chosen because spectroscopic fingerprints of the reaction,

e.g chemical shifts due to the C-Br bond scission and the new -C-C- bond formation, are already well-established in this surface 3, [5, 6, 15, 81].

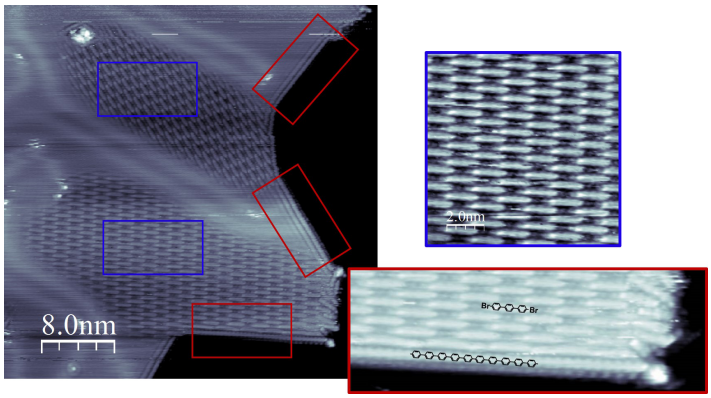

FIGURE 5.1: STM images acquired after the adsorption of DBTP on the Au(111) surface at about 330 ± 30 K . By zooming in the terrace (right up) and step (right down) sites, two different species are identified, i.e. self-assembled but non-reacted DBTP molecules and DBTP molecules that have already polymerized into larger oligomers. Image acquisition parameters: U_{bias} = -0.5 V I_{set}, = 50 pA.

The characterization of the bare c-Au (111) surface is presented in the following section.

5.2 c-Au (111)

5.2.1 The surface conformation

The advantage of employing a curved crystal is the ability to prepare a variety of different step types and step densities on the same sample under identical conditions thereby allowing to isolate the role of the steps as other factors, such as contamination, temperature variations etc. can be excluded.

The curved Au crystal used here has the (111) plane in the center and has a miscut of up to $\pm 15^{\circ}$ in the [-211] direction [119]. Thus, it exhibits various surface vicinal to the (111) plane with two different types of steps depending on the sign of the miscut angle. In particular a miscut toward the [2-1-1] direction leads to steps with $\{100\}$ microfacets while a miscut in the [-211] direction results in steps with $\{111\}$ microfacets [120]. A model depicting the sample geometry is shown in figure 5.2. From this point on we refer to $\{100\}$ and $\{111\}$ steps as **A** and **B** type respectively. The total coordination of the different surface atoms of c-Au (111) crystal are classified with colours in the figure 5.2 (c). On the one hand, the bulk (B, black), terrace (T, yellow) and step (S, green) atoms have equivalent coordination on both sides of the crystal. The B atom has the highest coordination with 12 atoms around, the T atom is surrounded by another 10 atoms and finally, the S atom is the least coordinated one with 7 atoms around. On the other hand, the coordination of the corner (C) atom is different depending on the step type. The corner atom has a coordination of 10 or 11 in A or B-steps, respectively.

The step density, or step to terrace atom ratio (S:T) variation across the crystal curvature follows the expression $W = h/\sin\alpha$ where W denotes the terrace width, h is the mono atomic step height (2.35 Å in the case of Au (111)) and α the miscut angle

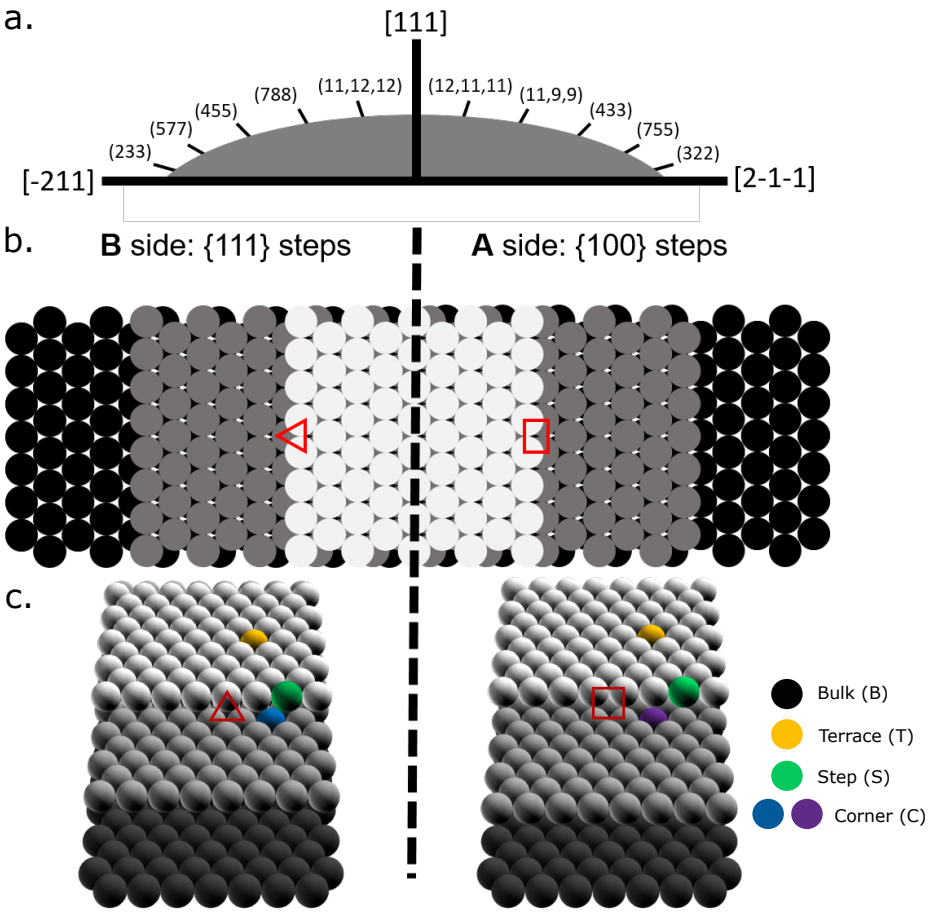

FIGURE 5.2: A model of the c-Au(111) crystal. (a) Macroscopic side view of the c-Au(111) crystal. The high symmetry directions and some of different vicinal surfaces are shown. (b) Atomic model of the c-Au(111) crystal, where B (red triangle) and A (red square) type of steps are distinguished. (c) Front view of the c-Au(111) crystal. In colours, the surface atoms with the different coordination are highlighted.

with respect to the (111) plane. Taking into account that $W = W_a n$, where W_a is the distance between two atomic rows in the [-211] surface lattice direction, one obtains n, which is the number of atomic rows per terrace. Since every terrace is terminated by one step (corner atoms as will become clear later, are not distinguished), we can express the S:T ratio as function of n, i.e. S:T $= 1 : n - 1$. The n, W and S:T values of some vicinal surfaces present on the c-Au (111) are listed in the figure 5.3.

5.2.2 Identification and quantification of the S:T atom ratio of the c-Au (111) crystal by high resolution XPS of the Au $4f_{7/2}$ core level

Clean c-Au (111)

In the previous section we have deduced the S:T atom ratio variations across the c-Au (111) from geometrical considerations (see figures 5.2, 5.3 and ref [120]). Here we establish an experimental verification by means of high resolution XPS.

a.

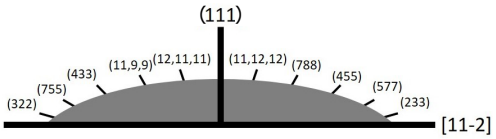

b.

{100}	Θ(deg)	n	W (nm)	S:T
Au(12,11,11)	2,38	23	5,7	1:22
Au(11,9,9)	5,57	10	2,4	1:9
Au(4,3,3)	8,05	7	1,7	1:6
Au(7,5,5)	9,45	6	1,4	1:5
Au(3,2,2)	11,4	5	1,2	1:4

{111}	Θ(deg)	n	W (nm)	S:T
Au(11,12,12)	2,27	24	5,83	1:23
Au(7,8,8)	3,51	16	3,83	1:15
Au(4,5,5)	5,76	10	2,33	1:8
Au(5,7,7)	8,47	7	1,58	1:6
Au(2,3,3)	10,0	6	1,33	1:5

FIGURE 5.3: Terrace width variation and the step vs terrace ratio across the c-Au (111) crystal. In (a) different surfaces planes vicinal to the (111) orientation and their respective location on the c-Au (111) crystal are indicated. The table shown in (b) summarizes the values found for the number of atomic rows per terraces *n*, the terrace width *W* and step to terrace ratio *S:T* for given surface planes.

The Au $4f_{7/2}$ core-level spectra measured in two different spots of the clean c-Au (111) is shown in the left graphs of the figure 5.4 (b). The black line represents the spectrum acquired at 0 mm, central part of the crystal, while the spectra acquired at +2.5 mm, the A edge, is shown in red. The dimensions of the crystal along its curvature are shown in the figure 5.4 (a). Due to the asymmetric peak shape of the spectra at least two components are required for deconvolution. Furthermore, the asymmetry becomes more pronounced toward the edge as the width of the black spectrum is slightly narrower and higher in intensity, whereas the red spectrum, in the low binding energy side is more intense. This difference is better appreciated in the right graph where only the low BE side of Au $4f_{7/2}$ CL is shown.

Several XPS studies have alredy addressed the origin of asymmetry of the surface core levels. Simultaneous works performed on the flat Au (111) by Citrin and *co workers* [121] as well as by Heimann and *co workers* [122] showed the deconvolution of Au $4f_{7/2}$ CL peak into two components attributed to the emission from bulk and surface atoms. A shift of 0.4 eV was established between the two peaks. The energy assignment of bulk (higher BE) and surface (lower BE) components was set considering that the core-hole screening, due to the lower coordination, was higher for the surface atoms than for the bulk atoms. In a similar way, the measurements performed in the vicinal Au (322) surface by [123] Prieto *et al*, established a 0.38 eV BE difference between surface and subsurface atoms. Interestingly, the identification of a third peak contribution to the Au $4f_{7/2}$ CL spectra was found by Westrate *et al* [124] when employing the vicinal Au (310) and Au (321) surfaces. These vicinals have high density of 6-fold coordinated step atoms and consequently they contribute to the deconvolution of Au $4f_{7/2}$ CL spectra with an additional peak, shifted 0.2 eV towards lower BE with respect to the terrace atoms. Discerning between different surface atom coordination by XPS has also been established in vicinal surfaces of different elements such as Rh (111) [125] or W (111) [126] and the magnitude of the binding energy shift with respect to the bulk atoms is being again ascribed to the coordination number of the atoms.

In the figure 5.5 (b), we present the deconvolution of the Au $4f_{7/2}$ CL peak measured on the A edge, B edge and centre part of the c-Au(111). In all three cases,

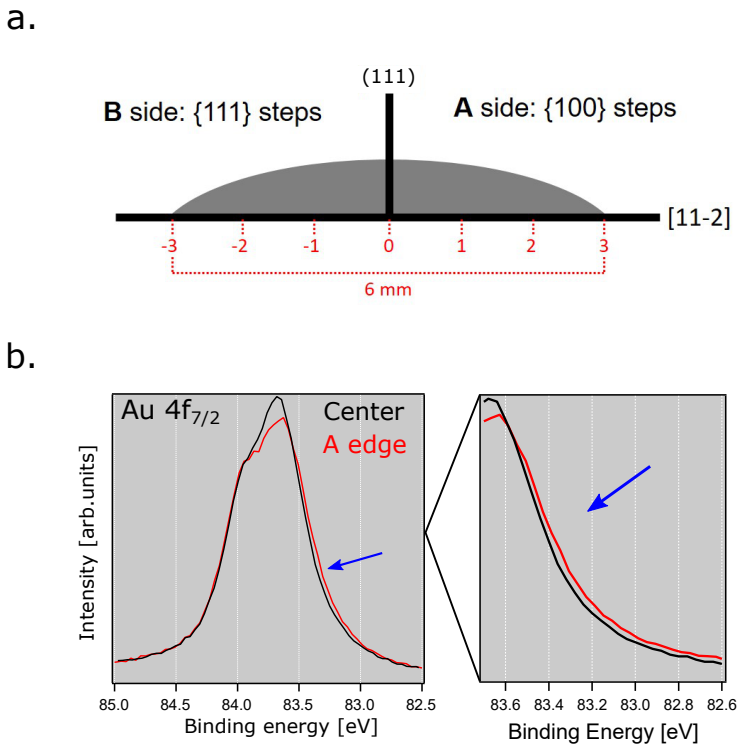

FIGURE 5.4: Differences on the Au $4f_{7/2}$ CL within the clean c-Au(111) surface. (a) Front view of the c-Au(111) crystal with the dimensions of the crystal along its curvature indicated beneath. (b) Au $4f_{7/2}$ CL spectra acquired at the centre (0 mm) in black and at the **A** edge (2,5 mm) in red.

the original spectrum is shown in white dashed lines and the result of the fitting is superimposed with a continuous black trace.

To reduce ambiguity in the fitting, we only distinguish three main contributions, bulk (B, black), terrace (T, yellow) and step (S, green). Kink atoms are disregarded as we do not have information on the relative abundance of kink atoms for the different surfaces, whereas corner atoms are disregarded as their coordination places them at a BE right in-between bulk and terrace atoms and we only seek to quantify the step contribution of the total core level intensity. Using these three components, we get the bulk (black), terrace (yellow) and step (green) peaks at 84.24 eV, 83.93 eV and 83.76 eV, respectively. We use E_F to correct the BE of all the spectra and afterwards the peak deconvolution is performed using a Doniach-Sunjich pair function, following the parameters used by Walter *et al* [112] for the core level fitting of a curved platinum surface and the parameters used by Gustafson *et al* and Weststrate *et al* [124, 125] on the above mentioned gold surfaces. The relative BE difference of the three different peaks and their full width half maximum (FWHM) are fixed for the peak deconvolution performed on the different parts of the c-Au(111) surface.

We find a decrease in BE of 310 $\sim$ meV (B-T), 170 $\sim$ meV (T-S), and 480 $\sim$ meV (B-S), for the bulk with respect to the terrace atoms, the step with respect to the terrace atoms, and the step with respect to the bulk atoms, respectively. Therefore, our model correlates the reduction of atomic-coordination of the different Au atoms with a CL shift of about 100 meV. If we look into the literature, Citring *et al.* [121] established on the one hand, a 380 meV core level energy difference between surface and bulk atoms used to fit the Au $4f_{7/2}$ CL spectrum on the flat Au (111) surface, close to

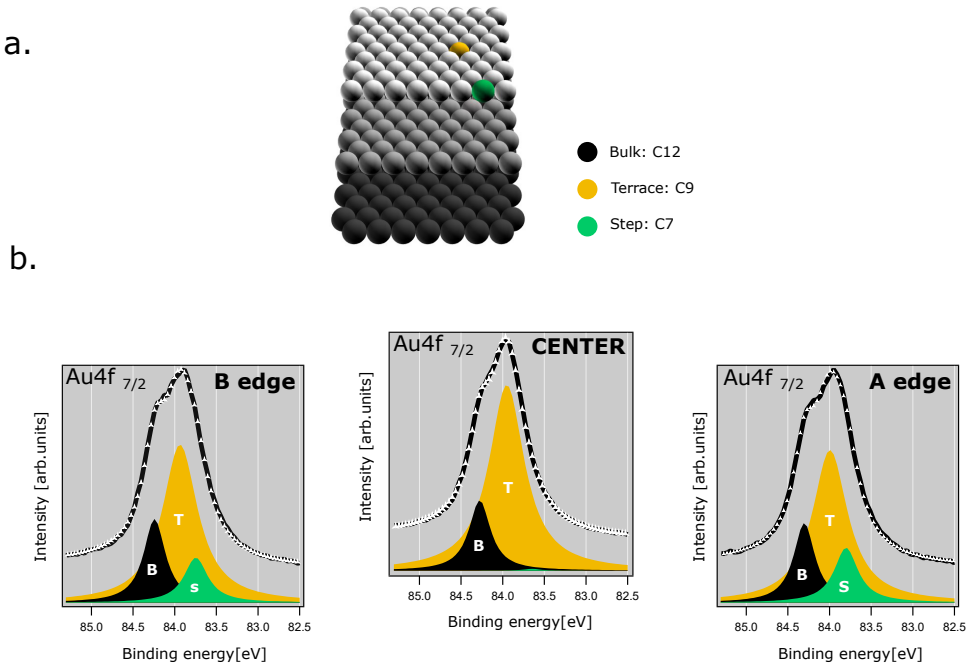

FIGURE 5.5: Step and terrace Au $4f_{7/2}$ CL peak deconvolution. (a) Front view of c-Au (111) surface steps. Atoms with different coordination are represented with different colours; green, yellow and black denote steps, terrace, and bulk atoms, respectively. In (b), from left to right, Au $4f_{7/2}$ CL peak deconvolutions of the B edge, center part and A edge are shown. Deconvoluted peaks are colour coded following the nomenclature introduced in (a).

the 310 meV shifting value we get for the bulk and terrace components. Westrate *et al.* [124] on the other hand, studied the Au (321) vicinal surface by photoemission, and similar to the case of Rh(335) studied by Gustafson *et al.* [125], they use a step component shifted 0.22-0.29 eV to lower energy than the terrace peak. Thus, the values we get and the model we propose here are in reasonable agreement with the reported values.

Importantly, in the B and A edge, the S:T ratio of the peak areas are 1 : 5.2 and 1 : 4.2, respectively. Thus, the values are in excellent agreement with the values of 1 : 5 and 1 : 4, respectively, derived from geometrical considerations in the section 5.3.

Therefore, we next compare the experimentally measured S:T ratio with the theoretically predicted values as function of the crystal position. For that, we deconvolute the Au $4f_{7/2}$ CL measured every 0.5 mm across the c-Au (111) starting from -2.5 mm (B edge) up to 2.5 mm (A edge) for a total of 13 points. Results are depicted in the figure 5.6. For every position, the sum of the areas of the bulk (black dots), terrace (orange triangle) and step (green rhombus) components are normalized to 1 (dashed blue line). The superimposed solid lines are guides to the eye to highlight the different contributions to the CL as a function of x. Afterwards, we obtain the experimental S:T ratios, plotted in continuous blue line, by dividing the step peak areas (green rhombus) to the terrace peak areas (orange traingles). Finally, the theoretically predicted S:T ratio (see section 5.2.1) is added in a continuous red line.

On the one hand, as expected for the bulk contribution, the area of the peak is constant for all z positions at 20 % of the total Au $4f_{7/2}$ CL signal intensity. On the other hand, the step contribution has its maximum at +2.5 mm (A edge) with an

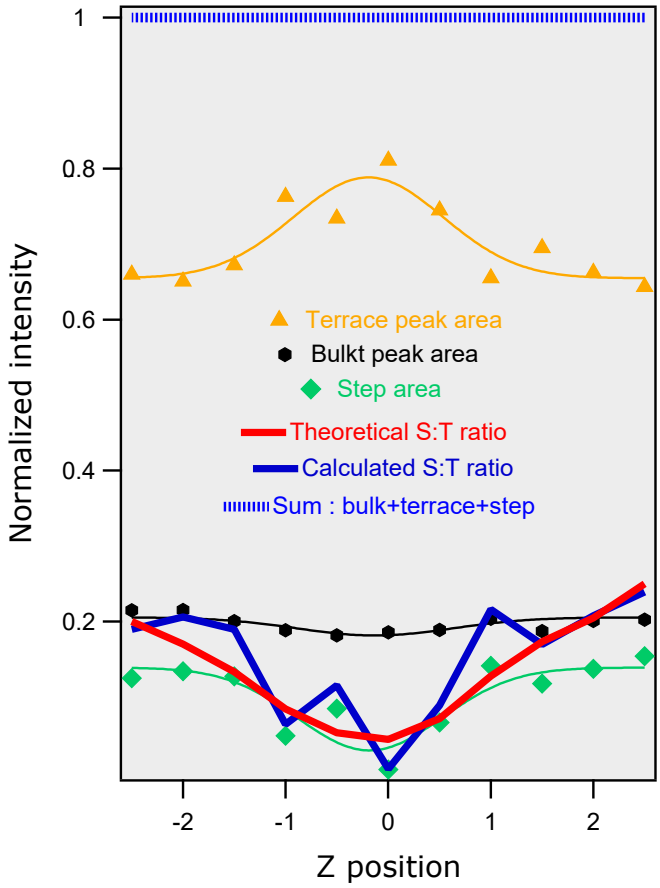

FIGURE 5.6: Experimentally measured S:T ratio compared to the theoretically predicted values. The area of the Au4f$_{7/2}$ CL deconvoluted peaks measured every 0.5mm on the c-Au(111) are shown. The yellow triangles represents the area of the terrace peak, the black squares the area under the bulk peak and the green rhombus the area under the step peak. Superimposed solid lines are guides to the eye. The blue dashed line is the area sum of the three peaks normalized to 1. The experimentally deduced S:T ratio is simply obtained by dividing the green rhombus and the yellow triangles, and the resulting points are shown and connected with the dark blue line. Finally, the red line is the expected S:T ratio from theory.

intensity contribution of 15.2 % whereas at -2.5 mm (B edge) it has a value of 12.5 % and is bellow the experimental resolution at the center. Consequently, the terrace contribution is maximized with 81 % at z = 0, and minimized with 64.6 % and 66 % at A and B edges, respectively. The terrace and step peak intensity variations give rise to an S:T ratio that has a minimum value at z = 0 and gradually increases toward the edges, in agreement with the theoretically predicted values (red line).

In conclusion, we have established that the bulk, terrace, and step contributions to the Au $4f_{7/2}$ CL can be quantified using high resolution XPS and a c-Au (111) crystal. Importantly, the S:T ratio expected from geometrical consideration is well reproduced by our CL deconvolution. Next, we study the adsorption interaction of DBTP on the c-Au (111).

Surface Au 4f $_{7/2}$ CL after the adsorption of a ML DBTP

Next, we evaluate how our Au$4f_{7/2}$ CL peak deconvolution model behaves after the deposition of a DBTP molecular layer on top of the c-Au(111). The measurements done at the **B** edge (at -2.5 mm), **A** edge (at 2.5 mm) and on the central part of the crystal (0 mm) are shown in the figure 5.7 (a). As before, the fitting results are shown in a continuum line style wheras in dashed lines, the real measurement are superimposed. Same peak parameters and constrains used in figure 5.5 are again employed here.

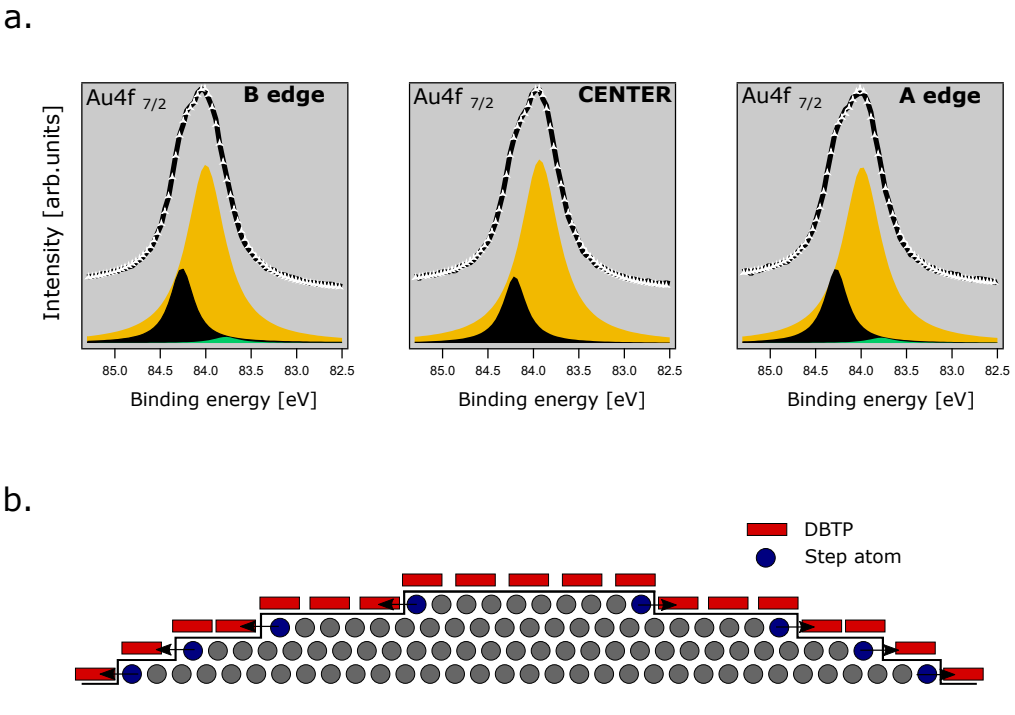

FIGURE 5.7: Surface Au $4f_{7/2}$ CL evolution after the adsorption of DBTP molecules at RT. In (a), from left to right, the Au$4f_{7/2}$ CL peak deconvolution performed on the B edge, center part and A edge is shown. The deconvolution leads to the black, yellow and green peaks that represents the bulk terrace and step atoms respectively. A front view representative model of the adsorption of DBTP on the c-Au (111) is shown in (b).

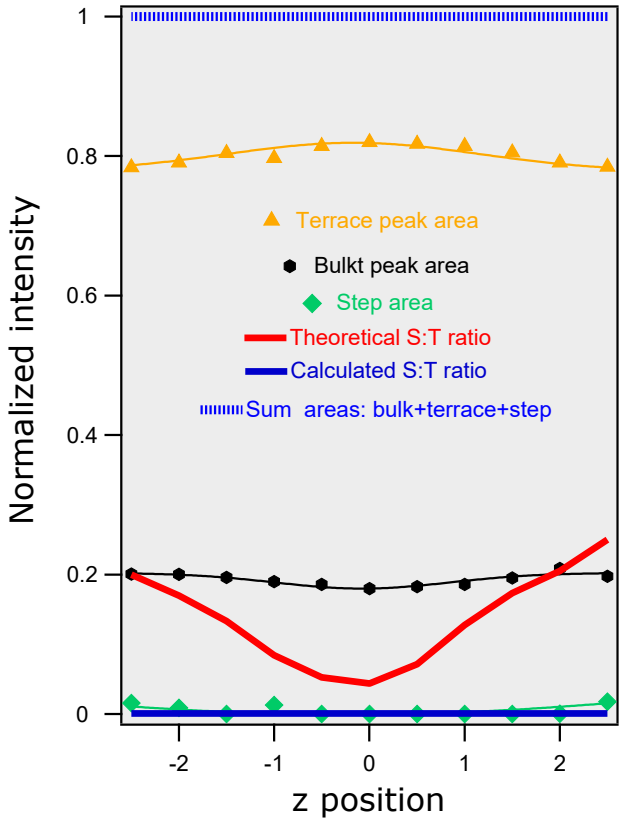

FIGURE 5.8: Experimentally measured S:T ratio compared to the theoretically expected values after the adsorption of DBTP molecules at RT. The area of the peaks deconvoluted from the Au4f$_{7/2}$ CL measured every 0.5mm on the c-Au(111) are shown. The yellow triangles represents the area of the terrace peak, the black squares the area under the bulk peak and the green rhombus the area under the step peak. Superimposed solid lines are guides to the eye. The blue dashed line is the sum of the three peaks normalized to 1. The experimentally deduced S:T ratio is simply obtained by dividing the green rhombus and the yellow triangles, and the resulting points are shown and connected with the dark blue line. Finally, the red line is the expected S:T ratio from theory.

With the molecular over-layer, in both B and A edge, the step peak component vanishes and only the terrace and bulk components remain in the Au4f$_{7/2}$ CL spectra. Interestingly, and as explained in more detailed in 5.8, the area of the terrace peak increases while the bulk area remains unchanged. This, is a direct consequence of the interaction of DBTP molecules with the surface steps, as sketched in the figure 5.7 (b). The molecule covers/interacts with the surface step atoms (marked in blue in the figure) and increases its effective coordination. Taking into account our model of 100 meV CL shift per atom reduction state, the step-molecule interaction leads to a CL shift of at least 100 meV toward higher BE and thereby the step peak area is added to the terrace peak area.

The consistency of our model is evaluated by deconvoluting the Au 4f$_{7/2}$ CL as function of c-Au (111) position as before. The results are shown in the figure 5.8. The measurement acquisition conditions and the evaluation and the line style of the presented data are the same as on figure 5.6

Again, the area of the bulk component (dark dots) is almost constant in z, and as for the clean surface, its value renders a 20 % of the total signal intensity. The step contribution on the contrary, is quenched and its intensity is effectively added to the terrace component, which now comprises a constant value close to 80 % of the total signal intensity in z. Thus, as introduced in the figure 5.7 (b), the results suggest that all surface steps, independently of the step side, are covered by molecules. Finally, due to the absence of the step peak contribution, the S:T ratio is close to 0 all across the c-Au (111).

Concluding, with our peak deconvolution model, we derived that the deposition of DBTP molecules covers the surface steps, and increases the effective coordination of step atoms, leading to a shift toward higher BE of the step component. Therefore, we have established unambitious that the prerequisite to studying the influence of steps on the Ullmann reaction, namely a signature of molecule step interaction, is full-filled.

5.3 C 1s and Br 3d CLs of DBTP on c-Au (111)

In this section we evaluate the adsorption interaction of DBTP molecules on the c-Au (111) by means of high resolution XPS and NEXAFS.

5.3.1 The RT phase

The XPS spectra acquired at RT after the adsorption of a mono layer of DBTP on the c-Au(111) crystal, is shown in the figure 5.9 (b). Its chemical structure is sketched in the figure 5.9 (a) and the energy position of the core levels constituting the molecule were described and explained previously in section 4.3.1 of the previous chapter 4. Contrary to the case of $GdAu_2$, the measurements presented here are performed in a synchrotron facility and consequently the quality of the data is significantly better. See section 2.5.1 and [127] for more details.

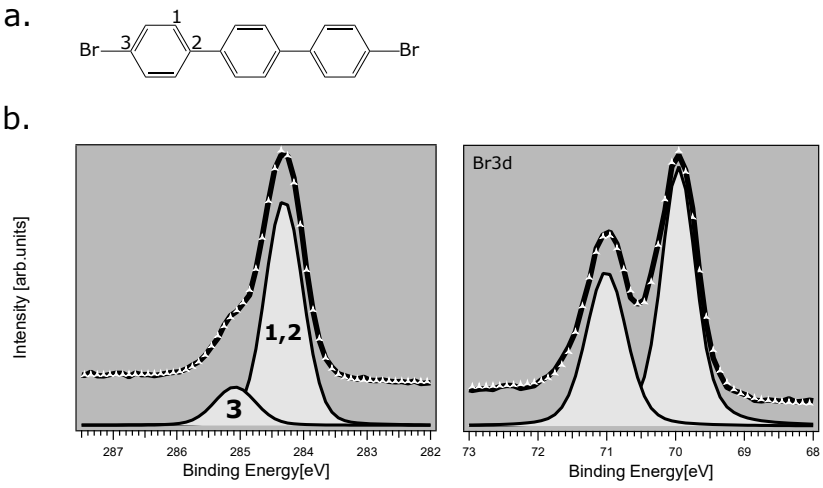

FIGURE 5.9: High resolution XPS of DBTP on c-Au (111) (a) Chemical structure of 4'4-dibromo-p-therpenyl (DBTP) molecule. (b) C 1s and Br 3d CL spectra measured for monolayer DBTP adsorbed on Au (111) at RT.

For the sake of simplicity, only the spectra acquired in the central part of the crystal (0 mm) are shown in the figure 5.9 (b). At RT, the C 1s spectrum (left panel)

presents an asymmetric peak with a shoulder like feature located at higher binding energies. Overall, the spectrum resembles the result obtained for the DBTP on $GdAu_2$ 4.2. In the same manner, the spectrum is fitted using two peaks. The peak (1,2) is located at 284.3 eV and corresponds to the C_1 and C_2 of the molecule, whereas the peak number 3 is shifted by 0.8 eV and represents the two C_3 atoms of the molecule.

On the right hand panel, the spin-orbit split doublet of the Br 3d CL is depicted. Its energy position matches the values found in the literature for several different polyaromatic molecules with bromine termination [79, 81, 91, 100]. From the integrated peak intensity analysis, we obtained a total of 1 C_3 : 8 $C_{1,2}$ and 1 Br : 9 C peak ratios, as expected for the intact molecule. We note that there is no trace of chemisorbed Br-Au species in the Br 3d CL in-line with the results obtained in chapter 4.

DBTP to map the surface local work function ϕ

The C1s and Br3d CL spectra measured for the DBTP molecules adsorbed on the crystal edges are plotted in the Figure 5.10. The orange spectra are measured at the B edge (-2.5 mm) while the blue are measured on the A edge (+2.5 mm). For comparison, we also include the reference spectra measured on the central part of the crystal (in black). The peak deconvolution used above (5.9 (b)) can be applied in both cases (it is not shown in the figure) and similar results are obtained once the observed small peak shifts are considered. This ensures that on both step edges the molecules are adsorbed intact.

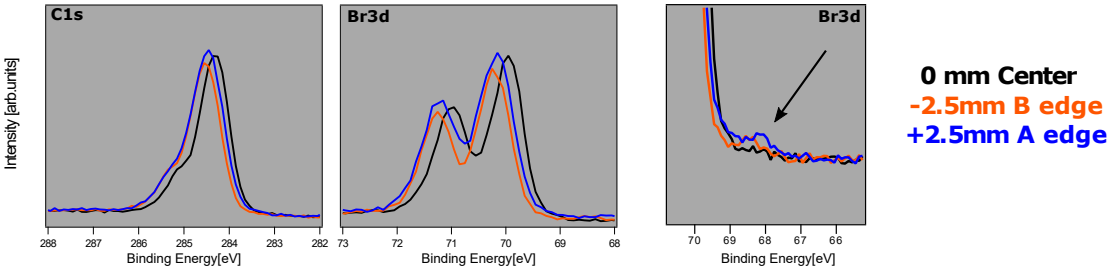

FIGURE 5.10: High resolution XPS of monolayer DBTP adsorbed on the step and terrace sites of the c-Au (111). The black spectra are the reference measurements acquired in the central part of the crystal (0 mm) while the orange and blue spectra are measured at -2.5 mm (B edge) and +2.5 mm (A edge) respectively. An amplification of the Br 3d CL low BE side is included in the right graph.

Before we can understand the observed CL shifts we recall that the formal definition of the BE of a CL, as introduced in section 2.2, is: BE = $E_{photon}-$ (KE $+\phi$) . Hence, any variations in work function will lead to changes in the BE. Here, since we correct the C 1s and Br 3d CL BE with respect to a reference CL BE (in our case the Au $4f_{7/2}$), local changes in the sample work function (as expected for different high index Au surfaces vicinal to the Au (111) [15, 128, 129] or upon molecule adsorption[49, 130]) will not show up in the analysis. However, this correction induces artificial shifts in CL BEs as observed above. When a molecule is brought into a sufficient proximity of a metal, there is an interface formation due to the differences in the chemical potentials of both systems (see also figure 5.11) . Electrons flow from one system to another until a charge neutrality point is reached, aligning the E_F of

the systems. As a consequence, in this interface, the VL is modified ($\triangle VL$) and so is the work function. The accurate determination of CL BE thus requires the determination of the ionization energy I_p (the energy required for removing an electron from the HOMO into vacuum) as well as the knowledge of the precise photon energy used during excitation of the core hole BE = $E_{photon} -$ (KE + I_P). While we have not measured the I_P in the present case, we can infer it if we assume that the I_P of DBTP aligns with the (local) vacuum level of the Au substrate. Under this assumption the variations of the C 1s and Br 3d CL BE as a function of c-Au(111) position translates directly into local changes in the ϕ_M as depicted in Figure 5.12.

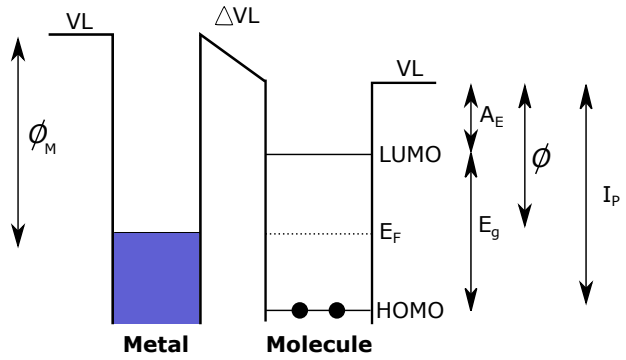

FIGURE 5.11: Representation of the electronic structure of the metal organic interface. The meaning of the different symbols are: ϕ= Work function, A_E= Electron affinity, E_g= Homo lumo gap and I_p= Ionization potential.

The BE shift of the C 1s CL of DBTP is plotted across the crystal curvature in the figure 5.12. Same graph (but not shown) is obtained for the energy variation of the Br 3d CL. The reference C 1s BE is 284.3 eV, measured at the center. The C 1s peak shifts in energy across the entire crystal, and for each side, the maximum value is located at the edges. On the B side , the shift is almost linear with the highest value being 0.22 eV, at +2.5 mm. On contrary, the A side shows some discontinuities and the highest value is 0.15 eV at +2.5 mm. Thus, the maximum C 1s energy shift is lower for (100) type of steps than for the (111) steps, as expected for their surface termination.

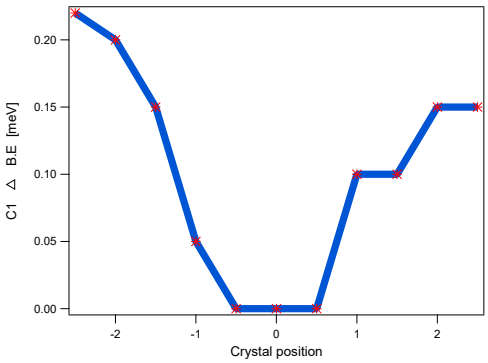

FIGURE 5.12: (a) C 1s CL energy variation as function of crystal spot. The energy reference of 0 is measured at the centre of the crystal.

Finally, we point out in the subtle changes we observed in the low BE side of the Br 3d CL spectra measured on the center and on the edges of the crystal, shown in

the figure 5.10 (c). The graph shows a small increase of the integrated intensity on the tail of the Br 3d CL on both step edges. The feature is close to the resolution limit, but it matches the BE of chemisorbed Br atoms [56, 91, 100] and hints toward partial molecular de-halogenation at the steps already at RT. Other possible scenarios that might explain the origin of the observed peak, such as partial molecular dehalogenation during evaporation, are disregarded as the molecule deposition was performed on the entire c-Au (111) simultaneously and from the same source.

In order to obtain the adsorption geometry of DBTP on the different parts of the c-Au (111), we perform polarization dependent NEXAFS measurements at the carbon K edge for the center, A edge and B edge of the crystal. The idea behind is to use the signal dichroism of the C 1s π^* resonance of DBTP to unravel whether the molecules adsorb tilted at the surface steps or are embedded in the terrace sites with the main molecular axis flat and parallel to the surface. We perform the measurements with the photon beam impinging parallel to the surface steps and varying p and s polarization of the incident light and in the partial electron yield (PEY) mode. The photon energy is calibrated using a reference value of 284.47 eV which corresponds to the gas phase adsorption spectrum of the C 1s in the CO molecule (C 1s->π^*), normally used as an absolute energy calibration reference.

This said, all three surface areas show a clear resonance close to 284.47 eV, marked with the straight line in the figure 5.13 (a). This feature, named (π_1^*), is assigned to an excitation of the C 1s CL level into the LUMO of the DBTP molecule [15, 56, 79]. Moreover, there is a second resonance feature (pointed out by the arrows) close to 285.8 eV, matching the chemical shift observed with XPS for the Br terminated C_3 atom (5.9). Thus, the fact that we observed the double feature in all three surface regions further proofs that DBTP is adsorbed intact all across the c-Au (111).

Concerning the molecular geometry, we observed a pronounced dichroism of the π_1^* resonance in the three positions. Considering a negligible amount of steps in the centre (S:T < 1:23), the observed dichroism (at least on the centre) indicates the twisting of adyacent phenyl rings of the DBTP molecule, as already reported on the Au (778) surface and by gas phase calculations [15, 102]. To discern if the signal arising from the steps is due to the twisting of the phenyl rings or due to molecules adsorbed tilted on the steps, in the figure 5.13 (b), we compare for the three surface regions, the dichroism of the π_1^* resonance by subtracting the integrated intensity of the p polarization with the s polarization. On the one hand, the signal for the B edge is almost equal to that of the centre, hence we discard molecules to adsorbed tilted on the B steps. On the other hand, there is an apparent higher dichorism of the π_1^* resonance on the A edge that might originated from the tilted adsorption configuration of the molecules. Nevertheless, due to the experimental challenges to perform reproducible NEXAFS measurements on the c-Au(111) crystal (see section of 2.3 experimental part), additional measurements are required to confirm these preliminarily results.

5.4 C 1s and Br 3d CLs of PPP on c-Au (111)

The evolution of the C 1s and Br 3d CLs of DBTP within the on-surface Ullmann coupling reaction have already been discussed for the $GdAu_2$ surface in the previous chapter 4.3. Two main reaction steps can be identified by XPS i.e the de-halogenation of DBTP, which produces a 2 eV shift of the Br CL, and the subsequent radical coupling, which induces an slight shifting and narrowing of the C 1s CL peak.

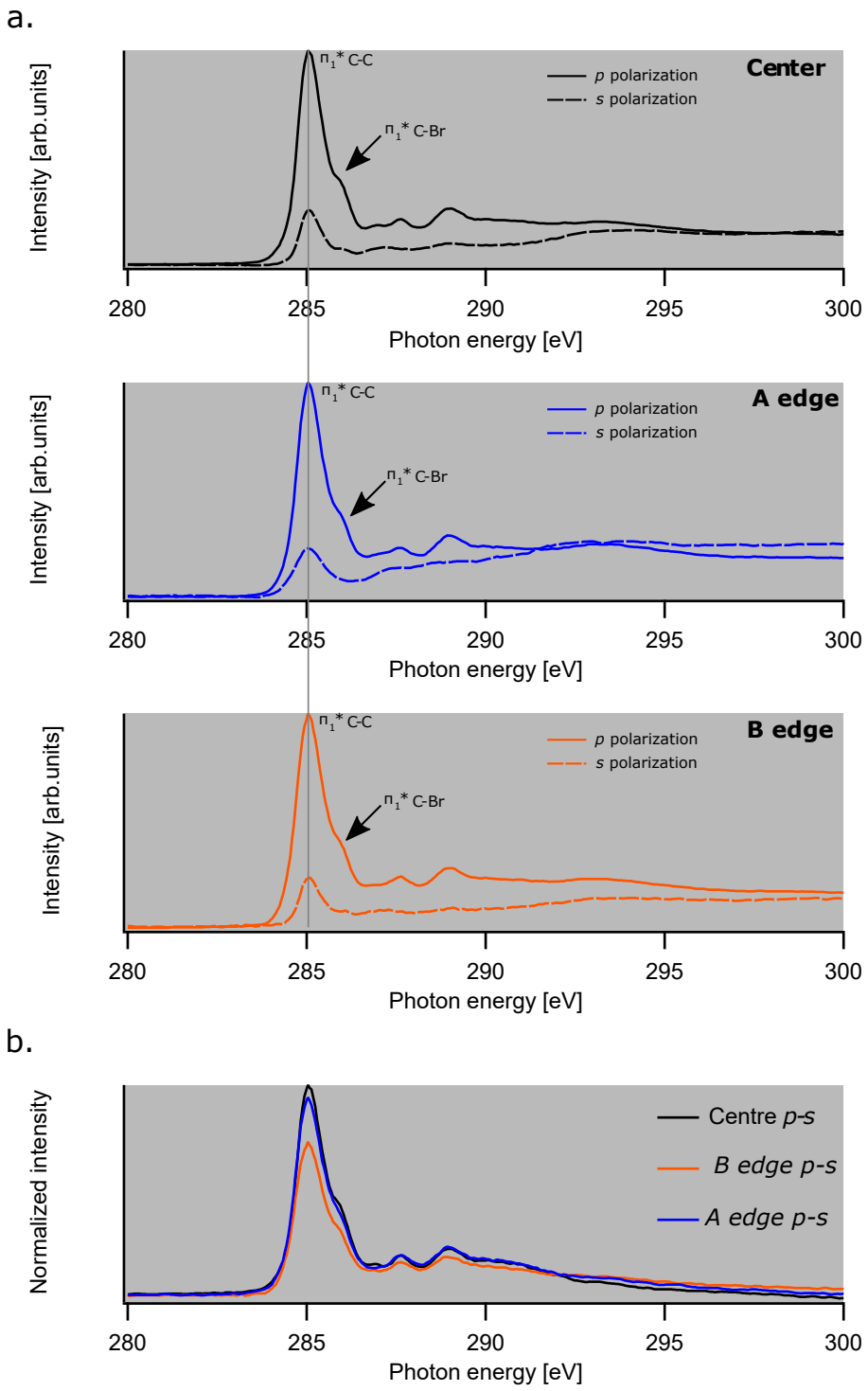

FIGURE 5.13: NEXAFS spectra acquired parallel to the steps/along the terrace, in both *s* and *p* polarization for DBTP monolayer on c-Au (111). In (a), from top to bottom, measurements acquired in the centre, A edge and B edge are shown respectively. In (b), the intensity difference between *s* and *p* polarization of the cases presented in (a) are gathered.

Here we deposit at RT a single layer of DBTP on the c-Au (111) and anneal the sample to 580K (the reaction is known to be completed at 400 K [81]). The reaction products are measured by XPS afterwards. As done in the previous section 5.9, we start by describing the results obtained on the central part of the c-Au (111) crystals, which are summarized on the figure 5.14.

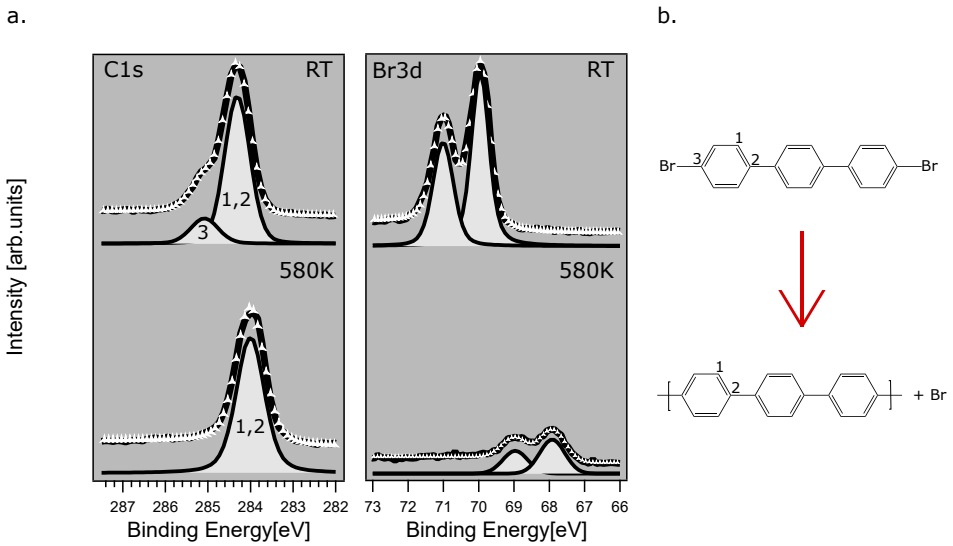

FIGURE 5.14: High resoluion XPS of PPP on the center part of c-Au (111). C 1s and Br 3d CLs of DBTP (RT) and PPP (580 K) are shown in (a). The chemical structure of the precursor molecule, DBTP, and the polymer, PPP, are depicted in (b).

On the one hand, after the annealing, the contribution of the C 1s peak number (3) completely disappears 5.14 (a). This, as discusses before, indicates that the C_3-Br bond is cleaved. On the contrary, the peak (1,2) remains unchanged. The fact that its total integrated intensity is preserved is a good indication of a successful radical coupling and subsequent polymerization [81]. On the other hand, the Br 3d doublet peak is shifted 2 eV towards lower binding energy, similar to the case found on $GdAu_2$ (4.4), and corresponds to Br atoms chemisorbed on the Au surface. The drop in the integrated intensity tells us that after annealing to 580 K most of the cleaved Br have desorbed. The temperature of 580 K is in very good agreement with the results obtained in our lab and discussed in chapter 4 (see also figure 4.3) . Overall, the XPS results indicate the formation of poly(p-phenylene) (PPP) wires.

The changes of the C 1s and Br 3d CL measured upon annealing on the stepped parts of the c-Au (111) are very similar. As shown in the first and second panel of the figure 5.15 (a), on both step edges the peak 3 contribution of the C 1s CL disappears and the Br 3d CL is shifted 2 eV towards lower BE. The CL shift between the different crystal spots is due to the local variation of the surface work function as discussed previously in section 5.12. Thus, the results suggest that the PPP is also formed at the steps.

Nonetheless, there are some subtle variations between the steps and the centre part that needs to be mentioned. The right panel of the figure 5.15 (a), is a magnification of the C 1s lower BE side. There is an small increase of the integrated intensity for the stepped parts, which is interpreted as the fusing of PPP chains and the formation of graphene nanorribons. On the flat Au (111), this only occurs at temperatures

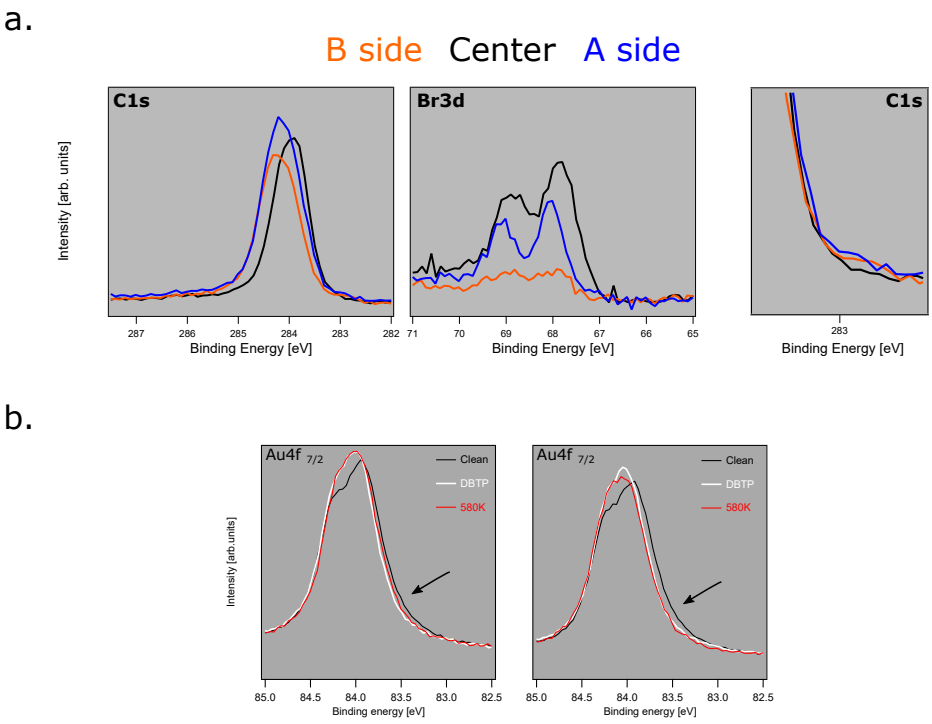

FIGURE 5.15: High resoluion XPS of PPP on the c-Au(111). In (a), the C1s and Br3d CL of PPP measured in the center (black), B step side (orange, -2.5mm) and in the A step side (yellow +2.5mm) are shown. A magnification of the C1s CL low BE side is included in the right graph. In (b), the Au4f$_{7/2}$ CL measured in the B (left panel) and A step sides (right panel) for the clean (black), DBTP covered (white) and PPP covered (red) surfaces is shown.

above 650 K [81]. Also, the Br 3d CL integrated intensity suggest that the desorption of Br atoms is higher on the steps and in particular on the B edge.

Like for the RT DBTP phase shown in section 5.7, the Au 4f$_{7/2}$ CL measured in the B and A step edge after the PPP formation is depicted in the figure 5.15 (b) in red colour. The integrated intensity is reduced at low BEs (compared to the clean surface) similar to the case after DBTP adsorption, we attribute this attenuation to PPP effectively quenching the step contribution. For comparison purposes we superimposed in the figure the Au 4f $_{7/2}$ CL spectra of RT DBTP (in white) and of the clean (black) surfaces. No significant changes are visible at the center of the crystal. Overall, these observations are in agreement with STM images 5.1, where PPP chains cover the lower and upper steps and are thereby quenching the step contribution of the Au 4f$_{7/2}$ CL intensity.

Interestingly, upon annealing, significant changes occurs also in the adsorption edge of the C 1s NEXAFS spectra when compare to the RT measurements (see figure 5.16). First of all, as shown in the top graph of the figure 5.16 (a), the double π_1^* resonance peak feature observed in the RT DBTP phase (the super imposed red spectrum), becomes a single resonance peak for the PPP (continuous black line) as expected from the XPS results and in-line with our interpretation of the DBTP NEXAFS data. Moreover, for all three surface areas, the π_1^* resonance is shifted towards lower photon energies. It is appealing to attribute this measured shift of the LUMO toward the Fermi energy due to a HOMO-LUMO gap reduction upon polymerization of DBTP into PPP. On the one hand, this picture agrees well with the known

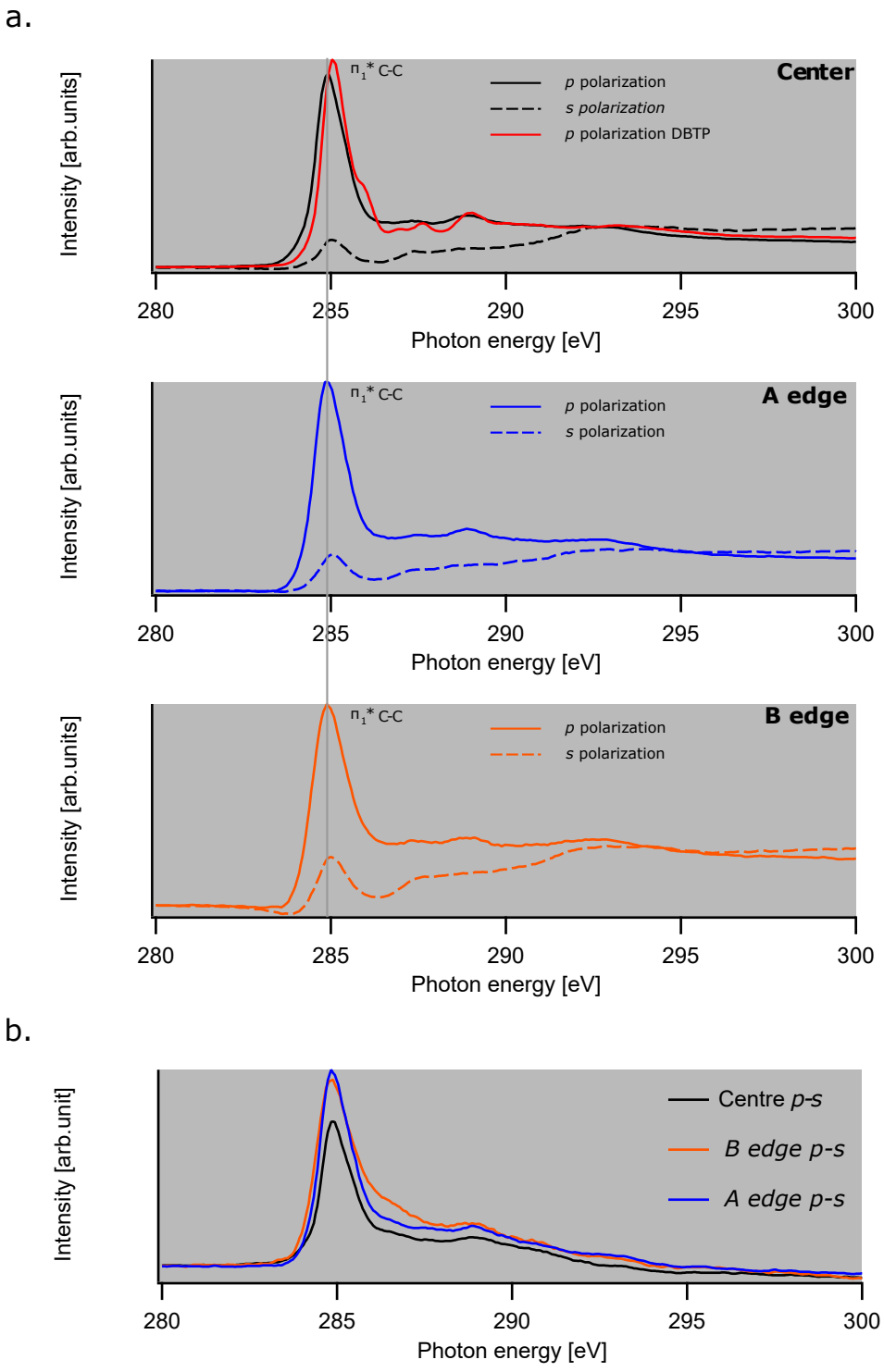

FIGURE 5.16: NEXAFS spectra acquired in the step direction in both s and p polarization for PPP on the c-Au(111). From top top bottom, in (a) the measurements acquired in the centre, A edge and B edge are shown respectively. In (b) In (b), the intensity difference between *s* and *p* polarization of the cases presented in (a) are gathered.

HOMO-LUMO gap reduction of PPP as a function of phenyl units (about 1 eV when increasing from three rings to an infinite polymer[131]). On the other hand, angle-resolved photoemission spectroscopy already resolved a shift of the 1 eV toward the Fermi energy for the HOMO level when going from DBTP to PPP [56].

For the geometrical considerations, as done in 5.13 for DBTP, we plot the π_1^* resonance signal dichroism in the three different surface regions in 5.16 (b). The fact that the dichroism is higher in the centre (black spectrum), excludes the possibility of having PPP adsorbed tilted on the steps, which indeed agrees with the STM results where PPP chains cover the lower and upper steps (see figure5.1). Therefore, the signal dichroism observed here for the three surface regions comes, again, from the twisting of the phenyl rings of PPP, as seen for DBTP. Interestingly, the fact that the signal is smaller in the steps implies that the twisting is lowered. In the C 1s CL XPS spectra of PPP measured on the step edges, we found indications of GNR formation. Since implicitly GNR are flat structures, the here presented NEXAFS observation agrees with the observation derived from XPS.

5.5 Determination of the Br-C bond cleavage as function of temperature and step to terrace ratio

So far we have demonstrated that the Ullmann-like aryl-aryl homocoupling of DBTP proceeds all across the c-Au (111) surface. However, our main goal is to see whether the energy barrier for achieving the reaction is lower at the steps or not. On the flat Au (111), the DBTP $\rightarrow$ PPP reaction proceeds at around 400 K. This temperature limit of (400 K) was established by Basagni et al. [81], and confirmed by us in the previous chapter, using temperature dependant XPS measurements 4.3. Here, by following the same approach, i.e. by monitoring *in-situ* the Br 3d CL while supplying thermal energy to the system, we unravel at which temperature the de-halogenation of DBTP molecules takes place on the different parts of the crystal. The results are shown in figure 5.17.

The temperature evolution of the Br 3d CL is followed *in-situ* by XPS in the three spots that we have been analysing all along the chapter, i.e Center, A and B edge of the crystal, respectively. For all three, the temperature is increased from 300 K up to 640 K within 10 minutes, i.e. at a rate of about 0.5 K / sec (note this is 10-20 times faster than the temperature ramps reported in chapter 4). During the measurements, a XPS spectrum is acquired every 5-10 s using a channel plate detector in the Br 3d CL energy range.

The characteristic $\approx$ 2eV shift of the Br 3d CL that evidences the transition from **Br-C** to **Br-Au**, is clearly resolved in every waterfall plot shown in the left column of figure 5.17. In order to establish a transition temperature from the plots, on the right column we plot the areas under the Br-C and Br-Au peaks separately, as function of temperature. Then, we fit the data with a Sigmod function and we select the temperature at which 50 % of Br-C intensity is dropped, as the transition reaction temperature.

In the centre (flat) part of the c-Au(111) crystal, figure 5.17 (a), the transition temperature is set at 425 K, and marked with the red lines in the figure. The determined transition temperature is about 25 K higher than deduced previously (section 4.3 of the chapter 4 and ref [81]). This discrepancy is likely a combination of experimental uncertainty in the absolute temperature calibration of the respective set-up and a physical effect since the temperature is increased about 10-20s faster on the c-Au

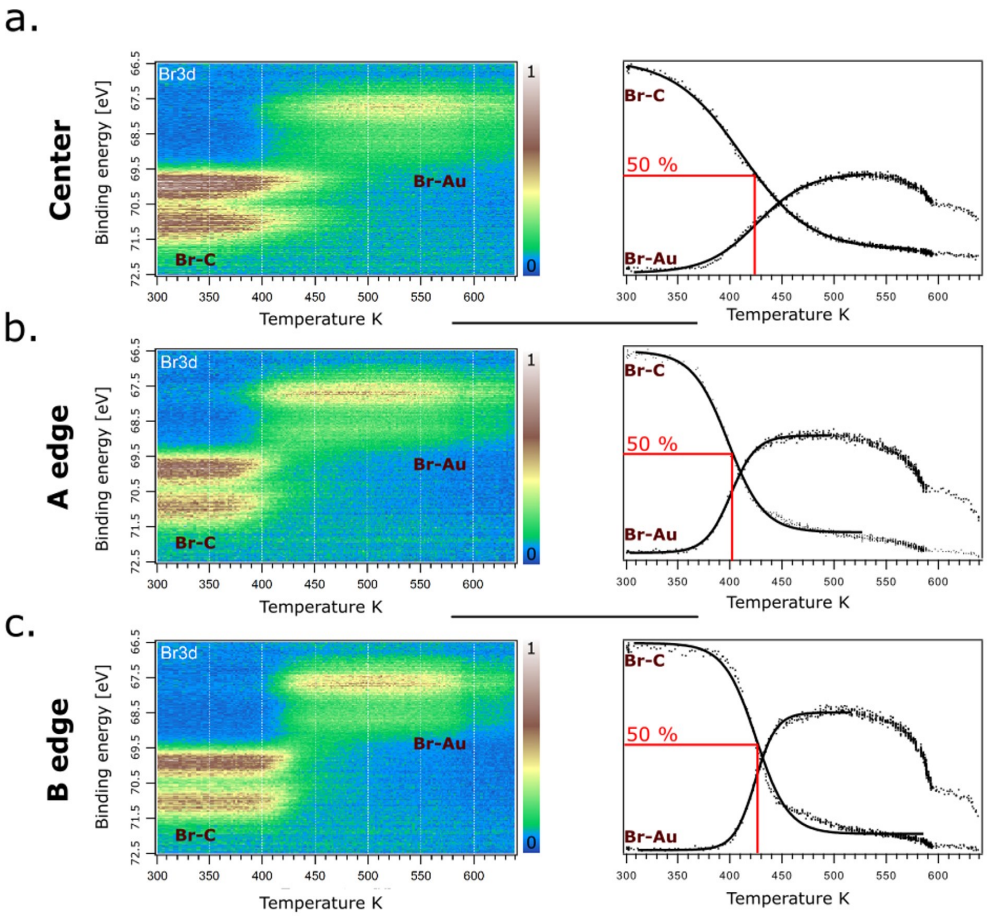

FIGURE 5.17: In the left collumn and from top to bottom, TD-XPS measurements performed on the center, A and B edges of the c-Au(111) crystal, for the Br 3d CL of a monolayer DBTP annealed from RT to 620 K. For all the measurements the binding energy is shown in the left axis and the temperature in the bottom axis. The intensity variations are characterized with the intensity colour pallet depicted in the right hand side. For each temperature ramp, in the right column, two intensity lines profiles, labelled as Br-C and Br-Au are shown as function of temperature. A Sigmod function (in continuum line style) is used to fit the data (in dots). The Br-C line represents the intensity area in between 71.5-69.5 eV and the Br-Au line the area between 69-67 eV. The point at which the Br-C intensity is dropped by 50 % is indicated with a red line in each plot.

(111) than for the flat Au (111) discussed in chapter 4. We will discuss the second aspect later in the chapter in more detail. Interestingly, on the A edge , figure 5.17 (b), the transition temperature is considerably reduced, and is set at 400 K, 25 K lower than in the centre part. In the B edge, figure 5.17 (c), on the contrary the transition temperature is established at 425 K, close to the value found in the center. Thus these measurements demonstrates that the de-halogenation temperature is lowered on the A steps, which means that enhancing the surface density of steps (i.e the **S:T** ratio), is a reasonable strategy to decrease the energy required for the molecular de-halogenation prior to polymerization.

Why the A steps , for this particular reaction, are more reactive than the B steps, is an intriguing question.

The most straightforward answer is that the atoms in the A steps $\{100\}$ are less coordinated (and have therefore more available charge) than the ones on the B steps $\{111\}$ (which have less available charge). The charge, as explained in the chapter 3, can weaken a covalent bond (by an addition of an electron to an antibonding MO for example), and favour its cleavage. Since there is more charge (or at least more easily accessible charge) in the A steps, it is reasonable to think that the reaction requires less temperature to proceed in this part of the crystal. Nevertheless, there are other factors that can produce differences in the reaction activation energy. For instance, the differences in the herringbone reconstruction present on the A and B steps [119, 120], could either lead to different molecular packings as well as to different diffusion paths. These effects, if present, besides the reaction activation energy could influence the reaction rates and consequently misconstrue the observed temperature difference interpretation.

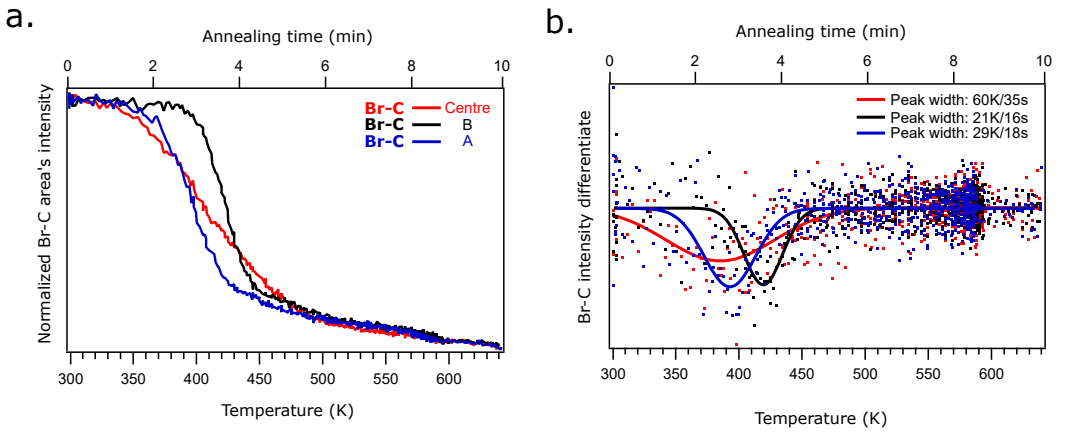

FIGURE 5.18: DBTP dehalogenation rate on the different parts of the c-Au (111) crystal. In (a), the three Br-C intensity line profiles shown in 5.17, are superimposed. In red is the profile measured in the centre, in black the one measured in the B side and in blue, the one measured on the A side. The differentiate signal of the line profiles are gathered in the figure (b).

The time interval in which the reaction proceeds, often called the *reaction rate*, is subject to the dynamics of the system, which besides the temperature (remember the collision theory explain in the chapter 3) is affected by the mobility (diffusion) of the DBTP molecules on the c-Au(111) surface. Thus, next, in the figure 5.18, we analyze the reaction rates in the centre, A and B side of the c-Au(111) crystal.

By definition, a chemical rate is defined as the change in concentration of a substance divided by the time interval during which this change is observed. Here, it is

expressed as $-\frac{\triangle DBTP}{\triangle t}$ where $\triangle[DBTP]$, is the difference between the concentration of $[DBTP]$ over the time interval $t_2 - t_1$. In order to make the rate become positive, the equation is preceded by a minus sign, since the concentration of a reactant decreases with time, and therefore is negative.

We get $\triangle[DBTP]$ from the slopes of the **C-Br** intensity line profiles shown in figure 5.17 (C-Br cleaved tells us that DBTP is consumed) whereas the time frame is defined by the annealing interval (identical for the three surface areas). In the figure 5.18 (a), the C-Br intensity profiles measured in the three surface areas are superimposed and plotted as function of time and annealing temperature. Already from the steepness of the curves, it is rather clear that the rate is higher on the steps than on the centre. The simplest way to quantify these rates out of the curves is to use the signal differentiate. In the figure 5.18 (b), we use a Gaussian function (continuous line) to fit the differentiate signal (dots) obtained from the Br-C spectra shown in figure 5.18 (a). The width of the peaks tells us the time period in which most of the Br-C bonds are cleaved, thus, the smaller the peak width the higher the rate.

In the centre part (red line), the width of the peak, which represents the decay of the Br-C signal, comprises a range of 60 K or the equivalent of 35 s out of the total 10 minutes ramp. In the A edge, the time frame is reduced to 18 s (29 K) and the fastest transition happens in the B edge, where it takes 16 s (21 K) to cleave most of the Br-C bonds. Thus, the reaction rate is highest on the B steps, then on the A steps and finally on the centre of the c-Au (111) crystal.

It is rather curious that the rate is higher on the B edge where the de-halogenation activation temperature as defined above is higher than on the A edge. Even thought, both rates are similar especially compared to the center part, where Br-C cleavage takes approximately two times longer to be completed. If we consider that surface steps promote the main molecular de-halogenation path, due to the lower amount of steps in the centre (S:T ratio of 1:23), molecules would have to diffuse to the steps sides to be activated and therefore, is reasonable to believe that the process takes longer.

Nevertheless, the de-halogenation signal appears even earlier on the centre than on both step edges. From high resolution XPS measurements taken for DBTP at RT (see figure 5.10), we know that this is not the case, i.e. chemisorbed Br atoms were only found on the step edges. Thus, the current result suggest that the de-halogenation rate might be slower (in the low temperature regime) in the steps than on the terrace. Here we have to keep in mind that a reaction rate, if there were no activation energy requirements, is limited by the rate at which reactant molecules come into contact, which in solution chemistry normally increases with temperature. However, on a surface the diffusion plays a big role. The trajectory at which reactants approach each other is often constrained by the surface (by diffusion energy barriers for example) and thus affects the rate. In order to unravel what causes the observed rate differences, we performed STM on the flat part of the crystal at temperatures close to the main de-halogenation process, to unravel the geometry of the system prior to the polymerization.

Models and experimental STM images of DBTP adsorbed on the regular Au (111) at RT and post annealed to $\approx$ 320 K are taken from [81] and shown in the figure 5.19 (a). The same model was used in the chapter 4 to explain the reaction activation energy found on the $GdAu_2$, and the same discussions used there can be applied in the present case. At RT, molecules are packed with their main axis almost parallel to the $[11\bar{2}]$ substrate direction. After post annealing to 320 K, the network is converted into a less dense network where molecules lie parallel to the $[1\bar{1}0]$ direction. The

a.

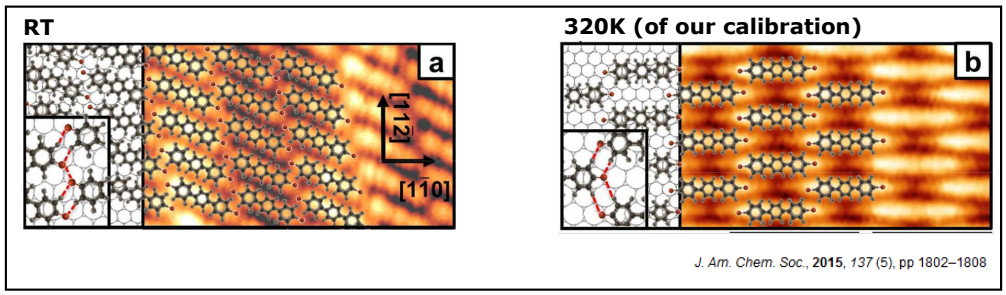

b.

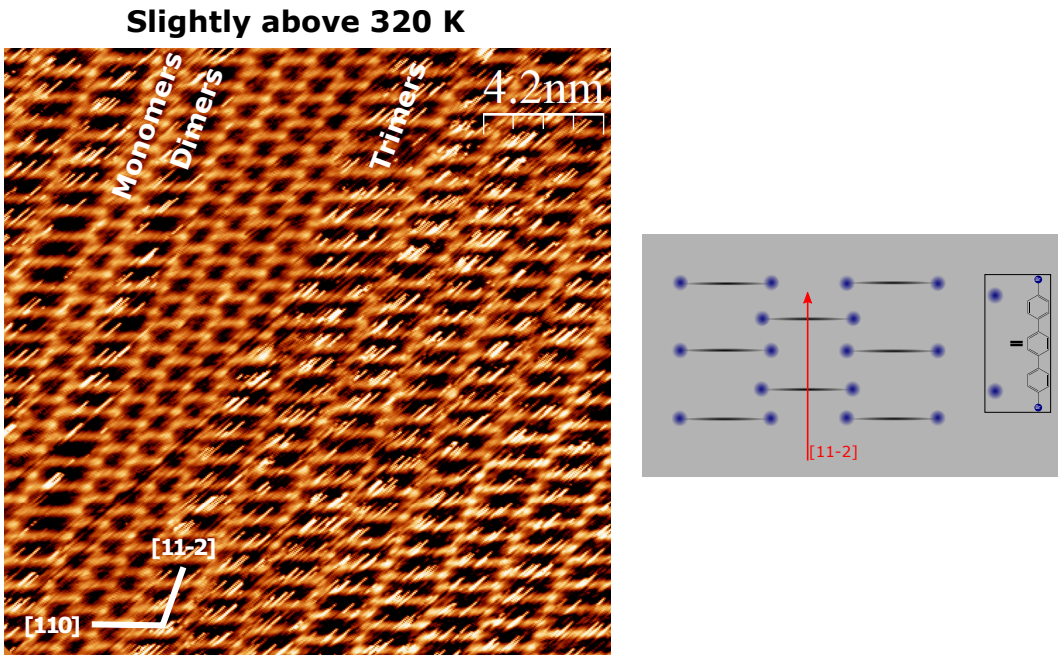

FIGURE 5.19: DBTP oligomerization on the terrace of Au (111). The two supramolecular phases of DBTP in Au (111) were found by Basagni *et al* [81] and are shown in (a). In (b), an STM image taken after post annealing to $\approx$ 325 K a monolayer of DBTP on Au (111). Monomers, dimers and trimers can be identified in the image. Acquisition parameters U_{bias} = 0.5 V I_{set}, = 50 pA. The diffusion direction of the molecules prior to the polymerization is shown in the right panel.

bright protrusions at the head and tail of each molecule are associated to the bromine atoms of DBTP. Interestingly, the second supra-molecular arrangement, favours the growth of the final polymer, since both, the direction and the perpendicular inter-spacing of the molecules, are the same as in the polymer [81]. In terms of reaction rate, it is reasonable to think that the reaction will proceed faster on a system where the initial supra-molecular phase is the one found at 320 K than the one found at RT, where the molecules would have to rearrange before polymerizing.

In order to see what precedes the above introduce supra molecular arrangement, we anneal the c-Au (111) sample to a slightly higher ($\approx$ 10-20 K) temperature and the resulting STM image, acquired on the flat part of the crystal, is shown in figure 5.19 (b). Interestingly, besides the DBTP phase (labelled as MONOMER) two and three times longer chains, with protrusions only at the edges, appear in the image following the same surface orientation. Moreover, contrary to the monomeric phase, fuzzy lines appear in between the longer chains. We interpret these changes as an indication of the polymerization of single molecules into oligomers (dimers and trimers in the figure).

Importantly, as illustrated by the model in the right panel, the formation of oligomers happens by the diffusion of DBTP molecules through the $[11\bar{2}]$ surface direction. This indicates that there is a preferential diffusion path for polymerization. If this diffusion path would be blocked for the molecules in the steps (due to a different geometrical arrangement or due to step confinement effects for example), it would explain the absence of a rate at low temperatures. Interestingly, trimers are the longest oligomers observed in the image. Within our model, both dimers and trimers requires the lateral diffusion ($[11\bar{2}]$) of a single DBTP molecule whereas the formation of higher order chains implies the diffusion of at least dimer molecules. The fact that the longest oligomers we observed are trimers, indicates that at this temperature, only single DBTP molecules are capable to diffuse. In a very simplistic picture, the longer the chains are, the higher the energy required to diffuse is, thus the reaction limiting factor here is the diffusion energy of DBTP. Thus, besides the activation energy, the reaction rate is clearly influenced by the molecule diffusion barriers.

So far, by temperature dependant XPS measurements and STM imaging, we have unravelled differences in the DBTP de-halogenation activation temperatures and rates, depending on the S:T ratio of the c-Au(111) surface. However, we see indication that the heating rate is too fast for specific reaction pathways to fully proceed before opening alternative pathways. Thus, next, we performed *time* and temperature dependent XPS measurements across the c-Au(111). The experiment consist on annealing the sample to the different temperature of interests, then thermalizing the sample for at least 30 minutes, and afterwards acquiring the spectra all across the c-Au (111) while continuously heating. The results are summarized in figure 5.20.

On the top left corner panel, the Br 3d CL of the RT DBTP phase is plotted as a function of the surface curvature. A single scan is measured every 0.25 mm all the way from -2.75 mm to +2.75 mm. The two bright lines located $\approx$ at 71 and 70 eV are the **Br-C** Br 3d CLs. Their energy position as function of the surface curvature, presents a curvy shape (highlighted with the black line) due to the local surface work function variations, as discussed in section 5.12. Although barely visible, there are traces of chemisorbed Br species in both step edges ($\approx$ 68-69 eV), in agreement with the STM images used as a motivation in the introduction, showing the step induced formation of PPP at RT in the sub monolayer regime (see section 5.1). We would expect to have a higher signal for the here presented monolayer system, however a monolayer coverage is intrinsically a barrier for the diffusion of the molecules and

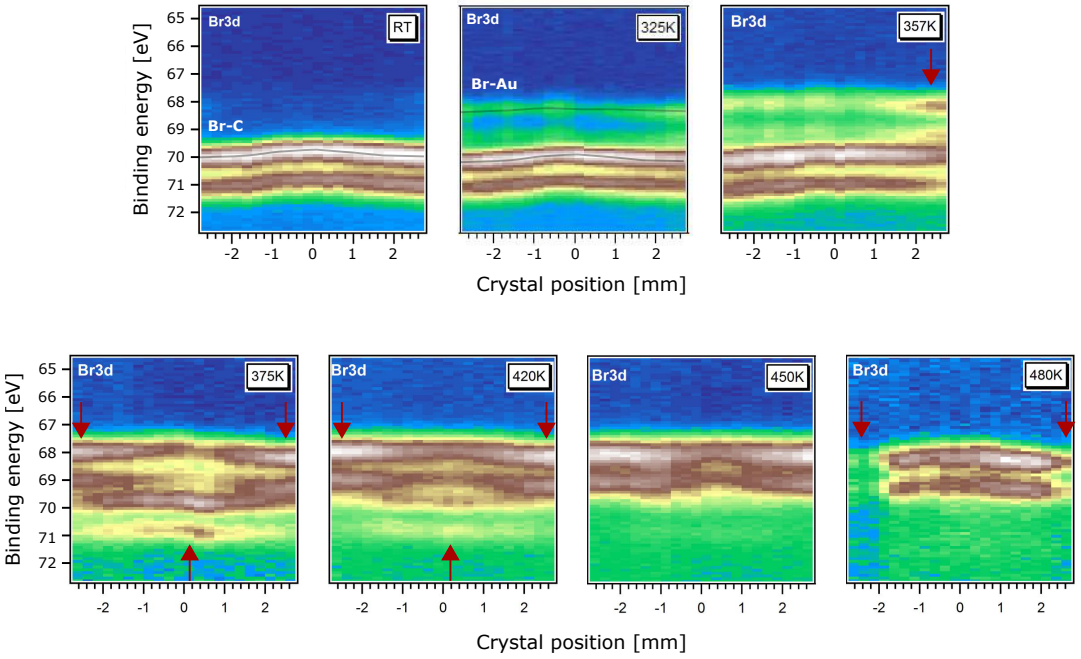

FIGURE 5.20: Set of measurements performed at different temperatures (marked on the right corner for each plot), showing the evolution of the Br 3d binding energy position (Y axis) as function of sample position (X axis). Prior measurement, each sample is thermalized for 30 minutes to the corresponding temperature. For visualization porpoises, a separate 1 to 0 intensity normalization is done for every temperature set. The colour scale is shown in the right edge.

thus, it is reasonable to think that only the molecules adsorbed on the steps in the right geometry, would react due to the higher catalytic power of the steps.

Annealing the sample to 325 K causes a generalized intensity growth at ≈ 68-69 eV which indicates the presence of chemisorbed Br-Au species all over the c-Au (111) crystal, contrary to the previous rate analysis observation (see figure 5.18). 25 % of the bromines are cleaved in the A edge and only the 15 % in the B edge and in the center. This on the one hand, indicates that steps (already at RT) and terrace atoms, are capable of activating the Ullmann reaction even at 325 K. Among them, the A steps are the most efficient catalyst. On the other hand, such a low reaction yields are likely a consequence of diffusion barriers. Indeed, by STM we have seeing that at this temperature only the diffusion of single DBTP molecules is permitted in the [11-2] surface preferential polymerization direction.

At 357 K, the overall intensity of chemisorbed Br atoms increases, however, as pointed out in the figure by the red arrow, the amount of de-halogenated molecules resolved on the A steps is considerably higher, whereas the B and centre part remain indistinguishable. 50 % of Br are cleaved in the A steps and 30 % in the B edge and in the center part.

Interestingly, upon annealing to 375 K, the de halogenation yield of B steps matches the one in the A steps (70 %) and in the center, only 50 % C-Br bonds are still cleaved. This means that whatever diffusion barrier the molecules where subject in the B steps at 357 K is overcome and thus the higher catalytic power of B steps with respect to the terrace atoms evidenced.

With further annealing, almost 100 % of Br-C bonds are cleaved in both step

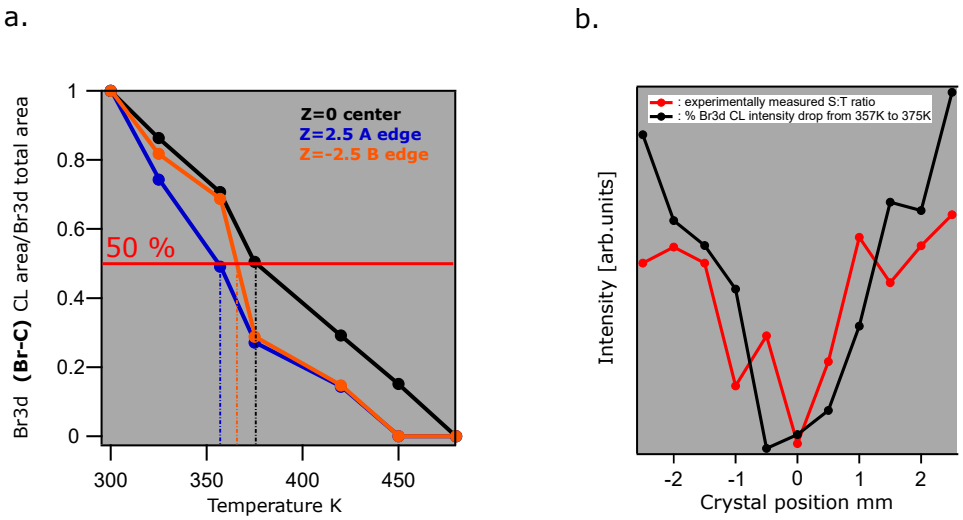

FIGURE 5.21: The Br 3d CL integrated intensity signal measured in the center (black), A edge (blue) and B edge (orange) as function of temperature is shown in (a). The temperature at which 50 % of signal drops is deduced from the the inter-crossing of the signals with the red line. Correlation of the surface S:T ratio with the molecular dehalogenation is shown in (b). The red line represents the experimentally obtained S:T ratio of the c-Au (111) crystal whereas the dark line represents the % of the Br 3d CL signal decay when going from 357 K to 375 K.

edges at 420 K and the same happens in the center once a temperature of 450 K is reached. Finally, at 480 K, the chemisorbed Br atoms start to desorb from the surface. Curiously the drop of Br-Au intensity is considerably higher on the very edge of the crystal. We conjecture that the higher presence of Br-Au near the centre is caused by the trapping of the Br atoms in between the polymeric chains, similar to the case found with the oligomers (see figure 5.19).

In order to clarify the here presented discussion, in the figure 5.21 (a), the percentage of Br-C bond cleaved for each annealing step on the A edge (blue line), B edge (orange line) and center (black line) of the crystal, is compared. For simplicity the maximum intensity is normalized to 1.

First of all, we establish a reaction transition temperature when 50 % of molecules are cleaved. We get 355 K, 365 K and 375 K transition temperatures for the A edge, the B edge and center, respectively. This values are much much lower than the 400 K (A edge) and 425 K (B edge and center) values reported from the fast annealing ramp experiment (see figure 5.17). Thus, the comparison of both experiments is a very nice example of how the yield of a chemical reaction, besides been subject to the catalytic properties of a surface, also depends on others factors such as the diffusion barriers of the molecules, as in the present case.

These diffusion effects are clearly visible in the graph. In the B steps for example, there is a clear transition point at 357 K. At lower temperatures the reaction rate is similar to the one found on the center whereas at higher temperatures it mimics the rate observed on the A steps. The sudden signal distinction from the center part indicates that the main diffusion barriers in the B steps is overcome at 357 K and consequently the higher catalytic activity of B steps starts playing a role. Interestingly, in the center, the signal reduction is almost linear with respect the temperature. In a purely catalytically process, the reaction rate is expected to increase exponentially

with temperature until at some point, there are so little unreacted molecules left that the rate abruptly drops due to the low probability of two molecules to encounter. Thus the observed linear behaviour resembles very nicely that for a certain oligomer length, there is a given diffusion energy barrier. The bigger the oligomer gets, the higher the diffusion barrier is and therefore the higher the temperature needed, explaining the linear dependence observed in the center and resembling a diffusion limited process.

Finally, in the figure 5.21 (b) we correlate the molecular dehalogenation with the amount of surface steps. For that, we plot the experimentally measured S:T ratio across the c-Au (111) crystal with respect the percentage of the Br 3d CL intensity attenuation observed when going from 357 K to 375 K. At this transition temperature diffusion barriers, at least on steps, are minimum. Since the lowest Br 3d signal attenuation is found in the center (due to the lower rate of the mechanism 1), its value is set to zero and used as an internal reference.

Interestingly, the S:T ratio (red) nicely correlates with the Br 3d CL attenuation demonstrating the higher catalytic activity and influence of step atoms in the dehalogenation process of the Ullmann coupling reaction.

5.6 Conclusions

In the present chapter we have probed that surface steps are better catalyst than surface terrace sites. We have successfully established the correlation between the C-Br bond scission temperature with the surface step to terrace (S:T) ratio. As a result, we have found a lowering of the reaction temperature of about 20 K between A or $\{100\}$ type of steps with respect to the terrace atoms and 10 K difference between B or $\{111\}$ type of steps and the terrace atoms. Consequently, A steps are found to be more efficient than the B steps.

To reach this conclusion, we have first successfully established a surface step to terrace ratio across the c-Au(111) by means of surface sensitive high resolution XPS measurements performed on the Au $4f_{7/2}$ CL. Upon DBTP deposition, molecules cover the surface steps and increase the effective coordination of step atoms. Therefore, we established the prerequisite to studying the influence of steps on the Ullmann reaction, namely a signature of molecule step interaction.

The reaction temperature differences as function of S:T ratio have been obtained by TD-XPS measurements performed with two different annealing procedures. In one, we increased the temperature at a rate of 0.5 K / sec (for a total of 10 min ramp) whereas in the other the sample was thermalized for 30 minutes at different temperatures. Overall, we obtained higher transition temperatures for the fast annealing ramp compared to the "slow" annealing ramp. The observed differences were ascribed to surface diffusion barriers after a preferential molecular diffusion path for the polymerization in the surface $[11\bar{2}]$ direction was established by STM measurements. This diffusion path turns out to be the reaction limiting factor in the surface terrace sites. High S:T density areas were also found to be subject to diffusion processes although the effect was found not to be as pronounced as on the terrace.

Concluding, we demonstrated that a curved crystal is a perfect template to systematically study the influence of the step density, which tuned continuously across the crystals curvature, while keeping all other reaction parameters identical for the entire surface. In concrete we probed that steps are efficient sites for triggering the Ullmann coupling reaction. In a future, the comparison of the here presented results with similar experiments performed in the sub monolayer regime, where intrinsically the molecular mobility is less constrained, is expected to shed some more light about the role played by surface steps in the Ullmann reaction.

Chapter 6

Ullmann coupling reaction of DBTP on TiO_2 (110)

6.1 Introduction

The mayor drawback toward device applications of on-surface synthesized carbon nanowires is the metallic template which acts as the catalyst in the Ullmann reaction. Inherently, molecular states will hybridize with the underlying substrate and an application, such as a carbon nanowire based field effect-transistor, requires a transfer of said wire from the metal film onto a more suitable, generally dielectric, substrate. Therefore, the next step is to either transfer or *in situ* produce the nano structures on technologically relevant surfaces such as insulators or semiconductors. Toward this end, few works have addressed this possibility: In 2011, *Kittelmann et al* [38] showed the covalent linking of halide-substituted benzoic acid molecules by thermal activation (contrary to the surface catalyzed reaction on coinage metals) on insulating calcite (104). The works performed by Olszowski *et al*. [39] and Kolmer *et al*. [40] probed the coupling of halogenated precursors on hydrogenated Ge(001) and rutile TiO_2 (011) semiconductor surfaces, respectively. However, in these works, the coupling products observed were rather short and very few compared to the results achieved on metal surfaces.

In this chapter, we use the rutile TiO_2 (110) metal oxide surface to accomplish the surface assisted Ullmann coupling reaction of DBTP and DITP molecules. Contrary to the previous works performed on insulator and semiconductors, we obtain higher reaction yields and substantially longer and more ordered polymers, as evidenced by STM, LEED and ARPES. Moreover, by using synchrotron radiation based techniques (XPS and NEXAFS) we address different reaction pathways and their mechanisms.

The choice of the rutile TiO_2 (110) substrate is motivated by the high dielectric constant of TiO_2 (110) as well as the knowledge available on this most intensively studied transition metal oxide surface [132]. Moreover, the inherent one dimensional surface anisotropy promotes alignment of suitable precursor molecules and will enhance the probability for the reaction. It is crucial to optimize intermolecular interaction that enhance the dehalogenation probability due to the expectedly low catalytic activity of the TiO_2 (110) surface compared to the prototypical coinage metal surfaces.

Before considering the Ullmann reaction we recall some of the inherent properties of the rutile TiO_2(110) surface: Like most transition metal oxides TiO_2 (110) is easily reduced when prepared by standard procedures under UHV conditions. Created and inherent defects, such as oxygen vacancies and interstitial titanium atoms, respectively, result in an effective n-type doping of the semiconducting TiO_2. Consequently, by controlling the amount of defects, the magnitude of charge available

for the reaction can be tuned (see section 6.2 for more details). Here, we studied near stoichiometric, highly reduced, and re-oxidized reduced TiO_2(110) surfaces. We will demonstrate bellow, the inherent surface defects, such as hydroxyl groups, oxygen vacancies and titanium interstitials (see section 6.2for more details) provide alternative reaction pathways. In this respect, it was demonstrated by *Benz et al*, the reductive coupling of aldehyde molecules is induced by (near) surface interstitial Ti atoms [133, 134], while *Kolmer et al* proposed the coupling of aryl halide molecules on the rutile TiO_2 (011) surface by the proton uptake from the surface hydroxyl groups and several works have adressed the higher catalytic activity of oxygen vacancies on the rutile TiO_2 (110) surface [135].

Throughout this chapter we first identify different reaction products throughout the homocoupling of DBTP precursors as a function as the aforementioned surface defects. Afterwards, we assign different pathways and mechanisms for the thus identified products.

6.2 The rutile TiO_2 (110)

The key advantage of surface science studies is the detailed knowledge and control of model substrates down to the atomic scale. Without this information, mechanistic interpretation of reactions can at best be speculative, at worst simply incorrect. Fortunatelly, for the rutile TiO_2 phase, many structural and electronic aspects are well characterized [132, 136].

The bulk-terminated TiO_2 (110) surface, shown in the figure 6.1, consist on the so-called bridging oxygens atoms (O_{2c} or O_b), 5-fold titanium atoms, Ti_{5c}, and in-plane oxygens (O_{3c}) atoms at the solid–vacuum interface, as sketched in figure 6.1 (a). The inherent surface anisotropy (indicated in the fourier transform of the STM image of the clean TiO_2 (110) surface in figure 6.1 (b)) is further enhanced by the O_b atoms which are protruding out of the surface plane, framing quasi one-dimensional trenches along the [001] direction. Under the given tunneling conditions the STM topography in figure 6.1 (b) images the O_b atoms as protrusions while Ti atoms are imaged as depressions. Consequently, the inherent surface defects, i.e., oxygen vacancies and hydroxyl groups are imaged as local maxima in the oxygen rows.

As introduced above the defects are produced in UHV by common sample preparation methods such as sputter [137] and annealing cycles [138, 139] and participate in most of the chemistry fround at the surface of TiO_2 (110) surface [135, 140–144].

The most common defects observed at room temperature are marked in blue in figure 6.1 (a) and are: (a) bridging oxygen vacancies **(O_v)**, formed during the sputter annealing cycles, (b) hydroxyl groups **(OH)**, predominantly formed due to water (H_2O) dissociation at O_v sites and (c) interstitial Ti (**i-Ti**) atoms. It is well established that O_v and interstitial i-Ti species donate two electrons per defect while surface hydroxyl groups (OH) donate only one electron.

In photoemission, figure 6.1 (c), the aforementioned defects lead to characteristic signatures in the VB region at BE $\approx$ 11 eV and at BE $\approx$ 1 eV as well as in the Ti $2p_{3/2}$ CL. While the origin of the OH feature in the VB at $\approx$ 11 eV is generally accepted, there is ongoing debate about the origin of the defect state (DS) observed at $\approx$ 1 eV, i.e. in particular whether O_v or i-Ti are the main source. However, regardless of its origin, it is established that the excess of charge giving rise to the DS is localized mainly around Ti atoms within the first three surface layers with the maximum weight at Ti atoms of the sub-surface layer. Additionally, an increase in the reduction state of Ti atoms produces a characteristic peak shape in the Ti 2p CL region,

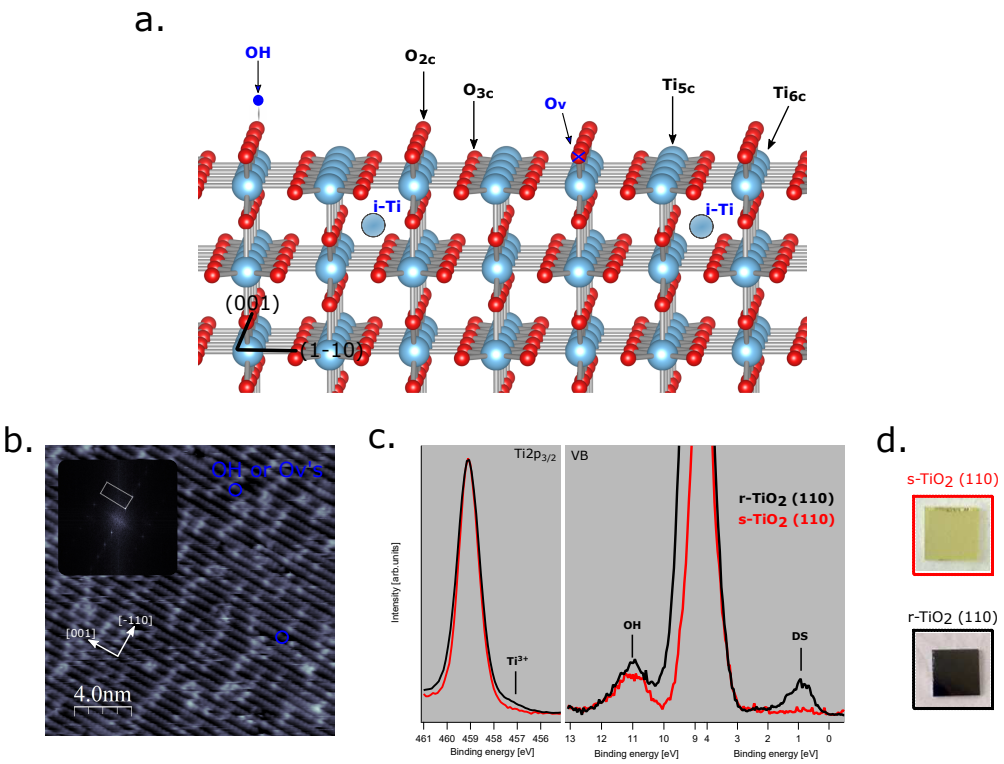

FIGURE 6.1: Description of the (110) surface of the rutile r-TiO_2. (a) A model representation of the TiO2 (110) surface, taken from [145]. Atoms with different coordination are marked with black arrows whereas typical surface defects are highlighted in blue. (b) STM image of a clean r-TiO_2(110) surface measured at U_{bias} = 2.0 V I_{set}, = 100 pA. In the FFT of the image, shown in the inset panel, the surface unit cell is marked with a white rectangle. (c) Photoemission spectroscopy measurements performed on the Ti 2p CL and VB of an stoichiometric (black) and reduced (red) surface. The characteristic peaks induced by the defects are included. (d) Real images of the stoichiometric (top) and reduced(bottom) rutile (110) crystals.

which is correlated to the presence of Ti atoms with a $Ti^{+2/+3}$ character, whereas stoichiometric Ti atoms are 4+.

In figure 6.1 (c) there are two spectra superimposed, labelled as s-TiO_2 (110) in red and r-TiO_2 (110) in black. The former corresponds to a stoichiometric sample with very few defects whereas the later is heavily reduced. These characterize features inherently only give insights into the (near) surface reduction state of the crystal due to the surface sensitive nature of the techniques employed. However, the reduction level of the bulk can easily be gauged as the crystal adopts an opaque colour upon reduction. Images of r-TiO_2 (110) and s-TiO_2 (110) crystals are shown in 6.1 (d). The reduced crystal is dark (opaque) whereas the stoichiometric crystal appears transparent. There are two important messages that we extract from the photoemission comparison of the clean surfaces. On the one hand, the DS peak and Ti^{3+} shoulder, fingerprints of the surface reduction state, are easily accessible by photoemission, as is evidenced by the peak appearance/absence on the r-TiO_2 / s-TiO $_2$ surfaces. On the other hand, it is interesting the fact that the OH peak is present in both surfaces. Under the reasonable assumption that the primary source of OH is, under the given experimental conditions, the dissociative splitting of H_2O

at O_vs, this indicates that a similar amount of O_vs is present on the surface for both samples. However, the DS at BE $\approx$ 1eV is clearly more intense on the r-TiO_2 (110) sample compared to the s-TiO_2 (110) surface where it is barely visible (at the given photon energy). Neglecting other contributions to the DS, we conjecture, that the increased DS intensity by similar OH intensity, directly reflects the increased amount of non-stoichiometric Ti atoms in the near surface region of the r-TiO_2(110) sample. A different source of non-stoichiometric Ti atoms was recently proposed by Miccio and co-workers [146]. They have shown that due to a particular type of step reconstruction (sawtooth reconstruction) the outermost titanium step atoms are not coordinated to the topmost oxygen atoms and thus, besides the non-stoichiometric interstitial atoms contribute to the intensity of the DS. Similarly, Karmakar and coworkers [137] could correlate between the increase of surface steps (produced by roughening of the sample by sputter and annealing cycles) with and increase of the Ti^{3+} related shoulder of the Ti 2p CL.

As we will see throughout this work, we can extract valuable information for interpreting the mechanism of the Ullmann coupling reaction from the evolution of the different defect-related spectroscopic fingerprints.

6.3 Reaction fingerprints

6.3.1 STM and LEED studies

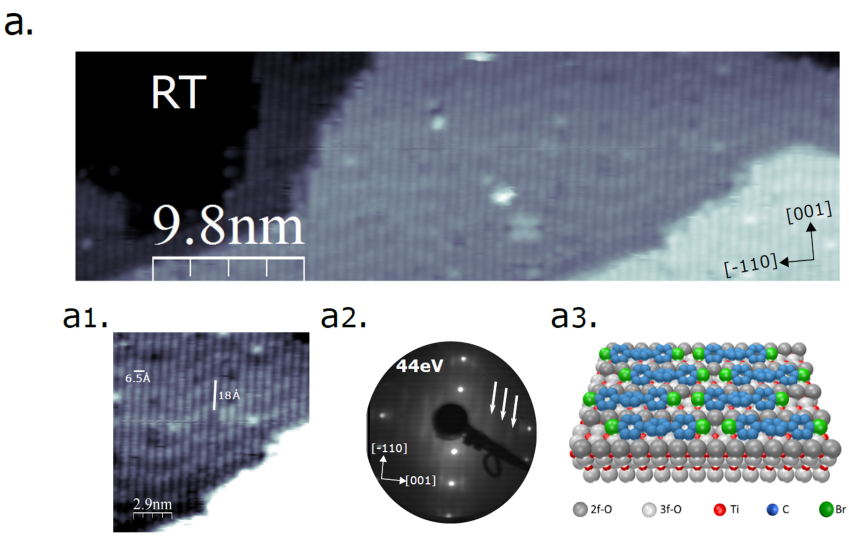

FIGURE 6.2: Adsorption geometry of DBTP on r- TiO_2 (110). (a) An STM overview image of a monolayer DBTP adsorbed on r-TiO_2(110) measured at U_{bias} = 1.8 V I_{set}, = 200 pA. In the close up STM image, (a1), different intra/inter-molecular periodicities are resolved. In (a2), the corresponding LEED pattern of the overview STM image is shown, and the molecule related diffraction spots are highlighted with the white arrows. In (a3), the adsorption model of DBTP is included. The model is taken from [56].

Upon evaporation of DBTP on top of the r-TiO_2 (110) surface held at RT, several stripes, highlighted with the white arrows in figure 6.2 (a2), appear in the LEED image, besides the characteristic spots of the clean surface. The separation between these stripes indicates a super-periodicity along the [001] direction of 2.1 $\pm$ 0.2 nm.

With saturation of the surface, see main figure 6.2 (a), the STM image exhibits well defined rows running along the [001] direction with a *wave-like* pattern superimposed. The distance between these rows is 6.5 ± 0.1 Å, equal to the lattice parameter of the clean substrate in the [110] direction. Higher resolution STM figure 6.2 (a1) reveals an intra-chain super-periodicity of 1.8 ± 0.2 nm along the [001] axis, close to the value deduced in LEED.

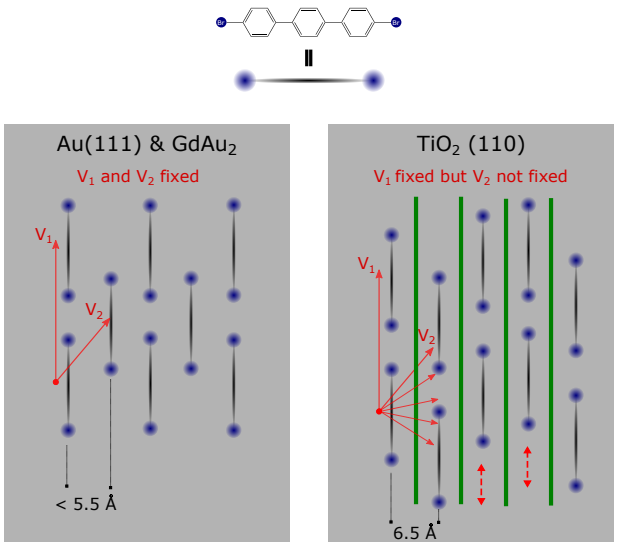

FIGURE 6.3: A model of the geometrical arrangements observed for DBTP on Au(111) (left panel), $GdAu_2$ (left panel) and in TiO_2 (110) (right panel). The DBTP molecule is represented with a black line and two blue circles, as depicted in the top part of the figure.

Tight-binding calculations performed by *Vasseur et al.* [56] for DBTP molecule in the gas phase, establishes a molecule length of 15.2 Å and an inter-molecular Br-Br distance at around 3.8 Å for two molecules facing each other due to the van-der-Walls interactions. Therefore, the periodicity of a one dimensional DBTP supramolecular chain is about 1.9 nm, in agreement with the values experimentally deduced from LEED and STM. Considering that we no longer observe the characteristic O vacancies suggest a one-dimensional arrangement of the DBTP molecules into supra-molecular chains embedded in between the bridging oxygen rows, as represented by the model shown in figure 6.2 (a3). Thus, as pointed out in the beginning, the high surface anisotropy forces the molecule to align in one dimension with the bromine atoms of adjacent molecules facing each other.

This molecular arrangement is almost identical to the one we found for DBTP prior to polymerization on Au (111) and $GdAu_2$ (see chapters 4 and 5). However, there is an additional factor in the TiO_2 (110) surface that makes the arrangement decisively different. To understand the origin of this difference, in figure 6.3 we draw the adsorption models of DBTP on Au (111), $GdAu_2$ and TiO_2 (110), respectively.

Regardless of the employed surface, for a monolayer coverage, DBTP molecules lie parallel to V_1 direction in the figure 6.3. The inter-molecular distance along this direction is fixed and subject to the molecule-molecule interactions. Importantly, on Au (111) and $GdAu_2$ (left panel of figure 6.3) the position of the molecules within one row with respect to adjacent rows is given by V_2. Thus, not only intra chain interactions giving rise to V_1, but also inter chain interaction giving rise to V_2, have to be taken into account. Interestingly, on the TiO_2 (110) surface, the inter-molecular

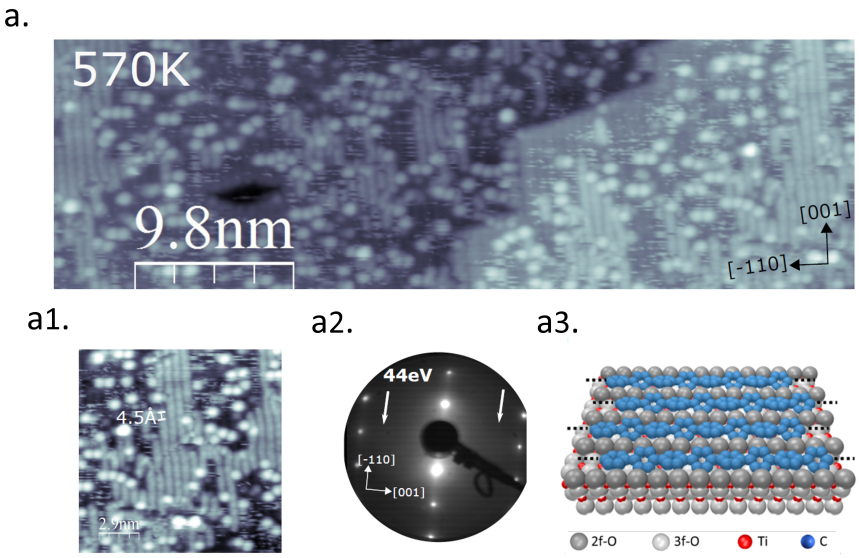

FIGURE 6.4: Adsorption geometry of PPP on r-TiO_2 (110). (a) An STM overview image of a monolayer DBTP adsorbed on r-TiO_2(110) and annealed to 570 K. STM image acquisition parameters U_{bias} = 1.8 V I_{set}, = 20 pA.. In the STM image, (a1), an intra molecular periodicity of Åis resolved. In (a2), the LEED pattern of the sample is shown, and the polymer related diffraction stripes are highlighted with the white arrows. In (a3) the adsorption model of PPP is included. The models is taken from [56].

interactions between molecules in adjacent rows is "interrupted" with the surface protruding oxygen atoms (represented with green lines in the left panel of the figure 6.3). As a consequence, the inter-molecular position is only restricted within the V_1 direction and contrary to the case on Au (111) or $GdAu_2$ there is not coherence between molecules in adjacent rows. This explains the striped diffraction pattern observed by LEED for DBTP on TiO_2 (110) in the [011] direction (see figure 6.2 (a2)). The lack of coherence between two adjacent rows give rise to multiple possible values of V_2 and consequently a random distribution of diffraction spots along this direction, whereas on Au (111) [81] and $GdAu_2$, as V_2 is fixed, we get discrete diffraction spots.

Next we anneal the sample to 570 K, since we know from the temperature dependant XPS ramps shown in the section 6.8, that at this temperature, the molecular de-halogenation has already proceed. The post-annealing of the sample leads to a clear transition characterized in LEED by the rapid disappearance of the supramolecular features and the appearance of two well defined- stripes, indicated by the white arrows, as well as the characteristic spots of the substrate, figure 6.4 (b2). The corresponding distance between the two strips along the [001] direction is about 4.2 Å and yields the 4.23 Å inter-phenyl distance calculated for PPP chains by DFT [147], as well as the one of 4.4 Å measured experimentally on Cu (110) [148].

The STM image 6.4 (b), reveals a rather non-uniform surface (compared to the supra-molecular phase) comprising stripes running along the [001] direction and single clusters randomly distributed. As discussed in detail in section 6.4.2, we infer a substantial desorption upon annealing based on XPS The bare TiO_2 (110) surface is readily identified in the overview image. In the high resolution image, figure 6.4

(b1), in the [110] direction, molecular chains show the same perpendicular spacing of 6.5 ±0.2 Å of that of the surface, however, an intra-chain periodicity of 4.5 ±0.3 Å is deduced from the topmost chain, which is in complete agreement with the formation of PPP chains running along oxygen rows, as depicted in figure 6.4 (b3). Once again, the lack of phase relation between two adjacent polymers is responsible for the stripe pattern observed in LEED [13, 56].

6.3.2 ARPES studies

The structural characterization of the RT and HT phases offers compelling evidence for the polymerization reaction. However, a clear signature of the polymerization is derived by measuring the valence band properties as demonstrated in te section 4.3.4 of chapter 4 for $GdAu_2$. Thus, next we directly mapped the electron dispersion relation of the pristine substrate and the RT and HT phases along the [001] direction with ARPES. The results are depicted in figure 6.5.

The clean substrate (left panel) is characterized by broad features appearing between -3.3 eV and -9 eV below E_F, which correspond to the valence bulk bands (bVB) with a predominantly O 2p character [149]. The characteristic DS, as introduced in section 6.2, is visible close to - 1 eV (indicated by the red arrow). For the RT phase (middle panel), the DBTP HOMO appears just over the bVB onset, around -2.9 eV highlighted with the arrow [150, 151] . Interestingly, the photoemission intensity of this feature is modulated along the [001] direction, with two maxima appearing at 0.6 and 1.4 $Å^{-1}$. This spectral weight distribution, already observed for similar molecules such as sexiphenyl [150], is intrinsically related to the topology of the HOMO state and its Fourier transform [150, 152, 153].

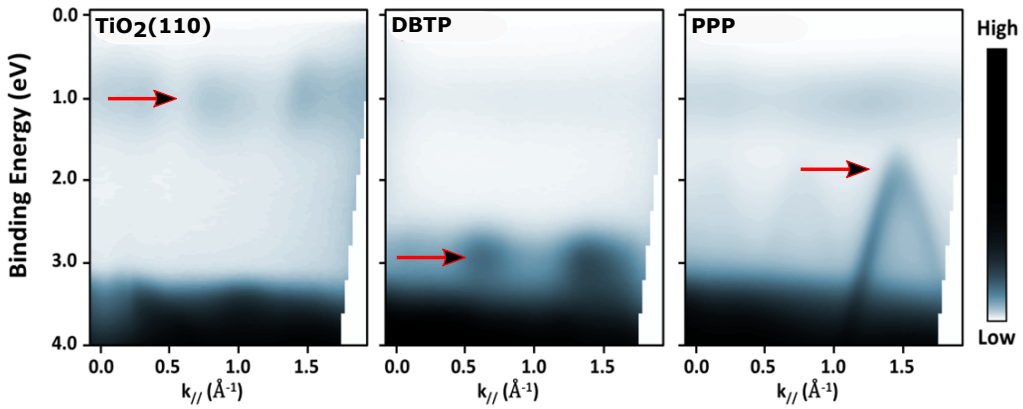

FIGURE 6.5: Electronic properties characterized by ARPES. Experimental ARPES data acquired along the [001] direction (left), after monolayer DBTP deposition at RT (middle), and after annealing the sample at 575 K (right). Figure based on [56].

After annealing the sample to 575 K, the discrete molecular level disappears and a new strongly dispersive band dominates the spectrum (right panel of the figure 6.5). The band dispersion resembles the PPP band on $GdAu_2$ and Au (111) [15] and is the expected one for an infinite chain of phenyl rings, as explained in the section 2.12 of chapter 3. The top of the band is located at - 2.06 eV, i.e. shifted 0.9 eV towards E_F compared to the DBTP HOMO. This shift direction and magnitude are similar to the ones observed on $GdAu_2$ and is tentatively assigned to the HOMO/LUMO gap

reduction expected for PPP [154]. The band apex is at 1.45 $Å^{-1}$ in agreement with the polymer periodicity of 4.2 $\pm$ 0.2 Å deduced by LEED.

Concluding, the characterization of the electronic properties the supramolecular DBTP phase and PPP polymer, as well as the geometrical analysis performed by LEED and STM clearly shows that the Ullmann polymerization of halogenated precursor is feasible on the semiconductor rutile TiO_2 (110) surface. Moreover, the high quality (sharpness and intensity) of the dispersion relation measured by ARPES implies that the average polymer length exceeds 20 phenyl rings, i.e. at least 6 triphenyl monomers have been covalently bonded, exceeding the short polymers measured previously [39, 40].

6.3.3 NEXAFS studies

We probe the molecular geometry and the unoccupied molecular levels with polarization dependent NEXAFS performed at the carbon K edge for the DBTP and PPP phases. Measurements are performed with *p* and *s* polarized light along the surface [001] direction, parallel to the molecule and polymer main axis. Results are shown in figure 6.6.

Both DBTP figure 6.6 (a) and PPP figure 6.6 (b), show a clear resonance close to 285 eV at *p* polarization . This feature, named π^*, is assigned to an excitation of the C 1s CL into the LUMO of the DBTP molecule or PPP polymer, respectively. DBTP shows a second resonance close to 285.8 eV, matching the chemical shift observed with XPS for the Br terminated C atoms (see section 6.11).

The π^* signal dichroism decreases upon polymerization and bromine desorption. To properly visualize this we plot in the figure 6.6 (c), the difference (*p*-*s*) of DBTP and PPP. The higher dichroism of DBTP is evident and interpreted as a flatter adsorption geometry of DBTP with respect to PPP. From gas phase calculations it is well established that the full twisting angle of adjacent phenyl rings is close to 40° in both DBTP and PPP [102]. Thus, our experimental measurements indicate that a stronger molecular substrate interaction flattens the phenyl rings of DBTP, while, after the polymerization, the PPP is decoupled from the surface and adopts a configuration closer to its gas phase structure. However, as we have seen in the STM images for the PPP phase (see figure 6.2 (b)), besides the well aligned polymers, several protrusions, with an apparent higher height than the polymers, emerge on the surface. They presumably have a molecular origin and therefore contribute to the NEXAFS spectra. As a consequence, the interpretation of the PPP signal dichroism is not conclusive.

Concordantly, upon annealing the π^* resonance shifts towards lower photon energies (pointed out with the arrow in the figure 6.6(b)). It is appealing to attribute this measured shift to the LUMO level shifting toward E_F due to a HOMO-LUMO gap reduction upon polymerization of DBTP into PPP. On the one hand, this picture agrees well with the known HOMO-LUMO gap shrinking of PPP as a function of phenyl units (about 1 eV when increasing from three rings to an infinite polymer [131]). On the other hand, we have already deduced from the ARPES measurements a shift of about 1 eV towards E_F for the HOMO level when going from DBTP to PPP.

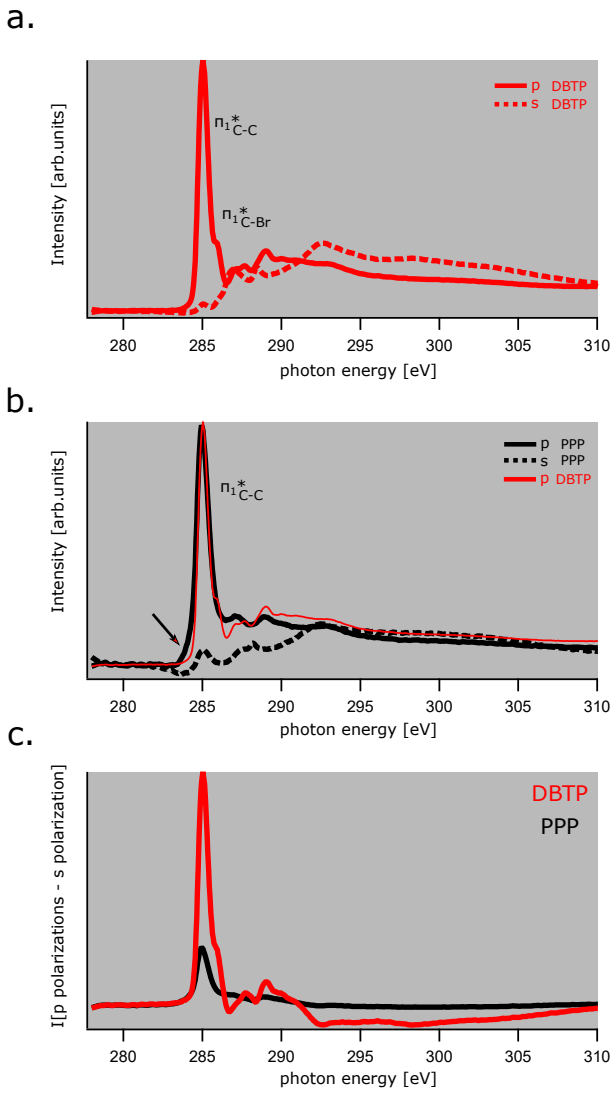

FIGURE 6.6: NEXAFS characterization of the C1s adsorption edge of DBTP (a) and PPP (b). Spectra are obtained in *p* polarization (solid lines) and *s*-polarization (dashed lines), respectively. For comparison in (b) the spectrum of DBTP is included as the red trace. The difference of spectra (*p*-*s*) are plotted for DBTP (red) and PPP (black) in (c).

6.4 Mechanistic aspects behind the Ullmann reaction on TiO_2 (110)

In this section we address several Ullmann reaction mechanism on TiO_2 (110) based on synchrotron photoemission spectroscopy.

6.4.1 Plausible reaction pathways

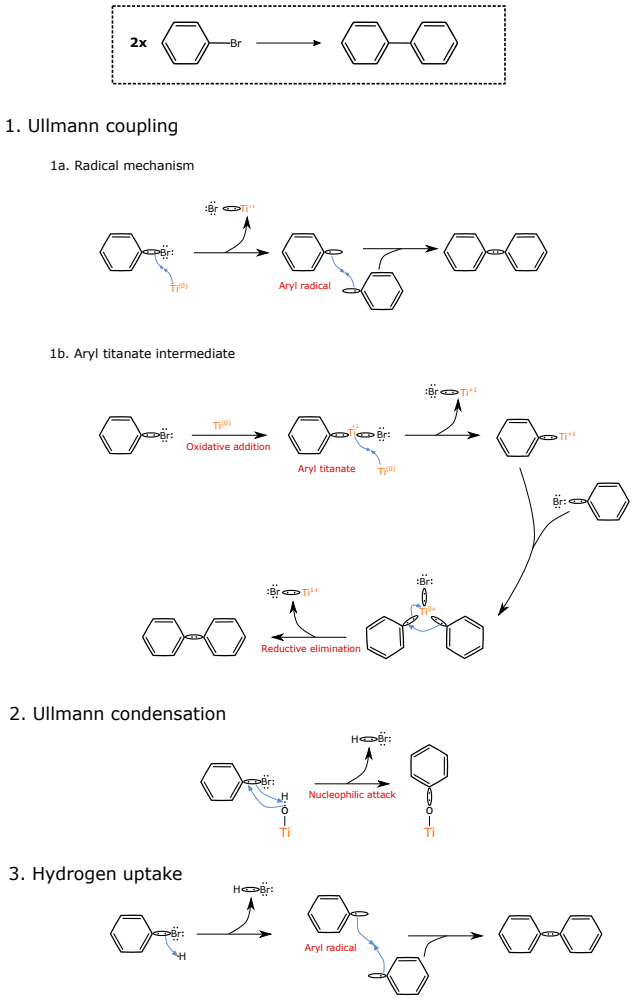

FIGURE 6.7: Possible Ullmann reaction pathways of aryl halide molecules on TiO_2 (110). Three reaction mechanisms, named (1) Ullmann coupling (2) Ullmann condensation (3) Hydrogen uptake, are introduced.

First of all we discuss the possible reaction mechanisms, taking into account surface and bulk properties of the TiO_2 (110) crystal (see figure 6.1 (c)) and the chemical interactions (mainly halogen-metal) necessary for the Ullmann reaction to proceed, explained in more detailed in chapter 3.

The proposed reaction pathways, shown in (6.7), are the following:

1. The "*classic*" Ullmann reaction described in coinage metals but with the titanium atoms.

2. The Ullmann condensation reaction. The nucleophilic attack of surface hydroxyl groups to the halogen bonded carbon atom of the precursor molecule.

3. The hydrogen uptake, where the interaction between the halogen and surface hydrogen atom leads to the formation of aryl radicals.

For simplicity, here we use an aryl bromide as the reaction precursor.

The regular Ullmann reaction

As explained in the chapter 3, the real mechanism behind the Ullmann reaction, even in solution chemistry, is still under debate. On surfaces, two main mechanism have been accepted that depending on the employed surface worked better or not. The main difference lies in the formation of a organometallic intermediate state which so far only observed on Cu and Ag but not on Au. Keeping this in mind, people have proposed the so called *radical mechanism* for the reactions happening on gold and the *intermediate mechanism* for the cases of copper and silver. Chemically, the difference lies in the amount of electrons donated by the catalyst, i.e. in the radical mechanism one electron is donated whereas in the intermediate mechanism the catalyst needs to be capable of donating at least two electrons. Nonetheless, both interpretations requires the oxidative addition of the metal catalyst and therefore we consider both reactions as part of the same group.

In figure 6.7 (a), we interpret both *radical* and *intermediate* mechanisms considering the titanium atom as a catalyst. The initial oxidization state of the atom is set to a reference value of (0) (which does not correspond to the prevalent oxidization state of Ti atoms in the TiO_2(110) crystal).

In the radical mechanism, figure 6.7 (1a), the initial step is the complexation of titanium atoms with the aryl halide molecule, which redistributes the charge around the C-Br bond towards the titanium. Subsequent, the outer sphere single electron transfer from the titanium to the aryl halide produces an aryl radical. Finally, the dimerization, in this case of two radicals, results in the termination of the sequence and the formation of a new C-C bond. A titanium bromide complex is formed as the reaction side-product. Overall one electron from the Ti atom is required for the reaction to proceed.

The second paths, shown in figure 6.7 (1b), involves the formation of an aryl titanate intermediate. A direct reaction of titanium atoms with aryl halides results in an initial oxidative addition step ($Ti^0 \rightarrow Ti^{+2}$) which is followed by a disproportionation (the titanium atom undergoes both oxidation and reduction to form two different products) and reductive elimination ($Ti^{+3} \rightarrow Ti^{+2}$) sequence. Again a titanium bromide complex is formed as a side product. Compared to the *radical* mechanism, the titanium atom has to be capable of donating three electrons throughout the reaction.

Now we consider the different titanium atoms present on the TiO_2(110) surface and their formal oxidation state, in order to discern which of the above presented mechanism is more likely to happen.

A titanium atom can have the following oxidation states; Ti^{n+} where *n=0,1,2,3,4* , although normally it is found as Ti^{4+} in TiO_2. Concomitantly, the commonly accepted picture of the ionic oxidation states in TiO_2 is a quadruply charged Ti^{4+} cation held together with O^{2-} anions by highly ionic bonds [155, 156]. Hence, in the rutile structure, the five fold and six fold coordinated titanium atoms are unable to further donate electrons and promoted the Ullmann reaction. However, as we introduce above, the TiO_2 crystal can be reduced and consequently $Ti^{<4+}$ species are formed.

In the community, there is still no consensus on the Ti-atoms oxidization state for the various defects. However, the most accepted interpretations, and the ones we base our discussion on, state that there are two types of reduced titanium species, both in the Ti^{3+} state: The titanium atoms in the oxygen vacancies and the interstitial titanium atoms, known to diffuse to the surface or subsurface at high temperature. Since both species only have a single electron available, we exclude the possibility of aryl-titanate formation and expect a radical mechanism.

Experimentally, photoemission fingerprints to identify the Ullmann reaction driven by Ti^{3+} species include the attenuation of the Ti 2p CL peak shoulder or the disappearance of the DS in the VB. This will be discussed in detail in section 6.4.2.

The Ullmann condensation reaction

The second reaction mechanism in figure 6.7 (2) , named the Ullmann condensation reaction, renders the synthesis of an ether compound with the formation of an aryl oxygen bond, instead of the -C-C- bond obtained in the *"classic"* Ullmann reaction. Also called the O-arylation process, the reaction itself is interesting in the pharmaceutical industry [157–159], and is accomplished combining aryl halides with molecules containing alcohol groups such as phenols in the presence of a copper catalyst. In the case of TiO_2 (110), the OH groups are present in the surface (formed by water splitting on the O_v's). Hence, the reaction is subject to an acid-base catalysis rather than an oxidation-reduction catalysis. The reaction proceed as follows; surface hydroxide groups replace the halogen atom of the molecule by the nucleophilic attack to the halogen bonded carbon atom (we recall in chapter 3.7 that this carbon is the most electropositive of all atoms within the molecule) and in the process an ether bond is formed and a hydrogen bromine molecule is released. The later, due to its small size, will probably desorbed right away from the surface into gas phase. The proposed mechanism if expected to be (to some extend) limited by the protection of the Br-C bond by the moleculr pi-system (see also chapter 3.7). Hence, it is likely that for this reaction to proceed, the charge around the carbon halogen bond has to be redistributed, and for that, again, the Ti^{3+} atoms are the likely candidates.

Experimentally, the disappearance of the OH related peak from the photoemission spectra and the observation of the new C-O bonds in the C 1s CL are expected signatures of this reaction. We further explore this possibility in section 6.4.2.

The Ullmann reaction by hydrogen uptake

Last, in figure 6.7 (3), we include the mechanism proposed by *Marek et al* for the polymerization of 10,10'-dibromo-9,9'-bianthryl (DBBA) on the rutile TiO_2 (011) 1x2 surface [40, 160]. The idea behind is the uptake of the acidic protons of the surface hydroxyl groups (instead of the nucleophilic attack performed by the oxigen atom) which leads to the formation of aryl radicals and the subsequent coupling. Thus the mechanism is in direct competition with the one shown in figure 6.7 (2), since in both cases, surface OH groups are the reaction activators.

By analysing the reaction products (-C-C- vs -C-O-) and performing temperature XPS ramps monitoring the OH-related (see figure 6.1) VB feature we can experimentally discern both reaction pathways. Moreover, the deprotonation of the OH group, leads to an effective oxidization of the surface. Thus, the attenuation of the DS can also indicate the presence of the proton uptake mechanism.

Other possibilities

There are other possibilities that can also induce the formation of PPP in TiO_2 (110) surface. For instance, in the previous two chapters, we observed that the self assembled structure of DBTP molecules can promote the dehalogenation of two molecular entities by steric effects without the requirement of a real catalyst. Even though for TiO_2 (110), due to its particular surface conformation, this process is restricted, different type of steric interactions, such as the one involving the halogen with surface oxygen atoms, can produce similar effects. Another possibility is that the reaction is simply thermally activated, explaining the rather poor reaction yield observed upon polymerization.

From here on, all these scenarios are considered for the data interpretation.

6.4.2 XPS to unravel the Ullmann reaction mechanism

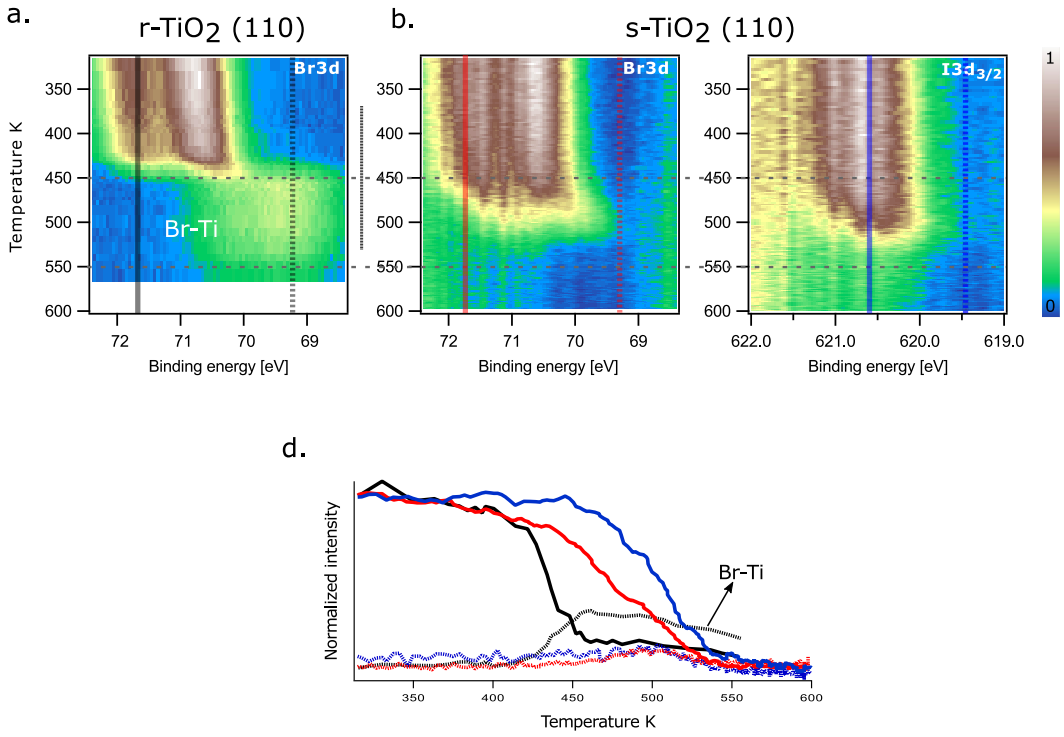

FIGURE 6.8: TD-XPS waterfall plots measured at the BEs were the halogen atom CL peak of DXTP (X=Br,I) appear. The temperature ramps are performed between RT and 600 K in three individual samples; (a) DBTP on r-TiO_2 (110), (b) DBTP on s-TiO_2 (110) and (c) DITP on s-TiO_2 (110). Constant energy intensity line profiles extracted from the different samples are collected in the figure (d) and distinguished with colours. The continuous line represents the case where the halogen atom is attached to the molecules (71.6 eV for Br and 620.5 eV for I) whereas in the dashed line (69.2 eV for Br and 619.4 eV for I) the halogen is already detached and chemisorbed on the surface.

To identify the different reaction pathways, we combine XPS measurements with systematic variations of halogen atoms (Br vs I) and reduction state of the surface (reduced vs stoichiometric).

First insight on the molecular de-halogenation process is obtained by stepwise annealing of the sample while monitoring Br 3p and I 3d CL signals, respectively. For all the measurement, we prepare a monolayer of DXTP (X= Br,I) molecules deposited at a sample temperature of 300 K, since, as described by *Vasseur et al* [56], the molecular growth is limited to a saturation coverage of a monolayer and ensures reproducibility among different sample preparations. Results are summarized in figure 6.8.

On the r-TiO_2(110) surface, figure 6.8 (a), the Br 3d CL, plotted as a function of temperature, shows two transition temperatures: until a temperature of 450 K, the Br3d peak is centred at around 70.7 eV indicating unreacted molecules. Then, at higher temperatures, the Br 3p is shifted to 69.35 eV while the overall intensity drops considerably, as shown by the black traces in figure 6.8 (d), and close to 520 K the Br 3d CL intensity vanishes completely. On the s-TiO_2 (110) surface, the picture is decisively different. Whereas the onset of a transition can be gauged at around 450 K, there is no shift toward lower BE seen for the Br 3d CL. Instead the CL signal vanishes comparably gradually up to about 500 K (red traces in figure 6.8 (d)). Interestingly, if we compare the dehalogenation of DBTP and DITP, red and blue traces in the figure 6.8 (d) respectively, the reaction temperature for the later is slightly higher. The earlier bromine dehalogenation is typical of for substitution reactions produce by nucleophilic attacks (where the reactivity follows the halogen electronegativity order) contradicts a metal catalyzed reaction pathway. Further information about this matter can be found in the chapter 3. Additionally, we note that the onset of the loss of Br (or I) intensity occurs later on the stoichiometric surface compared to the reduced one.

These striking differences in the CL evolution as a function of temperature for the reduced and nearly stoichiometric surface, strongly suggest different reaction mechanisms responsible for the C-Halogen bond scission. First, we address the likely candidate for the mechanism observed on the reduced surface.

Evidences of the classical Ullmann reaction

Measurements performed in the VB region and the Ti 2p CL for DBTP on r-TiO_2 (110) and s-TiO_2 (110) are shown in the figure 6.9 (a1) and (a2) respectively. A reference spectrum of the clean surface (black spectra) is also included. In the left panel, the peak close 1 eV is the above introduced DS. After DBTP deposition, orange lines, an additional molecular feature, indicated by the white arrows in figure 6.9 (a1) emerges close to BE = 2.7 eV in the VB region. The energy position is in good agreement with the HOMO level we previously observe in the ARPES measurement for the same phase (see figure 6.5). When looking at the DS, it appears slightly attenuated and shifted in energy compared to the pristine surface. Indeed, in reference [56] we reported a similar observation upon the deposition of halogenated precursor. By ARPES we observed a complete quenching of the DS and ascribed it to the surface interaction with halogen atoms in the molecule. Therefore, here we attribute the minimal peak attenuation and shift to the presence and interaction of the molecular over layer.

After heating the sample to 450 K (green trace) significant changes occur in both VB and Ti 2p CL spectra. First, the intensity of the molecular states is strongly reduced. This is due to molecular desorption as is evidenced in both STM and XPS temperature measurements (see section 6.2 and figure 6.11). Second, a rigid shift of the molecular state (marked by the white arrows) toward lower BE is seen. Again,

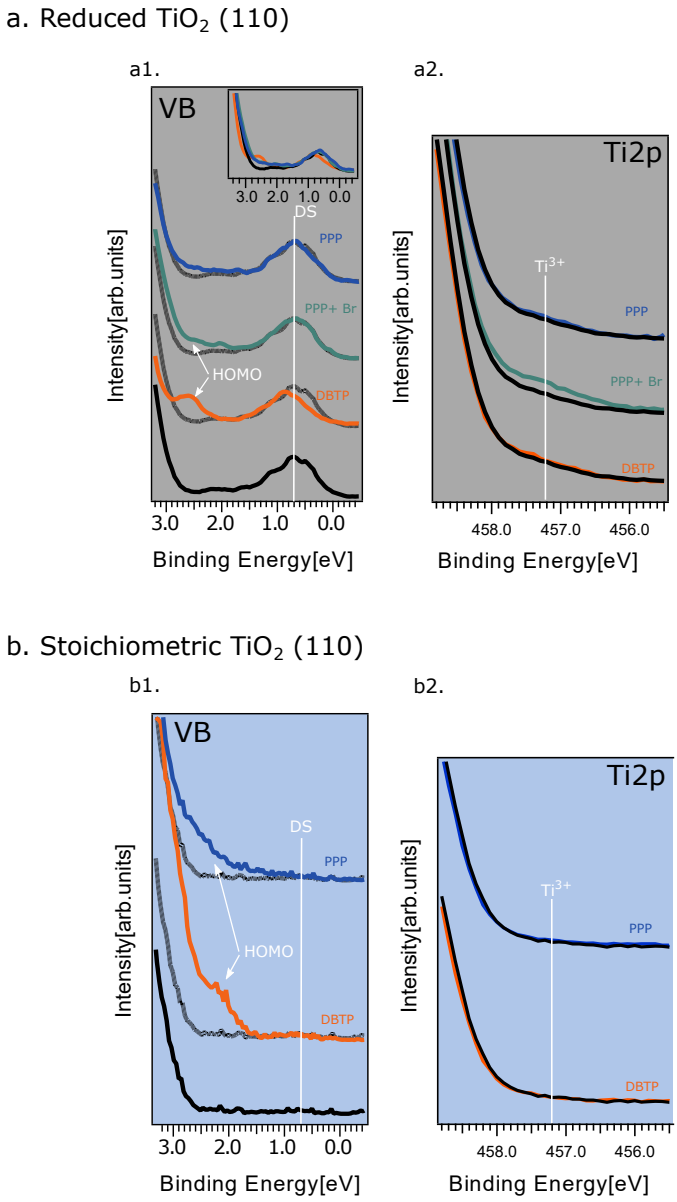

FIGURE 6.9: PS studies of DBTP and PPP covered surfaces with two different reduction states. Panels (a1) and (a2) show the VB and Ti 2p photoemission regions of the r-TiO_2 (110) respectively. Measurements are performed on the clean surface (black line) and DBTP covered sample at RT (orange line), 470 K (green line) and 520 K (blue line). The reference spectrum of the clean substrate is included for comparison and visualization purposes. The same nomeclature as in (a) is used in (b) for the stoichiometric s-TiO_2 (110) sample.

the magnitude of the shift agrees well with the ARPES measurements and in particular an overall increase of the intensity close to the DS is considered a fingerprint of the polymerization reaction. Interestingly, the DS state remains unaltered during the reaction. Superimposing the spectra, insets of the figure 6.9 (a1) illustrates the changes more clearly.

Surprisingly, despite the constant intensity of the DS, a clear increase of the Ti^{3+} related shoulder is observed in the Ti 2p CL. Note that these two observations are apparently contradictory, as an decrease in Ti oxidization state of the surface is inherently linked to an increase in the DS intensity. Thus, we must ascribe the presence of Ti atoms that are formally in a Ti^{3+} oxidization state to a new structure that does not partake in filling the DS. Indeed, we recall that at the given annealing parameters a significant amount of Br, shifted to metal-bond BE close to 69 eV, is present on the surface (a similar shift is observed in both c-Au(111) and $GdAu_2$ surfaces). Since any form of BrO can be expected to shift the Br CL toward higher BE compared to the DBTP case, we must conclude the presence of TiBr on the surface. Indeed, we predict this species are expected to be formed as the side products in the radical mechanism of the Ullmann reaction (see figure 6.7 (1)). However, if the Br atoms were to, e.g. replace oxygen atoms (as was observed for Cl atoms by Hebenstreit et al. before [161]), the surface would be formally reduced by one electron (a bridging oxygen atom takes $2e^-$ from the surface whereas the Cl atom only needs one), which would lead to an increase in the DS as well as an increase in the Ti^{3+} contribution of the Ti 2p CL. An exchange of a surface OH with a Br atom would leave the surface charge formally unchanged, thereby neither a change in the Ti 2p CL nor the DS is to be expected. Both scenarios are incompatible with our observations, thus, we consider a third scenario: For highly reduced TiO_2, i-Ti are known to diffuse to the surface at quite low temperatures, around 570 K, where they can react with O_2 to re-oxidize the surface [162]. In our case, the temperature of 470 K is substantially lower and the surface did not show any signs of the 2×1 reconstruction, nonetheless, the uptake of i-Ti from subsurface areas to either form organotitanates intermediates or radical species at the surface (with the release in both cases of a BrTi molecule) explains all observations. A similar conclusion was derived by Benz and co workers, after studying the reductive coupling of benzaldehyde to stilbene, known as the Mcmurry reaction, on the vacuum-reduced TiO_2 (110) surface [133, 163]. With temperature programmed reaction spectroscopy and STM measurements, they proof that subsurface Ti interstitial were the active sites triggering the reaction, while the oxygen vacancies sites alone did not account for the coupling process. Interestingly, they reported a reaction temperature of 490 K and attribute it to Ti interstitial diffusing the subsurface region, very close to the temperature (470 K) we are reporting here. Thus, we believed that the presence of i-Ti in the surface in the form of $Ti^{+x}Br_x$, enhances the contribution of reduced titanium atoms in the Ti 2p CL while leaving the DS and overall surface reduction unaffected and concurrently explaining the shift of the Br CL toward lower BE. If our hypothesis is correct, neither the side reaction products nor the intermediates should remain at higher temperatures. Indeed, further annealing the sample close to 570 K, all Br is desorbed (see figure and the Ti contribution in the Ti 2p CL is reduced while the DS intensity remains unchanged (blue spectrum in figure 6.9 (a2)).

Overall, the scenario also correlates with the absence of $Ti^{+x}Br_x$ species on the s-TiO_2 (see the TD-XPS measurements shown on figure 6.8) since inherently the surface has lower amounts of i-Ti than the r-TiO_2.

In the figure 6.9 (b), VB and Ti 2p measurements acquired on the s-TiO_2 (110) are presented, with the exception of the intermediate phase corresponding to the

$Ti^{+x}Br_x$ situation (green spectrum in figure 6.9 (a)). As on the r-TiO_2, upon the molecular deposition, new molecular features emerge (orange line) in the VB region and again, after annealing, this feature broadens and shifts towards Fermi (blue spectrum). During this process, both surface DS and Ti 2p CL remains unchanged.

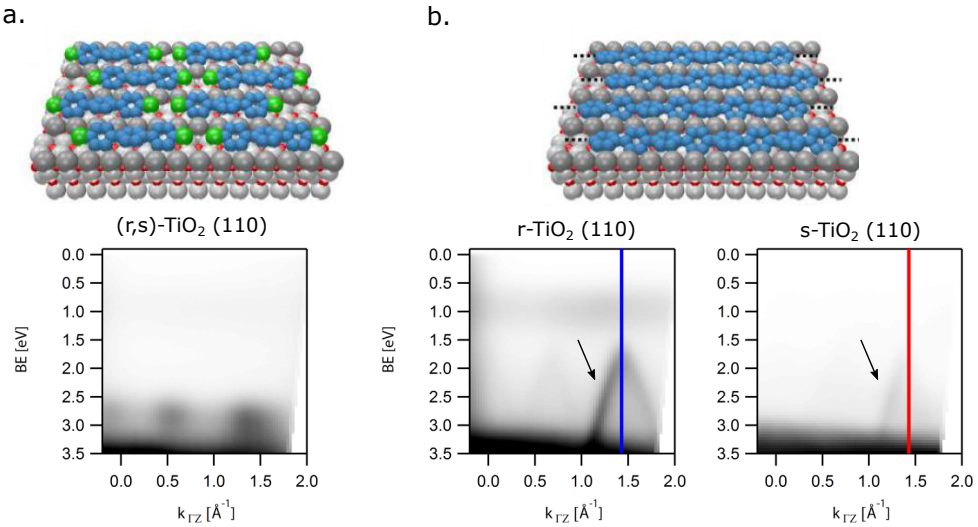

FIGURE 6.10: Experimental raw ARPES intensity maps acquired pn the reduced and stoichiometric TiO_2(110) surfaces for DBTP and PPP respectively. Since for DBTP the results are practically the same, in (a) only the intensity map of DBTP on the r-TiO_2(110) is shown. From left to right in (b), the PPP band dispersion measured on the r-TiO_2(110) and s-TiO_2(110) surface is shown respectively. The adsorption models are taken from [56].

It is interesting that the evolution of the molecular feature again suggest that the polymerization has proceed on the s-TiO_2 (110). We have confirmed this interpretation by ARPES. The electronic properties of DBTP and 525 K annealed DBTP sample on s-TiO_2(110) compared to the results obtained on the r-TiO_2 (110) surface are summarized in the figure 6.10. For the RT phase, panel (a), the HOMO level of DBTP presents equivalent electronic levels on both surfaces besides the expected work function differences. At high temperatures, panel (b), the band measured on the s-TiO_2 (110) is very faint but rather similar to the PPP band obtained in the r-TiO_2 (110). In both cases, the band apex is close 1.45 $Å^{-1}$ and at a maximum energy of around - 2.06 eV. The lower integrated intensity of the band measured on the s-TiO_2 (110) means that the amount of polymers from which the signal is originated is considerably lower.

While the identification of $Ti^{+x}Br_x$ species and the correlation with the Ti2p Cl on the r-TiO_2 surface clearly points toward a classic Ullmann-like reaction, it does neither exclude other reaction pathways taking place simultaneously nor can it explain the polymerization reaction observed on the s-TiO_2 surfaces where, in particular, no $Ti^{+x}Br_x$ species are seen. Therefore, we next proceeded to de-convolute the C 1s throughout the different steps of the reaction to gauge if only shifts toward lower BE - the *classic* ullmann reaction - are observed or if other contributions, in particular at higher BE - which may point toward Ullmann condensation-like reactions - are present as well.

Evidences supporting the Ullmann condensation reaction

Next we analyze the C 1s CL changes for a monolayer DBTP on r-TiO_2 (110) as function of the annealing temperature. The evolution of the C 1s line shape, shown in the figure 6.11 (a), agrees with the C-Br bond scission and the formation of the PPP (see section 4,5 for comparison), although, as for the Br 3d, the total peak intensity decays severely.

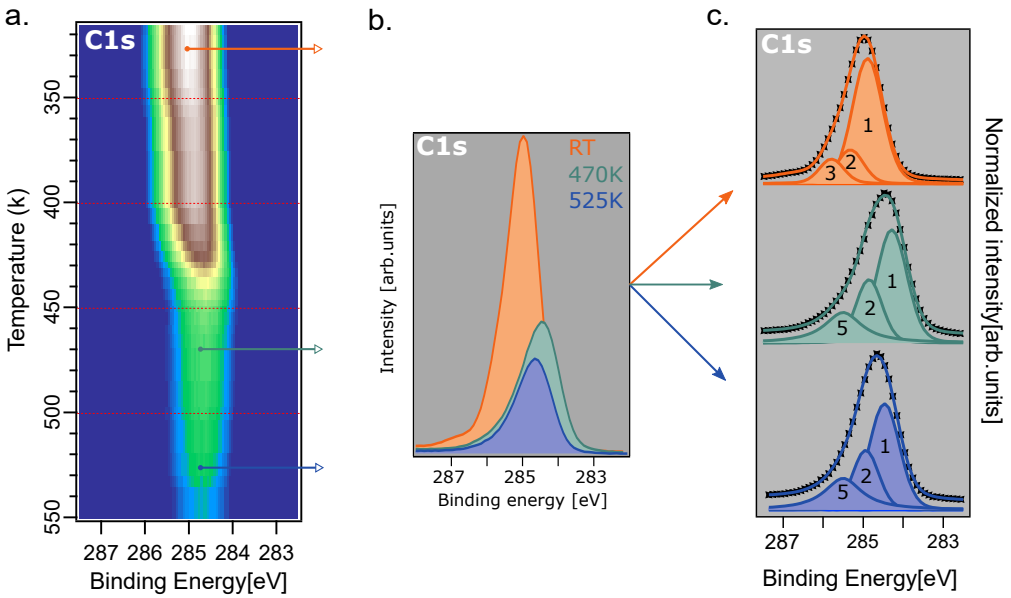

FIGURE 6.11: C 1s CL of DBTP and PPP on TiO_2 (110). (a) TD-XPS of DBTP C 1s CL spectra adsorbed on the r-TiO_2 (110). (b) C 1s CL high resolution XPS spectra extracted from (a) at RT, 470 K and 520 K respectively. The corresponding peak deconvolution is shown in (c).

A deeper information of the system is obtained by analyzing high resolution XP spectra for the three phases shown in figure 6.11 (b) *i.e* at RT, 470 K and 520 K respectively. Interestingly, at RT, top spectrum in figure 6.11 (c), the C 1s CL is deconvoluted into three peaks, contrary to the observations on the c-Au (111) and $GdAu_2$, where the deconvolution leads to two peaks; The most intense one, labelled "1", is centered at 284.9 eV and assigned to hydrogen saturated carbon atoms (C-H) of the DBTP molecule. Peaks "2" and "3" (285.4 eV and 285.8 eV, respectively) correspond to the carbon atoms in the para position of the phenyl rings i.e. the bridging C atoms (C-C) and Br bound C atoms (C-Br) respectively. An intensity ration of 4 (Peak 1) : 2 (Peak 2) : 1 (Peak 3) matches the chemical composition for different carbon atoms of the intact DBTP molecule.

After annealing, at 470 K, peak 1 and 2 rigidly shift 0.65 eV towards lower binding energy, following the trend observed on both c-Au(111) and $GdAu_2$ and in the literature [5, 56, 79]. Furthermore, a change to a 1 (peak 1) : 2 (peak 2) ratio matches the expectation for the ratio of C-C to C-H species in poly(p-phenylene) polymers. However, an additional feature, labelled as peak 5 , is needed to fit the CL and its presence is absent in the previously studied c-Au (111) and $GdAu_2$ surfaces. After annealing to 520 K (bottom blue curved) the relative intensity of all three peaks remains almost equal and they shift slightly back 0.25 eV towards higher binding energy probably by the work function changes induced by the desorption of surface chemisorbed bromine species.

Unambiguous assignment of peak 5 is challenging, but due to the relatively high BE of about 285.5 eV it can not be attributed to C-Ti species, as C-Metal bonds are found at lower BEs [79, 164]. Moreover, the fact that the peak is preserved at higher temperature indicates that the signal arises from a rather stable compound. We believed that indeed, the peak "5" is the fingerprint of the Ullmann condensation reaction and is originated from a new Ti-O-**C**-R (R being the molecular backbone) bond. Its energy position is in rather good agreement with molecules containing ether functional groups measured on TiO_2 (110) [134, 165, 166] by XPS and also explains why we see protrusions in STM at high temperatures besides the regular polymeric chains. However, its area is almost as big as peak "2", which is far to high if we consider that the Ullmann condensation reaction is a side reaction path. Most likely, the peak is a convolution of even more species and additional experimental and theoretical work is required for an unambitious assignment,

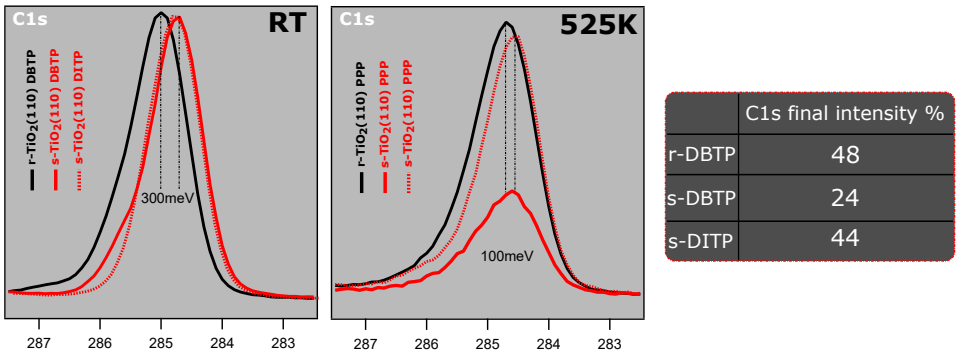

	C1s final intensity %
r-DBTP	48
s-DBTP	24
s-DITP	44

FIGURE 6.12: C 1s CL of of DBTP, DITP and PPP. The black line corresponds to the spectrum of DBTP (PPP) measured on r-TiO_2(110), the continuous red line to DBTP (PPP) on s-TiO_2 (110) and the dashed red lines to DITP (PPP) on s-TiO_2 (110). The table on the right hand side depicts the reduction in total C 1s intensity at 525 K compared to RT for the three cases as indicated.

Here, we include also the reaction on the stoichiometric s-TiO_2 (110) surface as VB measurements (figure 6.1) clearly show a similar amount of OH on both s-TiO_2 and r-TiO_2 surfaces. In figure 6.12 the C 1s CL of DBTP (red lines) and DITP (dashed red line) deposited at RT on the s-TiO_2 (110) and afterwards annealed to 525 K are plotted. For comparison, the spectra measured on the r-TiO_2 (110) are also included (in black). At RT, there is a 300 meV shift between the two surfaces which nicely coincides with the expected difference in the surface work functions [167]. Probably the most striking feature is the considerably higher desorption yield observed for DBTP on the stoichiometric surface compare to the reduced surface. This indirectly indicates that the main polymerization pathway happens via i-Ti following the classical Ullmann mechanism. Interestingly, the desorption yield of chemisorbed iodinated species is lower that the brominated ones. This behaviour is contrary to the observations on $GdAu_2$ discussed in chapter 4.9. In that case desorption of I occurred 100 K earlier than that of bromine, in agreement with the adsorption energies found for halide ions on noble metal surfaces [107]. The opposite behaviour observed here indicates an opposite adsorption energy of Br and I, respectively on the TiO_2 (110) surface.

In order to see whether the Ullmann condensation reaction is present on the s-TiO_2 (110), we again deconvolute the C 1s CL peaks measured at the above presented

temperatures for the DBTP and DITP and compare the results with the ones obtained on the r-TiO_2 (110). The results are summarized in the figure 6.13.

The RT phases are shown in the panel (a). Besides the work function induced shifts, in all cases three peaks comprises the C 1s CL spectrum. The intensity ratios are equal for all, and the only difference is the energy position of peak 3 vs peak 2 for the DITP. Whereas for DBTP the difference is 0.41 eV and 0.38 eV respectively on the r-TiO_2 (110) and s-TiO_2 (110) surfaces, for DITP the difference is 0.21 eV. The explanation is the higher electronegative character of Br vs I.

After annealing, peak 3 disappears and peak 5 emerges in all three cases. Thus, the presence of surface OH, even in the absence of i-Ti, can drive the Ullmann condensation reaction for halogenated monomeric precursors.

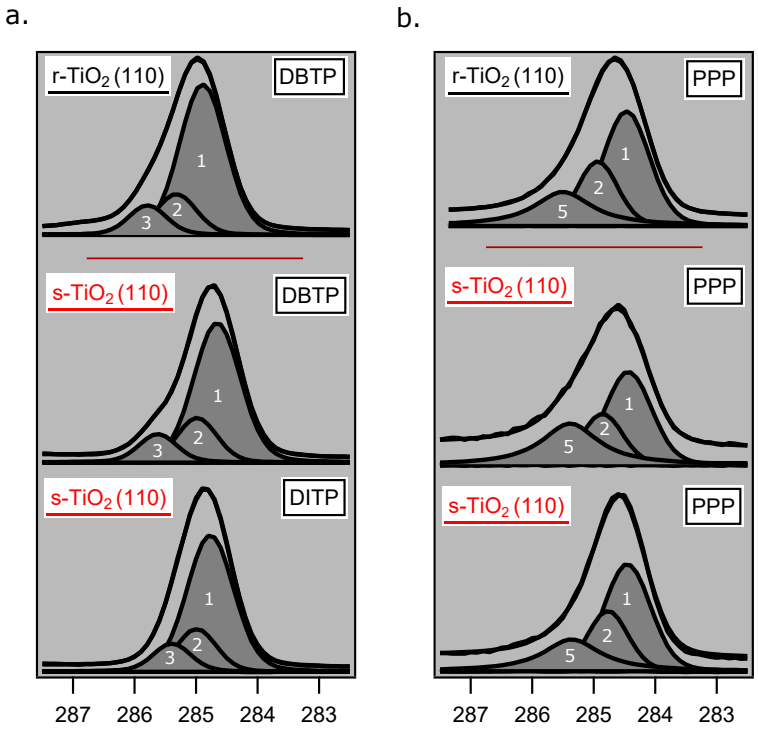

FIGURE 6.13: Set of C 1s peak deconvolution for DXTP (X=Br,I) in a) and PPP in b). Going by rows, in the first, the deconvolution of DBTP/PPP adsorbed r-TiO_2 is presented. In the second and third rows, the deconvolution of DBTP/PPP and DITP/PPP on the s-TiO_2 (110) surface is shown respectively.

Evidences for the hydrogen uptake scenario

Recently, a reaction mechanism for the aryl-halide homocoupling on metal oxide surfaces based on proton transfer was proposed [40, 160]. The first step of the reaction is the proton transfer from a surface hydroxyl group to the aryl-halide, followed by a migration of the proton to the C-halogen bond, thus activating it and allowing for the homocoupling reaction to proceed. The direct identification of the protonated hydrocarbons by XPS is difficult and the lifetime of the hydrogenated aryl-halides is unknown. Therefore, we focus on the evolution on the well-established hydroxyl feature in the VB of TiO_2 (110) surface as a function of annealing temperature for pristine and molecule covered surfaces.

On the clean TiO_2 (110) surface, figure 6.14 (a), the OH signal starts disappearing at around 450 K and is completely gone at 500 K, in accordance with literature, [144, 168]. During this process, the DS peak intensity is barely changed and thus unaffected by the desorption of surface hydroxyl groups[169–171].

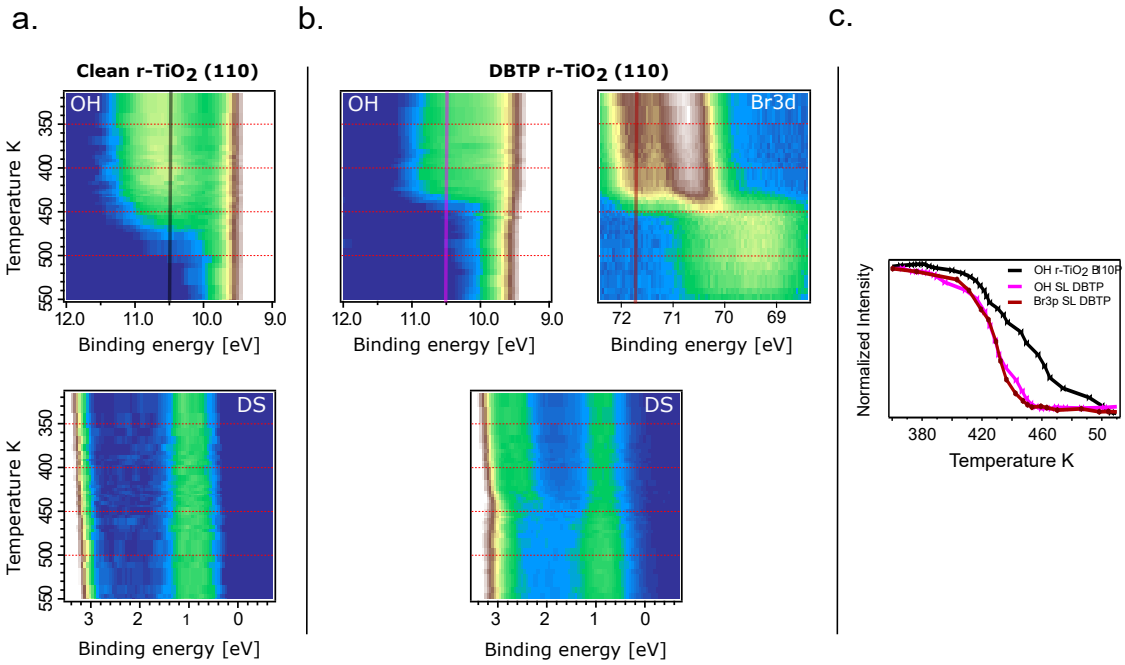

FIGURE 6.14: TD-XPS measurements performed at the BEs where surface OH and DS peak appear. The sample is annealed from RT to 550 K. The ramp performed on the clean r-TiO2 (110) surface is shown in (a), whereas in (b) the measurements taken after the deposition of a monolayer of DBTP are shown, including the evolution of the Br 3p CL. Intensity line profiles taken at a constant energy of 10.5 eV (OH) on the clean (black line) and molecule covered (pink line) samples are shown in (c), together with the Br 3p CL intensity line profile take at 70.5 eV (red line).

Surprisingly, if the same temperature ramp is applied to a DBTP covered surface, figure 6.14 (b), the OH signal is quenched earlier and coincides with the temperature at which the characteristic shift of the bromine CL occurs. These effect are better visualize in the figure 6.14 (c), where we show superimposed the intensity line profiles taken at 10.5 eV for the two OH ramps (in black the clean surface and in pink the DBTP covered surface) and at 71.8 eV for the Br3d CL.

On the clean surface (black line), the thermal desorption of OH groups starts at around 420 K and continues gradually until it is completed at around 500 K. On the contrary, with the molecular over layer (pink line), the OH intensity decay starts at similar temperatures but suddenly drops and is completed at 450 K. Interestingly, the intensity line measured simultaneously for the Br 3d peak, red line, follows exactly the same pattern. Along this line, the signals of the HOMO level of the DBTP, visible at around 2.7 eV on the waterfall plot of the DS (bottom graphs in figure 6.14 (b)), shifts in intensity (due to the polymerization and formation of a new less intense band at lower BE) at the same exact temperature where the de-halogenation occurs and OH group disappears.

Thus, the presented TD-XPS measurements directly correlates the de-bromination

of DBTP with the OH groups of the TiO_2 (110). Nevertheless it does not clarify whether the disappearance is related with the proton uptake scenario or the Ullmann condensation process since in both cases the OH is driving the reaction.

DBTP on the re-oxidized r-TiO_2 (110) surface

Lastly, in order to gain more insight on the reaction, we oxidize the r-TiO_2 (110) (from now on **o-TiO_2 (110)**) by exposing the sample to molecular oxygen at pressures around $1e^{-7}$ mbar for five minutes.

When molecular oxygen O_2 is adsorbed in the r-TiO_2 (110) surface, it acts as a scavenger of excess electrons originating from donor-specific sites, such as oxygen vacancies, OH, and interstitial Ti atoms [172–175].

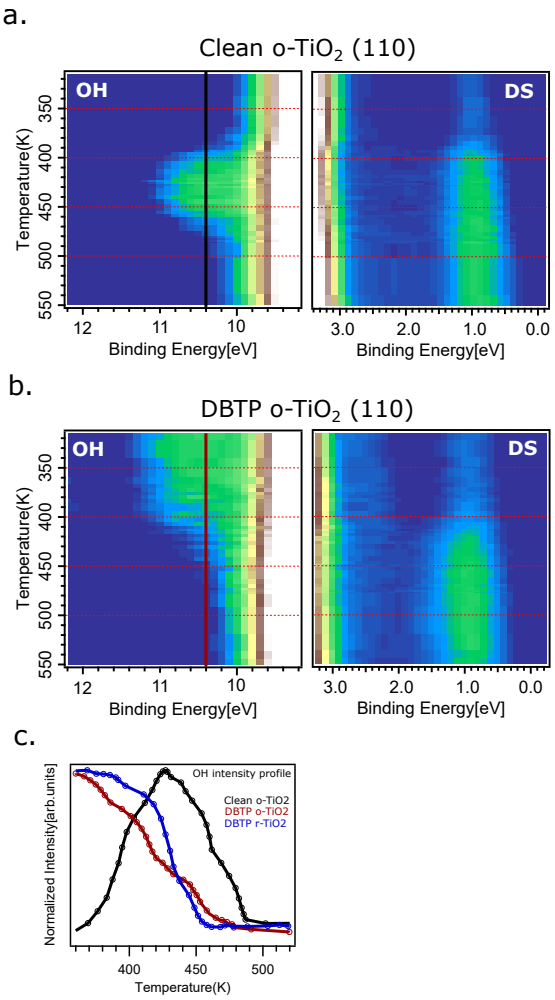

FIGURE 6.15: TD-XPS measurements performed on the o-TiO_2 (110). The temperature evolution of surface OH and DS measured on the clean (a) and DBTP covered (b) samples. OH intensity line proflies are gathered in (c).

STM based experiments have shown a dissociative adsorption of O_2 on the r-TiO_2 (110) surface, either at the oxygen vacancies with one O atom healing the vacancy and the other O atom leaving at a neighboring 5-fold-coordinated Ti (Ti_{5C}) sites as an adatom [172, 176, 177], or dissociated directly at Ti_{5c} sites , yielding paired O adatoms which may be caused by i-Ti [178]. Interestingly it was also reported that

the O_2 molecules can react with the hydroxyl groups, yielding HO2 species [159, 179] that are afterwards desorbed from the surface. Thus overall, the addition of O_2 into the r-TiO_2 (110) has interesting implications for our reaction since both presumably active sites such as surface OH groups and Ti^{3+} species are removed. Moreover, oxygen adatoms, likely acting as nucleophiles, are now present on the surface of the crystal.

Two XPS temperature ramps, performed on the clean o-TiO_2 (110) and the DBTP covered o-TiO_2 (110) are shown in figure 6.15 (a) and (b) respectively. In the clean surface, at RT, the OH peak is removed and the DS peak is barely visible due to the adsorption of O_2. Upon annealing, around 400 K, the intensity of both peaks emerge simultaneously. Hence, 400 K is enough to create surface oxygen vacancies and consequently the DS peak appears. Concomitantly, the water present in the experimental chamber (desorbed from the experimental parts due to the sample annealing) is dissociated at the vacancies and therefore the OH peak created. Further annealing the sample quenches the OH intensity while the DS intensity recovers, a similar evolution to the one observed in the clean r-TiO_2 (110) surface. This indicates that the charge "eaten" up by the chemisorbed O_2 becomes available again before the dehalogenation happens. Therefore, for both classical Ullmann like as well as Ti catalysed condensation reaction should be as efficient on the o-TiO_2 than it is on the r-TiO_2.

After DBTP deposition onto the o-TiO_2 (110) surface, the OH peak is recovered whereas the DS peak remains barely visible. The presence of the OH peak is an unexpected situation and we proposed two interpretations to explain its presence. One is that upon the molecular deposition process, due to the annealing of the evaporation cell, the sample is expose to water molecules. However, water has to be dissociated to from OH groups. This implies that either not all the oxygen vacancies are healed upon O_2 exposure, or there is a different surface active site capable of dissociating water. The other interpretation is that close to the energy position where the OH peak is located, DBTP has molecular levels. Further experiments are needed to clarify this point.

The changes produced upon annealing are best visualized in the intensity profiles shown in figure 6.15 (c). The intensity at the OH region vanishes earlier on the molecule covered surface (red line) than on the clean o-TiO_2 (110) (blue line) surface. This temperature is similar to the one found for the DBTP covered r-TiO_2 (110) surface (blue line) shown in the previous experiments and hence resembles similarities in the reaction behaviour.

6.5 Cobalt induced polymerization of DBTP on s-TiO_2 (110)

Dosing small amounts of active metals as catalyst onto a relatively inert substrate has emerged as a new strategy in on-surface synthesis. The main idea behind it is to deposit stoichiometric amounts of an external catalyst, normally metal atoms, to enhance the reactivity of a specific reaction. In the context of the Ullmann coupling, the strategy has been mainly employed on Au (111) surfaces. For example, the addition of stoichiometric amounts of copper atoms onto a Au (111) has shown to be an smart strategy to reduce the coupling temperature of halogenated precursors [106, 180]. In a similar way, palladium atoms have been used to polymerize halogen containing porphyrin molecules on Au (111) [181].

Here we use cobalt atoms as external catalysts to induced the polymerization of DBTP molecules on the s-TiO(2) (110) surface, to the best of our knowledge, the first semiconductor on which this strategy is employed.

We have decided to used the stoichiometric and not the reduced TiO_2 (110) surface in order to avoid and minimize the contribution of the *classical* Ullmann coupling reaction produced by i-Ti atoms (see section 6.4.2). For the experimental procedure, we first prepare a monolayer DBTP sample on the s-TiO_2 (110) and afterwards sublimated the Co atoms. Then, by STM, LEED, and photoemission techniques we gain inside of the system at different temperatures.

6.5.1 STM and LEED studies of cobalt induced polymerization of DBTP on s-TiO_2(110)

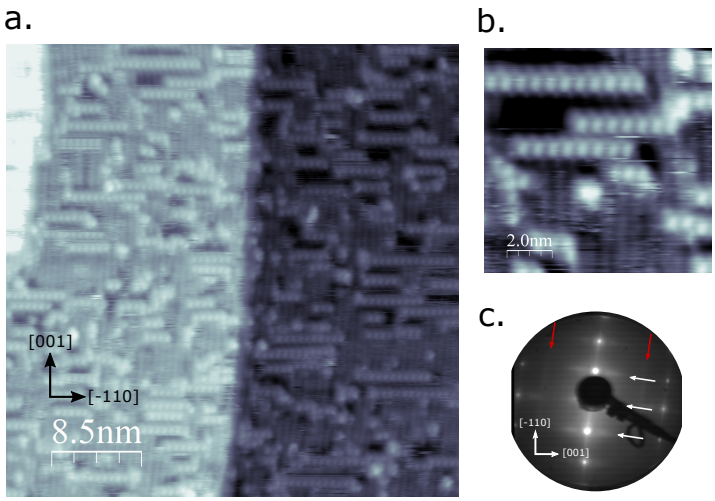

FIGURE 6.16: Overview (a) and high resolution (b) STM images measured after the deposition of cobalt atoms on a monolayer DBTP containing s-TiO_2 (110) sample and post-annealed to 420 K. Image acquisition parameters U_{bias} = 1.8 V I_{set}, = 50 pA. The LEED pattern of the sample is shown in (c) and measured with an energy of 45 eV.

An s-TiO_2 (110) sample containing a combination of DBTP and cobalt atoms is annealed to 420 K. At this temperature, in the cobalt free sample, DBTP molecules remain intact, however, with the addition of cobalt, a new super periodicity emerge in the surface. Besides the characteristic spots of the clean surface and the previously discussed molecular features (see figure 6.2 for more detail), new fuzzy stripes, marked with the white arrows, emerge in the LEED pattern 6.16 (c).

The overview STM image of the system, shown in the figure 6.16 (a), presents on the one hand stripes running along the surface [001] direction as expected for the organic over-layer. Due to the lack of intra molecular resolution, we can not account if the molecules are already polymerized or not. The LEED pattern shows two stripes (pointed with the red arrows) related to the inter-phenyl distance of 4.2 Å. Nevertheless, we can not elucidate whether these are the only molecular features (indication of a successful polymerization for the cobalt free case), or due to the super imposed intensity of the new diffraction spots.

On the other hand, new stripes with an apparent higher height, appear perpendicular to the main surface anisotropic direction. Thus the stripes run along the [-110] direction and have an overall periodicity of 6.5 Å, same of the lattice constant of the surface in this direction. We tentatively assign these protrusions as individual cobalt atoms which are also the origin of the new diffraction pattern observed by LEED. Within this interpretation, cobalt atoms are located in between the molecular

chains running on the [001] direction, see the close up STM image in figure 6.16 (b). Knowing that both DBTP and PPP adsorb preferentially in the surface trenches, we concluded that the cobalt atoms are adsorbed on top of the bridging oxygen atoms of the surface. This explains the apparent increased height and the periodicity in the [-110] direction. To unravel whether the molecular de-halogenation has already taken place or not we perform photoemission measurements.

6.5.2 XPS studies of cobalt induced polymerization of DBTP on s-TiO_2(110)

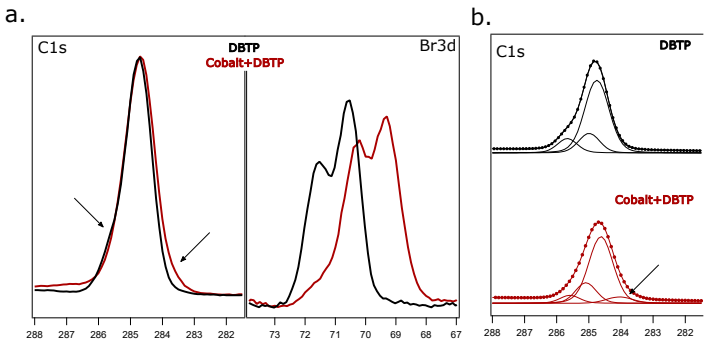

FIGURE 6.17: High resolution XPS of a monolayer DBTP on s-TiO_2 (110) with (red) and without cobalt (black). In (a) the C 1s and Br 3d CL peaks are shown whereas in (b) the peak deconvolution of the C 1s CL is included.

C1s and Br3d CLs of DBTP molecule deposited on the s-TiO_2 (110) at RT, with (red) and without (black) cobalt atoms are shown in figure 6.17 (a). The most striking feature is that even at RT, upon the addition of cobalt, the Br 3d CL shifts from 70.6 eV to 69.3 eV. The shift of 1.3 eV is equal to the one found on r-TiO_2 (110) (70.7 eV to 69.35 eV) at higher temperature and ascribed to the formation of TiBr species. The shift direction also coincides with chemisorbed Br species found on c-Au (111) and $GdAu_2$. Therefore, we ascribe the new Br 3d CL position to a Br_x^{-x}-Co_x^{+x} species with unknown coordination, indicating that the addition of cobalt facilitates the molecular de-halogenation on the s-TiO_2 (110) at RT.

Contrary to the previously discussed situations, here, the bromine intensity is preserved. Also, a small shoulder on the higher B.E side indicates that some of the molecules are still unreacted. This means that there is a non stoichiometric amount of cobalt atoms per bromine atoms in DBTP. The cobalt CL intensity is too low to quantify the amount of deposited Co atoms per Br.

The C 1s CL shown in figure 6.17 (a) also agrees with the observations seeing on the Br 3d CL. The deposition of cobalt atoms (red line) attenuates the peak intensity in the higher BE side in favour of an intensity increase in the low BE side (follow the arrows). This changes are interpreted in figure 6.17 (b), after deconvolving the C 1s CL peak. As discussed previously, the C 1s CL peak of DBTP is deconvoluted with three components (see also figure 6.11). The peak at 285.59 eV corresponds to the halogen bound carbon atoms whereas the other two peaks, located at 285.08 eV and at 284.6 eV, constitute the carbon atoms of the backbone of the molecule.

Interestingly, upon deposition of cobalt atoms, the integrated intensity of the higher BE peak decreases considerably in favour a new peak that emerges on the low BE side, at 284.1 eV. A similar behaviour was observed by Di Giovannantonio *et al* [79] for aryl halide molecules on Cu (110) and ascribed to the de-halogenation and

coordination of radical carbon atoms with the individual surface copper adatoms. In a similar way, we interpret the C 1s CL spectrum as a signature of the formation of an organometallic phase. Consequently, we infer that the addition of cobalt atoms promotes the "*intermediate mechanism*" of the classical Ullmann coupling reaction, rather than the "*radical mechanism*" observed on the r-TiO_2 (110) promoted by the subsurface i-Ti atoms. Taking into account that Co can have high oxidization states, the observation is in agreement with the organometallic interemdiate mechanism introduced in chapter 3 section 3.4.1.

Next we anneal the sample to induced the -C-C- homo coupling of the organometallic intermediates and answer the following questions:

1. Does the external catalyst (cobalt) decrease the coupling temperature and thus the reaction activation energy?
2. Is the reaction yield overall improved / has the desorption rate decrease?
3. Is the Ullmann condensation still present?

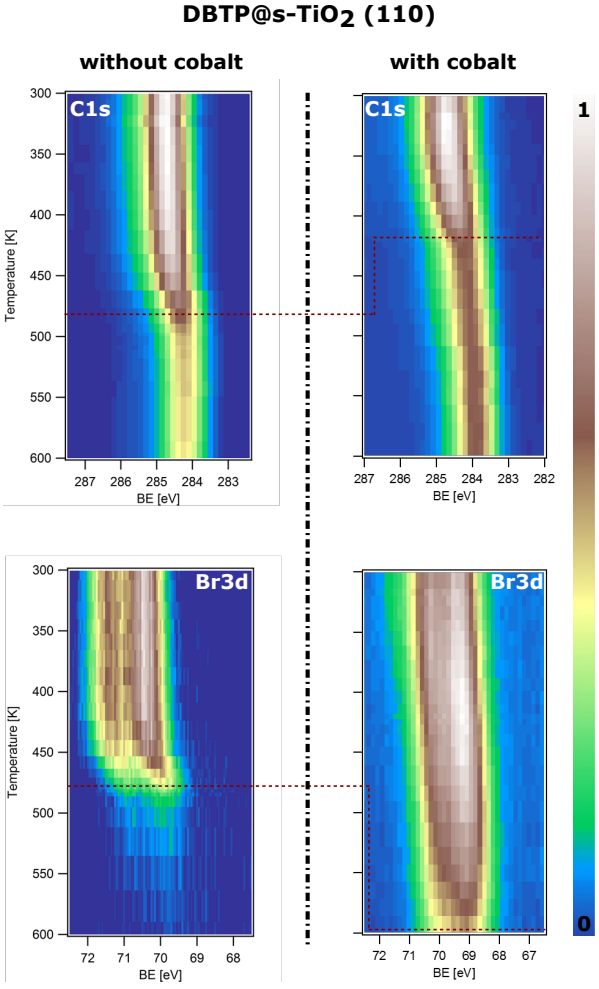

FIGURE 6.18: TD-XPS measured at the BEs where the C 1s and Br 3d CL of DBTP appear. The temperature is ramp up from RT to 600 K. The left column represents the pristine monolayer of DBTP on s-TiO_2 (110), whereas in the right column cobalt atoms were.

In figure 6.18, we present TD-XPS measurements performed on the C 1s and Br 3d CLs of DBTP on the s-TiO_2 (110), with and without cobalt atoms. The left column corresponds to the cobalt free sample while in the right column cobalt atoms were added subsequently.

As already shown in figure 6.8, the dehalogenation of DBTP on s-TiO_2 occurs at about 450 K. Both C 1s and Br 3d CLs shifts in energy and the intensity decreases considerably. At 600 K all bromine atoms are desorbed and the C 1s total intensity corresponds to the 24 % of the initial one.

The scenario is decisively different upon adding few cobalt atoms. On the one hand, a change in the C 1s CL is seen at 50 K lower than without cobalt. The peak gets narrower and shifts towards lower BE, as expected of a successful polymerization. Moreover, the final C 1s intensity at 600 K is 50 % of the initial one. Thus, Co atoms have reduced the reaction barrier and improved the reaction yield.

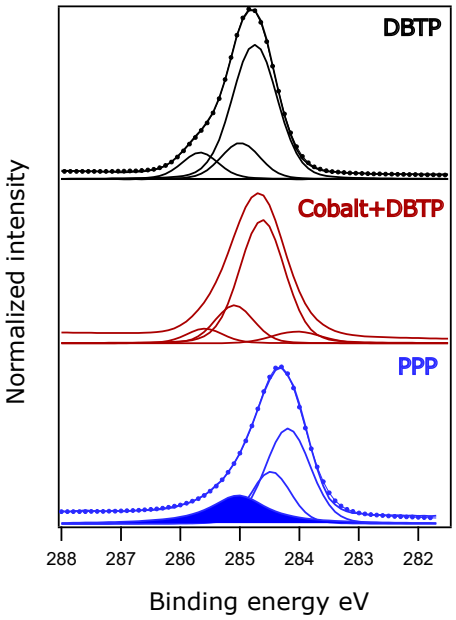

FIGURE 6.19: High resolution C1s CL peak deconvolution measured after the adsorption of DBTP on s-TiO_2 (110) in black, after the addition of cobalt atoms in red and after annealing to 600 K in blue.

On the other hand, the Br 3d Cl also shows considerable differences. Keeping in mind that the Br CL is already shifted after the addition of cobalt atoms (see figure 6.17), it is remarkable that the Br3d CL intensity remains unaltered until 550 K, whereas on the cobalt free sample, a complete desorption takes place below 500 K. Thus, adding cobalt atoms increases the adsorption energy of Br atoms on the surface. Combining the here presented Br 3d CL waterfall plot results and the new periodicity observed by STM and LEED after the addition of cobalt, our hypotheses suggesting the formation of an stable new Br_x^{-x}-Co_x^{+x} specie is reinforced.

In general, the TD-XPS measurements proofs that cobalt atoms can be used as a catalyst for the reaction on s-TiO_2 (110).

Finally, in figure 6.19, we deconvolute the C 1s CL of for the cobalt containing sample after having been annealed to 600 K. in order to unravel the presence of the Ullmann condensation side path. For comparison purposes, we include in the figure the spectra of DBTP (black) and DBTP + cobalt (red), which have been already introduced and explained in detail before (see figure 6.17 for more details). After the PPP

formation (bottom blue spectra), the lower and higher BE peaks present on the red spectra i.e the carbons of the organometallic phase and the halogen bonded carbon of unreacted molecules respectively, vanished. Instead, as highlighted with a blue area, a peak emerges at 285.03 eV, corresponding to the carbon atoms comprising ether groups. This means that, as seeing on the r-TiO_2 (110), the Ullmann condensation side reaction also happens after the addition of cobalt. This is not particularly surprising taking into account that the radicals formed in the organometallic phase are extremely reactive towards nucleophillic attacks. Therefore, although the cobalt addition has shown to considerably improve the total reaction yield, different reaction paths are still subject to the inherent properties of the TiO_2 surface.

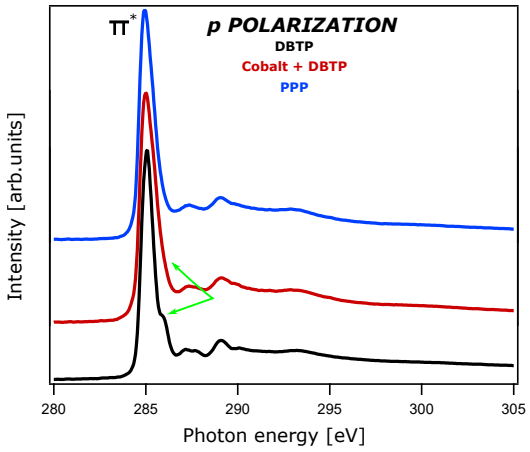

FIGURE 6.20: *p* polarized NEXAFS spectra of the C1s adsorption edge measured after the adsorption of DBTP on s-TiO_2 (110) (black), after the addition of cobalt atoms (red) and after annealing to 600 K (blue).

The above presented three phases (DBTP, DBTP+Cobalt & PPP) are also measured by NEXAFS and shown in the figure 6.20. Only the spectra acquired with *p* polarization are included where the π^* resonance gives the main adsorption feature. For better visualization porpoises the spectra are normalized to have the same intensity. In the raw data (not shown) the π^* resonance is more intense when Co was used to catalyze the reaction than on the pristine s-TiO_2 surface. As expected from XPS, NEXAFS also shows that the molecular de-halogenation already occurs upon the addition of cobalt at RT as is evident by the quenching of the high photon energy feature attributed to the chemical shift at the Br-C bond. Afterwards the evolution of the π^* agrees with the reported measurements for PPP.

The final confirmation of the cobalt induced polymerization reaction is obtained with ARPES, by measuring again the VB ofthe final reaction product along the surface [001] direction. Again, we compared the results with the ones obtained in the cobalt free r-TiO_2(110) and s-r$TiO_{(2)}$ samples. Results are summarized in figure 6.21. Without going much into details, the electronic properties of the molecular band obtained with the addition of cobalt, figure 6.21 (c), is similar in both energy and momentum to the PPP related bands obtained on the reduced (a) and stoichiometric surfaces (b), proving the successfully polymerization and hence the viability of promoting the reaction *via* an external catalyst.

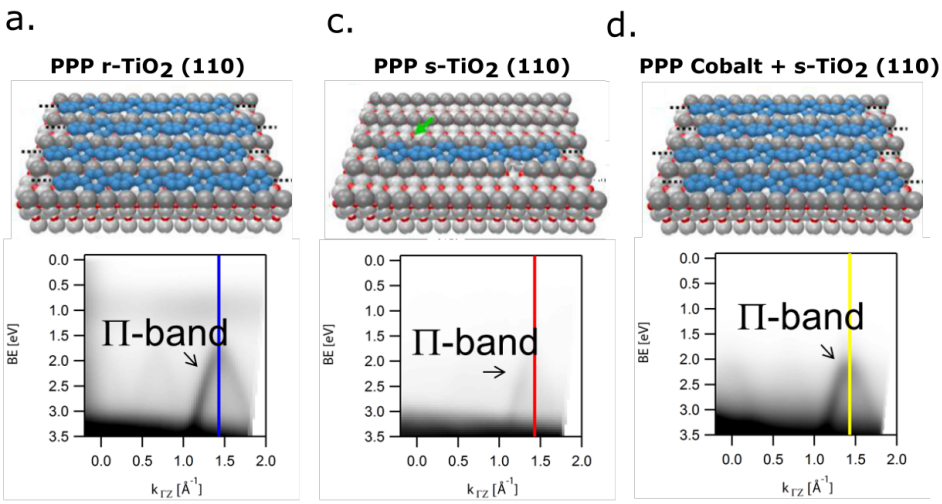

FIGURE 6.21: Comparison of raw ARPES maps measurements taken for PPP on (a) r-TiO_2 (110) surface, (b) s-TiO_2 (110) surface and (c) cobalt containing s-TiO_2 (110) surface.

6.6 Conclusion

Throughout this chapter, a successful Ullmann "based" polymerization reaction on the reduced and stoichiometric TiO_2 (110) surfaces has been established. By STM and LEED, we have identified long PPP chains and their electronic properties have been established by ARPES measurements. Finally with high resolution XPS and TD-XPS measurements, we have isolated different reaction mechanism and products.

The main mechanism was found to be promoted by i-Ti atoms. An intensity increase in the Ti 2p CL observed after the molecular dehalogenation while leaving the DS and overall surface reduction unaffected were the strongest indication supporting the i-Ti catalyzed mechanism. Besides, the temperature at which i-Ti diffuse to the surface was found to be close to the dehalogenation temperature. Importantly, due to the lower amount of i-Ti in the stoichiometric sample, lower reaction yields were found, further supporting the proposed mechanism.

A side reaction mechanism, named Ullmann condensation reaction, was found to act in parallel. The appearance of a high BE peak in the C 1s CL after the molecular dehalogenation was ascribed to the presence of ether (-C-O-) bonds, as consequence of the reaction of the molecule with the surface OH groups. Correlation between dehalogenation and surface OH signal disappearance was found by TD-XPS. Besides, compared to the clean surface, the OH signal disappeared 25 K earlier with the molecular overlayer, further supporting this interpretation. Finally, the appearance of bright protrusions in the STM upon polymerization was ascribed to the presence of the Ullmann condensation side reaction products.

Finally, the coupling reaction was successfully promoted by the addition of cobalt as an external catalyst. Interestingly, by XPS and STM, evidences of an organometallic intermediate phase were discovered, reinforcing our initial interpretation claiming that a catalyst must be capable of donating two electrons in order to promote the Ullmann reaction via the formation of organometallic species. The ultimate proved of the PPP formation was established by ARPES.

The highest reaction yield among all the isolated mechanism is achieved with the addition of an external catalyst and therefore is presented as a viable and appealing strategy to promote the Ullmann coupling reaction in other unconventional surfaces.

Chapter 7

Conclusions

7.1 Conclusions

The future of GNR based organic devices relies on new methods capable of either, *ex-situ* transferring atomically precise GNRs previously synthesize on model surfaces onto suitable semiconductor surfaces, or on new strategies capable of producing *in-situ* GNRs directly on semiconductors or other technologically appealing surfaces. The former requires strategies to reduce the energy cost of large scale GNR fabrication that are needed for the *ex-situ* transfer approach, while the latter still lacks the demonstration of GNR synthesis in sufficient quality for the realization *in-situ* device fabrication.

Throughout this thesis we have demonstrated that the possibility of *in-situ* growing GNRs onto technologically relevant surfaces is a viable strategy. As a consequence, we come up with a strategy that encourages the in-situ GNR production onto other significant surfaces. Besides, strategies for optimizing reaction yield and energy consumption while preserving the properties and extension of GNRs are provided.

Using a multitechnique approach, we have established the realization of poly-p-phenylene (PPP) wires *via* the Ullmann coupling reaction on the three $GdAu_2$, c-Au(111) and TiO_2(110) surfaces. The high electron mobility, an intrinsic characteristic of the PPP wires and a fingerprint of a successful polymerization, is identified on all three surfaces in the form of a highly dispersive electronic bands measured by ARPES. The identification of these PPP bands signifies an overall high reaction yields, as otherwise, due to the surface averaging nature of the technique, signals would be unresolvable.

Reaction yields, rates and mechanistic interpretations have been deduced for the three surfaces combining STM, LEED and photoemission experiments. Whereas the chemical fingerprints of the coupling reaction have been thoroughly established by XPS measurements, the interpretation of the reaction yields and rates required the incorporation of kinetic factors that were deduced from a structural changes observed by STM and LEED. Consequently diffusion processes were unravelled to influence the final reaction yield together with the catalytic properties of the surfaces.

The original supramolecular arrangement of 4,4"-Dibromop-terphenyl (DBTP) molecules prior to polymerization is found to be similar on all three surfaces, as demonstrated by STM and LEED analysis. This shows that intermolecular interactions can prevail the molecule surface interactions to a great extent, and therefore need to be considered as an important aspect in the future implementation of the reaction on other surfaces. The interplay between attractive and repulsive forces, largely related to the halogen atom of the molecule, aligns molecules with their main axis parallel to a given surface preferential direction. Additionally, on Au (111) and $GdAu_2$ surfaces, adjacent molecules are at fixed position whereas on TiO_2 (110) the

intrinsic surface conformation prevents adjacent molecules to "feel" each other. Consequently, PPP wires are synthesize in the direction where DBTP molecules were previously aligned. Interestingly, on the Au (111) surface the PPP growth is unravelled to be accomplished by intra-chain diffusion of adjacent molecules, contrary to the intuitive linear intra-chain coupling process. This results highlighted the importance of considering diffusion energy barriers for the polymerization reaction mechanism.

Using temperature dependant XPS, we provided the reaction transition temperatures. On the one hand, we have established a lower reaction activation temperature on the $GdAu_2$ surface compared to the bare Au (111). We were able to identify the underlying factors of the improved reaction condition: on the $GdAu_2$ alloy, the DBTP precursors are already favourably aligned at RT, while on Au (111) additional kinetic energy is needed and the rearrangement into the most favourable reaction geometry only takes place upon heating to about 350 K. This additional kinetic barrier leads to the measured difference in activation temperatures, rather than to differences in the surface catalytic properties. A better strategy to improved surface catalytic properties has been established on the curved Au (111) surface. We found steps with $\{100\}$ microfacets to be the most efficient sites for triggering the Ullmann reaction. We measured a 20 K reduction in the activation temperature when using the right kind of surface step orientation and density. Therefore, high step density surfaces are expected to promote the reaction at lower temperatures compared to the currently used flat Au (111) substrates.

Finally, on the TiO_2 (110) surface, optimized reaction temperatures and yields are achieved when cobalt is used as an external catalyst. Interestingly, by XPS and STM evidences of an organometallic intermediate phase were discovered, reinforcing our initial interpretation claiming that a catalyst must be capable of donating two electrons in order to promote the Ullmann reaction via the formation of organometallic species. The ultimate prove of the PPP formation was again established by ARPES, which in turn also evidences the substantial reaction yield accessible by surface averaging techniques.

Thus, the addition of an external catalyst is envisioned as an efficient addition to the on-suface Ullmann coupling approaches, and indeed the realization of GNRs in a very high yield on the model semiconductor TiO_2 (110) paves a new path towards the integration of these structures into multifunctional electronics devices.

Bibliography

[1] Frank Schwierz. "Graphene transistors". In: *Nat Nano* 5.7 (July 2010), pp. 487–496. ISSN: 1748-3387. URL: http://dx.doi.org/10.1038/nnano.2010.89.

[2] F. Bonaccorso et al. "Graphene photonics and optoelectronics". In: *Nat Photon* 4.9 (Sept. 2010), pp. 611–622. ISSN: 1749-4885. URL: http://dx.doi.org/10.1038/nphoton.2010.186.

[3] Young-Woo Son, Marvin L. Cohen, and Steven G. Louie. "Energy Gaps in Graphene Nanoribbons". In: *Phys. Rev. Lett.* 97 (21 2006), p. 216803. DOI: 10.1103/PhysRevLett.97.216803. URL: https://link.aps.org/doi/10.1103/PhysRevLett.97.216803.

[4] Yen-Chia Chen et al. "Molecular bandgap engineering of bottom-up synthesized graphene nanoribbon heterojunctions". In: *Nat Nano* 10.2 (Feb. 2015), pp. 156–160. ISSN: 1748-3387. URL: http://dx.doi.org/10.1038/nnano.2014.307.

[5] Dimas G. de Oteyza et al. "Substrate-Independent Growth of Atomically Precise Chiral Graphene Nanoribbons". In: *ACS Nano* 10.9 (2016). PMID: 27548516, pp. 9000–9008. DOI: 10.1021/acsnano.6b05269. eprint: http://dx.doi.org/10.1021/acsnano.6b05269. URL: http://dx.doi.org/10.1021/acsnano.6b05269.

[6] Leopold Talirz, Pascal Ruffieux, and Roman Fasel. "On-Surface Synthesis of Atomically Precise Graphene Nanoribbons". In: *Advanced Materials* 28.29 (2016), pp. 6222–6231. ISSN: 1521-4095. DOI: 10.1002/adma.201505738. URL: http://dx.doi.org/10.1002/adma.201505738.

[7] Pascal Ruffieux et al. "On-surface synthesis of graphene nanoribbons with zigzag edge topology". In: *Nature* 531.7595 (Mar. 2016), pp. 489–492. ISSN: 0028-0836. URL: http://dx.doi.org/10.1038/nature17151.

[8] Leopold Talirz et al. "On-Surface Synthesis and Characterization of 9-Atom Wide Armchair Graphene Nanoribbons". In: *ACS Nano* 11.2 (2017). PMID: 28129507, pp. 1380–1388. DOI: 10.1021/acsnano.6b06405. eprint: http://dx.doi.org/10.1021/acsnano.6b06405. URL: http://dx.doi.org/10.1021/acsnano.6b06405.

[9] Melinda Y. Han et al. "Energy Band-Gap Engineering of Graphene Nanoribbons". In: *Phys. Rev. Lett.* 98 (20 2007), p. 206805. DOI: 10.1103/PhysRevLett.98.206805. URL: https://link.aps.org/doi/10.1103/PhysRevLett.98.206805.

[10] Xiaolin Li et al. "Chemically Derived, Ultrasmooth Graphene Nanoribbon Semiconductors". In: *Science* 319.5867 (2008), pp. 1229–1232. ISSN: 0036-8075. DOI: 10.1126/science.1150878. eprint: http://science.sciencemag.org/content/319/5867/1229.full.pdf. URL: http://science.sciencemag.org/content/319/5867/1229.

[11] Dmitry V. Kosynkin et al. “Longitudinal unzipping of carbon nanotubes to form graphene nanoribbons”. In: *Nature* 458.7240 (Apr. 2009), pp. 872–876. ISSN: 0028-0836. URL: http://dx.doi.org/10.1038/nature07872.

[12] Liying Jiao et al. “Narrow graphene nanoribbons from carbon nanotubes”. In: *Nature* 458.7240 (Apr. 2009), pp. 877–880. ISSN: 0028-0836. URL: http://dx.doi.org/10.1038/nature07919.

[13] Guillaume Vasseur et al. “Quasi one-dimensional band dispersion and surface metallization in long-range ordered polymeric wires”. In: *Nature Communications* 7 (Jan. 2016), p. 10235. URL: http://dx.doi.org/10.1038/ncomms10235.

[14] Ryan R. Cloke et al. “Site-Specific Substitutional Boron Doping of Semiconducting Armchair Graphene Nanoribbons”. In: *J. Am. Chem. Soc.* 137.28 (July 2015), pp. 8872–8875. ISSN: 0002-7863. DOI: 10.1021/jacs.5b02523. URL: http://dx.doi.org/10.1021/jacs.5b02523.

[15] Andrea Basagni et al. “Tunable Band Alignment with Unperturbed Carrier Mobility of On-Surface Synthesized Organic Semiconducting Wires”. In: *ACS Nano* 10.2 (2016). PMID: 26841052, pp. 2644–2651. DOI: 10.1021/acsnano.5b07683. eprint: http://dx.doi.org/10.1021/acsnano.5b07683. URL: http://dx.doi.org/10.1021/acsnano.5b07683.

[16] F. Ullmann and Jean Bielecki. “Ueber Synthesen in der Biphenylreihe”. In: *Berichte der deutschen chemischen Gesellschaft* 34.2 (1901), pp. 2174–2185. ISSN: 1099-0682. DOI: 10.1002/cber.190103402141. URL: http://dx.doi.org/10.1002/cber.190103402141.

[17] F. Ullmann. “Ueber eine neue Bildungsweise von Diphenylaminderivaten”. In: *Berichte der deutschen chemischen Gesellschaft* 36.2 (1903), pp. 2382–2384. ISSN: 1099-0682. DOI: 10.1002/cber.190303602174. URL: http://dx.doi.org/10.1002/cber.190303602174.

[18] F. Ullmann. “Ueber eine neue Darstellungsweise von Phenyläthersalicylsäure”. In: *Berichte der deutschen chemischen Gesellschaft* 37.1 (1904), pp. 853–854. ISSN: 1099-0682. DOI: 10.1002/cber.190403701141. URL: http://dx.doi.org/10.1002/cber.190403701141.

[19] Elena Sperotto et al. “The mechanism of the modified Ullmann reaction”. In: *Dalton Trans.* 39 (43 2010), pp. 10338–10351. DOI: 10.1039/C0DT00674B. URL: http://dx.doi.org/10.1039/C0DT00674B.

[20] Carlo Sambiagio et al. “Copper catalysed Ullmann type chemistry: from mechanistic aspects to modern development”. In: *Chem. Soc. Rev.* 43 (10 2014), pp. 3525–3550. DOI: 10.1039/C3CS60289C. URL: http://dx.doi.org/10.1039/C3CS60289C.

[21] X.-L. Zhou, M. E. Castro, and J. M. White. “Interactions of UV photons and low energy electrons with chemisorbed benzene on Ag(111)”. In: *Surface Science* 238.1 (1990), pp. 215–225. ISSN: 0039-6028. URL: http://www.sciencedirect.com/science/article/pii/003960289090079N.

[22] Ming Xi and Brian E. Bent. “Iodobenzene on Cu(111): formation and coupling of adsorbed phenyl groups”. In: *Surface Science* 278.1â€“2 (1992), pp. 19 –32. ISSN: 0039-6028. DOI: http://dx.doi.org/10.1016/0039-6028(92)90580-Y. URL: http://www.sciencedirect.com/science/article/pii/003960289290580Y.

[23] Ming Xi and Brian E. Bent. "Mechanisms of the Ullmann coupling reaction in adsorbed monolayers". In: *Journal of the American Chemical Society* 115.16 (1993), pp. 7426–7433. DOI: 10.1021/ja00069a048. eprint: http://pubs.acs.org/doi/pdf/10.1021/ja00069a048. URL: http://pubs.acs.org/doi/abs/10.1021/ja00069a048.

[24] SW Hla et al. "Inducing all steps of a chemical reaction with the scanning tunneling microscope tip: Towards single molecule engineering". In: *Phys. Rev. Lett.* 85.13 (2000), pp. 2777–2780. ISSN: 0031-9007. DOI: 10.1103/PhysRevLett.85.2777.

[25] Gregory S. McCarty and Paul S. Weiss. "Formation and Manipulation of Protopolymer Chains". In: *Journal of the American Chemical Society* 126.51 (2004). PMID: 15612715, pp. 16772–16776. DOI: 10.1021/ja038930g. eprint: http://pubs.acs.org/doi/pdf/10.1021/ja038930g. URL: http://pubs.acs.org/doi/abs/10.1021/ja038930g.

[26] L. Grill et al. "Nano-architectures by covalent assembly of molecular building blocks". In: *Nature Nanotech.* 2 (2007), p. 687. URL: http://dx.doi.org/10.1038/nnano.2007.346.

[27] Jinming Cai et al. "Atomically precise bottom-up fabrication of graphene nanoribbons". In: *Nature* 466.7305 (July 2010), pp. 470–473. ISSN: 0028-0836. DOI: 10.1038/nature09211. URL: http://dx.doi.org/10.1038/nature09211.

[28] Leopold Talirz, Pascal Ruffieux, and Roman Fasel. "On-Surface Synthesis of Atomically Precise Graphene Nanoribbons". In: *Advanced Materials* 28.29 (2016), pp. 6222–6231. ISSN: 1521-4095. DOI: 10.1002/adma.201505738. URL: http://dx.doi.org/10.1002/adma.201505738.

[29] Mohamed El Garah, Jennifer M. MacLeod, and Federico Rosei. "Covalently bonded networks through surface-confined polymerization". In: *Surface Science* 613.0 (July 2013), pp. 6–14. ISSN: 0039-6028. URL: http://www.sciencedirect.com/science/article/pii/S0039602813000976.

[30] Robert Lindner and Angelika Kühnle. "On-Surface Reactions". In: *ChemPhysChem* 16.8 (2015), pp. 1582–1592. ISSN: 1439-7641. URL: http://dx.doi.org/10.1002/cphc.201500161.

[31] Lei Dong, Pei Nian Liu, and Nian Lin. "Surface-Activated Coupling Reactions Confined on a Surface". In: *Acc. Chem. Res.* 48.10 (Oct. 2015), pp. 2765–2774. ISSN: 0001-4842. DOI: 10.1021/acs.accounts.5b00160. URL: http://dx.doi.org/10.1021/acs.accounts.5b00160.

[32] Zongping Chen et al. "Synthesis of Graphene Nanoribbons by Ambient-Pressure Chemical Vapor Deposition and Device Integration". In: *J. Am. Chem. Soc.* 138.47 (Nov. 2016), pp. 15488–15496. ISSN: 0002-7863. DOI: 10.1021/jacs.6b10374. URL: http://dx.doi.org/10.1021/jacs.6b10374.

[33] Patrick B. Bennett et al. "Bottom-up graphene nanoribbon field-effect transistors". In: *Applied Physics Letters* 103.25 (2013), p. 253114. DOI: 10.1063/1.4855116. eprint: http://dx.doi.org/10.1063/1.4855116. URL: http://dx.doi.org/10.1063/1.4855116.

[34] Stephan Roche et al. "Graphene spintronics: the European Flagship perspective". In: *2D Materials* 2.3 (2015), p. 030202. URL: http://stacks.iop.org/2053-1583/2/i=3/a=030202.

[35] Carl-Georg Freiherr von Richthofen et al. "Probing the Radialene-Character in Triplesalophen Ligands by Spectroscopic and Structural Analysis". In: *The Journal of Organic Chemistry* 77.3 (2012). PMID: 22225401, pp. 1435–1448. DOI: 10.1021/jo202273s. eprint: http://dx.doi.org/10.1021/jo202273s. URL: http://dx.doi.org/10.1021/jo202273s.

[36] B. Hammer and J. K. Norskov. "Why gold is the noblest of all the metals". In: *Nature* 376.6537 (July 1995), pp. 238–240. URL: http://dx.doi.org/10.1038/376238a0.

[37] Ton V. W. Janssens et al. "Insights into the reactivity of supported Au nanoparticles: combining theory and experiments". In: *Topics in Catalysis* 44.1 (2007), p. 15. ISSN: 1572-9028. DOI: 10.1007/s11244-007-0335-3. URL: http://dx.doi.org/10.1007/s11244-007-0335-3.

[38] Markus Kittelmann et al. "On-Surface Covalent Linking of Organic Building Blocks on a Bulk Insulator". In: *ACS Nano* 5.10 (Oct. 2011), pp. 8420–8425. ISSN: 1936-0851. DOI: 10.1021/nn2033192. URL: http://dx.doi.org/10.1021/nn2033192.

[39] P. Olszowski et al. "Aryl Halide C–C Coupling on Ge(001):H Surfaces". In: *The Journal of Physical Chemistry C* 119.49 (2015), pp. 27478–27482. DOI: 10.1021/acs.jpcc.5b08883. eprint: http://dx.doi.org/10.1021/acs.jpcc.5b08883. URL: http://dx.doi.org/10.1021/acs.jpcc.5b08883.

[40] Marek Kolmer et al. "On-surface polymerization on a semiconducting oxide: aryl halide coupling controlled by surface hydroxyl groups on rutile TiO2(011)". In: *Chem. Commun.* (2015), pp. –. ISSN: 1359-7345. URL: http://dx.doi.org/10.1039/C5CC02989A.

[41] H. Rohrer G. Binnig. "Scanning tunneling microscopy". In: *IBM journal of research and development* 30.4 (1986), p. 335.

[42] J. Bardeen. "Tunnelling from a Many-Particle Point of View". In: *Phys. Rev. Lett.* 6 (2 1961), pp. 57–59. DOI: 10.1103/PhysRevLett.6.57. URL: http://link.aps.org/doi/10.1103/PhysRevLett.6.57.

[43] E.L. Wolft. "Principles of Electron Tunneling Spectroscopy". In: *Oxford University Press* (1985).

[44] J. Tersoff and D. R. Hamann. "Theory and Application for the Scanning Tunneling Microscope". In: *Phys. Rev. Lett.* 50 (25 1983), pp. 1998–2001. DOI: 10.1103/PhysRevLett.50.1998. URL: http://link.aps.org/doi/10.1103/PhysRevLett.50.1998.

[45] Flemming Besenbacher. "Scanning tunnelling microscopy studies of metal surfaces". In: *Reports on Progress in Physics* 59.12 (1996), p. 1737. URL: http://stacks.iop.org/0034-4885/59/i=12/a=004.

[46] Stephan Hüfner. *Photoelectron Spectroscopy: Pinciples and Applications*. Springer, 2003.

[47] John Wolstenholme Jhon F. Watts. *An Introduction to Surface Analysis by XPS and AES*. Wiley, 2005.

[48] "Table of physical and chemical constants (section 4.5.2): Attenuation lenght of electrons ins solids". In: (). URL: http://www.kayelaby.npl.co.uk/toc/.

[49] Hisao Ishii et al. "Energy Level Alignment and Interfacial Electronic Structures at Organic/Metal and Organic/Organic Interfaces". In: *Advanced Materials* 11.8 (1999), pp. 605–625. ISSN: 1521-4095. DOI: 10.1002/(SICI)1521-4095(199906)11:8<605::AID-ADMA605>3.0.CO;2-Q. URL: http://dx.doi.org/10.1002/(SICI)1521-4095(199906)11:8<605::AID-ADMA605>3.0.CO;2-Q.

[50] A. Einstein. "Über einen die Erzeugung und Verwandlung des Lichtes betreffenden heuristischen Gesichtspunkt". In: *Annalen der Physik* 322.6 (1905), pp. 132–148. ISSN: 1521-3889. DOI: 10.1002/andp.19053220607. URL: http://dx.doi.org/10.1002/andp.19053220607.

[51] F.J. Himpsel. "Angle-resolved measurements of the photoemission of electrons in the study of solids". In: *Advances in Physics* 32.1 (1983), pp. 1–51. DOI: 10.1080/00018738300101521. eprint: http://dx.doi.org/10.1080/00018738300101521. URL: http://dx.doi.org/10.1080/00018738300101521.

[52] M. Abadía et al. "Massive Surface Reshaping Mediated by Metal–Organic Complexes". In: *The Journal of Physical Chemistry C* 118.51 (2014), pp. 29704–29712. DOI: 10.1021/jp505802h. eprint: http://dx.doi.org/10.1021/jp505802h. URL: http://dx.doi.org/10.1021/jp505802h.

[53] Robert S. Swingle. "Quantitative surface analysis by x-ray photoelectron spectroscopy (ESCA)". In: *Analytical Chemistry* 47.1 (1975), pp. 21–24. DOI: 10.1021/ac60351a021. eprint: http://dx.doi.org/10.1021/ac60351a021. URL: http://dx.doi.org/10.1021/ac60351a021.

[54] Ariana L. Bramblett et al. "Determination of surface coverage for tetraphenylporphyrin monolayers using ultraviolet visible absorption and x-ray photoelectron spectroscopies". In: *Surface and Interface Analysis* 33.6 (2002), pp. 506–515. ISSN: 1096-9918. DOI: 10.1002/sia.1239. URL: http://dx.doi.org/10.1002/sia.1239.

[55] Xavier Wallart, Catherine Henry de Villeneuve, and Philippe Allongue. "Truly Quantitative XPS Characterization of Organic Monolayers on Silicon: Study of Alkyl and Alkoxy Monolayers on HSi(111)". In: *Journal of the American Chemical Society* 127.21 (2005), pp. 7871–7878. DOI: 10.1021/ja0430797.

[56] Guillaume Vasseur et al. " Band Dispersion along Conjugated Organic Nanowires Synthesized on a Metal Oxide Semiconductor". In: *Journal of the American Chemical Society* 138.17 (2016). PMID: 27115554, pp. 5685–5692. DOI: 10.1021/jacs.6b02151. eprint: http://dx.doi.org/10.1021/jacs.6b02151. URL: http://dx.doi.org/10.1021/jacs.6b02151.

[57] J Braun. "The theory of angle-resolved ultraviolet photoemission and its applications to ordered materials". In: *Reports on Progress in Physics* 59.10 (1996), p. 1267. URL: http://stacks.iop.org/0034-4885/59/i=10/a=002.

[58] Friedrich Reinert and Stefan Hüfner. "Photoemission spectroscopy—from early days to recent applications". In: *New Journal of Physics* 7.1 (2005), p. 97. URL: http://stacks.iop.org/1367-2630/7/i=1/a=097.

[59] Andrea Damascelli. "Probing the Electronic Structure of Complex Systems by ARPES". In: *Physica Scripta* 2004.T109 (2004), p. 61. URL: http://stacks.iop.org/1402-4896/2004/i=T109/a=005.

[60] Roald Hoffmann. *Solid and Surfaces:A Chemist's View of Bonding in Extended Structures*. Wiley, 1989.

[61] Joaching Stöhr. *NEXAFS Spectroscopy*. Springer, 1992.

[62] J.J. Rehr and A.L. Ankudinov. "Progress in the theory and interpretation of {XANES}". In: *Coordination Chemistry Reviews* 249.1–2 (2005). Synchrotron Radiation in Inorganic and Bioinorganic Chemistry, pp. 131 –140. ISSN: 0010-8545. DOI: http://dx.doi.org/10.1016/j.ccr.2004.02.014. URL: http://www.sciencedirect.com/science/article/pii/S0010854504000414.

[63] J. Stöhr and D. A. Outka. "Determination of molecular orientations on surfaces from the angular dependence of near-edge x-ray-absorption fine-structure spectra". In: *Phys. Rev. B* 36 (15 1987), pp. 7891–7905. DOI: 10.1103/PhysRevB.36.7891. URL: http://link.aps.org/doi/10.1103/PhysRevB.36.7891.

[64] Georg Hahner. "Near edge X-ray absorption fine structure spectroscopy as a tool to probe electronic and structural properties of thin organic films and liquids". In: *Chem. Soc. Rev.* 35 (12 2006), pp. 1244–1255. DOI: 10.1039/B509853J. URL: http://dx.doi.org/10.1039/B509853J.

[65] F Jona, J A Strozier Jr, and W S Yang. "Low-energy electron diffraction for surface structure analysis". In: *Reports on Progress in Physics* 45.5 (1982), p. 527. URL: http://stacks.iop.org/0034-4885/45/i=5/a=002.

[66] Alicia Casitas and Xavi Ribas. "Insights into the Mechanism of Modern Ullmann–Goldberg Coupling Reactions". In: *Copper-Mediated Cross-Coupling Reactions*. John Wiley & Sons, Inc., 2013, pp. 253–279. ISBN: 9781118690659. DOI: 10.1002/9781118690659.ch7. URL: http://dx.doi.org/10.1002/9781118690659.ch7.

[67] Jonas Björk, Felix Hanke, and Sven Stafström. "Mechanisms of Halogen-Based Covalent Self-Assembly on Metal Surfaces". In: *Journal of the American Chemical Society* 135.15 (2013). PMID: 23506285, pp. 5768–5775. DOI: 10.1021/ja400304b. eprint: http://dx.doi.org/10.1021/ja400304b. URL: http://dx.doi.org/10.1021/ja400304b.

[68] Joseph F. Bunnett and Jhong Kook Kim. "Alkali metal promoted aromatic "nucleophilic" substitution". In: *Journal of the American Chemical Society* 92.25 (1970), pp. 7464–7466. DOI: 10.1021/ja00728a038. eprint: http://dx.doi.org/10.1021/ja00728a038. URL: http://dx.doi.org/10.1021/ja00728a038.

[69] C. L. Jenkins and J. K. Kochi. "Homolytic and ionic mechanisms in the ligand-transfer oxidation of alkyl radicals by copper(II) halides and pseudohalides". In: *Journal of the American Chemical Society* 94.3 (1972), pp. 856–865. DOI: 10.1021/ja00758a025. eprint: http://dx.doi.org/10.1021/ja00758a025. URL: http://dx.doi.org/10.1021/ja00758a025.

[70] Henk L. Aalten et al. "The copper catalysed reaction of sodium methoxide with aryl bromides. A mechanistic study leading to a facile synthesis of anisole derivatives". In: *Tetrahedron* 45.17 (1989), pp. 5565 –5578. ISSN: 0040-4020. DOI: http://dx.doi.org/10.1016/S0040-4020(01)89502-8. URL: http://www.sciencedirect.com/science/article/pii/S0040402001895028.

[71] Theodore Cohen, John Wood, and Albert G. Dietz. "Organocopper intermediates in the exchange reaction of aryl halides with salts of copper(I). The possible role of copper(III)". In: *Tetrahedron Letters* 15.40 (1974), pp. 3555 –3558. ISSN: 0040-4039. DOI: http://dx.doi.org/10.1016/S0040-4039(01)91965-3. URL: http://www.sciencedirect.com/science/article/pii/S0040403901919653.

[72] Alois Fürstner. "Chemistry of and with Highly Reactive Metals". In: *Angewandte Chemie International Edition in English* 32.2 (1993), pp. 164–189. ISSN: 1521-3773. DOI: 10.1002/anie.199301641. URL: http://dx.doi.org/10.1002/anie.199301641.

[73] Afsaneh Feiz et al. "Continuous flow room temperature reductive aqueous homo-coupling of aryl halides using supported Pd catalysts". In: *Scientific Reports* 6 (Sept. 2016), p. 32719. URL: http://dx.doi.org/10.1038/srep32719.

[74] Stefan Schlögl, Wolfgang M. Heckl, and Markus Lackinger. "On-surface radical addition of triply iodinated monomers on Au(111)—the influence of monomer size and thermal post-processing". In: *Surface Science* 606.13–14 (2012), pp. 999 –1004. ISSN: 0039-6028. DOI: http://doi.org/10.1016/j.susc.2012.02.011. URL: http://www.sciencedirect.com/science/article/pii/S0039602812000623.

[75] Marco Bieri et al. "Two-Dimensional Polymer Formation on Surfaces: Insight into the Roles of Precursor Mobility and Reactivity". In: *Journal of the American Chemical Society* 132.46 (2010). PMID: 21043454, pp. 16669–16676. DOI: 10.1021/ja107947z. eprint: http://dx.doi.org/10.1021/ja107947z. URL: http://dx.doi.org/10.1021/ja107947z.

[76] Johanna Eichhorn et al. "On-Surface Ullmann Coupling: The Influence of Kinetic Reaction Parameters on the Morphology and Quality of Covalent Networks". In: *ACS Nano* 8.8 (2014). PMID: 25036422, pp. 7880–7889. DOI: 10.1021/nn501567p. eprint: http://dx.doi.org/10.1021/nn501567p. URL: http://dx.doi.org/10.1021/nn501567p.

[77] Sören Zint et al. "Imaging Successive Intermediate States of the On-Surface Ullmann Reaction on Cu(111): Role of the Metal Coordination". In: *ACS Nano* 11.4 (2017). PMID: 28346826, pp. 4183–4190. DOI: 10.1021/acsnano.7b01109. eprint: http://dx.doi.org/10.1021/acsnano.7b01109. URL: http://dx.doi.org/10.1021/acsnano.7b01109.

[78] Hermann Walch et al. "Material- and Orientation-Dependent Reactivity for Heterogeneously Catalyzed CarbonBromine Bond Homolysis". In: *The Journal of Physical Chemistry C* 114.29 (2010), pp. 12604–12609. DOI: 10.1021/jp102704q. eprint: http://dx.doi.org/10.1021/jp102704q. URL: http://dx.doi.org/10.1021/jp102704q.

[79] Marco Di Giovannantonio et al. "Insight into Organometallic Intermediate and Its Evolution to Covalent Bonding in Surface-Confined Ullmann Polymerization". In: *ACS Nano* 7.9 (2013). PMID: 23987501, pp. 8190–8198. DOI: 10.1021/nn4035684. eprint: http://dx.doi.org/10.1021/nn4035684. URL: http://dx.doi.org/10.1021/nn4035684.

[80] Rico Gutzler et al. "Ullmann-type coupling of brominated tetrathienoanthracene on copper and silver". In: *Nanoscale* 6 (5 2014), pp. 2660–2668. DOI: 10.1039/C3NR05710K. URL: http://dx.doi.org/10.1039/C3NR05710K.

[81] Andrea Basagni et al. "Molecules–Oligomers–Nanowires–Graphene Nanoribbons: A Bottom-Up Stepwise On-Surface Covalent Synthesis Preserving Long-Range Order". In: *Journal of the American Chemical Society* 137.5 (2015). PMID: 25582946, pp. 1802–1808. DOI: 10.1021/ja510292b. eprint: http://dx.doi.org/10.1021/ja510292b. URL: http://dx.doi.org/10.1021/ja510292b.

[82] Emily A. Lewis et al. "Atomic-scale insight into the formation, mobility and reaction of Ullmann coupling intermediates". In: *Chem. Commun.* 50 (8 2014), pp. 1006–1008. DOI: 10.1039/C3CC47002D. URL: http://dx.doi.org/10.1039/C3CC47002D.

[83] Alex Saywell et al. "Manipulating the Conformation of Single Organometallic Chains on Au(111)". In: *The Journal of Physical Chemistry C* 118.3 (2014), pp. 1719–1728. DOI: 10.1021/jp409323g. eprint: http://dx.doi.org/10.1021/jp409323g. URL: http://dx.doi.org/10.1021/jp409323g.

[84] Tuan Anh Pham et al. "Comparing Ullmann Coupling on Noble Metal Surfaces: On-Surface Polymerization of 1,3,6,8-Tetrabromopyrene on Cu(111) and Au(111)". In: *Chemistry – A European Journal* 22.17 (2016), pp. 5937–5944. ISSN: 1521-3765. DOI: 10.1002/chem.201504946. URL: http://dx.doi.org/10.1002/chem.201504946.

[85] E. Charles H. Sykes et al. "Substrate-Mediated Interactions and Intermolecular Forces between Molecules Adsorbed on Surfaces". In: *Accounts of Chemical Research* 36.12 (2003). PMID: 14674785, pp. 945–953. DOI: 10.1021/ar9702861. eprint: http://dx.doi.org/10.1021/ar9702861. URL: http://dx.doi.org/10.1021/ar9702861.

[86] Gregory S. McCarty and Paul S. Weiss. "Formation and Manipulation of Protopolymer Chains". In: *Journal of the American Chemical Society* 126.51 (2004). PMID: 15612715, pp. 16772–16776. DOI: 10.1021/ja038930g. eprint: http://dx.doi.org/10.1021/ja038930g. URL: http://dx.doi.org/10.1021/ja038930g.

[87] Manh-Thuong Nguyen, Carlo A. Pignedoli, and Daniele Passerone. "An ab initio insight into the Cu(111)-mediated Ullmann reaction". In: *Phys. Chem. Chem. Phys.* 13 (1 2011), pp. 154–160. DOI: 10.1039/C0CP00759E. URL: http://dx.doi.org/10.1039/C0CP00759E.

[88] Weihua Wang et al. "Single-Molecule Resolution of an Organometallic Intermediate in a Surface-Supported Ullmann Coupling Reaction". In: *Journal of the American Chemical Society* 133.34 (2011). PMID: 21761920, pp. 13264–13267. DOI: 10.1021/ja204956b. eprint: http://dx.doi.org/10.1021/ja204956b. URL: http://dx.doi.org/10.1021/ja204956b.

[89] S; Sharma V.K Milazzo G; Caroli. *Tables of standard electrode potentals*. Wiley, 1985.

[90] B; Jordon J Bard A.J; Parsons. *Standard potentials in aqueous solutions*. Dekker, 1985.

[91] Min Chen et al. "Combined Photoemission and Scanning Tunneling Microscopy Study of the Surface-Assisted Ullmann Coupling Reaction". In: *The Journal of Physical Chemistry C* 118.13 (2014), pp. 6820–6830. DOI: 10.1021/jp4121468. eprint: http://dx.doi.org/10.1021/jp4121468. URL: http://dx.doi.org/10.1021/jp4121468.

[92] Kyung-Hoon Chung et al. "Electronic structures of one-dimensional metal-molecule hybrid chains studied using scanning tunneling microscopy and density functional theory". In: *Phys. Chem. Chem. Phys.* 14 (20 2012), pp. 7304–7308. DOI: 10.1039/C2CP23295B. URL: http://dx.doi.org/10.1039/C2CP23295B.

[93] Riccardo Ferrando, Julius Jellinek, and Roy L. Johnston. "Nanoalloys: From Theory to Applications of Alloy Clusters and Nanoparticles". In: *Chemical Reviews* 108.3 (2008). PMID: 18335972, pp. 845–910. DOI: 10.1021/cr040090g. eprint: http://dx.doi.org/10.1021/cr040090g. URL: http://dx.doi.org/10.1021/cr040090g.

[94] Feng Gao and D. Wayne Goodman. "Pd-Au bimetallic catalysts: understanding alloy effects from planar models and (supported) nanoparticles". In: *Chem. Soc. Rev.* 41 (24 2012), pp. 8009–8020. DOI: 10.1039/C2CS35160A. URL: http://dx.doi.org/10.1039/C2CS35160A.

[95] Naoki Toshima and Tetsu Yonezawa. "Bimetallic nanoparticles-novel materials for chemical and physical applications". In: *New J. Chem.* 22 (11 1998), pp. 1179–1201. DOI: 10.1039/A805753B. URL: http://dx.doi.org/10.1039/A805753B.

[96] Raghu Nath Dhital et al. "Low-Temperature Carbon–Chlorine Bond Activation by Bimetallic Gold/Palladium Alloy Nanoclusters: An Application to Ullmann Coupling". In: *Journal of the American Chemical Society* 134.50 (2012). PMID: 23198971, pp. 20250–20253. DOI: 10.1021/ja309606k. eprint: http://dx.doi.org/10.1021/ja309606k. URL: http://dx.doi.org/10.1021/ja309606k.

[97] Martina Corso et al. "Au(111)-Based Nanotemplates by Gd Alloying". In: *ACS Nano* 4.3 (2010). PMID: 20146459, pp. 1603–1611. DOI: 10.1021/nn901345s. eprint: http://dx.doi.org/10.1021/nn901345s. URL: http://dx.doi.org/10.1021/nn901345s.

[98] Christian Wäckerlin et al. "Controlling spins in adsorbed molecules by a chemical switch". In: *Nature Communications* 1 (Aug. 2010), p. 61. URL: http://dx.doi.org/10.1038/ncomms1057.

[99] Steffen Kahle et al. "The Quantum Magnetism of Individual Manganese-12-Acetate Molecular Magnets Anchored at Surfaces". In: *Nano Letters* 12.1 (2012). PMID: 22181658, pp. 518–521. DOI: 10.1021/nl204141z. eprint: http://dx.doi.org/10.1021/nl204141z. URL: http://dx.doi.org/10.1021/nl204141z.

[100] Konstantin A. Simonov et al. "Effect of Substrate Chemistry on the Bottom-Up Fabrication of Graphene Nanoribbons: Combined Core-Level Spectroscopy and STM Study". In: *The Journal of Physical Chemistry C* 118.23 (2014), pp. 12532–12540. DOI: 10.1021/jp502215m. eprint: http://dx.doi.org/10.1021/jp502215m. URL: http://dx.doi.org/10.1021/jp502215m.

[101] D. Briggs. "Handbook of X-ray Photoelectron Spectroscopy C. D. Wanger, W. M. Riggs, L. E. Davis, J. F. Moulder and G. E.Muilenberg Perkin-Elmer Corp., Physical Electronics Division, Eden Prairie, Minnesota, USA, 1979. 190 pp. 195". In: *Surface and Interface Analysis* 3.4 (1981), pp. v–v. ISSN: 1096-9918. DOI: 10.1002/sia.740030412. URL: http://dx.doi.org/10.1002/sia.740030412.

[102] C. Ambrosch-Draxl et al. “First-principles studies of the structural and optical properties of crystalline poly(*para* -phenylene)”. In: *Phys. Rev. B* 51 (15 1995), pp. 9668–9676. DOI: 10.1103/PhysRevB.51.9668. URL: http://link.aps.org/doi/10.1103/PhysRevB.51.9668.

[103] Arunabh Batra et al. “Probing the mechanism for graphene nanoribbon formation on gold surfaces through X-ray spectroscopy”. In: *Chem. Sci.* 5 (11 2014), pp. 4419–4423. DOI: 10.1039/C4SC01584C. URL: http://dx.doi.org/10.1039/C4SC01584C.

[104] M. Ormaza et al. “High Temperature Ferromagnetism in a GdAg2 Monolayer”. In: *Nano Letters* 16.7 (2016). PMID: 27247988, pp. 4230–4235. DOI: 10.1021/acs.nanolett.6b01197. eprint: http://dx.doi.org/10.1021/acs.nanolett.6b01197. URL: http://dx.doi.org/10.1021/acs.nanolett.6b01197.

[105] M. Corso et al. “Rare-Earth Surface Alloying: A New Phase for $GdAu_2$”. In: *Phys. Rev. Lett.* 105 (1 2010), p. 016101. DOI: 10.1103/PhysRevLett.105.016101. URL: http://link.aps.org/doi/10.1103/PhysRevLett.105.016101.

[106] Ke Ji Shi et al. “Ullmann coupling reaction of aryl chlorides on Au(111) using dosed Cu as a catalyst and the programmed growth of 2D covalent organic frameworks”. In: *Chem. Commun.* 52 (56 2016), pp. 8726–8729. DOI: 10.1039/C6CC03137D. URL: http://dx.doi.org/10.1039/C6CC03137D.

[107] Anna Ignaczak and J.A.N.F. Gomes. “Quantum calculations on the adsorption of halide ions on the noble metals”. In: *Journal of Electroanalytical Chemistry* 420.1 (1997), pp. 71 –78. ISSN: 1572-6657. DOI: http://dx.doi.org/10.1016/S0022-0728(96)04815-2. URL: http://www.sciencedirect.com/science/article/pii/S0022072896048152.

[108] Tzu-Chun Tseng et al. “Charge-transfer-induced structural rearrangements at both sides of organic/metal interfaces”. In: *Nat Chem* 2.5 (May 2010), pp. 374–379. ISSN: 1755-4330. URL: http://dx.doi.org/10.1038/nchem.591.

[109] Mehdi D. Esrafili and Golamreza Mahdavinia. “Nitrogen-doping improves surface reactivity of carbon nanocone”. In: *Superlattices and Microstructures* 62 (2013), pp. 140 –148. ISSN: 0749-6036. DOI: http://dx.doi.org/10.1016/j.spmi.2013.07.015. URL: http://www.sciencedirect.com/science/article/pii/S0749603613002358.

[110] G.A Somorjai. “The surface science of heterogeneous catalysis”. In: *Surface Science* 299 (1994), pp. 849 –866. ISSN: 0039-6028. DOI: http://dx.doi.org/10.1016/0039-6028(94)90702-1. URL: http://www.sciencedirect.com/science/article/pii/0039602894907021.

[111] T. Zambelli et al. “Identification of the "Active Sites" of a Surface-Catalyzed Reaction”. In: *Science* 273.5282 (1996), pp. 1688–1690. ISSN: 0036-8075. DOI: 10.1126/science.273.5282.1688. eprint: http://science.sciencemag.org/content/273/5282/1688.full.pdf. URL: http://science.sciencemag.org/content/273/5282/1688.

[112] Andrew L. Walter et al. “X-ray photoemission analysis of clean and carbon monoxide-chemisorbed platinum(111) stepped surfaces using a curved crystal”. In: *Nature Communications* 6 (Nov. 2015), p. 8903. URL: http://dx.doi.org/10.1038/ncomms9903.

[113] John T. Yates Jr. "Surface chemistry at metallic step defect sites". In: *Journal of Vacuum Science & Technology A: Vacuum, Surfaces, and Films* 13.3 (1995), pp. 1359–1367. DOI: 10.1116/1.579564. eprint: http://dx.doi.org/10.1116/1.579564. URL: http://dx.doi.org/10.1116/1.579564.

[114] Masatake Haruta. "Size- and support-dependency in the catalysis of gold". In: *Catalysis Today* 36.1 (1997), pp. 153 –166. ISSN: 0920-5861. DOI: http://dx.doi.org/10.1016/S0920-5861(96)00208-8. URL: http://www.sciencedirect.com/science/article/pii/S0920586196002088.

[115] Geoffrey C. Bond. "Gold: A relatively new catalyst". In: *Gold Bulletin* 34.4 (2001), pp. 117–119. ISSN: 2190-7579. DOI: 10.1007/BF03214823. URL: http://dx.doi.org/10.1007/BF03214823.

[116] Ronnie T. Vang et al. "Controlling the catalytic bond-breaking selectivity of Ni surfaces by step blocking". In: *Nat Mater* 4.2 (Feb. 2005), pp. 160–162. ISSN: 1476-1122. URL: http://dx.doi.org/10.1038/nmat1311.

[117] Junjie Zhang et al. "Step Edge Assisted Direct Linear Alkane Coupling". In: *Chemistry – A European Journal* (2016), n/a–n/a. ISSN: 1521-3765. DOI: 10.1002/chem.201605744. URL: http://dx.doi.org/10.1002/chem.201605744.

[118] Alex Saywell et al. "Polymerization on Stepped Surfaces: Alignment of Polymers and Identification of Catalytic Sites". In: *Angewandte Chemie International Edition* 51.21 (2012), pp. 5096–5100. ISSN: 1521-3773. DOI: 10.1002/anie.201200543. URL: http://dx.doi.org/10.1002/anie.201200543.

[119] M Corso et al. "Electronic states in faceted Au(111) studied with curved crystal surfaces". In: *Journal of Physics: Condensed Matter* 21.35 (2009), p. 353001. URL: http://stacks.iop.org/0953-8984/21/i=35/a=353001.

[120] S Rousset et al. "Self-ordering of Au(111) vicinal surfaces and application to nanostructure organized growth". In: *Journal of Physics: Condensed Matter* 15.47 (2003), S3363. URL: http://stacks.iop.org/0953-8984/15/i=47/a=009.

[121] P. H. Citrin, G. K Wertheim, and Y. Baer. "Core-Level Binding Energy and Density of States from the Surface Atoms of Gold". In: *Phys. Rev. Lett.* 41 (20 1978), pp. 1425–1428. DOI: 10.1103/PhysRevLett.41.1425. URL: http://link.aps.org/doi/10.1103/PhysRevLett.41.1425.

[122] P. Heimann, J.F. van der Veen, and D.E. Eastman. "Structure-dependent surface core level shifts for the Au(111), (100), and (110) surfaces". In: *Solid State Communications* 38.7 (1981), pp. 595 –598. ISSN: 0038-1098. DOI: http://dx.doi.org/10.1016/0038-1098(81)90947-9. URL: http://www.sciencedirect.com/science/article/pii/0038109881909479.

[123] Mauricio J. Prieto et al. "Promotion Effect of Platinum on Gold's Reactivity: A High-Resolution Photoelectron Spectroscopy Study". In: *The Journal of Physical Chemistry C* 120.19 (2016), pp. 10227–10236. DOI: 10.1021/acs.jpcc.5b08983. eprint: http://dx.doi.org/10.1021/acs.jpcc.5b08983. URL: http://dx.doi.org/10.1021/acs.jpcc.5b08983.

[124] C.J. Weststrate et al. "{CO} adsorption on Au(3 1 0) and Au(3 2 1): 6-Fold coordinated gold atoms". In: *Surface Science* 603.13 (2009), pp. 2152 –2157. ISSN: 0039-6028. DOI: http://dx.doi.org/10.1016/j.susc.2009.04.026. URL: //www.sciencedirect.com/science/article/pii/S0039602809003082.

[125] J. Gustafson et al. "Identification of Step Atoms by High Resolution Core Level Spectroscopy". In: *Phys. Rev. Lett.* 91 (5 2003), p. 056102. DOI: 10.1103/PhysRevLett.91.056102. URL: http://link.aps.org/doi/10.1103/PhysRevLett.91.056102.

[126] Xubing Zhou and J. L. Erskine. "Surface core-level shifts at vicinal tungsten surfaces". In: *Phys. Rev. B* 79 (15 2009), p. 155422. DOI: 10.1103/PhysRevB.79.155422. URL: http://link.aps.org/doi/10.1103/PhysRevB.79.155422.

[127] A. Chaudhuri et al. "Local Methylthiolate Adsorption Geometry on Au(111) from Photoemission Core-Level Shifts". In: *Phys. Rev. Lett.* 102 (12 2009), p. 126101. DOI: 10.1103/PhysRevLett.102.126101. URL: http://link.aps.org/doi/10.1103/PhysRevLett.102.126101.

[128] Ada Della Pia et al. "Electronic Structure Evolution during the Growth of Graphene Nanoribbons on Au(110)". In: *The Journal of Physical Chemistry C* 120.13 (2016), pp. 7323–7331. DOI: 10.1021/acs.jpcc.5b11884. eprint: http://dx.doi.org/10.1021/acs.jpcc.5b11884. URL: http://dx.doi.org/10.1021/acs.jpcc.5b11884.

[129] Herbert B. Michaelson. "The work function of the elements and its periodicity". In: *Journal of Applied Physics* 48.11 (1977), pp. 4729–4733. DOI: 10.1063/1.323539. eprint: http://dx.doi.org/10.1063/1.323539. URL: http://dx.doi.org/10.1063/1.323539.

[130] Slawomir Braun, William R. Salaneck, and Mats Fahlman. "Energy-Level Alignment at Organic/Metal and Organic/Organic Interfaces". In: *Advanced Materials* 21.14-15 (2009), pp. 1450–1472. ISSN: 1521-4095. DOI: 10.1002/adma.200802893. URL: http://dx.doi.org/10.1002/adma.200802893.

[131] J. L. Bredas et al. "Chain-length dependence of electronic and electrochemical properties of conjugated systems: polyacetylene, polyphenylene, polythiophene, and polypyrrole". In: *J. Am. Chem. Soc.* 105.22 (Oct. 1983), pp. 6555–6559. ISSN: 0002-7863. DOI: 10.1021/ja00360a004.

[132] Ulrike Diebold. "The surface science of titanium dioxide". In: *Surface Science Reports* 48.5-8 (Jan. 2003), pp. 53–229. ISSN: 0167-5729. URL: http://www.sciencedirect.com/science/article/pii/S0167572902001000.

[133] Lauren Benz et al. "McMurry Chemistry on TiO2(110): Reductive CC Coupling of Benzaldehyde Driven by Titanium Interstitials". In: *Journal of the American Chemical Society* 131.41 (2009). PMID: 19778050, pp. 15026–15031. DOI: 10.1021/ja905522c. eprint: http://dx.doi.org/10.1021/ja905522c. URL: http://dx.doi.org/10.1021/ja905522c.

[134] Lauren Benz et al. "Molecular Imaging of Reductive Coupling Reactions: Interstitial-Mediated Coupling of Benzaldehyde on Reduced TiO2(110)". In: *ACS Nano* 5.2 (2011). PMID: 21229961, pp. 834–843. DOI: 10.1021/nn103144u. eprint: http://dx.doi.org/10.1021/nn103144u. URL: http://dx.doi.org/10.1021/nn103144u.

[135] Oier Bikondoa et al. "Direct visualization of defect-mediated dissociation of water on TiO2(110)". In: *Nat Mater* 5.3 (Mar. 2006), pp. 189–192. ISSN: 1476-1122. URL: http://dx.doi.org/10.1038/nmat1592.

[136] Chi Lun Pang, Robert Lindsay, and Geoff Thornton. "Chemical reactions on rutile TiO2(110)". In: *Chem. Soc. Rev.* 37.10 (2008), pp. 2328–2353. ISSN: 0306-0012. URL: http://dx.doi.org/10.1039/B719085A.

[137] P. Karmakar, G. F. Liu, and J. A. Yarmoff. "Sputtering-induced vacancy cluster formation on $TiO_2(110)$". In: *Phys. Rev. B* 76 (19 2007), p. 193410. DOI: 10.1103/PhysRevB.76.193410. URL: http://link.aps.org/doi/10.1103/PhysRevB.76.193410.

[138] K. Mitsuhara et al. "The source of the Ti 3d defect state in the band gap of rutile titania (110) surfaces". In: *The Journal of Chemical Physics* 136.12 (2012), p. 124707. DOI: 10.1063/1.3697866. eprint: http://dx.doi.org/10.1063/1.3697866. URL: http://dx.doi.org/10.1063/1.3697866.

[139] W Göpel et al. "Surface defects of TiO2(110): A combined XPS, XAES AND ELS study". In: *Surface Science* 139.2 (1984), pp. 333 –346. ISSN: 0039-6028. DOI: http://dx.doi.org/10.1016/0039-6028(84)90054-2. URL: http://www.sciencedirect.com/science/article/pii/0039602884900542.

[140] Jesper Matthiesen et al. "Observation of All the Intermediate Steps of a Chemical Reaction on an Oxide Surface by Scanning Tunneling Microscopy". In: *ACS Nano* 3.3 (2009), pp. 517–526. DOI: 10.1021/nn8008245. eprint: http://dx.doi.org/10.1021/nn8008245. URL: http://dx.doi.org/10.1021/nn8008245.

[141] Tracy L. Thompson, Oliver Diwald, and John T. Yates. "CO2 as a Probe for Monitoring the Surface Defects on TiO2(110)Temperature-Programmed Desorption". In: *J. Phys. Chem. B* 107.42 (Oct. 2003), pp. 11700–11704. ISSN: 1520-6106. DOI: 10.1021/jp030430m. URL: http://dx.doi.org/10.1021/jp030430m.

[142] Zhen Zhang and John T. Yates. "Electron-Mediated CO Oxidation on the TiO2(110) Surface during Electronic Excitation". In: *Journal of the American Chemical Society* 132.37 (2010). PMID: 20806898, pp. 12804–12807. DOI: 10.1021/ja106207w. eprint: http://dx.doi.org/10.1021/ja106207w. URL: http://dx.doi.org/10.1021/ja106207w.

[143] R. Schaub et al. "Oxygen Vacancies as Active Sites for Water Dissociation on Rutile $TiO_2(110)$". In: *Phys. Rev. Lett.* 87 (26 2001), p. 266104. DOI: 10.1103/PhysRevLett.87.266104. URL: http://link.aps.org/doi/10.1103/PhysRevLett.87.266104.

[144] Markus B Hugenschmidt, Lara Gamble, and Charles T Campbell. "The interaction of H2O with a TiO2(110) surface". In: *Surface Science* 302.3 (1994), pp. 329 –340. ISSN: 0039-6028. DOI: http://dx.doi.org/10.1016/0039-6028(94)90837-0. URL: http://www.sciencedirect.com/science/article/pii/0039602894908370.

[145] "METADISE". In: (). URL: http://http://metadise.org/w/Lesson_2.

[146] Luis A. Miccio et al. “Interplay between Steps and Oxygen Vacancies on Curved TiO2(110)”. In: *Nano Letters* 16.3 (2016). PMID: 26752001, pp. 2017–2022. DOI: 10.1021/acs.nanolett.5b05286. eprint: http://dx.doi.org/10.1021/acs.nanolett.5b05286. URL: http://dx.doi.org/10.1021/acs.nanolett.5b05286.

[147] C. Ambrosch-Draxl et al. “First-principles studies of the structural and optical properties of crystalline poly(para-phenylene)”. In: *Phys. Rev. B* 51 (15 1995), pp. 9668–9676. DOI: 10.1103/PhysRevB.51.9668. URL: http://link.aps.org/doi/10.1103/PhysRevB.51.9668.

[148] J. A. Lipton-Duffin et al. “Synthesis of Polyphenylene Molecular Wires by Surface-Confined Polymerization”. In: *Small* 5.5 (2009), pp. 592–597. ISSN: 1613-6829. DOI: 10.1002/smll.200801943. URL: http://dx.doi.org/10.1002/smll.200801943.

[149] David O. Scanlon et al. “Band alignment of rutile and anatase TiO2”. In: *Nat Mater* 12.9 (Sept. 2013), pp. 798–801. ISSN: 1476-1122. URL: http://dx.doi.org/10.1038/nmat3697.

[150] Peter Puschnig et al. “Reconstruction of Molecular Orbital Densities from Photoemission Data”. In: *Science* 326.5953 (2009), pp. 702–706. ISSN: 0036-8075. DOI: 10.1126/science.1176105. eprint: http://science.sciencemag.org/content/326/5953/702.pdf. URL: http://science.sciencemag.org/content/326/5953/702.

[151] HeimelG. et al. “Charged and metallic molecular monolayers through surface-induced aromatic stabilization”. In: *Nat Chem* 5.3 (Mar. 2013), pp. 187–194. ISSN: 1755-4330. URL: http://dx.doi.org/10.1038/nchem.1572.

[152] G. Koller et al. “Intra- and Intermolecular Band Dispersion in an Organic Crystal”. In: *Science* 317.5836 (2007), pp. 351–355. ISSN: 0036-8075. DOI: 10.1126/science.1143239. eprint: http://science.sciencemag.org/content/317/5836/351.pdf. URL: http://science.sciencemag.org/content/317/5836/351.

[153] Hannes Offenbacher et al. “Orbital tomography: Molecular band maps, momentum maps and the imaging of real space orbitals of adsorbed molecules”. In: *Journal of Electron Spectroscopy and Related Phenomena* 204.Pt A (Oct. 2015), pp. 92–101. ISSN: 1873-2526. URL: http://www.ncbi.nlm.nih.gov/pmc/articles/PMC4691939/.

[154] Luis Cardenas et al. “Synthesis and electronic structure of a two dimensional [small pi]-conjugated polythiophene”. In: *Chem. Sci.* 4 (8 2013), pp. 3263–3268. DOI: 10.1039/C3SC50800E. URL: http://dx.doi.org/10.1039/C3SC50800E.

[155] Donald B. Rogers et al. “Crystal chemistry of metal dioxides with rutile-related structures”. In: *Inorganic Chemistry* 8.4 (1969), pp. 841–849. DOI: 10.1021/ic50074a029. eprint: http://dx.doi.org/10.1021/ic50074a029. URL: http://dx.doi.org/10.1021/ic50074a029.

[156] Marisa Scrocco. “X-ray photoelectron spectra of Ti4+ in TiO2. Evidence of band structure”. In: *Chemical Physics Letters* 61.3 (1979), pp. 453 –456. ISSN: 0009-2614. DOI: http://dx.doi.org/10.1016/0009-2614(79)87148-1. URL: http://www.sciencedirect.com/science/article/pii/0009261479871481.

[157] Henri-Jean Cristau et al. "A General and Mild Ullmann-Type Synthesis of Diaryl Ethers". In: *Organic Letters* 6.6 (2004). PMID: 15012063, pp. 913–916. DOI: 10.1021/ol036290g. eprint: http://dx.doi.org/10.1021/ol036290g. URL: http://dx.doi.org/10.1021/ol036290g.

[158] Dawei Ma and Qian Cai. "N,N-Dimethyl Glycine-Promoted Ullmann Coupling Reaction of Phenols and Aryl Halides". In: *Organic Letters* 5.21 (2003). PMID: 14535713, pp. 3799–3802. DOI: 10.1021/ol0350947. eprint: http://dx.doi.org/10.1021/ol0350947. URL: http://dx.doi.org/10.1021/ol0350947.

[159] Qi Zhang et al. "(2-Pyridyl)acetone-Promoted Cu-Catalyzed O-Arylation of Phenols with Aryl Iodides, Bromides, and Chlorides". In: *The Journal of Organic Chemistry* 74.18 (2009). PMID: 19673481, pp. 7187–7190. DOI: 10.1021/jo9012157. eprint: http://dx.doi.org/10.1021/jo9012157. URL: http://dx.doi.org/10.1021/jo9012157.

[160] Marek Kolmer et al. "Polymerization of Polyanthrylene on a Titanium Dioxide (011)-(2×1) Surface". In: *Angewandte Chemie International Edition* 52.39 (2013), pp. 10300–10303. ISSN: 1521-3773. DOI: 10.1002/anie.201303657. URL: http://dx.doi.org/10.1002/anie.201303657.

[161] E.L.D. Hebenstreit et al. "The adsorption of chlorine on TiO2(1 1 0) studied with scanning tunneling microscopy and photoemission spectroscopy". In: *Surface Science* 505 (2002), pp. 336 –348. ISSN: 0039-6028. DOI: http://dx.doi.org/10.1016/S0039-6028(02)01385-7. URL: http://www.sciencedirect.com/science/article/pii/S0039602802013857.

[162] Michael Bowker and Roger A. Bennett. "The role of Ti 3+ interstitials in TiO 2 (110) reduction and oxidation". In: *Journal of Physics: Condensed Matter* 21.47 (2009), p. 474224. ISSN: 0953-8984. URL: http://stacks.iop.org/0953-8984/21/i=47/a=474224.

[163] Lauren Benz et al. "Molecular Imaging of Reductive Coupling Reactions: Interstitial-Mediated Coupling of Benzaldehyde on Reduced TiO2(110)". In: *ACS Nano* 5.2 (2011). PMID: 21229961, pp. 834–843. DOI: 10.1021/nn103144u. eprint: http://dx.doi.org/10.1021/nn103144u. URL: http://dx.doi.org/10.1021/nn103144u.

[164] Andrea Basagni et al. "On-surface photo-dissociation of C-Br bonds: towards room temperature Ullmann coupling". In: *Chem. Commun.* 51.63 (2015), pp. 12593–12596. ISSN: 1359-7345. DOI: 10.1039/C5CC04317D.

[165] Qing Yuan et al. "Photocatalytic Cross-Coupling of Methanol and Formaldehyde on a Rutile TiO2(110) Surface". In: *Journal of the American Chemical Society* 135.13 (2013). PMID: 23488967, pp. 5212–5219. DOI: 10.1021/ja400978r. eprint: http://dx.doi.org/10.1021/ja400978r. URL: http://dx.doi.org/10.1021/ja400978r.

[166] A. R. Head S. Chaudhary and J. Schnadt. "Xray photoelectron spectroscopy study of adsorption of (3-mercaptopropyl)trimethoxysilane and n- propyltriethoxysilane on a rutile TiO2(110) surface". In: *Advance Materials Letters* 6.4 (2015), pp. 279–283.

[167] Andriy Borodin and Michael Reichling. "Characterizing TiO2(110) surface states by their work function". In: *Phys. Chem. Chem. Phys.* 13 (34 2011), pp. 15442–15447. DOI: 10.1039/C0CP02835E. URL: http://dx.doi.org/10.1039/C0CP02835E.

[168] Michael A. Henderson. "An HREELS and TPD study of water on TiO2(110): the extent of molecular versus dissociative adsorption". In: *Surface Science* 355.1 (1996), pp. 151 –166. ISSN: 0039-6028. DOI: http://dx.doi.org/10.1016/0039-6028(95)01357-1. URL: http://www.sciencedirect.com/science/article/pii/0039602895013571.

[169] Cristiana Di Valentin, Gianfranco Pacchioni, and Annabella Selloni. "Electronic Structure of Defect States in Hydroxylated and Reduced Rutile $TiO_2(110)$ Surfaces". In: *Phys. Rev. Lett.* 97 (16 2006), p. 166803. DOI: 10.1103/PhysRevLett.97.166803. URL: http://link.aps.org/doi/10.1103/PhysRevLett.97.166803.

[170] Richard L. Kurtz et al. "Synchrotron radiation studies of H2O adsorption on TiO2(110)". In: *Surface Science* 218.1 (1989), pp. 178 –200. ISSN: 0039-6028. DOI: http://dx.doi.org/10.1016/0039-6028(89)90626-2. URL: http://www.sciencedirect.com/science/article/pii/0039602889906262.

[171] C. M. Yim, C. L. Pang, and G. Thornton. "Oxygen Vacancy Origin of the Surface Band-Gap State of $TiO_2(110)$". In: *Phys. Rev. Lett.* 104 (3 2010), p. 036806. DOI: 10.1103/PhysRevLett.104.036806. URL: http://link.aps.org/doi/10.1103/PhysRevLett.104.036806.

[172] Estephania Lira et al. "Dissociative and molecular oxygen chemisorption channels on reduced rutile TiO2(110): An {STM} and {TPD} study". In: *Surface Science* 604.21–22 (2010), pp. 1945 –1960. ISSN: 0039-6028. DOI: https://doi.org/10.1016/j.susc.2010.08.004. URL: http://www.sciencedirect.com/science/article/pii/S0039602810003213.

[173] Shijing Tan et al. "Molecular Oxygen Adsorption Behaviors on the Rutile TiO2(110)-1×1 Surface: An in Situ Study with Low-Temperature Scanning Tunneling Microscopy". In: *Journal of the American Chemical Society* 133.6 (2011). PMID: 21247169, pp. 2002–2009. DOI: 10.1021/ja110375n. eprint: http://dx.doi.org/10.1021/ja110375n. URL: http://dx.doi.org/10.1021/ja110375n.

[174] M. P. de Lara-Castells and Jeffrey L. Krause. "Theoretical study of the UV-induced desorption of molecular oxygen from the reduced TiO2 (110) surface". In: *The Journal of Chemical Physics* 118.11 (2003), pp. 5098–5105. DOI: 10.1063/1.1545093. eprint: http://dx.doi.org/10.1063/1.1545093. URL: http://dx.doi.org/10.1063/1.1545093.

[175] Anthoula C. Papageorgiou et al. "Electron traps and their effect on the surface chemistry of TiO2(110)". In: *Proceedings of the National Academy of Sciences* 107.6 (2010), pp. 2391–2396. DOI: 10.1073/pnas.0911349107. eprint: http://www.pnas.org/content/107/6/2391.full.pdf. URL: http://www.pnas.org/content/107/6/2391.abstract.

[176] Zhuo Wang et al. "Adsorption of CO on Rutile TiO2 (110)-1 × 1 Surface with Preadsorbed O Adatoms". In: *The Journal of Physical Chemistry C* 114.42 (2010), pp. 18222–18227. DOI: 10.1021/jp1059165. eprint: http://dx.doi.org/10.1021/jp1059165. URL: http://dx.doi.org/10.1021/jp1059165.

[177] Yingge Du, Zdenek Dohnálek, and Igor Lyubinetsky. "Transient Mobility of Oxygen Adatoms upon O2 Dissociation on Reduced TiO2(110)". In: *The Journal of Physical Chemistry C* 112.7 (2008), pp. 2649–2653. DOI: 10.1021/jp077677u. eprint: http://dx.doi.org/10.1021/jp077677u. URL: http://dx.doi.org/10.1021/jp077677u.

[178] Stefan Wendt et al. "The Role of Interstitial Sites in the Ti3d Defect State in the Band Gap of Titania". In: *Science* 320.5884 (2008), pp. 1755–1759. ISSN: 0036-8075. DOI: 10.1126/science.1159846. eprint: http://science.sciencemag.org/content/320/5884/1755.full.pdf. URL: http://science.sciencemag.org/content/320/5884/1755.

[179] Yingge Du et al. "Imaging Consecutive Steps of O2 Reaction with Hydroxylated TiO2(110): Identification of HO2 and Terminal OH Intermediates". In: *The Journal of Physical Chemistry C* 113.2 (2009), pp. 666–671. DOI: 10.1021/jp807030n. eprint: http://dx.doi.org/10.1021/jp807030n. URL: http://dx.doi.org/10.1021/jp807030n.

[180] Tao Lin et al. "Steering On-Surface Polymerization with Metal-Directed Template". In: *Journal of the American Chemical Society* 135.9 (2013), pp. 3576–3582.

[181] Jinne Adisoejoso et al. "A Single-Molecule-Level Mechanistic Study of Pd-Catalyzed and Cu-Catalyzed Homocoupling of Aryl Bromide on an Au(111) Surface". In: *Chemistry – A European Journal* 20.14 (2014), pp. 4111–4116. ISSN: 1521-3765. DOI: 10.1002/chem.201304443. URL: http://dx.doi.org/10.1002/chem.201304443.